

# The overall oxygen transfer coefficient and interfacial area in aerated model hydrocarbon-based bioprocesses

by

Peter Graham Hollis

*Thesis presented in partial fulfilment  
of the requirements for the degree*



*of*  
**MASTER OF ENGINEERING  
(CHEMICAL ENGINEERING)**

*in the Faculty of Engineering  
at Stellenbosch University*

Supervisor: Prof. K. G. Clarke

March 2015

# Declaration

By submitting this thesis electronically, I declare that the entirety of the work contained therein is my own, original work, that I am the sole author thereof (save to the extent explicitly otherwise stated), that reproduction and publication thereof by Stellenbosch University will not infringe any third party rights and that I have not previously in its entirety or in part submitted it for obtaining any qualification.

Date: .....

Copyright © 2015 Stellenbosch University  
All rights reserved.

# Abstract

Bioconversion of hydrocarbons to value-added intermediates and products has significant industrial potential using both prokaryotic and eukaryotic organisms. In particular, alkanes can be converted to an expansive range of commercially important products using aerobic bioprocesses under mild process conditions. Coupled with the relative abundance of alkanes derived from gas to liquid (GTL) technologies, such as those employed by SASOL, South Africa, the commercial potential for bioconversion of alkanes is large. However, unlike carbohydrate substrates, alkane feedstocks are devoid of oxygen in their molecular structure. This means that the entire oxygen demand needs to be met by oxygen transfer. Furthermore, a decline in oxygen transfer in aqueous-hydrocarbon dispersions with increasing alkane concentration has been observed to result from depression of the overall volumetric oxygen transfer coefficient ( $K_La$ ). Therefore, understanding  $K_La$  and the fundamental parameters underpinning its behaviour is critical to ensuring the bioprocess is kinetically, rather than transport, limited in terms of both operation and scale-up.

Previous studies have examined  $K_La$  in aerated-alkane-aqueous systems. In light of the importance of oxygen transfer in bioprocesses, this study expands on the  $K_La$  understanding in 3-phase studies by including a fourth solid phase, thus more closely representing a hydrocarbon-based bioprocess. The project aimed to determine the impact of agitation, alkane concentration and solid loading on the Sauter mean bubble diameter ( $D_{SM}$ ), gas hold-up and specific interfacial area ( $a$ ) and correlate these parameters to  $K_La$ . This ultimately determined which parameter was dominant over a range of process conditions. Furthermore, concurrent measurement of the  $K_La$  and interfacial area meant the behaviour of the liquid side oxygen transfer coefficient ( $K_L$ ) could be defined, providing further insight into how changes in the process conditions impact on  $K_La$ .

Experiments were conducted in a 5 litre stirred tank bioreactor containing  $n$ -C<sub>14–20</sub> straight chain alkane, sparged with air at 0.8 vvm. In line with process conditions typical of a hydrocarbon-based bioprocess,  $K_La$  and  $a$  were measured for agitation rates from 450 to 1000 RPM, alkane concentrations from 2 to 20% v/v and yeast solids from 1 to 10 g/l.  $K_La$  was measured using the gassing out procedure using a dissolved oxygen (DO) probe which measured the response of the system to a step change in the sparge gas oxygen pressure. The probe response lag ( $\tau_p$ ),

equal to the time taken for the probe to reach 63.2% of the saturation DO concentration, was determined for every set of process conditions. The inverse of  $\tau_P$ ,  $K_P$  was taken into account when calculating  $K_La$  from the DO probe response. The area was calculated from  $D_{SM}$  and gas hold-up.  $D_{SM}$  was quantified using high speed photography and image analysis was performed in Matlab<sup>®</sup> using bespoke routines. Elimination of optical distortion and the development of an adequate light source was key to acquiring clear images.

Both  $K_La$  and interfacial area were found to be affected by changes in agitation, alkane concentration and yeast loading. An increase in agitation increased the  $K_La$  over the entire range of alkane concentration and yeast loading. Similarly, an increase in agitation resulted in an increase in interfacial area, underpinned by a decrease in the  $D_{SM}$ . It is therefore likely that the interfacial area plays a dominant role in defining  $K_La$  when considering an increase in agitation. Increases in alkane concentration resulted in a peak in  $K_La$  between 2.5 and 5% alkane concentration while further increases in alkane concentration depressed  $K_La$ . This peak was not observed in interfacial area, where an increase in alkane concentration resulted only in a decrease in interfacial area, thus indicating a positive influence of  $K_L$  on  $K_La$  at low alkane concentrations. Further increases in alkane concentration beyond those creating the peak  $K_La$  resulted in  $K_La$  depression, suggesting that the increasing viscosity imparted by the alkane decreases both  $K_L$  and interfacial area.

Increased yeast loading had opposing effects at low and high agitation rates. At low agitation rates, increased loadings were observed to increase  $K_La$ , while increased loadings at high agitation rates caused a decrease in  $K_La$ . This behaviour was also evident in interfacial area, suggesting that in this regime  $K_La$  was defined by interfacial area behaviour.

Increased yeast loading was observed to depress the  $K_La$  for all alkane concentrations when examined at a constant midpoint agitation rate. This trend was not evident in interfacial area, which increased with increasing yeast loading at the same agitation rate. The positive influence of yeast on interfacial area was likely caused by adhesion of the yeast particles to the bubble surface, lowering the  $D_{SM}$  by preventing coalescence. The disagreement between the  $K_La$  and interfacial area results suggested that yeast loading impacted negatively on  $K_L$ , which had an over-riding negative impact on  $K_La$ .

The use of reliable methods for the determination of both interfacial area and  $K_La$  were demonstrated for application in model hydrocarbon-based bioprocesses. The combined results offer a unique insight into how changes in the process conditions impact independently on  $K_L$  and interfacial area, which when combined ultimately defined the  $K_La$  behaviour. Quantification of the relative magnitude of the impact each parameter had on  $K_La$  contributed toward a fundamental understanding of oxygen transfer in model hydrocarbon-based bioprocesses.

## Abstract (Afrikaans)

Biologiese omsetting van koolwaterstowwe na produkte met finansiële waarde het beduidende industriële potensiaal met behulp van beide prokariotiese en eukariotiese organismes. In die besonder, kan alkane omgeskakel word na 'n uitgebreide reeks van kommersieel belangrike produkte met behulp van aerobiese bioprosesse onder ligte prosesse voorwaardes. Tesame met die relatiewe oorvloed van alkane afgelei van GTL tegnologie, soos dié van Sasol, Suid-Afrika, die kommersiële potensiaal vir bioconversie van alkane is groot. Maar, in teenstelling koolhidrate substrate, alkaan voerstowwe is beroof van suurstof in hul molekulêre struktuur. Dit beteken dat die hele suurstof vereiste moet nagekom word deur suurstof oordrag. Verder het 'n afname in suurstof oordrag in waterige-koolwaterstof dispersies met toenemende alkaan konsentrasie waargeneem te lei van depressie van die algehele volumetriese suurstofoordragkoëffisiënt ( $K_La$ ). Daarom verstaan  $K_La$  en die fundamentele parameters onderliggend sy gedrag is van kritieke belang om te verseker dat die bioproses is kineties, eerder as vervoer, beperk in terme van beide werking en skaal-up van bioprosesse.

Vorige studies het  $K_La$  in deurlug-alkaan-waterige stelsels ondersoek. In die lig van die belangrikheid van suurstof oordrag in bioprosesse hierdie studie brei uit op die  $K_La$  begrip in drie-fase studies deur die insluiting van 'n vierde soliede fase, dus meer nou wat 'n koolwaterstof-gebaseerde bioproses. Die doel van die projek is om die impak van vermengingstempo, alkaan konsentrasie en soliede inhoud op die Sauter gemiddelde borrel deursnee ( $D_{SM}$ ), gas-vasvanging en spesifieke gas-vloistof oppervlakarea ( $a$ ) te kwantifiseer en korreleer met  $K_La$  gedrag. Dit sou definieer die dominante parameter oor 'n verskeidenheid van prosesse voorwaardes. Verder, gelyktydige meting van die  $K_La$  en oppervlakarea kan die gedrag van die vloeistof-kant suurstofoordragkoëffisiënt ( $K_L$ ) gedefinieer. Dit sal verskaf verdere insig in hoe die veranderinge in die prosesse voorwaardes impak op  $K_La$ .

Eksperimente was uitgevoer in 'n 5 liter belugte geroerde tenk bioreaktor bevat  $n$  - C<sub>14-20</sub> regu-tketting alkane, met lug met lug deurgeborrel by 0.8 VVM. In lyn met die prosesse voorwaardes tipies van 'n koolwaterstof-gebaseerde bioproses,  $K_La$  en  $a$  was gemeet vir vermengingstempos van 450-1000 RPM, alkaan konsentrasies van 2-20 % v/v en gas vastestowwe van 1 tot 10 g / l.  $K_La$  is gemeet deur die vergassinguit prosedure met behulp van 'n suurstoffmeter wat die reaksie van die stelsel na 'n stap verandering in die voer gas suurstof druk gemeet het.

Die suurstoffmeter reaksie vertraging ( $\tau_P$ ), gelyk aan die tyd wat dit neem vir die suurstoffmeter 63.2 % van die versadiging DO konsentrasie te bereik, is bepaal vir elke prosesopset. Die inverse van  $\tau_P$ ,  $K_P$  is in ag geneem by die berekening van  $K_{La}$  uit die suurstoffmeter reaksie. Die gas-vloistof oppervlak is bereken vanaf  $D_{SM}$  en gas hold-up.  $D_{SM}$  is gekwantifiseer met behulp van hoër spoed fotografie en beeld analise is uitgevoer in Matlab<sup>®</sup> roetines. Uitskakeling van optiese vervorming en die ontwikkeling van 'n voldoende ligbron was die sleutel tot die verkryging van helder beelde.

Beide  $K_{La}$  en grens oppervlakarea gevind geraak word deur veranderinge in vermengingstempo, alkaan konsentrasie en gis laai. 'N toename in geroer het die  $K_{La}$  verbeter oor die hele reeks van alkaan konsentrasie en gis laai. Net so, 'n toename in geroer het gelei tot 'n toename in grens oppervlak, ondersteun deur 'n afname in die  $D_{SM}$ . Dit is dus waarskynlik dat die grens oppervlak speel 'n dominante rol in die definisie van  $K_{La}$  by die oorweging van 'n toename in roering. Stygings in alkaan konsentrasie gelei tot 'n hoogtepunt in  $K_{La}$  tussen 2.5 en 5 % alkaan konsentrasie terwyl verdere verhogings in alkaan konsentrasie druk die  $K_{La}$  af. Die piek was nie in oppervlakarea duidelik, waar 'n toename in alkaan konsentrasie gelei net tot 'n afname in oppervlakarea, dus dui op 'n positiewe invloed van  $K_L$  op  $K_{La}$  teen lae alkaan konsentrasies waargeneem. Verdere stygings in alkaan konsentrasie verder as die skep van die piek  $K_{La}$  gelei tot  $K_{La}$  depressie, wat daarop dui dat die toenemende viskositeit meegedeel deur die alkaan verminder beide  $K_L$  en grens oppervlak.

Verhoogde gis laai het opponerende effekte teen 'n lae en hoër vermengingstempo. By lae vermengingstempo, 'n verhoging in gis laai waargeneem  $K_{La}$  te verhoog, terwyl 'n verhoging in gis laai op 'n hoër vermengingstempo veroorsaak 'n afname in  $K_{La}$ . Hierdie gedrag was ook duidelik in grens oppervlak, wat daarop dui dat daar in hierdie regime  $K_{La}$  gedefinieer deur grens oppervlak gedrag.

Verhoogde gis laai waargeneem die  $K_{La}$  te onderdruk vir alle alkaan konsentrasies wanneer ondersoek teen 'n konstante middelpunt vermengingstempo. Hierdie tendens was nie duidelik in tussenvlak gebied, wat verhoog met toenemende gis laai op dieselfde geroer koers. Die positiewe invloed van gis op grens oppervlak is waarskynlik veroorsaak deur adhesie van die gis deeltjies aan die borrel oppervlak, die verlaging van die  $D_{SM}$  deur die voorkoming van die saamsmelting van gasborrels. Die meningsverskil tussen die  $K_{La}$  en grens oppervlakarea resultate voorgestel dat gis laai negatiewe uitwerking op  $K_L$ , met 'n dominante negatiewe impak op  $K_{La}$ .

Die gebruik van 'n betroubare metodes vir die bepaling van beide oppervlakarea en  $K_{La}$  gedemonstreer vir toepassing in model koolwaterstof-gebaseerde bioprosesse. Die gekombineerde resultate bied 'n unieke insig in hoe die veranderinge in die proses voorwaardes impak onafhanklik op  $K_L$  en oppervlakarea, wat wanneer gekombineer gedefinieer die  $K_{La}$  gedrag. Kwantifisering van die relatiewe grootte van die impak elke parameter het op  $K_{La}$  bygedra tot 'n fundamentele

*ABSTRACT (AFRIKAANS)*

**vi**

begrip van suurstof oordrag in model koolwaterstof-gebaseerde bioprosesse.

# Acknowledgements

I would like to offer my most sincere thanks to the following people, who made this body of work possible:

Firstly, Prof. Clarke for her time, knowledge, experience and encouragement that she gave so willingly. Her confidence in my research has been a source of inspiration. The skills I have learnt under her guidance will remain with me in all that I do.

Linda for the motivation, encouragement and understanding over the years.

Mom and Dad, for your love, never ending support, and giving me everything I ever needed to succeed.

My friends at the faculty, for the good times, the motivation and the coffee.

Finally, the DST-NRF Centre of Excellence in Catalysis (c\*change) and the Department of Process Engineering for funding and supporting this project.

**The more that you read,  
the more things you will know.  
The more that you learn,  
the more places you'll go.**  
- Dr. Seuss



# Contents

<b>Declaration</b>	<b>i</b>
<b>Abstract</b>	<b>ii</b>
<b>Abstract (Afrikaans)</b>	<b>iv</b>
<b>Acknowledgements</b>	<b>vii</b>
<b>Nomenclature</b>	<b>xviii</b>
<b>1 Introduction</b>	<b>1</b>
<b>2 Literature Review</b>	<b>4</b>
2.1 Alkane-Based Bioprocesses . . . . .	5
2.1.1 Use of Alkanes as a Bioprocess Feedstock . . . . .	5
2.1.2 Metabolism of Alkane Substrates . . . . .	6
2.1.3 Oxygen Solubility in Alkanes . . . . .	7
2.1.4 Oxygen Supply in Alkane Substrates . . . . .	9
2.1.5 Alkane Viscosity . . . . .	10
2.2 Oxygen Transfer . . . . .	11
2.2.1 Oxygen Transfer Mechanisms . . . . .	13
2.2.2 Resistance to Oxygen Transfer in Aerated Aqueous Systems . . . . .	13
2.2.3 Diffusion Theory in Aqueous Systems . . . . .	13
2.2.4 Oxygen Transfer Mechanisms in Aqueous Systems . . . . .	15
2.2.5 Oxygen Transfer Mechanisms in Hydrocarbon-Aqueous Systems . . . . .	23
2.2.6 Spreading Coefficient of Alkanes . . . . .	24
2.2.7 Oxygen Transfer Mechanisms in Hydrocarbon-Aqueous Systems Con- taining Solids . . . . .	28
2.3 Overall Volumetric Oxygen Transfer Coefficient . . . . .	32
2.3.1 Overall Volumetric Oxygen Transfer Coefficient in Hydrocarbon-Aqueous Systems . . . . .	33
2.3.2 Overall Volumetric Oxygen Transfer Coefficient in Hydrocarbon-Aqueous System with Suspended Solids . . . . .	37

2.4	Factors Affecting Overall Volumetric Oxygen Transfer Coefficient . . . . .	37
2.4.1	Effect of Agitation on the Overall Volumetric Oxygen Transfer Coefficient	38
2.4.2	Effect of Hydrocarbon Concentration on the Overall Volumetric Oxygen Transfer Coefficient . . . . .	40
2.4.3	Effect of Solids on the Overall Volumetric Oxygen Transfer Coefficient	42
2.5	Dissolved Oxygen Measurement . . . . .	50
2.5.1	Chemical Methods . . . . .	50
2.5.2	Biological Methods . . . . .	50
2.5.3	Physical Methods . . . . .	50
2.5.4	Effect of System Conditions on the Probe Response Lag . . . . .	55
2.6	Measurement of Interfacial Area . . . . .	58
2.7	Conclusions . . . . .	60
<b>3</b>	<b>Research Scope and Hypotheses</b>	<b>61</b>
3.1	Research Scope . . . . .	61
3.2	Hypotheses . . . . .	61
3.3	Objectives . . . . .	63
<b>4</b>	<b>Experimental Materials and Apparatus</b>	<b>64</b>
4.1	Materials . . . . .	64
4.1.1	Hydrocarbon . . . . .	64
4.1.2	Non-Viable Yeast Solids . . . . .	65
4.2	Apparatus . . . . .	66
4.2.1	Bioreactor System . . . . .	66
4.2.2	Temperature Control . . . . .	68
4.2.3	Dissolved Oxygen Probe . . . . .	71
4.2.4	Camera and Lighting . . . . .	71
4.2.5	Elimination of Optical Distortion . . . . .	72
4.2.6	Microscope Photography . . . . .	74
<b>5</b>	<b>Experimental Methodology</b>	<b>76</b>
5.1	Determination of Overall Volumetric Oxygen Transfer Coefficient . . . . .	76
5.1.1	Probe Maintenance and Transmitter Calibration . . . . .	76
5.1.2	Determination of the Probe Response Lag . . . . .	77
5.1.3	Determination of Overall Volumetric Oxygen Transfer Coefficient . . .	78
5.1.4	Data Reproducibility and Benchmarking . . . . .	80
5.2	Determination of Interfacial Area . . . . .	82
5.2.1	Calculation of Interfacial Area . . . . .	82
5.2.2	Determination of Bubble Diameter . . . . .	83
5.3	Yeast Deactivation . . . . .	88

<i>CONTENTS</i>	<b>x</b>
5.4 Experimental Design . . . . .	89
5.4.1 Impact of Agitation, Alkane Concentration and Solid Loading on $K_{La}$ , $K_P$ and $a$ . . . . .	90
5.4.2 Analysis of Variance . . . . .	92
<b>6 Results and Discussion</b>	<b>94</b>
6.1 Influence of System Parameters on $K_P$ . . . . .	94
6.2 Influence of System Parameters on the $K_{La}$ . . . . .	101
6.2.1 The Influence of Agitation Rate and Alkane Concentration on $K_{La}$ at Constant Yeast Loading . . . . .	103
6.2.2 Influence of Yeast Loading on $K_{La}$ . . . . .	105
6.3 Influence of System Parameters on Interfacial Area . . . . .	109
6.3.1 Influence of Agitation Rate and Alkane Concentration on Interfacial Area at Constant Yeast Loading . . . . .	110
6.3.2 The Influence of Yeast Loading on Interfacial Area . . . . .	118
<b>7 Conclusion</b>	<b>126</b>
<b>8 Recommendations</b>	<b>129</b>
8.1 Contributions Resulting from this Project . . . . .	129
8.2 Proposal for PhD . . . . .	129
8.2.1 Objectives of the PhD Study . . . . .	130
8.2.2 Additional Contributions . . . . .	131
8.3 Proposed Timeline . . . . .	132
<b>References</b>	<b>133</b>
<b>A Influence of System Parameters on <math>D_{SM}</math> and Gas Hold-Up: Additional Data</b>	<b>145</b>
A.1 Influence of Agitation and Alkane Concentration . . . . .	145
A.2 Influence of Agitation and Yeast Loading . . . . .	147
A.3 Influence of Alkane Concentration and Yeast Loading . . . . .	149
<b>B Overall Volumetric Oxygen Transfer Coefficient Determination Code</b>	<b>151</b>
<b>C Image Recognition Code</b>	<b>156</b>
<b>D Statistical Model Validation</b>	<b>164</b>
<b>E Image Acquisition Methodology</b>	<b>169</b>
E.1 Development of Lighting Solution . . . . .	169
E.1.1 Backlit Halogen Lighting . . . . .	169
E.1.2 External Light Emitting Diode Lighting . . . . .	170

*CONTENTS***xi**

E.1.3	Internal Light Emitting Diode Lighting . . . . .	172
E.1.4	Internal Fluorescent Lighting . . . . .	172
E.2	Development of Photography Methodology . . . . .	175
E.3	Camera Specifications . . . . .	178
<b>F</b>	<b>Dissolved Oxygen Probe</b>	<b>179</b>
F.1	Operating Principle . . . . .	179
F.2	Dissolved Oxygen Probe Diagram . . . . .	180
F.3	Polarising the Dissolved Oxygen Probe . . . . .	181
F.4	Dissolved Oxygen Probe Specifications . . . . .	182
<b>G</b>	<b>Dissolved Oxygen Transmitter Calibration</b>	<b>183</b>
G.1	Dissolved Oxygen Transmitter Specifications . . . . .	183
<b>H</b>	<b>Derivation of the Second Order Probe Response Model</b>	<b>184</b>

# List of Figures

2.1	Flow diagram of oxidative pathways for <i>n</i> -alkane metabolism in yeasts (Adapted from Walker (1998)) . . . . .	7
2.2	Variation in oxygen solubility for various oil volume fractions at 25°C (Adapted from Ngo and Schumpe (2012)) . . . . .	8
2.3	Variation in oxygen solubility versus alkane chain length. [1] - Makrarczy <i>et al.</i> (1976), [2] - Blanc and Batiste (1970), [3] - Hesse and Battino (1996), [4] - da Silva <i>et al.</i> (2006), [5] - Ngo and Schumpe (2012), [6] - Cascaval <i>et al.</i> (2006); Galaction <i>et al.</i> (2004b); Rols <i>et al.</i> (1990) (Adapted from Clarke and Correia (2008)) . . . . .	9
2.4	Variation of viscosity for various carbon chain lengths reported in literature . . . . .	11
2.5	Effect of alkane viscosity on fluid viscosity as reported in literature . . . . .	12
2.6	$K_L a$ values for different viscosities in a glycerol system . . . . .	12
2.7	Steps necessary for oxygen transfer from bubble to cell (Adapted from Doran (1995)) . . . . .	14
2.8	Concentration gradient of component A driving mass transfer across area <i>a</i> (Adapted from Doran (1995)) . . . . .	15
2.9	Oxygen concentration gradients for gas-liquid mass transfer (Adapted from Doran (1995)) . . . . .	16
2.10	Surface renewal theory model (Adapted from Hines and Maddox (1985)) . . . . .	19
2.11	Possible pathways for oxygen transfer pathways from gas bubbles to microorganisms in aqueous-alkane systems (Adapted from Rols <i>et al.</i> (1990)) . . . . .	23
2.12	Oil droplet coming into contact with gas bubble, detailing the interfacial area created between the phases (Adapted from Tadmor (2004)) . . . . .	25
2.13	Possible effect of spreading coefficient on the mass transfer pathway in an gas-liquid-liquid dispersion . . . . .	27
2.14	Diagram depicting gas bubble with a single layer of solid particles adhering to the interface, showing both the actual fraction of surface coverage ( $\zeta$ ) and the maximum possible fraction of surface coverage ( $\zeta_{max}$ ) (Adapted from Vinke <i>et al.</i> (1993)) . . . . .	30
2.15	Individual Factors Contributing to the Overall Volumetric Oxygen Transfer Coefficient (Adapted from Garcia-Ochoa and Gomez (2009)) . . . . .	33
2.16	bla . . . . .	34

2.17	Enhancement followed by suppression of $K_La$ with addition of alkane to an aqueous system (Adapted from Clarke <i>et al.</i> (2006)) . . . . .	35
2.18	Oxygen Transfer Coefficient Different Bubble Sizes (Adapted from Alves <i>et al.</i> (2004)) . . . . .	39
2.19	Effect of solid concentration on probe response time ( $\tau_P$ ) as a function of agitation (adapted from Ruchti <i>et al.</i> (1981)) . . . . .	57
4.1	None-viable yeast solid size distribution . . . . .	65
4.2	Bioreactor used for Experiments, Adapted from Correia (2007) . . . . .	67
4.3	Rushton Turbine Geometry . . . . .	67
4.4	Bioreactor Headplate Geometry (Adapted from (Toledo, 2013)) . . . . .	68
4.5	Water Recirculation Configuration for Accurate Temperature Control . . . . .	69
4.6	Final Experimental Set Up Depicting Camera Location and Water Recirculation	70
4.7	Bioreactor and Water Jacket in Operation . . . . .	70
4.8	Mettler Toledo M300 transmitter used for DO measurement . . . . .	71
4.9	Final Set Up for Recording the Interfacial Area (Not to Scale) . . . . .	72
4.10	Design of the Perspex Box . . . . .	73
4.11	Perspex Box Designed to Remove Optical Distortion . . . . .	73
4.12	Zeiss AxioStar Plus Binocular Microscope . . . . .	74
4.13	Camera Configuration for Microscope Photography . . . . .	75
5.1	DO Probe Reproducibility in Pure Water at 25°C, 725 RPM . . . . .	77
5.2	Experimental Set Up for Probe Response Lag Determination . . . . .	78
5.3	Experimental Set Up for gassing out procedure (GOP) . . . . .	79
5.4	Dissolved Oxygen Concentration . . . . .	79
5.5	Comparison of $K_La$ values obtained in this study (solid markers) with the experimental results of Clarke and Manyuchi (2012) (open markers) with variation in agitation . . . . .	80
5.6	Comparison of $K_La$ values obtained in this study (solid markers) with the experimental results of Clarke and Manyuchi (2012) (open markers) with variation in alkane concentration . . . . .	81
5.7	Comparison of $K_La$ values obtained in this study (solid markers) with the experimental results of Clarke and Manyuchi (2012) (open markers) with variation in yeast loading . . . . .	81
5.8	Measurement of the Gas Hold Up . . . . .	83
5.9	The Original Image Before Cropping . . . . .	84
5.10	Image After Cropping . . . . .	85
5.11	Increased Contrast . . . . .	86
5.12	Bubble Boundaries . . . . .	86
5.13	Bubbles Dilated and Filled . . . . .	87

5.14	Small Objects Removed . . . . .	87
5.15	Image Recognition Results . . . . .	88
5.16	Yeast Cells Before (Left) and After (Right) Deactivation . . . . .	89
5.17	Comparison of active and deactivated yeast cells at 400 x magnification . . . . .	90
5.18	Comparison of active and deactivated yeast cells at 400 x magnification . . . . .	91
5.19	CCD Factor Levels, Experiment Set 1 . . . . .	91
6.1	Determination of the probe response lag and $K_p$ for the first centre point experimental configuration (all parameters mid (0) level) . . . . .	95
6.2	Reproducibility of DO response ( $C_p/C^*$ ) for the two centre point runs (all parameters mid (0) level) . . . . .	95
6.3	Model comparisons for the prediction of DO from the first experimental configuration (agitation = 561 RPM, alkane concentration = 5.35%v/v, yeast loading = 2.82 g/l) . . . . .	96
6.4	Comparison of the $K_La$ results derived using the first ( $K_p$ excluded) and second order ( $K_p$ included) models with 0% to 20% (v/v) $n$ -C <sub>14-20</sub> between 450 and 1000 RPM . . . . .	97
6.5	Pareto chart for the effect of independent variables and interaction on $K_p$ within a 95% confidence interval . . . . .	98
6.6	The effect of agitation and alkane concentration on $K_p$ at constant mid (0) yeast loading . . . . .	99
6.7	The effect of agitation and yeast loading on $K_p$ at medium alkane concentration . . . . .	100
6.8	The effect of alkane concentration and yeast loading on $K_p$ at constant mid (0) agitation . . . . .	101
6.9	Pareto chart for the effect of independent variables and interaction on $K_La$ within a 95% confidence interval . . . . .	102
6.10	$K_La$ enhancement factor with changes in agitation rate and alkane concentration at constant yeast loadings . . . . .	104
6.11	$K_La$ enhancement factor with changes in agitation rate and yeast loading at constant alkane concentrations . . . . .	106
6.12	$K_La$ enhancement factor with changes in alkane concentration and yeast loading at constant agitation rates . . . . .	108
6.13	Pareto chart for the effect of independent variables and interaction on interfacial area within a 95% confidence interval . . . . .	109
6.14	Interfacial area with changes in agitation rate and alkane concentration at constant yeast loadings . . . . .	111
6.15	$D_{SM}$ with changes in agitation rate and alkane concentration at constant (mid-point) yeast loading . . . . .	112

6.16	Gas hold up with changes in agitation rate and alkane concentration at constant (midpoint) yeast loading . . . . .	113
6.17	Bubble size distribution and $D_{SM}$ for varied alkane concentration at constant midpoint agitation . . . . .	114
6.18	$K_L$ with changes in agitation rate and alkane concentration at constant (midpoint) yeast loading . . . . .	115
6.19	Bubble size distribution and $D_{SM}$ for varied alkane concentration at constant midpoint agitation . . . . .	117
6.20	Interfacial area with changes in agitation rate and yeast loading at constant alkane concentrations . . . . .	119
6.21	$D_{SM}$ with changes in agitation rate and yeast loading at constant midpoint (0) alkane concentration . . . . .	120
6.22	Gas hold up with changes in agitation rate and yeast loading at constant midpoint (0) alkane concentration . . . . .	120
6.23	$K_L$ with changes in agitation rate and yeast loading at constant midpoint (0) alkane concentration . . . . .	121
6.24	Interfacial area with changes in alkane concentration and yeast loading at constant agitation rates . . . . .	122
6.25	$D_{SM}$ with changes in alkane concentration and yeast loading at constant midpoint (0) agitation rate . . . . .	123
6.26	Gas hold up with changes in alkane concentration and yeast loading at constant midpoint (0) agitation rate . . . . .	123
6.27	$K_L$ with changes in alkane concentration and yeast loading at constant midpoint (0) agitation rate . . . . .	124
A.1	$D_{SM}$ (a) and gas hold-up (b) with changes in agitation rate and alkane concentration at constant low (-1) yeast loading . . . . .	145
A.2	$D_{SM}$ (a) and gas hold-up (b) with changes in agitation rate and alkane concentration at constant high (+1) yeast loading . . . . .	146
A.3	$D_{SM}$ (a) and gas hold-up (b) with changes in agitation rate and yeast loading at constant low (-1) alkane concentration . . . . .	147
A.4	$D_{SM}$ (a) and gas hold-up (b) with changes in agitation rate and yeast loading at constant high (+1) alkane concentration . . . . .	148
A.5	$D_{SM}$ (a) and gas hold-up (b) with changes in alkane concentration and yeast loading at constant low (-1) agitation rate . . . . .	149
A.6	$D_{SM}$ (a) and gas hold-up (b) with changes in agitation rate and yeast loading at constant high (+1) agitation rate . . . . .	150
D.1	Observed vs. predicted values for $K_P$ . . . . .	164
D.2	Normal probability plot for $K_P$ . . . . .	164



D.3	Observed vs. predicted values for $K_{La}$ . . . . .	165
D.4	Normal probability plot for $K_{La}$ . . . . .	165
D.5	Observed vs. predicted values for interfacial area . . . . .	166
D.6	Normal probability plot for interfacial area . . . . .	166
D.7	Observed vs. predicted values for $D_{SM}$ . . . . .	167
D.8	Normal probability plot for $D_{SM}$ . . . . .	167
D.9	Observed vs. predicted values for gas hold-up . . . . .	168
D.10	Normal probability plot for gas hold-up . . . . .	168
E.1	Initial Lighting Configuration for Recording the Interfacial Area (Not to Scale)	169
E.2	Initial Lighting Configuration for Recording the Interfacial Area . . . . .	170
E.3	12 Volt light emitting diode (LED) Strip Light . . . . .	171
E.4	Second Set Up for Recording the Interfacial Area (Not to Scale) . . . . .	171
E.5	Third Set Up for Recording the Interfacial Area (Not to Scale) . . . . .	172
E.6	Design and Manufacture of Bioreactor Light Fitting . . . . .	173
E.7	Location of 28mm Port Used for Installing Fluorescent Light (Indicated by 1) .	174
E.8	Prototype Waterproof Housing for Fluorescent Light . . . . .	174
E.9	Relationship Between Depth of Field and Aperture with Desired Aperture Circled	175
E.10	Focus Grid, Camera Configuration and Field of View Aperture for Photography	177
F.1	12mm Mettler Toledo <sup>®</sup> Inpro <sup>®</sup> 6800 Dissolved Oxygen Probe Exploded View (Toledo, 2013) . . . . .	180

# List of Tables

2.1	Products from Alkanes Using Bioprocesses (Clarke and Correia, 2008) . . . . .	6
2.2	The impact of contact angle on the equilibrium spreading coefficient . . . . .	26
2.3	Literature Studies on Biological Solids and their Effect on $K_{La}$ , $K_L$ and Interfacial Area . . . . .	44
2.4	Literature Studies on Non-Biological Solids and their Effect on $K_{La}$ , $K_L$ and Interfacial Area . . . . .	45
2.5	Literature Studies on Non-Biological Solids and their Effect on $K_{La}$ , $K_L$ and Interfacial Area . . . . .	46
2.6	Literature Studies on Non-Biological Solids and their Effect on $K_{La}$ , $K_L$ and Interfacial Area . . . . .	47
2.7	Summary of methodologies for $K_{La}$ determination (Moutafchieva <i>et al.</i> , 2013) .	51
2.8	Dissolved Oxygen Probe Response in Literature . . . . .	55
4.1	$n$ -C <sub>14-20</sub> composition as determined using gas chromatography (GC) . . . . .	64
4.2	Physical properties of $n$ -C <sub>14-20</sub> as supplied by Sasol Wax (via Organic Synthesis)	65
4.3	Bioreactor Geometry, Adapted from Correia (2007) . . . . .	66
5.1	Factor Levels for Dependent Variables, Experiment Set 1 . . . . .	91
5.2	Running order and factor levels, experiment set 1 . . . . .	92
6.1	ANOVA for $K_P$ using a linear model with two way interaction . . . . .	97
6.2	ANOVA for $K_{La}$ using a quadratic model with two way interaction . . . . .	102
6.3	ANOVA for interfacial area using a quadratic model with two way interaction .	110
8.1	Proposed timeline for completion of PhD . . . . .	132
E.1	mvBlueFox 124G Compact Industrial CCD and CMOS Camera Specifications	178
F.1	Depolarisation and Repolarisation Time . . . . .	181
F.2	12mm Mettler Toledo® Inpro® 6800 Dissolved Oxygen Probe Specifications, Adapted from (Toledo, 2013) . . . . .	182
G.1	Dissolved Oxygen Transmitter M300 Specifications, Adapted from (Toledo, 2013)	183

# Nomenclature

## Variables

$a$	Interfacial area per unit working volume . . . . .	[ m <sup>2</sup> /m <sup>3</sup> ]
$A_b$	Bubble surface area . . . . .	[ m <sup>2</sup> ]
$A_{OW}$	Oil-water interfacial area area . . . . .	[ m <sup>2</sup> ]
$A_{OG}$	Oil-gas interfacial area area . . . . .	[ m <sup>2</sup> ]
$A_{WG}$	Water-gas interfacial area area . . . . .	[ m <sup>2</sup> ]
$C$	Dissolved oxygen concentration . . . . .	[ mol/m <sup>3</sup> ]
$C_1$	Initial dissolved oxygen concentration . . . . .	[ mol/m <sup>3</sup> ]
$C_A$	Molar concentration of component A . . . . .	[ mol/m <sup>3</sup> ]
$C_L$	Actual molar concentration of oxygen on the liquid side of the gas-liquid interface [ mol/m <sup>3</sup> ]	
$C_L^*$	Actual liquid phase oxygen concentration in equilibrium with the gas phase oxygen concentration . . . . .	[ mol/m <sup>3</sup> ]
$C_{Li}$	Actual initial oxygen molar concentration on the liquid side of the gas-liquid interface [ mol/m <sup>3</sup> ]	
$C_P$	Molar concentration of oxygen on the liquid side of the gas-liquid interface as mea- sured by probe . . . . .	[ mol/m <sup>3</sup> ]
$C_P^*$	Liquid phase oxygen concentration in equilibrium with the gas phase oxygen concen- tration as measured by probe . . . . .	[ mol/m <sup>3</sup> ]
$D_{SM}$	Sauter mean bubble diameter	

## NOMENCLATURE

xix

$D_A$	Intraparticle diffusion coefficient	[m <sup>2</sup> /s]
$D_{AB}$	Binary diffusion coefficient, A into B	[m <sup>2</sup> /s]
$D_e$	Equivalent bubble diameter	[μm]
$d_p$	Solid particle diameter	[μm]
$d_v$	Bubble volume diameter	[μm]
$d_s$	Bubble surface diameter	[μm]
$E_0$	Enhancement factor	
$J_A$	Molar flux of species A	[mol/m <sup>2</sup> .s]
$J_G$	Gas side oxygen molar flux	[mol/m <sup>2</sup> .s]
$J_L$	Liquid side oxygen molar flux	[mol/m <sup>2</sup> .s]
$k_L$	Liquid-side oxygen transfer coefficient	[m/s]
$k_G$	Gas-side oxygen transfer coefficient	[m/s]
$K_L$	Overall liquid-side oxygen transfer coefficient	[m/s]
$K_G$	Overall gas-side oxygen transfer coefficient	[m/s]
$K_{La}$	Overall volumetric oxygen transfer coefficient	[s <sup>-1</sup> ]
$K_P$	Inverse dissolved oxygen probe response lag	[s <sup>-1</sup> ]
$m_p$	Solid particle distribution ratio	
N	Impeller speed	[RPM]
$N_A$	Transfer rate of species A	[mol/m <sup>3</sup> .s]
$N_G$	Gas side transfer rate	[mol/m <sup>3</sup> .s]
$N_L$	Liquid side transfer rate	[mol/m <sup>3</sup> .s]
$N_b$	Number of bubbles per unit reactor volume	
P	Power input into reactor	[W]
s	Rate of surface renewal	[s <sup>-1</sup> ]

## NOMENCLATURE

xx

$S_{eq}$	Equilibrium spreading coefficient	
$S_{eq}$	Initial spreading coefficient	
$t_s$	Penetration theory contact time . . . . .	[ s ]
V	Reactor working volume . . . . .	[ m <sup>3</sup> ]
$V_b$	Bubble volume . . . . .	[ m <sup>3</sup> ]
$V_s$	Superficial gas velocity . . . . .	[ m/s ]
vvm	Gas flow volume per unit volume liquid per minute . . . . .	[ min <sup>-1</sup> ]

**Greek Letters**

$\alpha_{max}$	Maximum angle of covered bubble in particle bubble adhesion model . . . . .	[ ° ]
$\gamma_{OG}$	Oil-gas surface tension . . . . .	[ d/cm ]
$\gamma_{OW}$	Oil-water surface tension . . . . .	[ d/cm ]
$\gamma_{WG}$	Water-gas surface tension . . . . .	[ d/cm ]
$\Phi_0$	Oil volume fraction	
$\epsilon_G$	Gas hold-up	
$\mu$	Average time of exposure . . . . .	[ s ]
$\rho$	Density . . . . .	[ kg/m <sup>3</sup> ]
$\delta_G$	Gas film thickness . . . . .	[ $\mu$ m ]
$\delta_L$	Liquid film thickness . . . . .	[ $\mu$ m ]
$\tau_P$	Dissolved oxygen probe response lag . . . . .	[ s ]
$\tau_P$	Residence time of a solid particle on a bubble . . . . .	[ s ]
$\theta_0$	Equilibrium Young contact angle . . . . .	[ ° ]
$\theta$	Young contact angle . . . . .	[ ° ]
$\theta_E$	Effective contact angle . . . . .	[ ° ]

- $\zeta$  Fraction of surface coverage in particle bubble adhesion model
- $\zeta_{max}$  Maximum fraction of surface coverage in particle bubble adhesion model

### Acronyms

- ATP** adenosine triphosphate
- CCD** central composite design
- CMC** carboxymethyl cellulose
- DO** dissolved oxygen
- DOF** depth of field
- GC** gas chromatography
- GOP** gassing out procedure
- GTL** gas to liquid
- LED** light emitting diode
- OTR** oxygen transfer rate
- OUR** oxygen utilization rate
- PBA** particle bubble adhesion
- PSP** pressure step procedure
- PT** penetration theory
- SRT** surface renewal theory
- STR** stirred tank reactor
- TFT** two film theory

# Chapter 1

## Introduction

A study by The World Bank (2009) estimated that 150 billion cubic meters of natural gas was being flared and vented annually world-wide, which represented roughly one quarter of the United States' annual gas consumption. In addition to gas flaring being harmful to the environment through the release of unnecessary greenhouse gases (400 million tons of CO<sub>2</sub> per annum), the energy wasted through flaring in Sub-Saharan Africa alone could fulfil half of the continent's energy requirement (The World Bank, 2009). However, combined with Sasol's pioneering work in GTL technology, this energy source can be harnessed and converted into a range of high-value energy and chemical products, including liquid fuels, oils, waxes, alkanes and naphtha (Sasol, 2011).

Alkanes are traditionally used for their fuel value, however an alternative and potentially more effective use is by conversion to high-value commodity products using microorganisms. A large number of bacterial and yeast strains have been identified in literature as being capable of utilizing *n*-alkanes as a carbon and energy source (Wentzel *et al.*, 2007). Possible products include amino acids, organic acids, carbohydrates, vitamins, enzymes, coenzymes, antibiotics, lipids and nucleic acids (Fukui and Tanaka, 1980), the application of which are widespread in modern life. Biofunctionalisation also offers a high degree of selectivity, whereby only the targeted compounds are converted to increase the yield of a specific product. This capability is further enhanced by the fact that conversion typically takes place under moderate temperature and pressure conditions, obviating the need for specialized reaction vessels required for conventional synthetic catalysts.

The use of alkanes as a bioprocess feedstock presents a number of engineering challenges caused by the nature of the alkane substrate. Some of the difficulties include the immiscibility of the alkane with the aqueous phase, potential explosion and fire risks, volatility, inhibition of microbial growth, environmental damage, mass transfer limitation between phases (Schmid *et al.*, 1998), and the provision of adequate oxygen transfer to the conversion organisms.

In carbohydrate bioprocesses, up to half of the oxygen demand is met by the substrate itself. However, for an alkane-based substrate, the only supply of oxygen to the broth is via oxygen transfer from an external source. The requisite oxygen transfer rate is higher under these conditions, and it has been shown experimentally that the oxygen demand for yeast growth using an alkane substrate was 2.9-times higher than in a comparable carbohydrate substrate (Shennan and Levi, 1974).

Oxygen transfer difficulties are exacerbated during scale-up from lab-scale to pilot plant and production processes and this becomes proportionally more important as the size of the operation increases. Oxygen transfer is one of the vital criteria considered when scale-up is being implemented (Rao *et al.*, 1967). Insufficient oxygen transfer rate (OTR) in any alkane-based bioprocess can lead to it being transport, rather than kinetically, limited and this will deliver sub-optimal results (Clarke *et al.*, 2006). It becomes evident that there is a significant need for the accurate quantification of the complex behaviour of OTR, the corresponding overall volumetric oxygen transfer coefficient ( $K_La$ ), and the interfacial area ( $a$ ) available for adequate oxygen transfer to take place.

Despite a significant number of literature sources investigating OTR and  $K_La$  in hydrocarbon-aqueous dispersions (Clarke and Correia, 2008), their behaviour remains challenging to predict. Even fewer studies have examined the effect of solid particles on  $K_La$  and work that has been done focusses on particle sizes, solid densities and loadings that are not directly applicable to hydrocarbon-based bioprocesses. A typical bioprocess would compose an organism, such as *Saccharomyces cerevisiae*, with a size of approximately 6  $\mu\text{m}$ , at concentrations around 10 g/l. On the contrary literature studies have examined systems using glass beads (520-722  $\mu\text{m}$  at 1-16.5% v/v by Zheng *et al.* (1995), 53-88  $\mu\text{m}$  1-16.5% v/v by Joosten *et al.* (1977) 150  $\mu\text{m}$  at 0-30 %v/v by Albal *et al.* (1983)), silica sand (<5  $\mu\text{m}$  at 0-16% v/v by Alper *et al.* (1980), <45 and 350-800  $\mu\text{m}$  at 0-30 % v/v by Gollakota and Guin (1984)) and diatomaceous earth (6.6  $\mu\text{m}$  at 0.5-15% v/v by Schumpe and Deckwer (1987), <50  $\mu\text{m}$  at 2.5-10% v/v by Oguz *et al.* (1987), 6.84  $\mu\text{m}$  at 0-2% v/v by Ozkan *et al.* (2000)). While such studies are useful for examining  $K_La$  trends, their direct applicability to bioprocesses is questionable. This highlights the need for consolidation and examination of the  $K_La$  behaviour specifically aimed at accurate quantification of the oxygen transfer in hydrocarbon-based bioprocesses.

Recent research has been directed towards  $K_La$  behaviour in hydrocarbon-aqueous systems. To build on this knowledge base of  $K_La$  behaviour in aerated hydrocarbon-aqueous dispersion, this study aimed to provide a new understanding of oxygen transfer and interfacial area in hydrocarbon-based systems containing solids, a system which more closely models and aerated hydrocarbon bioprocess. In this study,  $K_La$  and interfacial area behaviour were examined in a model hydrocarbon-based bioprocess, consisting of two liquid phases (aqueous and alkane), sparged gas and solids at different configurations defined by the agitation rate, alkane concen-



tration, and solid loading within the bioreactor. Changes to the experimental configuration were performed according to a full factorial design, while maintaining operating conditions which closely mimic behaviour potentially encountered in operational bioprocesses. Temperature, pressure and alkane chain length were held constant.

$K_La$  was determined using the gassing out procedure (GOP) in conjunction with a polarographic dissolved oxygen (DO) probe including a probe response lag. Analysis of the interfacial area was done optically, through the application of high-speed photography and image analysis software to extract bubble size distributions, and ultimately the Sauter mean bubble diameter ( $D_{SM}$ ). The results were combined with the gas hold up in the reactor, yielding the interfacial area per unit reactor volume.

Combining these two experimental outputs allowed for investigation into the dominant factor driving changes in the  $K_L$  or interfacial area for each set of operating conditions, either via changes to the hydrodynamic or physiochemical properties of the system. Ultimately, accurate quantification of oxygen transfer will contribute to a fundamental understanding of  $K_La$  behaviour in complex multiphase systems, with meaningful application in optimisation and scale-up of aerobic hydrocarbon-based bioprocesses.

## Chapter 2

# Literature Review

Mass transfer in multiphase systems, and particularly bioprocesses, is significantly more complex than for chemical systems (Galaction *et al.*, 2004a). Provision of an adequate supply of oxygen is essential for aerobic respiration of micro-organisms and is a primary factor in the optimisation and enhancement of their metabolic rate. A significant number of studies are devoted to understanding the oxygen transfer rate, overall volumetric oxygen transfer coefficient ( $K_La$ ), and gas-liquid interfacial area ( $a$ ) available for the transfer of oxygen from the source to the metabolic site. Despite this, the understanding of how both changes in  $K_La$  and interfacial area are caused by variations in system parameters, and how fluid properties and fluid dynamics which underpin this behaviour in bioprocesses is incomplete.

A considerable amount of literature is devoted to gas-liquid mass transfer in mechanically agitated vessels. However, there are significant discrepancies in the findings resulting in a lack of consensus on understanding and predicting  $K_La$  values in microbial broths.  $K_La$  results are known to be affected by the system geometry, the range of the operating variables, the substrate composition, number of phases and the  $K_La$  determination method (Montes *et al.*, 1999). These factors underline the need for a systematic study of oxygen transfer in multiphase systems to allow for understanding  $K_La$  in these systems as well as the factors that underpin its behaviour.

Key to understanding what drives  $K_La$  is examination of the interfacial area behaviour under the same conditions. The study of interfacial area in multiphase systems has progressed rapidly with the advent of high speed digital photography. In the past, alternative methods such as chemical reactions (oxidation of aluminium alkyl used by Bossier III *et al.* (1973), absorption of CO<sub>2</sub> in NaOH solution used by Das *et al.* (1985)), or bubble sampling with capillary tubes (Barigou and Greaves, 1992) were time consuming, which restricted the sample sizes and number of bubbles used to find the specific interfacial area within a system. The advent of powerful image analysis tools alongside image capturing methodologies as pioneered by Galindo *et al.* (2005), Bailey *et al.* (2005), Bouaifi *et al.* (2001) amongst others, the process is more user-friendly, faster and

consequently inherently more accurate.

This literature study aims to provide insight into the field of oxygen transfer in multiphase bioprocesses, building on current understanding whilst addressing flaws, gaps and discrepancies in understanding.

The potential use of organisms for the biofunctionalisation of alkanes of varying chain lengths is discussed, followed by the theory describing gas-liquid mass transfer in aerated-aqueous systems including various models for mass transfer and potential causes of mass transfer resistance. This understanding is then applied to oxygen transfer in three-phase aqueous-hydrocarbon dispersions and finally extended to four-phase systems comprising aqueous hydrocarbon dispersion containing solids. The components of the 4-phase system are selected such that they represent a model bioprocess. The factors that underpin  $K_La$  and interfacial area behaviour in this model hydrocarbon based bioprocess are considered, along with their relative impacts and the possible pathways through which oxygen uptake occurs.

## 2.1 Alkane-Based Bioprocesses

### 2.1.1 Use of Alkanes as a Bioprocess Feedstock

Alkanes are saturated hydrocarbons consisting of carbon and hydrogen atoms linked by single bonds. These typically represent a major component in fuels and oils, and are vital to numerous industries. There are a number of different isomers of alkanes, namely linear (*n*-alkanes), cyclic (*cyclo*-alkanes) and branched (*iso*-alkanes), and all are essentially insoluble in water. Besides being flammable, alkanes are notably unreactive, which is a source of concern when they are disposed of in the environment (Wentzel *et al.*, 2007).

An efficient use of alkanes can be made by conversion to higher value commodity products by micro-organisms. Both prokaryotic and eukaryotic organisms are capable of utilizing alkanes as a carbon and energy source using specialized enzyme systems and metabolic pathways (Wentzel *et al.*, 2007). Bioconversion is an attractive alternative use of alkanes, in the light of difficulties in achieving similar levels of conversion and selectivity using synthetic chemistry.

Using specialized enzyme systems and metabolic pathways, micro-organisms are able to convert alkanes to a range of industrially useful intermediates and products. The range of bacteria and fungi that can perform this task is large, and the number of intermediate products even greater. Just some of the feasible products derived from alkanes using bioprocesses are shown in Table 2.1 (Clarke and Correia, 2008). A further advantage of the use of alkanes as a substrate is the hydrophobicity and preferential solubility of products from a bioprocess in the alkane phase. This has the potential to greatly simplify the product purification, and in addition remove products that act as inhibitors to microbial growth (Clarke and Correia, 2008).

Combined with the relative abundance of alkane by-products, derived from GTL technologies (SASOL, South Africa), the commercial potential for biofunctionalisation of alkanes to useful and valuable products is high ignored, making a strong case for their use as a feedstock in this study.

Table 2.1: Products from Alkanes Using Bioprocesses (Clarke and Correia, 2008)

Functional Group	Product
Amino Acids	L-glutamate, L-lysine, L-threonine, L-isoleucine, L-valine, L-serine, L-homoserine, L-ornithine, L-citrulline, L-tyrosine, L-phenylalanine, L-alanine, L-tryptophan, L-leucine, L-proline
Organic Acids	Ketoglutarate, citrate, isocitrate, 2-methylisocitrate*, fumarate, malate, succinate, anglyceric acid, dicarboxylic acids* (C <sub>4</sub> -C <sub>18</sub> )
Carbohydrates/Lipids	Rhamnolipids*, terhalose*, glucose, heteropolysaccharides, mannitol, erythritol, arabitol
Nucleic Acids etc.	Inosine, hypoxanthine, orotate, orotidine, nucleosides, guanilic acid, inosinic acid, adenylic acid, cyclic-AMP, DNA, RNA
Vitamins, Coenzymes	Riboflavin, flavin (vitamin B <sub>12</sub> )*, B <sub>6</sub> , B <sub>12</sub> , biotin*, coenzyme A*, cytochrome C*, porphyrin, pteridine, ergosterol*, carotenoids, xanthophylls, coenzyme Q*
Antibiotics	Phenazine derivatives, cepharosporins, cryomycin, corynecins
Enzymes	Protease, lipase, catalase*, aa oxidase, uricase*, glycerol-P dehydrogenase*
Linear Alcohols	Octanol, hexadecanol, longer chain alcohols
Monocarboxylic Acids	Octanoate
Wax Esters	Cetyl palmitate, Didecyldecane-1,10-diol
Polyhydroxyalkanoates	PHB, PHB/HV, PHAs (C <sub>3</sub> -C <sub>14</sub> )
Biosurfactants	Glycolipids, fatty acids, neutral lipids, phospholipids, lipopeptides, lipoproteins
Dioic Acids	Adipic acid, maleic acid, sebacic acid, azelaic acid, dodecanedioic acid

\*Specifically produced using alkanes as a carbon source.

### 2.1.2 Metabolism of Alkane Substrates

The ability of organisms to metabolise hydrocarbon substrates has been studied for application in environmental and industrial biotechnology industries, with the treatment of oil spills and single cell protein production being pertinent examples (Boulton and Ratledge, 1984; Shennan and Levi, 1974). Most readily consumed are straight-chain alkanes in the C<sub>10</sub>-C<sub>20</sub> range, with the lower end of this range (C<sub>10</sub>-C<sub>14</sub>) reported to give faster growth rates and are used prefer-

entially (Shennan and Levi, 1974). A number of yeast genera possess the ability to metabolise *n*-alkanes, including: *Candida*, *Pichia*, *Kloeckera*, *Torulopsis*, *Rhodotorula* and *Saccharomyces* (Walker, 1998). Other organisms also capable of metabolising alkanes are *Pseudomonas*, *Mycobacteria* and certain molds (Shuler and Kargi, 2009). *n*-Alkanes with less than 9 carbon atoms are not typically assimilated by yeasts, but oxidation has been shown to take place when *n*-nonane or shorter is utilized as a substrate by yeasts (Shennan and Levi, 1974).

The first step necessary for organisms to utilize alkane substrates is to internalise the alkane, which is problematic because of the low solubility of hydrocarbons in water. This involves passive uptake of the *n*-alkane using lipopolysaccharide cell wall structures which control adhesion and emulsification of the hydrophobic alkane, primarily reducing interfacial surface tension (Walker, 1998). Once inside the cells, the alkane is oxidised by incorporation of molecular oxygen at the terminal carbon chain yielding a primary alcohol. The oxidation takes place in the microsome (Figure 2.1). The resulting fatty acid is catabolised in the peroxisome by  $\beta$ -oxidation, following which further metabolism generates acetyl coenzyme A (CoA) before entering the mitochondrion (Walker, 1998; Shennan and Levi, 1974).

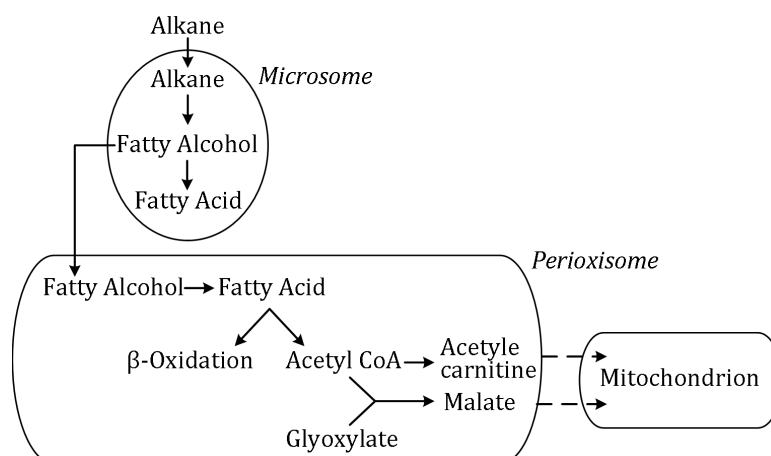


Figure 2.1: Flow diagram of oxidative pathways for *n*-alkane metabolism in yeasts (Adapted from Walker (1998))

The dissolved oxygen level has a marked influence on the activity of the cytochrome P450 monooxygenase system which catalyses the first step of alkane degradation in yeasts (Riege *et al.*, 1989). Consequently, the supply of oxygen to the cells is core to the regulation of the metabolic rate within cells and therefore the overall performance of the process.

### 2.1.3 Oxygen Solubility in Alkanes

Oxygen solubility in pure alkanes is many times that of water in the range of chain lengths that are applicable to bioprocesses. By way of example, (Ju and Ho, 1989) found that solubility of oxygen in *n*-hexadecane was over 8 fold that of water. The increased solubility has a marked

impact on the oxygen transfer in a hydrocarbon based bioprocess and changes in the oxygen transfer rate can be significant. Figure 2.2 illustrates the increase in oxygen solubility with an increase in oil fraction in an aqueous system for various oils studied in literature.

However, the magnitude of the reported increase in solubility is debated in literature. In the case of dodecane ( $n\text{-C}_{12}$ ) the solubility has been reported as 260 mg/L (Makranczy *et al.*, 1976), 182 mg/L (Hesse and Battino, 1996), 305 mg/L (Blanc and Batiste, 1970) and 255.4 mg/l (Ngo and Schumpe, 2012), all at 25°C. It should be noted that some studies have reported the solubility of  $n$ -dodecane as 54.9 mg/l at 35°C (Cascaval *et al.*, 2006; Galaction *et al.*, 2004b; Rols *et al.*, 1990). Discrepancies in reported solubilities are not specific to dodecane, with similar variations being reported for  $n$ -hexadecane ( $n\text{-C}_{16}$ ): 340 mg/l (Ju and Ho, 1989), 322 mg/l (Ho *et al.*, 1990), 190 mg/l (Makranczy *et al.*, 1976) and 255 mg/l (Blanc and Batiste, 1970). These solubilities all lie in the range of 22 to 30°C. Notwithstanding, the reported values represent an increase in solubility over that of oxygen from air in pure water (7.65 mg/l at 20°C and 1 atm (Weiss, 1970)). This increase in solubility is carried over to alkane-aqueous dispersions, increasing the solubility of oxygen in the system as a whole. Ju and Ho (1989) found that the solubility of oxygen will increase 3-4 times for a 10% hexadecane-aqueous system. The increase solubility contributes to an increase in the oxygen transfer driving force, with a resulting increase in the OTR (for the same  $K_La$ ).

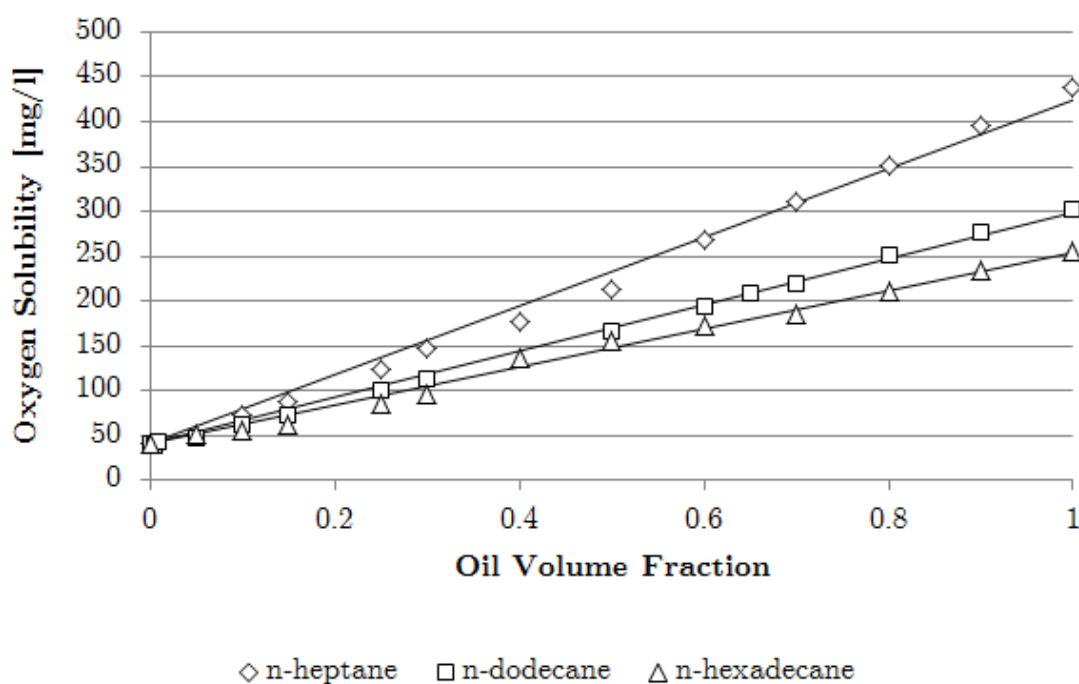


Figure 2.2: Variation in oxygen solubility for various oil volume fractions at 25°C (Adapted from Ngo and Schumpe (2012))

The alkane carbon chain length is known to play a role in the solubility of oxygen, typically

showing a drop in solubility for an increase in chain length as shown in Figure 2.3. Despite a decrease in solubility caused by an increase in carbon chain length, the solubility of oxygen in pure alkanes is at least 20 times that of pure water. Therefore, the effect the hydrocarbon concentration may have on the oxygen solubility of the system will be pronounced.

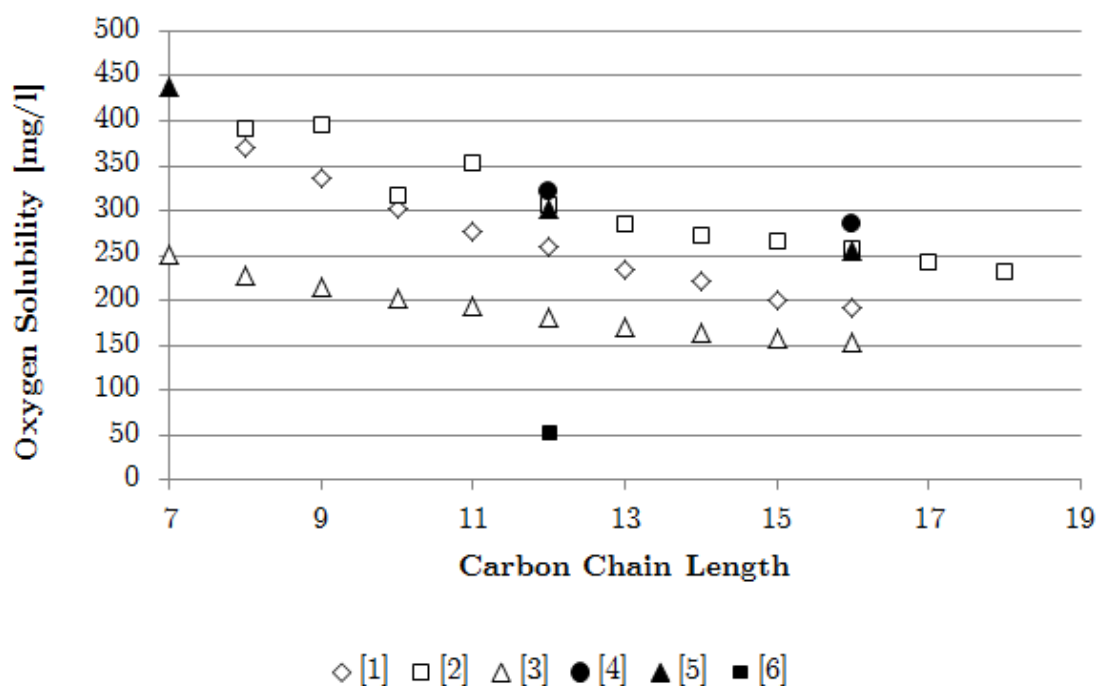


Figure 2.3: Variation in oxygen solubility versus alkane chain length. [1] - Makranczy *et al.* (1976), [2] - Blanc and Batiste (1970), [3] - Hesse and Battino (1996), [4] - da Silva *et al.* (2006), [5] - Ngo and Schumpe (2012), [6] - Cascaval *et al.* (2006); Galaction *et al.* (2004b); Rols *et al.* (1990) (Adapted from Clarke and Correia (2008))

### 2.1.4 Oxygen Supply in Alkane Substrates

The availability and affordability of alkanes as a bioprocess feedstock has been established, as has the ability of certain organisms to effectively metabolise it, specifically under aerobic conditions. The next question is the adequacy of the oxygen supply to the site of cellular respiration. Shuler and Kargi (2009) state that a suitable oxygen supply plays a vital role in ensuring the process is limited by intrinsic kinetics rather than mass transfer, and becomes correspondingly more important as the scale of the process increases. Consequently, operation of an oxygen-deficient system would result in reduced yields making oxygen transfer the key criterion for the scale-up of any aerobic bioprocess (Rao *et al.*, 1967; Montes *et al.*, 1999).

Given the basic suitability of alkanes as a feedstock, the feasibility of a functional bioprocess using alkanes needs to be addressed. One disadvantage with a hydrocarbon feedstock is the lack of a native oxygen source in the alkane molecular structure, regardless of carbon chain length.

This means that the entire cellular oxygen requirement needs to be supplied by gas-liquid mass transfer. This is in stark contrast to system using carbohydrate substrates, which would require at most half of the oxygen to be transferred for the same level of oxygen availability (Humphrey, 1967; Shennan and Levi, 1974). Einsele *et al.* (1972) found that oxygen demand using an alkane substrate was 2.5 times that compared with a carbohydrate substrate for the synthesis of one unit of cell mass, using *Candida tropicalis*. The oxygen transfer rate using hexadecane was found to be in the range of 450-650 mmol O<sub>2</sub>·h<sup>-1</sup> · l<sup>-1</sup>, dropping to 150-380 mmol O<sub>2</sub>·h<sup>-1</sup> · l<sup>-1</sup> when using glucose. By way of comparison, Moo-Young *et al.* (1971) report an oxygen demand of 240 mmol O<sub>2</sub>·h<sup>-1</sup> · l<sup>-1</sup> for *Candida lipolytica* on an *n*-alkane substrate. This nearly three-fold increase in oxygen demand in alkane based bioprocess has also been reported by Humphrey (1967), Moo-Young (1975) and Darlington (1964).

However, despite the improved oxygen solubility in alkanes, and the effective use of hydrocarbons as oxygen vectors in carbohydrate-based bioprocess, oxygen transfer may still be a significant limitation for hydrocarbon-based bioprocesses. Alkanes have been shown to depress  $K_{La}$  below that of water (Clarke and Correia, 2008; Correia *et al.*, 2010) and the increase in oxygen solubility does not necessarily compensate for the decrease in  $K_{La}$ . Under these conditions, depression of the OTR results. Bioprocesses are especially vulnerable to oxygen transfer limitations under low agitation conditions which are necessary for shear-sensitive organisms. These factors underline the importance of the quantification of  $K_{La}$  behaviour in hydrocarbon aqueous dispersions to ensure optimal transport rates for the successful design, operation and scale-up of industrial bioprocesses.

### 2.1.5 Alkane Viscosity

In addition to the increases solubility, the addition of alkane to an aqueous system changes the physical properties of the bulk fluid, including the viscosity. As the fraction of hydrocarbon is increased, so too does the viscosity. Literature has shown extensively that the viscosity of an hydrocarbon increases with chain length (Figure 2.4).

A number of proposed mechanisms describe the impact of the increased viscosity on the oxygen transfer, and subsequently the  $K_{La}$ . These primarily act through changes in the interfacial area, with an impact on the bubble formation at the sparger, and bubble coalescence and break-up in the bulk fluid. The most fundamental consequence of an increased viscosity is a decrease in the turbulence in the system which reduces the energy of any eddy currents. The damping of turbulence is amplified by the thickening of the fluid film surrounding the gas bubbles caused by the increased viscosity (Gogate *et al.*, 2000). Fundamentally, this will reduce the bubble break-up meaning the diameter of the bubbles is larger. A further consequence of larger bubbles is an accelerated rise time (the time it takes a bubble to rise to the liquid surface in the system) and low residence time, reducing the gas hold up in the system at any time (Arjunwadkar *et al.*,



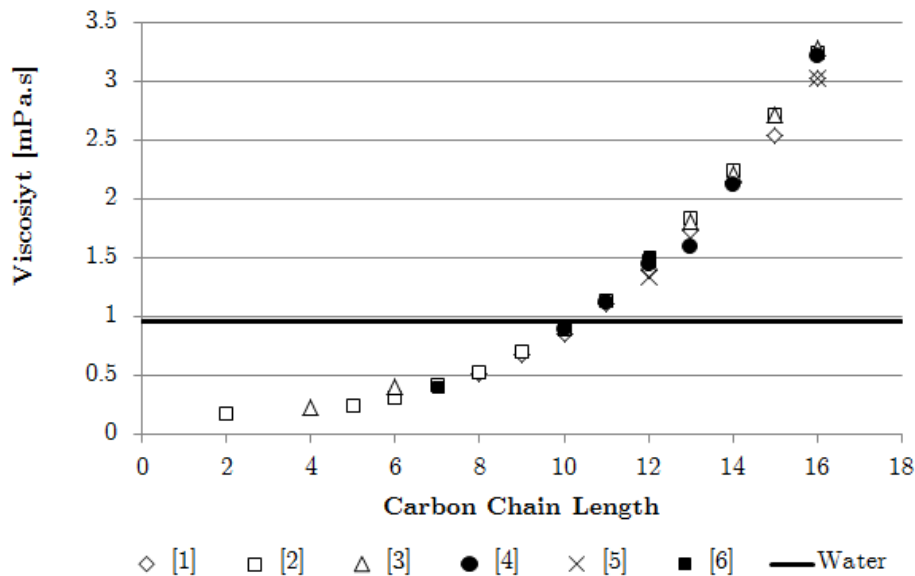


Figure 2.4: Variation of viscosity for various carbon chain lengths reported in literature (adapted from Correia (2007))

[1] - Lide (2004), [2] - Viswanath and Natavajan (1989), [3] - Golubev and Petrov (1959), [4] - Correia (2007), [5] - McMillan and Wang (1987), [6] - Kundu *et al.* (2003)

1998; Nocentini *et al.*, 1993). O' Connor *et al.* (1990) used different reasoning for an observed increase in bubble size: a higher viscosity will cause liquid films to form slower, trapping more air in each bubble and thus forming larger bubbles. The net result is a decrease in the total interfacial area, resulting in the depression of the  $K_La$ .

Correia (2007) found a steady increase in viscosity with an increase in the alkane concentration in a stirred tank reactor (STR) (Figure 2.5) and postulated that an observed depression of  $K_La$  above 5 % (v/v) and 800-12000 RPM was caused by the increased viscosity. Ozbek and Gayik (2001) examined the impact of viscosity on  $K_La$  in STR systems using 10, 20, 30, 50, 50 and 100% glycerol-aqueous solutions (Figure 2.6). A steady decrease in  $K_La$  is observed, as defined by an exponential relationship, with the exponent in this case being a function of agitation speed, reactor geometry and bulk fluid composition.

## 2.2 Oxygen Transfer

In bioprocessing, it is commonplace to experience non-uniform distribution of components, phases, compounds and organisms in the bioreactor which leads to concentration gradients. In the case of aerobic bioprocesses a concentration gradient is caused by the supply of oxygen to bioreactor for culture growth. Oxygen is present in high concentrations in the bubbles within the bulk liquid phase, compared with the rest of the bioreactor, and this concentration gradient

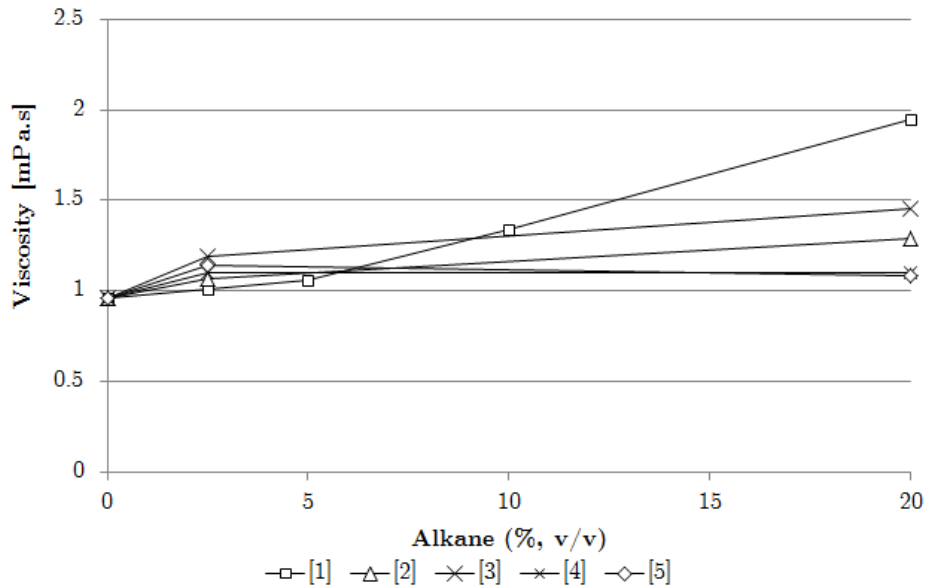


Figure 2.5: Effect of alkane viscosity on fluid viscosity as reported in literature

[1] - Correia (2007), [2] - Manyuchi (2010) - with solids (1g/l, 3 $\mu$ m), [3] - Manyuchi (2010) - with solids (10g/l, 3 $\mu$ m), [4] - Manyuchi (2010) - with solids (1g/l, 14 $\mu$ m), [5] - Manyuchi (2010) - with solids (10g/l, 14 $\mu$ m)

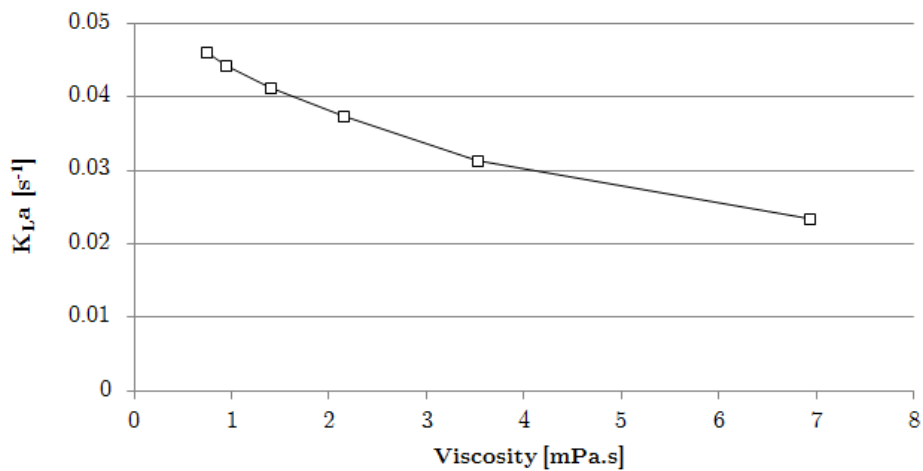


Figure 2.6:  $K_{L,a}$  values for different viscosities in a glycerol system (Redrawn from Ozbek and Gayik (2001))

drives the transfer of oxygen from the bubbles into the medium (Doran, 1995). The movement of molecules under the influence of a concentration gradient is referred to as molecular diffusion. The rate of diffusion is vital to cellular performance for micro-organisms in the bioreactor. Maintenance of the metabolic activity of cells depends the overall oxygen consumption rate which must be less than or equal to the rate of oxygen supply to the system. Consequently, it is necessary to understand the oxygen transfer process and the resistances oxygen transfer

encounters, especially in hydrocarbon-based bioprocesses.

### 2.2.1 Oxygen Transfer Mechanisms

The OTR in aerated microbial suspensions in aqueous media has been modelled using several proposed mechanisms, the most common of which is the two film theory (TFT). Other models include the penetration theory (PT) and an extension of this, the surface renewal theory (SRT). While models to predict the OTR in aqueous systems have been well documented, the OTR in systems containing an additional immiscible phase such as in hydrocarbon - based bioprocess is not well understood. The elucidation of the mechanisms of the transfer in these systems would facilitate the development of an accurate predictive model of OTR.

### 2.2.2 Resistance to Oxygen Transfer in Aerated Aqueous Systems

For any aerobic bioprocess, for oxygen transfer to take place, the oxygen needs to overcome a series of resistances as it moves from source (bubbles) to sink (cells). The gas bubbles represent the regions of high oxygen concentration, while the bulk liquid has a low oxygen concentration. This creates the concentration gradient necessary to power the diffusion. The rate of diffusion is controlled by eight resistances, in series, involved in the movement of the oxygen molecules from the bubble to the site of the intracellular reaction (Doran, 1995). These are (with reference to Figure 2.7): diffusion through bulk gas phase in the bubble to gas-liquid interface (step 1); diffusion through the internal stagnant gas film surrounding the bubble (step 2); penetration of the gas-liquid interface (step 3); diffusion through the external stagnant liquid film surrounding the bubble (step 4); movement through the bulk liquid (step 5); diffusion through the stagnant film surrounding the individual cells or cell pellets (step 6); penetration of the liquid-cell interface (step 7); transport to site of reaction (step 8).

The magnitude of the resistance each step of the overall oxygen transfer resistance is dependent on a number of properties of the system, including the composition of the components, the degree of mixing, bubble sizes and interfacial absorption characteristics Doran (1995). Through analysis of the system, the rate limiting step limiting oxygen transfer can be identified as the diffusion of oxygen through the stagnant liquid film surrounding the bubbles (step 4) or, in the case of pelleted cells only, the diffusion through solid pellets (step 6). The resistance caused by the liquid film is due to oxygen's limited solubility in water (7.65 mg/l at 20°C and 1 atm (Weiss, 1970)) when supplied as air.

### 2.2.3 Diffusion Theory in Aqueous Systems

As an introduction to diffusion in bioprocesses, initial discussion is restricted to binary mixtures (gas and liquid), specifically the mass transfer of oxygen from the gaseous phase to an aqueous liquid phase. As shown in Figure 2.8, an uneven distribution of gaseous component in a liquid

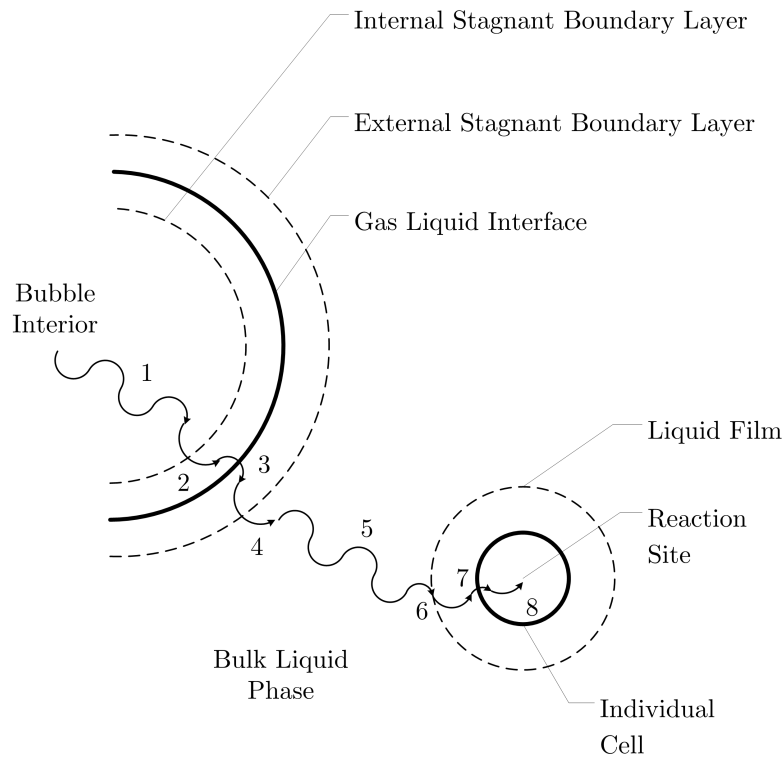


Figure 2.7: Steps necessary for oxygen transfer from bubble to cell (Adapted from Doran (1995))

system creates a concentration gradient. Concentration of A ( $C_A$ ) varies from  $C_{A1}$  to  $C_{A2}$  as a function of distance  $Z$ , causing molecules of A to diffuse away from regions of high concentration to an area of lower concentration. This transfer takes place through a cross sectional area perpendicular to the direction of diffusion (Doran, 1995). Fick's First Law states that molar flux is proportional the concentration gradient. This relationship is shown in Equation 2.1, where  $J_A$  is the molar flux of component A,  $N_A$  is the rate of oxygen transfer, interfacial area is the cross sectional area available for oxygen transfer.

$$J_A = \frac{N_A}{a} = -D_{AB} \cdot \frac{dC_A}{dZ} \quad (2.1)$$

Rearranging Equation 2.1 yields the rate of oxygen transfer caused by diffusion in Equation 2.2. The binary diffusion coefficient ( $D_{AB}$ ) describes the diffusivity of component A in B,  $C_A$  is the concentration of A and  $Z$  is the distance. Therefore,  $\frac{dC_A}{dZ}$  describes the concentration gradient. The negative sign before  $D_{AB}$  in Equation 2.1 indicates the direction of mass transfer is always from high to low concentration (in Figure 2.8  $\frac{dC_A}{dZ}$  is positive, while the mass transfer takes place in the negative  $y$ -direction) (Doran, 1995).

$$N_A = -D_{AB} \cdot a \cdot \frac{dC_A}{dZ} \quad (2.2)$$

From Equation 2.2, it is clear how the rate of diffusion can be enhanced: increasing the concentration gradient ( $\frac{dC_A}{dz}$ ), increasing the area per unit volume available for oxygen transfer ( $a$ ), or increasing the diffusivity ( $D_{AB}$ ).

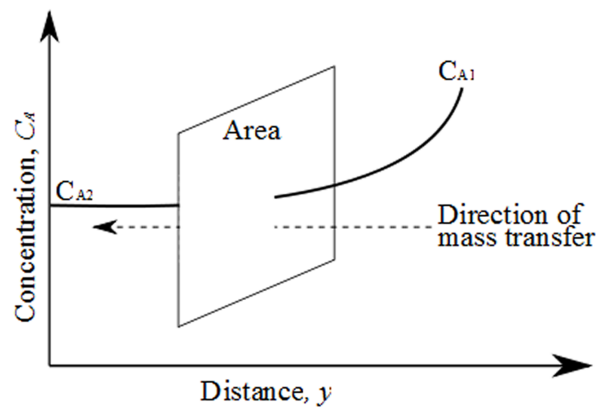


Figure 2.8: Concentration gradient of component A driving mass transfer across area  $a$  (Adapted from Doran (1995))

## 2.2.4 Oxygen Transfer Mechanisms in Aqueous Systems

Where there is direct contact between two different phases (liquid-liquid or gas-liquid), fluid velocity is fundamentally zero, and diffusion is the sole method of mass transfer across the phase boundary. Based on this, there are a number of theoretical models to describe the oxygen diffusion process in aqueous systems. The most common is the TFT, based on the assumption that fluid turbulence decreases as one approaches a fluid interface. Two additional models are examined, namely the SRT, and an extension of this, the PT.

Nernst (1904) developed the concept of the TFT, based on the premise that fluid turbulence is damped as the gas-liquid interface of the bubble is approached and hypothesises a stagnant layer (or film) on either side of the interface where oxygen transfer in the stagnant layers is dependent solely on the rate of molecular diffusion (Figure 2.9), as described by Ficks' Law (Equation 2.1). These layers are hypothetical, as fluid turbulence continues up to any interface (Cussler, 2000). Nonetheless, this model is useful to describe oxygen transfer at the interface where oxygen diffuses from the bubbles to the liquid phase, across the phase boundary, powered by the oxygen concentration gradient (discussed in Section 2.2.2).

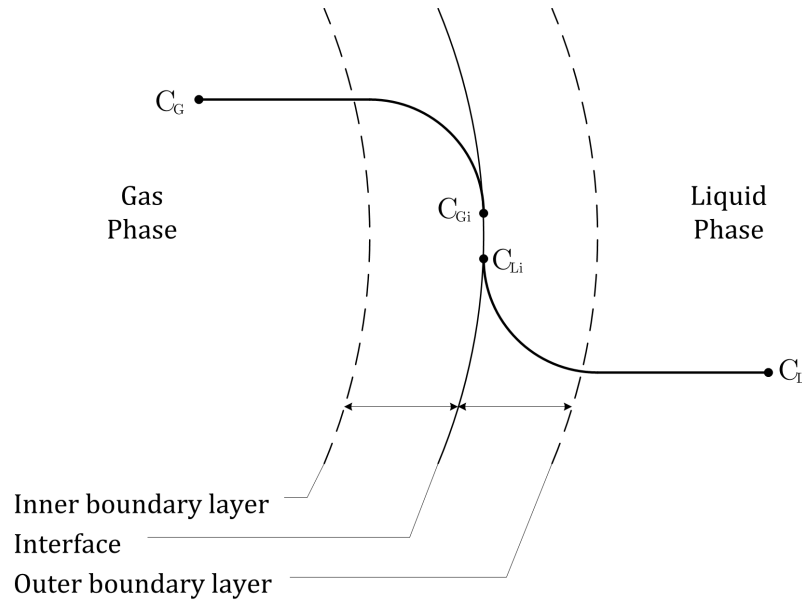


Figure 2.9: Oxygen concentration gradients for gas-liquid mass transfer (Adapted from Doran (1995))

To derive the TFT, the concentration gradient in Ficks' Law (Equation 2.1) is integrated over the film thickness ( $\delta$ ) with the driving force provided by the difference between the oxygen concentration in the bulk liquid ( $C_L$ ) and the concentration of oxygen on the liquid side of the gas-liquid interface ( $C_{Li}$ ) (Equation 2.3).

$$J_A = \frac{D_{AB}}{\delta} \cdot (C_{Li} - C_L) \quad (2.3)$$

$N_A$  is the molar flux per unit volume, and is obtained from  $J_A$  by the incorporation of the specific interfacial area ( $a$ ), the ratio of the transfer area to liquid volume (Equation 2.4). The liquid side oxygen transfer coefficient ( $k_L$ ) is equal to  $\frac{D_{AB}}{\delta}$  (Equation 2.5).

$$N_A = \frac{D_{AB}}{\delta} \cdot a \cdot (C_{Li} - C_L) \quad (2.4)$$

$$N_L = k_L \cdot a \cdot (C_{Li} - C_L) \quad (2.5)$$

Similarly for the gas side, the rate of oxygen transfer through the boundary layer is given in Equation 2.6, where  $k_G$  is the gas phase oxygen transfer coefficient,  $C_G$  is the concentration of oxygen in the gas bulk, and  $C_{Gi}$  is the concentration of oxygen at the gas interface.

$$N_G = k_G \cdot a \cdot (C_G - C_{Gi}) \quad (2.6)$$

For equilibrium to be true,  $C_{Gi}$  and  $C_{Li}$  need to be related. For most dilute gas concentrations, equilibrium concentration in the liquid phase is a linear function of that in the gas phase (Equation 2.7), where  $m$  is defined as the distribution factor.

$$C_{Gi} = m \cdot C_{Li} \quad (2.7)$$

To eliminate the difficult to measure interfacial concentrations, Equation 2.7 is substituted into Equations 2.5 and 2.6, to yield Equations 2.8 and 2.9 respectively.

$$\frac{N_L}{k_L \cdot a} = \frac{C_{Gi}}{m} - C_L \quad (2.8)$$

$$\frac{N_G}{k_G \cdot a} = C_G - m \cdot C_{Li} \quad (2.9)$$

Division of Equation 2.5 by  $m$  followed by addition to Equation 2.8 eliminates  $C_{Li}$  and yielding the overall oxygen transfer rate ( $N_A$ ) (Equation 2.10). In the same fashion, multiplication of Equation 2.6 by  $m$  and addition to Equation 2.9 eliminates  $C_{Gi}$  yields Equation 2.11.

$$N_A \left( \frac{1}{m \cdot k_{Ga}} + \frac{1}{k_{La}} \right) = \frac{C_G}{m} - C_L \quad (2.10)$$

$$N_A \left( \frac{1}{k_{Ga}} + \frac{m}{k_{La}} \right) = C_G - m \cdot C_L \quad (2.11)$$

Together, Equations 2.10 and 2.11 define the overall oxygen transfer coefficients. The overall liquid phase oxygen transfer coefficient ( $K_{La}$ ) is defined by Equation 2.12, while similarly the overall gas phase oxygen transfer coefficient ( $K_{Ga}$ ) is defined by Equation 2.13.

$$\frac{1}{K_{La}} = \frac{1}{m \cdot k_{Ga}} + \frac{1}{k_{La}} \quad (2.12)$$

$$\frac{1}{K_{Ga}} = \frac{1}{k_{Ga}} + \frac{m}{k_{La}} \quad (2.13)$$

Substitution of Equations 2.12 and 2.13 into 2.10 and 2.11 yields Equations 2.14 and 2.15, both of which describe the rate of oxygen transfer.

$$N_A = K_{La} \left( \frac{C_G}{m} - C_L \right) \quad (2.14)$$

$$N_A = K_G a (C_G - m \cdot C_L) \quad (2.15)$$

Applying this to a bioprocess where oxygen transfer is controlled by the liquid phase (due to oxygen being sparingly soluble in water), Equation 2.15 applies. With  $\frac{C_G}{m}$  equal to the liquid phase oxygen concentration in equilibrium with the gas phase,  $C_L^*$ , Equation 2.14 becomes Equation 2.16 which defines the OTR.

$$OTR = K_L a \cdot (C_L^* - C_L) \quad (2.16)$$

The TFT model predicts that sub-optimal OTR can be enhanced through increases in  $K_L a$  and/or the concentration gradient.  $K_L a$  is increased by amplified turbulence both through augmentation of the transfer area and reduction of the thickness of the stagnant liquid layer. The concentration gradient is increased via improved solubility, affected either through an increased partial pressure of oxygen in the sparge gas, an increased total pressure, or addition of an immiscible liquid with high oxygen solubility (e.g. hydrocarbon).

By necessity, the use of Equation 2.16 is dependent on the following assumptions (Benedek and Heideger, 1970): concentration of oxygen is uniform throughout the reactor,  $K_L a$  is constant throughout the reactor, and composition of incoming gas is constant. These assumptions are acceptable given the turbulent conditions inside the reactor. Also implicit in the TFT is the assumption that the volume of oxygen held within the thin stagnant liquid film is negligible compared with the total volume of oxygen passing through the system (Lewis and Whitman, 1924). This implies that from the first initial moment of gas-liquid contact, a steady state oxygen concentration profile is established in the stagnant liquid film. This is not the case because the liquid film oxygen concentration must be equal to the oxygen concentration of the bulk fluid at the instant of gas-liquid contact. When contact is made, the oxygen penetrates the liquid film forming a concentration gradient, only later reaching steady state (Higbie, 1935). For the duration of this transient period (the so-called "penetration period"), the TFT is not valid. The impact of a questionable steady state assumption is confirmed experimentally where a linear relationship between the oxygen transfer coefficient and diffusivity, while experimental results suggest a square-root dependence (Perlmutter, 1961).

While not always being the most effective theory for modelling complex systems accurately, the TFT remains valuable for several reasons. It highlights the boundaries to oxygen transfer in a way that is simple to envisage, and clearly shows how oxygen transfer can be hampered by a phase interface (Cussler, 2000). It is also readily augmented to include multiple fluid phases.

The most significant problem with modelling the molecular diffusion through a stagnant boundary layer is the instability of the fluid caused by turbulence in the system. An improvement was



offered by Higbie (1935) who developed the PT on a basis of unsteady-state oxygen diffusion. The basic concept is represented in Figure 2.10. This theory states that the liquid-gas interface consists of a vast number of minute fluid elements, each of which come into contact with the phase interface for an average period of time (Hines and Maddox, 1985). The fluid elements then move back into the bulk phase to be replaced by another fluid element. Elements only come into contact with the interface once another element moves away, meaning that the number of elements at the interface is constant with time. Only while the fluid elements are in contact with the interface does oxygen transfer take place in the normal direction (Seader and Henley, 2006). This model is far more suitable for the oxygen transfer in a turbulent flow regime, where eddy currents continually expose fresh liquid surfaces to the oxygen and high turbulence doesn't allow the fluid film at the interface to establish a steady state concentration gradient (Danckwerts, 1951).

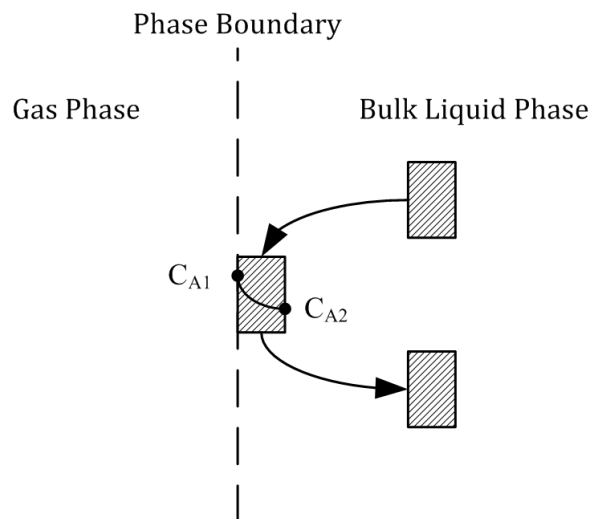


Figure 2.10: Surface renewal theory model (Adapted from Hines and Maddox (1985))

While the fluid elements are in contact with the phase interface, unsteady-state diffusion takes place, which is governed by Fick's second law, shown in Equation 2.17 subject to the following boundary conditions applicable to a semi-infinite medium:

$$\begin{array}{llll} C_A = C_{A2} & \text{at} & t = 0 & \text{for} & 0 \leq Z \leq \infty \\ C_A = C_{A1} & \text{at} & z = 0 & \text{for} & t > 0 \\ C_A = C_{A2} & \text{at} & z = \infty & \text{for} & t > 0 \end{array}$$

$$D_{AB} \cdot \frac{d^2 C_A}{dX^2} = \frac{dC_A}{dt} \quad (2.17)$$

Applying boundary conditions applicable to a semi-infinite medium, and the Laplace transform, Equation 2.17 is solved to give the change in oxygen concentration at any time during contact

of the liquid element with the interface as a fraction of the change in oxygen concentration over the entire contact time of the element. This is termed the fractional accomplished concentration change, or  $\theta$ . Differentiation of  $\theta$  with respect to penetration distance and substitution into Equation 2.1 provides the instantaneous molar flux at the interface per unit area ( $J_{A,t}$ ) (Equation 2.18). The instantaneous molar flux is then integrated with respect to time to yield the total molar flux at the interface per unit area ( $J_A$ ) (Equation 2.19). If  $J_A$  is combined with the specific interfacial area  $a$  to give the molar transfer per unit volume, Equation 2.19 becomes Equation 2.20.

$$J_{A,t} = \sqrt{\frac{D_{AB}}{\pi \cdot t}} \cdot (C_{Li} - C_B) \quad (2.18)$$

$$J_A = 2 \cdot \sqrt{\frac{D_{AB}}{\pi \cdot t_s}} \cdot (C_{Li} - C_B) \quad (2.19)$$

$$N_A = 2 \cdot \sqrt{\frac{D_{AB}}{\pi \cdot t_s}} \cdot a \cdot (C_{Li} - C_B) \quad (2.20)$$

Substitution of  $K_L = 2 \sqrt{\frac{D_{AB}}{\pi \cdot t_s}}$  into Equation 2.20 yields Equation 2.5, making the transfer coefficient proportional to  $\sqrt{D_{AB}}$ , a relationship that is supported by experimental results (Higbie, 1935).

The PT is restricted by the difficulty associated with measuring the contact time. It is usually estimated using an empirical correlation where contact time is defined as a function of reactor geometry, fluid viscosity, density and velocity (Seader and Henley, 2006). The accuracy of the model depends on the accuracy of the empirical correlation, risking skewed results should an incorrect value of  $t_s$  be employed.

Fundamental to the rationale behind the PT is the fact that liquid elements spend an identical amount of time at the phase interface. Oxygen transfer can only take place while the fluid elements are in contact with the phase interface, and subsequently the equal contact times imply that the amount of oxygen transfer per liquid element is the same regardless of its location on the phase interface. For a system with turbulent conditions and rising bubbles, this does not provide a complete description of the oxygen transfer taking place.

This limitation was addressed by the introduction of the SRT (Danckwerts, 1951), a modification of the PT, which assumes that the probability of any fluid element being replaced is independent of the length time for which it is in contact with the gas-liquid interface. To incorporate the non uniform contact times, a residence time distribution was applied to the liquid elements at the phase interface. The residence time distribution is incorporated into the model

using a distribution function  $F(t)$  representing the fraction of liquid elements with a contact time of less than  $t$  within boundary conditions  $F(0) = 0$  and  $F(\infty) = 1$ . The probability that any given liquid element will spend time  $t$  at the gas-liquid interface is given by  $\Phi(t)$  (Danckwerts, 1951).

Consequently the surface area is composed of liquid elements having ages between  $t$  and  $t + dt$ , the distribution of which is defined as  $\Phi(t)dt$ . At steady state the liquid elements entering the age group  $t \rightarrow (t + dt)$  is equal to the area leaving the age group  $(t - dt) \rightarrow t$  is equal to  $\Phi(t)dt$  less the portion of the area replaced by fresh liquid elements at time  $dt$  (Danckwerts, 1951), which is defined as the fraction rate of liquid surface renewal ( $s$ ), as shown in Equation 2.21.

$$\begin{aligned}\Phi(t)dt &= \Phi(t - dt)dt(1 - sdt) \\ \Phi(t) &= \Phi(t) - \frac{d\Phi}{dt}dt - s\Phi(t)dt \\ \therefore \frac{d\Phi}{dt} &= s\Phi(t)\end{aligned}\quad (2.21)$$

Given that  $\Phi(t)$  is a distribution function, it follows that  $\int_0^{\infty} \Phi(t) = 1$ . Combining this with Equation 2.21, the surface age distribution function is defined in Equation 2.22.

$$\Phi(t) = se^{-st} \quad (2.22)$$

Intrinsic to the surface age distribution function is the assumption that the entire surface area is uniformly accessible, meaning any liquid element has an equal probability of making contact with any point of the surface area. Once the surface age distribution function is known, it can be incorporated into the PT (Seader and Henley, 2006). The instantaneous rate of absorption into a liquid of infinite depth given normal diffusion is taking place is shown in Equation 2.23, with the integrated rate average in Equation 2.24.

$$N_{A_t} = \sqrt{\frac{D_{AB}}{\pi t}} \cdot a \cdot (C_{Li} - C_B) \quad (2.23)$$

$$(N_A)_{AVG} = \int_0^{\infty} \Phi(t)N_{A_t}dt \quad (2.24)$$

Combination of Equations 2.22, 2.23 and 2.24 and integrating yields the molar transfer rate (Equation 2.25), with  $K_L = \sqrt{D_{AB} \cdot s}$ .

$$N_A = \sqrt{D_{AB} \cdot s} \cdot a \cdot (C_{Li} - C_B) \quad (2.25)$$

Similar to the PT, the SRT defines the mass oxygen transfer coefficient as being proportional to the square root of the diffusivity. It improves on the PT by removing the assumption that all liquid elements have the same contact time through implementation of a residence time distribution function. This provides a more feasible mechanism in turbulent regimes (Hines and Maddox, 1985). However, as with the contact time ( $t_s$ ) for the penetration theory, the fractional rate of surface renewal ( $s$ ) is difficult to estimate. While neither the PT nor the SRT are perfect models, the theory on which the SRT is based is physically more realistic in a turbulent STR, while offering an improvement over the TFT.

The relationship between  $K_L$  and diffusivity for the TFT, PT and SRT is summarised below. It is clear that while each model represents a different relationship between  $K_L$  and  $D_{AB}$ , the PT and SRT both predict  $K_L$  to be proportional to  $\sqrt{D_{AB}}$ , which for gas-liquid mass transfer has been found to offer a close approximation (Versteeg *et al.*, 1987). While unlikely that any one model will describe  $K_L$  over the full range of process conditions, it does allow for examination of the impact an experimental parameter has on the oxygen diffusivity.

Film theory

$$K_L = \frac{D_{AB}}{\delta_L} \quad (2.26)$$

Penetration theory

$$K_L = 2 \sqrt{\frac{D_{AB}}{\pi \cdot t_s}} \quad (2.27)$$

Surface renewal theory

$$K_L = \sqrt{D_{AB} \cdot s} \quad (2.28)$$

### 2.2.5 Oxygen Transfer Mechanisms in Hydrocarbon-Aqueous Systems

While the TFT provides a simplified description of the oxygen transfer taking place, it ignores the presence of a second liquid hydrocarbon phase. Rols *et al.* (1990) augment the TFT to include a hydrocarbon phase in the model. While the addition of a second liquid phase has the potential to increase oxygen transfer by exploiting the increased solubility of oxygen in hydrocarbons (Rols *et al.*, 1990), it needs to be offset by the negative impact the hydrocarbon has on the oxygen transfer caused by increased bulk fluid viscosity. This interaction means that oxygen transfer can either be enhanced or depressed, depending on the regime in which the bioprocess is operated.

Typical model bioprocesses contain 4 phases creating additional phase interfaces and parallel pathways available for oxygen transfer, as illustrated in Figure 2.11. With reference to the figure, the first pathway is identical to a single liquid phase dispersion with oxygen crossing the gas-liquid phase boundary, diffusing through the bulk liquid to the cell. The second pathway illustrates adhesion of the cell to the gas bubble, with this phase boundary providing the only resistance. For pathway number 3, oxygen transfers from the gas bubble to the aqueous phase followed by the hydrocarbon phase, before returning back to the aqueous phase and finally to the cell. The efficiency of this pathway is dependent on the diffusivity and solubility in each phase. Pathway number 4 allows oxygen transfer directly to the hydrocarbon phase before transferring to the aqueous phase and the cell respectively. Finally, in pathway 5, oxygen moves from the gas phase to the hydrocarbon and then directly to the cell. A sixth possible pathway (not documented in literature) involves oxygen transfer from gas to water to organic to cell.

The feasibility and likelihood that one of more of these pathways is used is ultimately dependent on the process conditions, the hydrocarbon and cellular interaction, and the relative surface tension of the gas-water and gas-hydrocarbon interfaces.

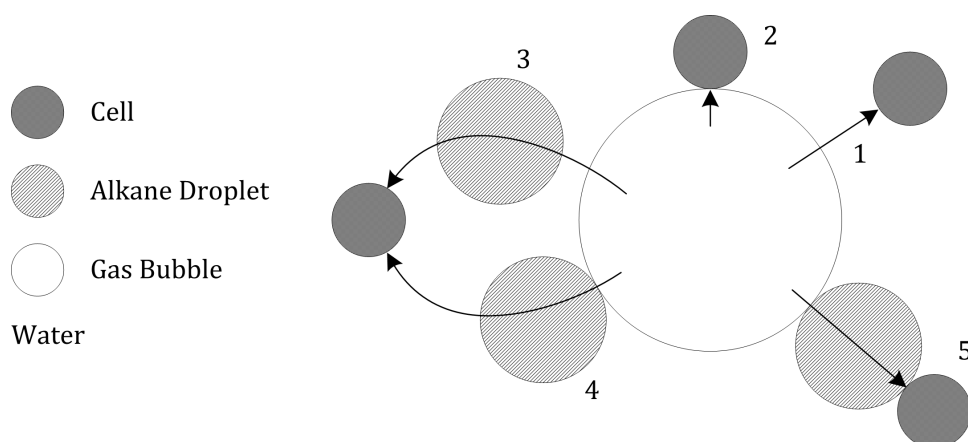


Figure 2.11: Possible pathways for oxygen transfer pathways from gas bubbles to microorganisms in aqueous-alkane systems (Adapted from Rols *et al.* (1990))

Rols *et al.* (1990) examined an aqueous system containing *n*-dodecane, and found that addition of 0.1 volume fraction organic phase increased the  $K_{La}$  5-fold, and concluded that the *n*-dodecane acted either at the gas-liquid interface, or in the gas-liquid boundary layer at the gas bubbles. The observed increase in oxygen transfer is hypothesised as being a function of the behaviour of the organic phase, possibly acting as a surface-active agent and reducing the surface tension of the water phase. This increases the gas-liquid interfacial area for a constant gas hold-up, increasing  $K_{La}$  (Rols *et al.*, 1990). The increased oxygen transfer can also be explained through the assumption that alkane forms droplets which act as rigid spheres and promote interfacial turbulence and mixing in the aqueous film surrounding the bubbles. McMillan and Wang (1987) suggest that the presence of oil drops in the liquid film could enhance the oxygen permeability, enhancing the oxygen transfer. This view isn't supported by Rols *et al.* (1990), who found that the positive spreading coefficient (described in detail in Section 2.2.6) would instead lead to the alkane coating the bubble surface rather than forming droplets, a theory backed by experimental observation. This makes it clear that the pathway is a function of the nature and interaction of the phases in the bioprocess.

### 2.2.6 Spreading Coefficient of Alkanes

The interaction between the phases in a bioprocess defines the oxygen transfer pathway. To classify this behaviour, a derived metric known as the spreading coefficient can be used. This coefficient is a measure of the tendency for an oil phase to form droplets (beads) or alternatively a film when it comes into contact with a phase interface. This tendency is a function of the surface energies of the oil, the surface the oil comes into contact with and the environment. As an isolated suspended oil droplet comes into contact with a gas bubble, the droplet flattens against the bubble surface, adopting a lens-like profile (shown in Figure 2.12). The contact between the bubble and droplet creates three interfacial areas: oil-water ( $A_{OW}$ ), oil-gas ( $A_{OG}$ ) and water-gas ( $A_{WG}$ ). The droplet will continue to spread until the forces acting on it reach equilibrium, as determined by the oil-gas ( $\gamma_{OG}$ ), oil-water ( $\gamma_{OW}$ ) and water-gas ( $\gamma_{WG}$ ) interfacial tensions (Tadmor, 2004).

A energy balance is given in Equation 2.29 where the net change in work done by the oil droplet is the sum of the product of each interfacial tension and the change in area of the respective region, plus the work driven by a theoretical change in volume (Tadmor, 2004).

$$\delta w = \gamma_{OW} \cdot dA_{OW} + \gamma_{OG} \cdot dA_{OG} + \gamma_{WG} \cdot dA_{WG} + \Delta P dV \quad (2.29)$$

As the droplet spreads,  $A_{OG}$  increases at the same rate as  $A_{WG}$  decreases such that  $dA_{OG} = -dA_{WG}$ , while the change in volume  $dV$  remains zero (incompressible fluids). Assessing the energy balance for the point at which the oil droplet stops spreading and reaches equilibrium

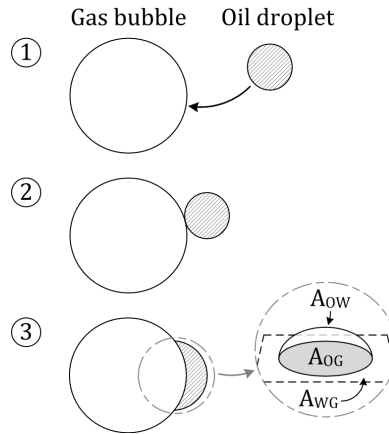


Figure 2.12: Oil droplet coming into contact with gas bubble, detailing the interfacial area created between the phases (Adapted from Tadmor (2004))

( $\delta w = 0$ ), Equation 2.29 can be rewritten as Equation 2.30.

$$\begin{aligned} 0 &= \gamma_{OW} \cdot dA_{OW} + dA_{OG}(\gamma_{OG} - \gamma_{WG}) \\ &= \gamma_{OW} \cdot \frac{dA_{OW}}{dA_{OG}} + (\gamma_{OG} - \gamma_{WG}) \end{aligned} \quad (2.30)$$

For a constant volume, the ratio of the rate of change of the oil-water to the oil-gas area is equal to the cosine of the contact angle  $\theta_0$  (Equation 2.31) (Tadmor, 2004):

$$\frac{dA_{OW}}{dA_{OG}} = \cos\theta_0 \quad (2.31)$$

Substitution of Equation 2.31 into Equation 2.30 yields Young's Equation shown in Equation 2.32 (Young, 1805). By rearranging and subtracting  $\gamma_{OW}$  from each side, Equation 2.32 can be rearranged to Equation 2.33, allowing for consideration of the implication of the contact angle when determining the wetting behaviour through use of the equilibrium spreading coefficient,  $S_{eq}$ . The two possible outcomes are given in Table 2.2 below. In case 1, for an oil forming a film on the gas-liquid interface, the contact angle can only be equal to 0 and consequently  $S_{eq}$  is 0. In case 2, with  $0 < \theta_0 \leq 180$ , the droplet will reach equilibrium on the gas bubble surface with a defined contact angle. This state is known as partial wetting, with a negative  $S_{eq}$ . At no stage can  $S_{eq}$  be greater than 0 as the  $(\cos\theta_0 - 1)$  term in Equation 2.33 can only be less than 0.

$$\begin{aligned} 0 &= \gamma_{OG} + \gamma_{OW} \cdot \cos\theta_0 - \gamma_{WG} \\ \gamma_{OW} \cdot \cos\theta_0 - \gamma_{OW} &= \gamma_{WG} - \gamma_{OG} - \gamma_{OW} \end{aligned} \quad (2.32)$$

$$\gamma_{OW} \cdot (\cos\theta_0 - 1) = \gamma_{WG} - (\gamma_{OG} + \gamma_{OW}) \equiv S_{eq} \quad (2.33)$$

Table 2.2: The impact of contact angle on the equilibrium spreading coefficient

Case	Description	$\theta_0$	$\cos\theta_0$	$\gamma_{OW} \cdot (\cos\theta_0 - 1)$	$S_{eq}$
1	Complete Wetting	$\theta_0 = 0$	$\cos\theta_0 = 1$	$\gamma_{OW} \cdot (\cos\theta_0 - 1) = 0$	$S_{eq} = 0$
2	Partial Wetting	$0 < \theta_0 \leq 180$	$-1 \leq \cos\theta_0 < 1$	$\gamma_{OW} \cdot (\cos\theta_0 - 1) < 0$	$S_{eq} < 0$

The wetting behaviour at the initial moment of contact between the gas bubble and the oil droplet and at equilibrium conditions differs. Absorption of water molecules onto the gas-liquid interface lowers the surface energy (Bonn *et al.*, 2009) and consequently the drop will have a finite static contact angle,  $\theta$ , which is not the same as  $\theta_0$ .  $\theta$  is found by replacement  $\gamma_{WG}$  by  $\gamma_{W0}$  in Equation 2.33 to yield Equation 2.34.  $\gamma_{WG}$  is less than  $\gamma_{G0}$  and as a result the initial spreading coefficient,  $S_i$ , can be greater than 0 for a spreading oil.

$$S_i = \gamma_{W0} - (\gamma_{OG} + \gamma_{OW}) \quad (2.34)$$

The initial spreading coefficient provides a starting point for characterisation of the likely oxygen transfer path, since it defines the behaviour of the oil droplet as it comes into contact with a gas bubble. For spreading oils ( $S_i > 0$ , Figure 2.13b), it is highly probable that the oxygen transfer will take place in series, moving from the gas phase directly into the oil phase and subsequently, either through the aqueous phase to the cell (Figure 2.11, path 4) or directly to a cell adhering to its surface (Figure 2.11, path 5). Cell adherence (and hence path 5) is a more likely occurrence with hydrocarbon-utilising microorganisms which have exhibited hydrophobic protruberances on their cell membranes. On the other hand ( $S_i < 0$ , Figure 2.13a), for beading oils any of the pathways (Figure 2.11, paths 1 to 5) could apply. The cells can use oxygen present in the bulk aqueous phase, or oxygen from the oil phase, with more than one of these pathways potentially taking place in parallel.



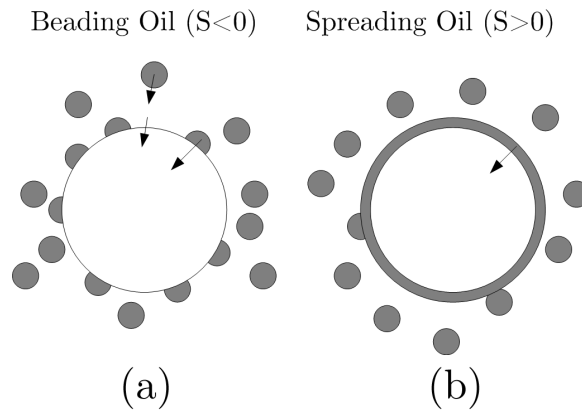


Figure 2.13: Possible effect of spreading coefficient on the mass transfer pathway in an gas-liquid-liquid dispersion

Pinho and Alves (2010) found an increase in the fractional saturation of heptane in the exhaust gas at point at which phase inversion occurred, with a corresponding change in the spreading coefficient. This relates to an increase in the oxygen transfer in a gas-liquid-liquid system, and it becomes obvious that the spreading coefficient has a role to play in this behaviour. Pinho and Alves (2010) are in agreement with the hypothesis that the spreading coefficient can be used to classify the oxygen transfer pathway.

Rols and Goma (1989) presented visual evidence of the spreading behaviour of *n*-dodecane on gas bubbles. As the alkane droplet contacted the gas bubble, it began to form a film. The film grew drop by drop, as the bubble contacted more alkane. The  $S_i$  of this system was  $+0.6$  dyn/cm (greater than zero), indicating that *n*-dodecane was a spreading oil in an aerated aqueous system. Similar behaviour was found for forane ( $S_i = +16.5$  dyne/cm) in the same study. Similarly, Yoshida *et al.* (1970) measured the spreading coefficient for toluene ( $S_i = +8.7$  dyne/cm) and oleic acid ( $S_i = +24.1$  dyne/cm) in a aerated aqueous dispersions. These combined findings support the use of the spreading coefficient as an indication of the behaviour of a dispersed oil phase.

The use of the spreading coefficient to definitively predict oxygen transfer behaviour is not without difficulties. It can be difficult to experimentally determine the necessary interfacial surface tensions required to calculate the spreading coefficient. Furthermore, the coefficient fails to account for variable thickness of the oil film coating the bubble's surface, and the fraction of the interfacial area covered by the oil in the case of spreading oils, bead sizes and their distribution over the bubble surface in the case of beading oils (Dumont and Delmas, 2003). Therefore, while the spreading coefficient can be used to predict the possible behaviour of an oil phase and characterize possible transfer pathways used by oxygen, investigation into  $K_La$  is necessary to firmly establish the impact of hydrocarbon concentration in model hydrocarbon-

based bioprocesses.

### 2.2.7 Oxygen Transfer Mechanisms in Hydrocarbon-Aqueous Systems Containing Solids

Systems containing solids have been the focus of recent research, driven by interest in biological waste water treatment and gasification processes in Fischer-Tropsch synthesis. A fundamental parameter key to efficacious operation of these processes is gas-liquid mass transfer which has an impact on all aspects of the process, and can ultimately determine the overall efficiency. Literature offers conflicting reports on the impact of solids on oxygen transfer and the impact solids have the  $K_L$  and the interfacial area available for oxygen transfer individually. Key to understanding how and why the presence of particles affects oxygen transfer behaviour in bioprocesses is classification of the particle types and the impact they have on oxygen transfer.

Classification of solid particles would allow for the prediction of mass transfer behaviour within a multiphase system when solid particles are introduced. Armed with this theoretical knowledge of the impact of solids on the fundamental working of oxygen transfer mechanisms and pathways, attention can be given to the effect of solids on the system  $K_La$  and interfacial area, and allow for better diagnosis of systems operating in a mass transfer limited regime. The most recent and successful attempt at the classification of solid particles in multiphase systems is the review by Ruthiya *et al.* (2003) which postulates the mass transfer behaviour in a system can be described by one of four mechanisms, explained in Sections 2.2.7.1 to 2.2.7.4.

#### 2.2.7.1 Shuttling

Shuttling is based on the premise that solid particles act as vehicles for gas-liquid mass transfer by moving gas from the gas phase by absorbing at the stagnant film and desorbing in the bulk liquid phase, thereby increasing the system's  $K_L$  (Holstvoogd *et al.*, 1988; Beenackers and Van Swaaij, 1993). Alper *et al.* (1980) found that adding activated carbon increased  $K_La$  by up to 4 fold in a water-CO<sub>2</sub> system. They state that this is due to the ability of the activated carbon to penetrate the stagnant liquid boundary layer at the phase interface, absorb the solute from the gas, move back into the bulk liquid, and desorb the gas into the bulk liquid phase. Zhang *et al.* (2006) theorise a similar behaviour with finely dispersed liquid particles with a higher affinity for the gas solute than the bulk liquid. However, while active particles can be used to enhance the gas-liquid oxygen transfer, the behaviour cannot be considered typical of metabolising organisms, which would not desorb the oxygen back into the bulk fluid.

#### 2.2.7.2 Hydrodynamic Effects

The hydrodynamic effects refer to changes in oxygen transfer and concentration gradient due to the influences of four physical hydrodynamic phenomena. The first of these is thinning of the

gas-liquid interface boundary layer caused by collision with particles, promoting diffusion. The second impact of solids is relevant to particles larger than the boundary layer thickness which (a) increases turbulence near the gas-liquid interface, promoting the rate of surface renewal, thus enhancing  $K_L$ , or (b) the increase in viscosity caused by the particles damps turbulence at the interface, depressing  $K_L$  (Godbole *et al.*, 1990). The third hydrodynamic effect of solids is enhancement of surface renewal through changes in coalescence behaviour caused by the presence of solid particles (Kluytmans *et al.*, 2003). The final impact is relevant to particles smaller than the liquid film thickness which decrease  $K_L$  by occupying volume that would ordinarily have been available to liquid available for oxygen transfer and having a physical blocking effect.

Depending on the details of the system, biologically active particles could feasibly impart all of this behaviour on oxygen transfer within a bioprocess, giving this regime merit as an explanation for variations in  $K_L a$ . Ultimately, much of this behaviour is determined by particle bubble adhesion (PBA). The quantity of solids adhering to the gas-liquid interface is determined by a balance of adhesion and shear stress forces. Higher agitation causes an increase in shear stress, meaning that the shear stress force overcomes the adhesion force, removing particles from the gas-liquid interface. Consequently, the impact of PBA on oxygen transfer decreases with increasing agitation (Ruthiya *et al.*, 2003; Vinke *et al.*, 1991).

To model PBA, Vinke *et al.* (1991) show that for static conditions particles adhere to the surface of gas bubbles, with the fraction of the surface of the gas bubble covered dependent on the relative sizes of the gas bubble and solid particles, the transport properties, and the effective contact angle ( $\theta_E$ ). This is defined as the angle between a flat gas-liquid surface, and a flat wall. The maximum angle of the bubble surface that can be covered ( $\alpha_{max}$ ) is found using Equation 2.35 (Vinke *et al.*, 1991), with the enhancement factor ( $E_0$ ) defined in Equation 2.36. This system is depicted in Figure 2.14.

$$2 \cdot \alpha_{max} - \sin(2 \cdot \alpha_{max}) = \frac{4}{\pi} \cdot \frac{2\gamma}{1 + \gamma} \left( \frac{\left(\frac{2}{8}\right) \cdot \theta_E^2}{E_0(1 + \gamma)} - 1 \right) \quad (2.35)$$

$$E_0 = \frac{\text{initial gas absorption flux into suspension}}{\text{initial gas absorption into particle free liquid}} \quad (2.36)$$

Equation 2.35 is only true for a system in a stagnant fluid, although it can also be adapted to give  $\zeta_{max}$ , the maximum possible fraction of surface coverage in turbulent conditions. Vinke *et al.* (1993) found that  $\alpha_{max}$  does not decrease significantly, even at fluid speeds close to the terminal rise velocity of the bubble, meaning that the fraction of the bubble covered by the solids is relatively unchanged despite rising quickly through the bioreactor. However, at higher fluid velocities in line with highly agitated bioprocesses, the solid particles were found to adhere to

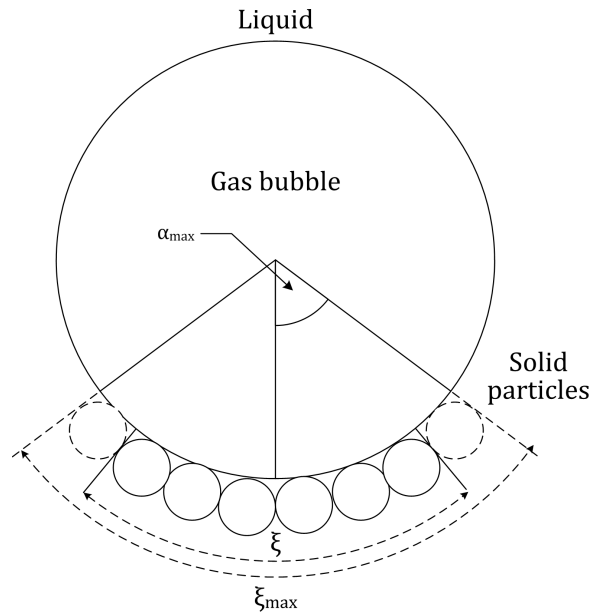


Figure 2.14: Diagram depicting gas bubble with a single layer of solid particles adhering to the interface, showing both the actual fraction of surface coverage ( $\zeta$ ) and the maximum possible fraction of surface coverage ( $\zeta_{max}$ ) (Adapted from Vinke *et al.* (1993))

the trailing end of the bubble (Vinke *et al.*, 1991). Consequently, despite turbulent conditions in a bioprocess, there is adhesion of solid particles to the bubble surface.

To illustrate this phenomenon, TFT can be applied to the system with simplified geometry. The bubble surface can be divided into two areas: the portion covered by solid particles, and the remainder left uncovered, defined by the distribution ratio ( $m_p$ ). Oxygen therefore has two pathways to follow from the gas bubble to the bulk liquid phase. and the flux through the covered section of the bubble is found by modifying Equation 2.6 through the inclusion of  $m_p$  to yield Equation 2.37 (Vinke *et al.*, 1993).

$$J_A = K_L \cdot (C^* - C(t)/m_p) \quad (2.37)$$

Applying the residence time of a solid particle on the bubble ( $\tau$ ), the time averaged solute flux through the portion of the gas-liquid interface covered by solid particles can be found. In combination with an overall unsteady mass balance the time averaged flux of solute through the covered area of the bubble, and multiplication with the interfacial area per unit volume, the total rate of mass transfer is found using Equation 2.38.

$$N_{TOT} = a(K_L(C^* - C_L(t)) + \zeta(\epsilon \cdot K_{LS} \cdot C^*) - K_L(C^* - C_L(t))) \quad (2.38)$$

Equation 2.38 represents the oxygen transfer through the entire available interfacial area, for both covered and uncovered sections. This model doesn't take into account layering of particles,

i.e. particles adhering on top of one another at the phase interface. Vinke *et al.* (1993) found that the model for mass transfer holds despite layering of particles, with any enhancement of mass transfer being caused by the particles adhered directly onto the interface.

### 2.2.7.3 Stabilization of Bubbles

Solid particles contribute to more stable gas bubbles, with reduced bubble coalescence resulting in an increase in the mass transfer area (Kluytmans *et al.*, 2003). This is primarily caused by the adhesion of solid particles to the surface of the bubbles, and acts as a barrier to coalescence. As a consequence, the bubble size distribution shifts to the smaller end of the spectrum, increasing the total interfacial area available for oxygen transfer. Ruthiya *et al.* (2003) quote five different physical property types that influence the adhesion of particles to the gas-liquid interface: (i) surface tension, (ii) liquid viscosity and density, (iii) ionic forces, (iv) wettability of the particles and (v) particle size. With the exception of (i) and (iii), the remaining properties are all a function of the chemical and physiochemical properties of the solid particles in question. In a bioprocess, these properties would change depending on the organism in use. Further complicating the matter are examples in literature where nutrient limitation can cause the behaviour of biomass to change, as found by Smit *et al.* (1992). During flocculation testing with *Saccharomyces cerevisiae* MYP1, their study found that the hydrophobicity and flocculation behaviour is dependent on the organism's growth phase, as well as nutrient limitations. Consequently, accurate quantification and prediction of the impact of these properties would typically have to be investigated on a case-by-case basis.

### 2.2.7.4 Reaction Enhancement

Solid particles catalyse reactions in the stagnant boundary at the gas liquid interface, increasing conversion and mass transfer (van der Zon *et al.*, 1999). This mechanism does not necessarily stand alone, and can enhance the boundary layer mixing and coalescence inhibition. The boundary layer mechanism would typically apply to a bioprocess where the bulk fluid is oxygen limited, and the increase in oxygen concentration in the boundary layer is enough to support the metabolic requirements of the biomass. However, this would not be an efficient operating regime for the bioprocess, reducing the likelihood of the mechanism being dominant in this application.

### 2.2.7.5 Particle Type Classification

As detailed in the previous sections, the (Ruthiya *et al.*, 2003) method of classification relies on the analysis of the system's reaction to the addition of solid particles. The root cause of the specific particle properties that bring about these phenomena, and a rigorous understanding of why certain properties in a solid particle can be attributed to a change in mass transfer behaviour, is fundamental to grasping the theory of the operation. A fundamental solution is proposed

to classify the particle type based on the type of activity the particle demonstrates within the multiphase system. Consequently, solid particles can be split into four main groups.

The first category contains particles that actively participate as a transport vehicle in oxygen transfer in the system. These are typically particles with high porosity that have the ability adsorb oxygen in areas of higher concentration (at the gas-liquid interface), and desorb in areas of lower concentration. This type of particle is known as physically active, and a good example of this particle type is activated carbon. Physically active particles are known to increase  $K_La$  in certain systems, and have been widely reported in literature.

The second group contains particles that perform metabolic reactions associated with cellular respiration, consuming nutrients in substrate and converting it to adenosine triphosphate (ATP). A fundamental property for this particle type is the ability to absorb and consume oxygen, without any desorption taking place. These particles are termed biologically active, and include any organism performing cellular respiration.

A third group is for particles that catalyse reactions in the boundary layer at the gas-liquid interface in a multiphase system, known as chemically active. Beenackers and Van Swaaij (1993) state that if the diameter of the catalyst particles is smaller than the boundary layer, and if the chemical reaction proceeds at a high enough rate, catalytic particles can enhance mass transfer from gas to liquid phases. This category of particles also introduces possible saturation effects as the reaction proceeds with time, as well as catalyst deactivation, and should therefore be applied with care.

The final category is for particles that have no effect other than their presence, and termed inactive. Rather than impacting oxygen transfer in a direct manner, these use a number of alternative pathways, such as increased surface turbulence and surface renewal at the gas-liquid interface, diffusion blocking, as well as impact on bubble break-up and coalescence.

## 2.3 Overall Volumetric Oxygen Transfer Coefficient

Bioprocesses are operated under conditions (temperature, pressure, pH, power input, biomass and nutrient concentration) that are optimized for the specific requirements of the organism to ensure the production of a desirable product. Alongside this, mode of operation (batch, fed-batch or continuous) is pre-defined based on other requirements. Consequently, because of the multitude of variables that define the system, the OTR is not easy to predict or measure. Different phenomena are simultaneously taking place, each with a different driving force and outcome. The relative magnitude of each outcome is also affected by changes in scale, reactor operation mode and environmental conditions (temperature, pressure, humidity). Therefore, while the fundamental basis of the OTR (as defined by Equation 2.6) is the concentration gradient (which is determined by the oxygen solubility) and  $K_La$  (which is a grouped parameter,

comprising the product of the liquid side oxygen transfer coefficient,  $K_L$ , and the interfacial surface area per unit volume,  $a$ ), it is important to recognise the role of other factors which underpin the behaviour of  $K_L$ , interfacial area and the oxygen concentration gradient. The complex relationship of parameters is outlined in Figure 2.15.

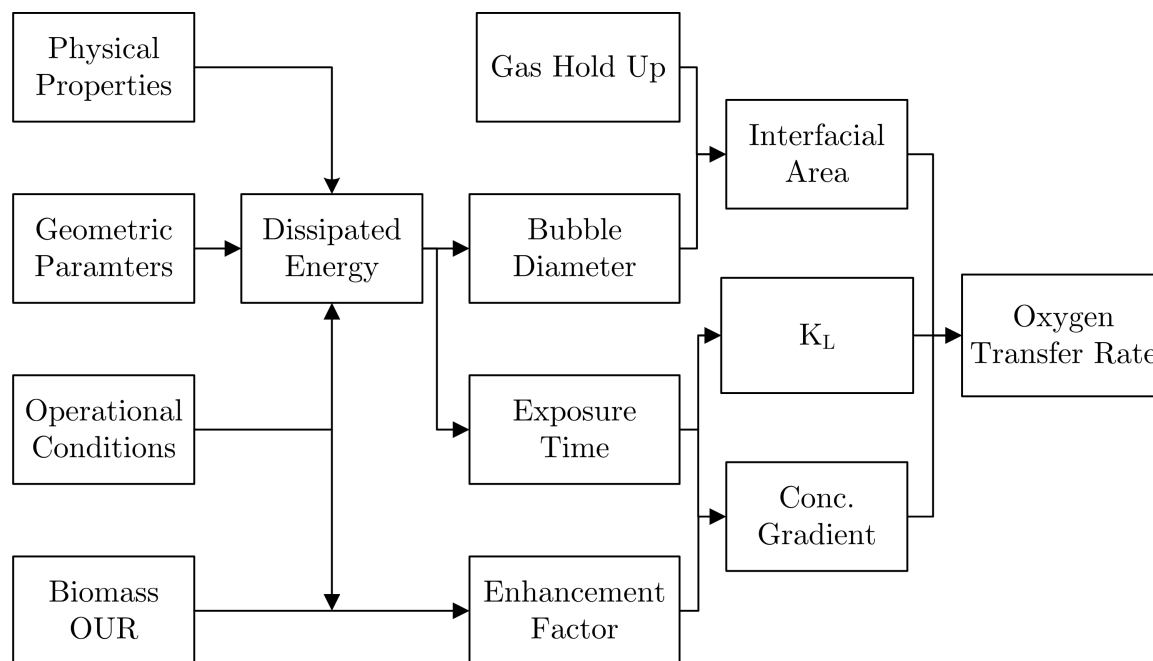


Figure 2.15: Individual Factors Contributing to the Overall Volumetric Oxygen Transfer Coefficient (Adapted from Garcia-Ochoa and Gomez (2009))

To ensure the optimal efficiency of a hydrocarbon bioprocess in terms of oxygen transfer, care should be taken to operate the system in a regime where the presence of the hydrocarbon enhances, rather than depresses, oxygen transfer. Key to quantifying the regions of enhanced oxygen transfer is understanding the overall volumetric oxygen transfer coefficient ( $K_La$ ) in hydrocarbon-based systems. This understanding also needs to be expanded to include a solid phase, to bring the system in line with a model hydrocarbon-based bioprocess. Subsequent discussion is directed at understanding the impact of alkane and solid particles on  $K_La$ , and  $K_La$  behaviour under different operating conditions.

### 2.3.1 Overall Volumetric Oxygen Transfer Coefficient in Hydrocarbon-Aqueous Systems

The behaviour of  $K_La$  in hydrocarbon systems is dependent on both the hydrocarbon concentration and the level of turbulence. Inclusion of hydrocarbon as an additional liquid phase impacts on the physiochemical properties of the bulk fluid, such as viscosity and surface tension. The OTR depends directly on the relative magnitudes of the  $K_La$  and the driving force created by the oxygen concentration gradient driven by the oxygen solubility (Equation 2.6). This means that

the increase in oxygen solubility in the bulk fluid (with concomitant increase in the gas-liquid concentration gradient) may not be able to offset the negative effects of the increased viscosity imparted by the hydrocarbon (with concomitant depression of  $K_{La}$ ). Clarke *et al.* (2006) has shown the  $K_{La}$  reaches a plateau and beyond 10%v/v  $n\text{-C}_{10-13}$ , the  $K_{La}$  is depressed. Depression of the  $K_{La}$  is especially evident at low agitation rates (less than 800 RPM), with very low agitation rates (below 600 RPM) not yielding any  $K_{La}$  enhancement, even at low alkane concentrations. These trends show an optimal  $K_{La}$ , at an agitation rate between 1000 and 1200 RPM and an alkane concentration between 5 and 10%. This means that the effect of the alkane on the oxygen transfer is a function of the concentration as well as the properties of the system. Figure 2.16 describes some of the trends observed in literature in terms of the ratio of  $K_{La}$  to  $K_{La}$  in pure water ( $K_{La}^*$ ) with changes in hydrocarbon concentration.

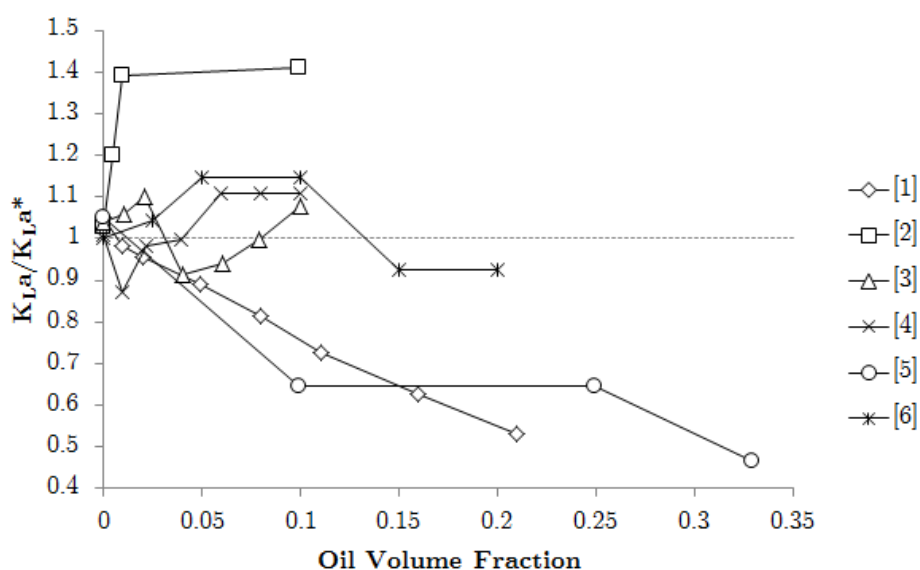


Figure 2.16: Variation of oxygen  $K_{La}$  for various oil volume fractions reported in literature (adapted from Ngo and Schumpe (2012))

[1] - liquid paraffin (bubble column) (Yoshida *et al.*, 1970), [2] -  $n$ -dodecane (bubble column) (da Silva *et al.*, 2006), [3] -  $n$ -hexadecane (STR) (Hassan and Robinson, 1977), [4] -  $n$ -dodecane (STR) (Hassan and Robinson, 1977), [5] -  $n$ -hexadecane (bubble column) (Nielsen *et al.*, 2003), [6] -  $n\text{-C}_{13-14}$  (STR) (Clarke *et al.*, 2006)

Clarke and Correia (2008) consolidated three distinct trends which evident in hydrocarbon-based system reported in literature, namely Types 1, 2 and 3. In systems displaying Type 1 behaviour,  $K_{La}$  increases, passes through a maximum and subsequently decreases with increasing hydrocarbon volume fraction. Type 2 behaviour indicates that  $K_{La}$  increase, with no subsequent decrease with increasing hydrocarbon volume fraction. Finally, in Type 3 behaviour  $K_{La}$  is constant or decreasing with increasing hydrocarbon volume fraction.

Type 1 behaviour displays a distinct peak in the  $K_{La}$ , enhancing the oxygen transfer over what



is possible in pure aqueous systems, followed by a decline. This trend is illustrated in trend [5] in Figure 2.16. The peak in  $K_La$  was reported at different oil phase volume fractions for each hydrocarbon type in STRs: 5% (v/v) for  $n$ -C<sub>12–13</sub> (Clarke *et al.*, 2006) (see Figure 2.17), 10% (v/v) for  $n$ -C<sub>10–13</sub> (Correia *et al.*, 2010), 10% (v/v) for  $n$ -C<sub>16</sub> (Nielsen *et al.*, 2005), 1% with silicone oil and 2% with soybean oil (Maia *et al.*, 1999).

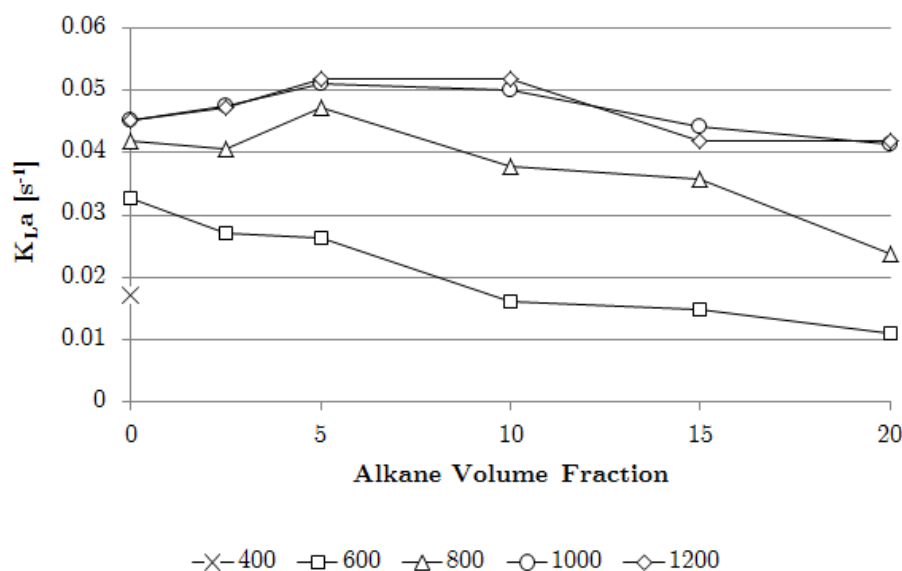


Figure 2.17: Enhancement followed by suppression of  $K_La$  with addition of alkane to an aqueous system (Adapted from Clarke *et al.* (2006))

Type 1 behaviour is not restricted to aerated hydrocarbon-aqueous systems, and has been observed in hydrocarbon systems containing micro-organisms. Liu *et al.* (1994) found that for a *Saccharomyces cerevisiae* fermentation, a volume fraction of 0.25% of lard oil enhanced  $K_La$ , which was similar to the enhancement for a volume fraction of 1% olive oil. McMillan and Wang (1987) found in *Escherichia coli* suspensions, the maximum  $K_La$  was achieved with a volume fraction of 30% PFC-40. Using *Aerobacter aerogenes*, Rols and Goma (1989) also demonstrated type 1 behaviour exhibiting a maximum at 16.7% volume fraction of  $n$ -dodecane.

In these studies, there is no trend describing the hydrocarbon volume fraction which generates the most significant  $K_La$  enhancement. Clearly the properties of the hydrocarbon phase have an impact on the behaviour of the  $K_La$ . Ngo and Schumpe (2012) cite the reason for variation in  $K_La$  behaviour is the spreading coefficient (as discussed in Section 2.2.6). A second cause for the variations is proposed by Clarke and Correia (2008) is system geometry which is thought to play a major role. More significant  $K_La$  enhancement trends were observed in STRs, as opposed to airlift reactors and bubble columns as witnessed by Jia *et al.* (1996) who report a maximum  $K_La$  at just 2%  $n$ -dodecane and perfluorocarbon in an air-lift reactor. Similarly, Jia *et al.* (1996) also report a maximum at 4% using C<sub>12–26</sub> in a similar reactor.

When examining Type 2 behaviour, it is evident that it can be further subdivided into two trends:  $K_{La}$  steadily increasing with oil phase concentration, and  $K_{La}$  increasing up until a maximum, at which point it plateaus as the oil phase concentration is increased further (as can be observed in curve [2] in Figure 2.16). Studies conducted by Liu *et al.* (1994); Cascaval *et al.* (2006); Galaction *et al.* (2004a); Yoshida *et al.* (1970, 1977); Kundu *et al.* (2003) and Dumont *et al.* (2006) all found a maximum value for  $K_{La}$  at the maximum hydrocarbon concentration, regardless of the hydrocarbon and reactor type. One possible explanation for the lack of a maximum value for  $K_{La}$  under these circumstances may be insufficient experimental data at the hydrocarbon phase concentrations at which a peak could exist, disguising the true  $K_{La}$  behaviour.

Type 3 behaviour describes systems where no  $K_{La}$  enhancement is evident with the addition of a hydrocarbon phase. This behaviour is thought to be fundamentally dependent on the level of turbulence inside the reactor. In studies where this behaviour was observed in STRs, the agitation was very low. Bi *et al.* (2001) found no change in  $K_{La}$  at 135 RPM irrespective of the ethanol concentration (a range of 0-8 g/l was examined), but as soon as the agitation was increased (400-600 RPM) the  $K_{La}$  was increased 4 fold. Clarke *et al.* (2006) observed depression of the  $K_{La}$  with the agitation anything less than 800 RPM, again independent of alkane concentration. Yoshida *et al.* (1970) found a steady decline in  $K_{La}$  enhancement with increasing kerosine fraction, but in this case the extent of the depression was largely independent of the agitation levels. The same study observed a similar trend under identical operating conditions in a bubble column, this time independent of the superficial velocity.

It is apparent that the through careful selection of the alkane volume content in a system, enhancement of  $K_{La}$  compared with a pure aqueous system can be observed, a theory reinforced by the Type 1 system behaviour observed in Clarke *et al.* (2006). A number of possible theories have been promoted to explain this behaviour. The first entails the alkane phase coating the bubble surface and act as a surface active agent, reducing the surface tension which increased the interfacial area for a constant gas holdup (Rols *et al.*, 1990; Yoshida *et al.*, 1970). Secondly, the alkane droplets act as rigid spheres, and increase the turbulence and mixing in the boundary layer, enhancing diffusion (Rols *et al.*, 1990). Finally, the alkane acts as a active intermediary (vector) for transport of oxygen from the gas to the liquid phase (Rols *et al.*, 1990) as in Figure 2.11.

However these theories fail to explain Type 3 behaviour observed by Yoshida *et al.* (1970). It is argued that this decrease is caused by the negative spreading coefficient of the kerosine in water (beading behaviour), reducing the effective interfacial area available for oxygen transfer, a theory supported by Rols and Goma (1989). However, the kerosine fraction in Yoshida *et al.* (1970) was shown to have negligible impact on the gas hold up, likely indicating that the size distribution and rise time of the bubble population is independent of kerosine fraction resulting

in a net decrease in the interfacial area and depressing  $K_La$ .

It is therefore evident that presence of a hydrocarbon phase can simultaneously have positive and negative effects on  $K_La$ . The relative magnitude of these effects shifts with hydrocarbon concentration, and need to be balanced to yield the optimal operating conditions for enhanced oxygen transfer.

### 2.3.2 Overall Volumetric Oxygen Transfer Coefficient in Hydrocarbon-Aqueous System with Suspended Solids

To mimic a typical hydrocarbon-based bioprocess, the system needs to include a solid phase (to represent microorganisms) in the hydrocarbon-aqueous dispersion. This can be in the form of physically, biologically or chemically active or completely inert particles. Each has a different effect on the mass transfer based on the properties of the particles. As discussed in Section 2.2.7, the presence of solids introduce a new set of challenges when trying to understand the oxygen transfer in the system and can include addition of further resistance to mass transfer by physically blocking molecular diffusion; changes in the physiochemical properties (density, viscosity, surface tension) of the fluid in the system; changes in the rate of surface renewal and interfacial surface turbulence at the gas-liquid interface; modification of the bubble coalescence behaviour due to particle adhesion on the bubble surface; acting as transport vehicles for molecular oxygen (in the case of physically active solid particles); and influencing the liquid side oxygen transfer coefficient,  $K_L$  (Beenackers and Van Swaaij, 1993).

Maia *et al.* (1999) examined the effect of antifoam compounds (polypropylene glycol, silicone and soybean oil) on gas-liquid mass transfer in an SRT containing *Pseudomonas putida* and found that antifoam acted primarily on  $K_L$ , especially at low concentrations. The antifoam has a minor influence on interfacial area through an increase in the gas holdup.

It is clear that the presence of solid particles in the system affect both the  $K_L$  and interfacial area, and the underlying cause for an observed change in  $K_La$  can be difficult to define. As such, this study is poised to elucidate the potential effects the presence of solids can have on  $K_La$  in a hydrocarbon dispersion, driven by any combination of the above factors. The subsequent sections deal independently with the system derived factors responsible for imparting a trend on  $K_La$  behaviour, and together will form a cohesive platform describing the current understanding of oxygen transfer in a model hydrocarbon based bioprocess.

## 2.4 Factors Affecting Overall Volumetric Oxygen Transfer Coefficient

$K_La$  is known to be affected by a number of process parameters, such as the rate of agitation, the hydrocarbon concentration, the solid loading and the particle diameter. However, the effect

of variation of these process parameters on  $K_La$  are generally studied independently, and while this offers some understanding of the underlying causes of changes in  $K_La$  behaviour, it fails to take the interaction between the parameters into account. It is necessary to understand how changes to the system as a whole impact on the  $K_La$  and ultimately the oxygen transfer.

## 2.4.1 Effect of Agitation on the Overall Volumetric Oxygen Transfer Coefficient

$K_La$  is increased by a higher rate of agitation (Correia and Clarke, 2009; Correia, 2007; Clarke and Correia, 2008). In order to understand the cause of this behaviour, it must be remembered that  $K_La$  is a lumped term, consisting of  $K_L$ , the liquid side oxygen transfer coefficient, and interfacial area, the interfacial surface area per unit volume between the gas phase in the bubbles and the bulk liquid phase. Both  $K_L$  and interfacial area are affected by changes in agitation, and needs to be studied individually, as discussed in Sections 2.4.1.1 and 2.4.1.2 respectively. The interfacial area is related to the gas hold up,  $\varepsilon_G$ , and the inverse of the Sauter mean bubble diameter,  $D_{32}$  (Rhodes, 2008)(see Equation 2.39). The Sauter mean diameter is defined as the diameter of a sphere that has the same volume to surface area ratio as that of the bubble in question.

$$D_{SM} = 6 \cdot \frac{V_b}{A_b} \quad (2.39)$$

### 2.4.1.1 Effect of Agitation on Oxygen Transfer Coefficient

Alves *et al.* (2004) conducted a study on the effect of rate of agitation on  $K_L$  using a solution of aqueous  $\text{Na}_2\text{SO}_4$ , 0.3 M, the results of which are given in Figure 2.18. It is clear that an increase in the agitation does have a positive effect on  $K_L$ , with a peak forming at 450 RPM. The same study went on to show that  $K_L$  was approximately 5 times greater in systems with bubbles larger than 2.5 mm diameter compared to bubbles smaller than 2.5 mm, findings supported by Calderbank and Moo-Young (1961).

One possible explanation is that smaller bubbles behave more as rigid spheres, while the large bubbles take longer to stabilise, a theory first suggested by Froessling (1938). The dependence of  $K_L$  on bubble size has been attributed to hydrodynamic differences between large, oscillating bubbles and small bubbles behaving like rigid spheres. The large bubbles generated enhanced internal gas circulation as a result of the movement of the gas-liquid interface, which has a positive influence on oxygen transfer. The same is not true of small, rigid bubbles.

Improvement of the oxygen transfer rates in large bubbles is suggested to result from a marked effect of surface rigidity on  $K_L$ . Calderbank and Moo-Young (1961) reported values of  $K_L$  of  $4.56 \times 10^{-2}$  cm/s for larger bubbles, and  $1.27 \times 10^{-2}$  cm/s for small rigid bubbles. Akita and

Yoshida (1974) also observed a decrease in  $K_L$  with decreasing bubble size.

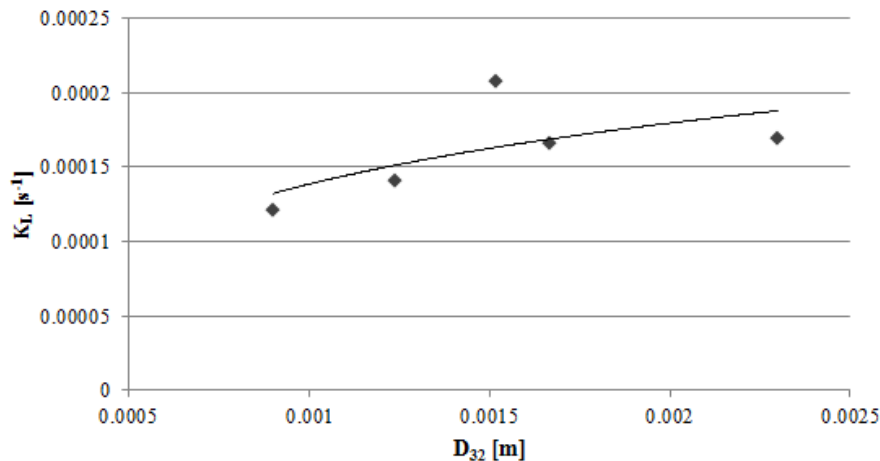


Figure 2.18: Oxygen Transfer Coefficient Different Bubble Sizes (Adapted from Alves *et al.* (2004))

Another factor promoting  $K_L$  with an increase in agitation rates is the decrease in resistance to molecular diffusion due to thinning of the stagnant layer thickness at high turbulence, as suggested by the TFT. Additionally, a number of correlations have also been reviewed by Clarke and Correia (2008) which predict  $K_L$  increases with an increase in bulk fluid turbulence.

#### 2.4.1.2 Effect of Agitation on Interfacial Area

Correia *et al.* (2010) demonstrated that the  $D_{SM}$  decreased with increasing agitation rates, regardless of the composition of the systems investigated. This was attributed to the increased dynamic turbulence, which gives rise to increased bubble breakup (Correia *et al.*, 2010).

As noted in the review by Clarke and Correia (2008), an increase in turbulence results in a decrease in the average bubble size, and an increase in the interfacial surface area. There are a number of correlations linking interfacial area,  $P/V$ ,  $N$  and the superficial gas velocity,  $V_s$ . These factors are not independent in their influence on interfacial area, and therefore their interactions between one another, as well as their effect on the system, need to be considered.

As noted by the positive exponents of the correlations in Clarke and Correia (2008), an increase in agitation results in an increase in the interfacial surface area. This is caused by the larger shear forces acting on the bubbles, reducing their coalescence behaviour. This drop in bubble size, and lower rise velocity, results in increased residence time, and correspondingly an increase in gas hold up (Barigou and Greaves, 1996). The effects of these parameters on interfacial area are described by Equation 2.39.

Barigou and Greaves (1992) found a very direct inverse relationship between agitation speed and  $D_{32}$ . An increase in agitation from 100 to 200 RPM decreased the  $D_{32}$  from 2.75 mm to 1.4

mm. The study also found a pronounced shift in the bubble size distribution towards the smaller bubble sizes with an increase in agitation.

## 2.4.2 Effect of Hydrocarbon Concentration on the Overall Volumetric Oxygen Transfer Coefficient

The addition of a hydrocarbon to the system changes the  $K_L a$  behaviour through the bulk fluid viscosity ( $\mu$ ) and fluid surface tension ( $\sigma$ ). These physiochemical properties are defined by the hydrocarbon concentration, hydrocarbon type as well as hydrocarbon chain length (Koide *et al.*, 1976; Zaharadnik *et al.*, 1992; Clarke and Correia, 2008).

Queimada *et al.* (2003) states that there is a linear relationship between the natural logarithm of the surface tension and inverse viscosity for systems containing n-alkanes (Equation 2.40).

$$\ln(\sigma) = \ln(A) + \frac{B}{\mu} \quad (2.40)$$

A and B are constants for the system. This has been shown to be valid for n-alkanes in the range  $n\text{-C}_2\text{H}_6$  -  $n\text{-C}_6\text{H}_{14}$ , benzene, toluene, xylenes, phenol and other aromatics, alcohols in the range  $\text{CH}_3\text{OH}$  -  $\text{C}_4\text{H}_9\text{OH}$ , ketones and water (Queimada *et al.*, 2003).

### 2.4.2.1 Effect of Hydrocarbon Concentration on Oxygen Transfer Coefficient

Hydrocarbon addition increases the viscosity of the bulk liquid phase in the reactor, resulting in a decrease in shear force acting on the bubbles, and decreasing  $K_L$ . Furthermore, more viscous fluids have been shown to have more resistance to oxygen transfer through the liquid-gas interface (Garcia-Ochoa and Gomez, 2005; Yagi and Yoshida, 1974). The concept behind this theory is that an increase in viscosity suppresses bubble recirculation in the reactor (less vertical bubble movement) and that the diffusivity of the gas into the fluid is correspondingly reduced.

Clarke and Correia (2008) suggested that  $K_L$  is negatively influenced by the addition of hydrocarbons to the system. The extent of the decrease was found to be dependent on the chain length and concentration of the hydrocarbon. The review reported decreases in  $K_L$  of 44, 50 and 62.5 % for *n*-hexanol, *n*-heptanol and *n*-octanol respectively. The major cause of the negative influence of hydrocarbon on  $K_L$  is thought to be the surfactant effect of the hydrocarbon, causing a decrease in surface tension at the bubble-fluid interface. The drop in surface tension corresponds to a decrease in the bubble surface mobility, meaning the bubble behaves more as a rigid sphere. Therefore, there is a drop in internal motion, and  $K_L$  is reduced (Clarke and Correia, 2008).

These results have been shown experimentally, with a study by Calderbank and Moo-Young

(1961) who found a steady decrease in  $K_L$  with an increase in oil concentration from 14 - 69.5%. To test whether the decrease in  $K_L$  is driven by the surfactant effect of the hydrocarbon, Yagi and Yoshida (1974) also found a decrease in  $K_L$  with a 0.1% addition of surfactant. Combined, these results give a strong indication that a drop in surface tension brought about by the addition of hydrocarbon is at least partially responsible for the observed decreases in  $K_L$ .

#### 2.4.2.2 Effect of Hydrocarbon Addition on Interfacial Area

The interfacial area is determined by the bubble size and gas hold-up, both of which are affected by the addition of hydrocarbon through changes to the bulk fluid viscosity and surface tension. In addition to the concentration of the hydrocarbon, the chain length of the hydrocarbon is known to be an important factor, as each hydrocarbon has different effects on the fluid in the reactor.

Correia *et al.* (2010) found that increased hydrocarbon concentration increases the interfacial area in the system. The interfacial area is related to the bubble size via an inverse power relationship, where smaller bubbles have a larger surface area per unit volume. In turn, the bubble size is determined partly by the surface tension and viscous forces, and with an increase in hydrocarbon concentration there is a corresponding decrease in surface tension and bubble size. In addition to the reduction of surface tension, coalescence of bubbles is decreased (Clarke and Correia, 2008; Das *et al.*, 1985), increasing the residence time and gas hold up in the bioreactor. Furthermore, long chain hydrocarbons increase hold up significantly more than short chain hydrocarbons, underlining the effect of chain length on the system.

Hydrocarbon addition not only affects the surface tension, but also increases the viscosity of the bulk fluid. The increase in viscosity decreases the turbulence in the system, which increases the size of the boundary layers as defined in the TFT. This means that more force is required to break bubbles up, and therefore breakup is less likely to take place, in addition to the increased coalescence caused by the increased viscosity. Finally, another factor thought to have an effect on bubble size is the slower formation of the liquid film around the gas during bubble formation. This means that more gas is captured before the formation of the bubble is complete (Clarke and Correia, 2008). Combined, these factors result in an increase in mean bubble size in the system for a constant gas hold-up, which alone would mean a decrease in the interfacial surface area. Furthermore, due to larger bubble sizes, the rise time is decreased, meaning a smaller gas hold up.

Das *et al.* (1985) experienced an increase, followed by a decrease in interfacial area with increasing toluene concentration, leaving a distinct maximum at around 15% (v/v). This is largely attributed to an increase in the average bubble diameter, and a peak in the gas hold up trend at the same toluene concentration. The relative change of the gas hold up and mean bubble diameter determine the interfacial area for a certain toluene concentration (Das *et al.*, 1985).

It is clear that the effect of hydrocarbon addition to the bioprocess has opposing effects. The reduction in surface tension decreases  $D_{SM}$ , promoting interfacial area, while the viscosity damps turbulence and enhances bubble coalescence, depressing interfacial area. The balance of these counteracting effects ultimately defines the effect of hydrocarbon addition on interfacial area.

### 2.4.3 Effect of Solids on the Overall Volumetric Oxygen Transfer Coefficient

The inclusion of a solid phase is required to more accurately model a hydrocarbon bioprocess for examination of the oxygen transfer in these systems. It has been established that  $K_La$  is heavily dependent on the system properties, which are in turn altered by the addition of solids. There are a number of factors that affect how the solids will behave in the system, namely solid type, density ( $\rho$ ), solid loading (wt%) and particle size ( $d_p$ ). A summary of literature examining biological solids and solid loadings on  $K_L$ , interfacial area and  $K_La$  is given in Table 2.3.

Biologically active solids are defined as having (in the case of aerobic organisms) the ability to absorb and consume oxygen, without any desorption taking place. Following deactivation, the impact of this particle type on oxygen transfer can be studied in simulated model bioprocesses. Two main impacts of the presence of biologically active solids in the bulk liquid on  $K_La$  are observed in literature. The first is the physical blocking effect the particles have, hindering oxygen transfer by adhering to the gas-liquid interface. This is apparent in the results of a study of *Propionibacterium shermanii*, *Saccharomyces cerevisiae*, *Penicillium chrysogenum* pellets and *Penicillium chrysogenum* free cell suspensions by Galaction *et al.* (2004a), who found that with the exception of the *P. chrysogenum* pellets, any increase in the microorganism concentration lead to the decrease of  $K_La$  values. In the case of the *P. chrysogenum* pellets, an initial increase in  $K_La$  was observed, followed by an overall decline. When these results are compared the results using simulated broths (with identical viscosities without biomass), it was found that the  $K_La$  was consistently lower for systems containing organisms. It is concluded that an additional mechanism causing the depression of  $K_La$  in the systems containing organisms is a physical blocking effect at the gas-liquid interface. The magnitude of the blocking effect dependent on the organism type, as witnessed by larger decreases observed for *P. chrysogenum* free mycelial suspensions. These findings are supported by Cascaval *et al.* (2006), who performed similar experiments, with the inclusion of a hydrocarbon phase (*n*-dodecane). It was found that when comparing simulated broths (without solid phase but at a comparable viscosity) with conventional broths, the presence of biomass negatively impacts on  $K_La$  through modification of the hydrodynamic characteristics of the bulk liquid phase and physical blocking of adsorption on the bubble surface.

The second impact brought about by the presence of biological solids, the  $K_La$  depression, is attributed to the increase in the apparent viscosity driven by the solid particles, a conclusion



supported by both Galaction *et al.* (2004a) and Cascaval *et al.* (2006). The increase of viscosity, a direct result of an increase in biomass, drives two direct major effects on oxygen mass transfer, namely the reduction of bulk liquid turbulence and an increase in bubble coalescence.

The impact of non-biological solids is summarised in Table 2.4. Alper *et al.* (1980) found that finely powdered activated carbon (falling into the physically active particle category) was able to increase  $K_L$  considerably by facilitating gas transfer in glucose solutions. Pal *et al.* (1982) agreed with this when they demonstrated that fine activated carbon particles (1.7-4.33  $\mu\text{m}$ ) added to a oxidising sodium sulphide system in the range of 0.1 to 2.0 weight percent could increase the rate of absorption up to 14 fold. On the contrary, Schumpe *et al.* (1987) found no improvement in absorption in an aqueous system when the activated carbon particle diameter was in the same region as the liquid side diffusion film. However, they did find that activated carbon has a coalescence hindering effect in ionic solutions, preventing small 'ionic' bubbles from coalescing, increasing the overall surface area. It is clear that the impact of physically active particles is very system dependent, and suggests that the mechanisms at play are complex. However, the potential for an increase in the oxygen transfer remains with the inclusion of physically active particles, and should be assessed within the specific system in question. The effectiveness of a physically active particle (activated carbon) forms the basis of a hypothesis of this study and is discussed in subsequent sections.

Particle density has also shown to impact on  $K_L a$  behaviour. Schumpe *et al.* (1987) found that low concentrations ( $< 10 \text{ g/l}$ ) of fine, high density particles like aluminium oxide ( $\rho = 3180 \text{ kg/m}^3$ ,  $\phi = 8.1 \mu\text{m}$ ) or diatomaceous earth ( $\rho = 2360 \text{ kg/m}^3$ ,  $\phi = 6.6 \mu\text{m}$ ) increased  $K_L$  based on hydrodynamic effects on the bubbles.

Mena *et al.* (2005) state that the smaller the particle size, the larger the negative effect on  $K_L a$ . They further state that the effect on  $K_L a$  using larger particles is a combination of simultaneous changes in  $K_L$  and interfacial area. Manyuchi (2010) is in agreement with these findings, finding that the  $K_L a$  decreased from  $0.0500 \text{ s}^{-1}$  for a solid particle size of  $3\mu\text{m}$  to  $0.0250 \text{ s}^{-1}$  for  $14\mu\text{m}$  in a system containing 2.5 %v/v  $\text{C}_{14-20}$  at a solid loading of 1 g/l. The drop in  $K_L a$  is suspected to be a result of a decrease in the surface area available for oxygen transfer (Miyachi *et al.*, 1981).

In order to better elucidate the underlying causes of the  $K_L a$  behaviour in systems containing solids, further discussion in subsequent sections is divided into the impacts of solids on  $K_L$  and interfacial area independently.

Table 2.3: Literature Studies on Biological Solids and their Effect on  $K_{La}$ ,  $K_L$  and Interfacial Area

Reference	Solid	Particle Size [ $\mu\text{m}$ ]	Volume Fraction [%]	Solid Density [ $\text{kg}/\text{m}^3$ ]	Liquid	Comments
Galaction <i>et al.</i> (2004a)	<i>Propionibacterium manii</i>		30.5/120.5 g/l		Water	Increase in microorganism concentration lead to the decrease in $K_{La}$ values. Blocking effect, dependent on particle type.
	<i>Saccharomyces cerevisiae</i>		33.5-150 g/l			
	<i>Penicillium chrysogenum</i> pellets	1.6-1.75 mm	5-36.5 g/l			
	<i>Penicillium chrysogenum</i> free cell		4-36.5 g/l			
Amaral <i>et al.</i> (2008)	<i>Yarrowia lipolytica</i>		0-10g/l		Perfluoro-decalin	Reduction in $K_{La}$ with the increasing cell concentration.
Cascaval <i>et al.</i> (2006)	<i>Propionibacterium manii</i>		30.5-120g/l		<i>n</i> -Dodecane	Increase of apparent viscosity by biomass accumulation. <i>S. cerevisiae</i> blocks interface between organic and aqueous phases.
	<i>Saccharomyces cerevisiae</i>		43-150g/l			

Table 2.4: Literature Studies on Non-Biological Solids and their Effect on  $K_L a$ ,  $K_L$  and Interfacial Area

Reference	Solid	Particle Size [ $\mu\text{m}$ ]	Volume Fraction [%]	Solid Density [ $\text{kg}/\text{m}^3$ ]	Liquid	Comments
Joosten <i>et al.</i> (1977)	Glass Beads	88	0-40	2500	Kerosene	$K_L a$ increasing with small increase in solid loading, sharp decrease above 20%. Low $\rho$ solid caused greatest drop in $K_L a$ .
	Glass Beads	53	0-40	2500		
	Sugar	74-150	0-40	1590		
	Polypropylene	53-105	0-40	946		
	Polypropylene	250	0-40	946		
Ozturk and Schumpe (1987)	Polyethylene(A)	24.6	5.1-36.2	940	Ligroin, Tetralin	High $\rho$ solid increase $K_L a$ for liquids with low $\rho$ and $\mu$ .
	Polyethylene(B)	106	1.2-34.8	965		
	Polyvinylchloride	82	0.8-36.8	1380		
	Aluminium Oxide	10.5	0-11.6	3180		
Miyachi <i>et al.</i> (1981)	$\text{CaCO}_3$	1.2-10	0-10	2750	Water	$K_L a$ higher for larger particles. Reduction of $a$ likely cause of drop in $K_L a$ . More turbulence in liquid film for larger particles results in higher $K_L$ .
Mena <i>et al.</i> (2005)	Calcium Alginate	1.2, 2.1	0, 5, 10	1023	Water	Solids negatively affect $K_L a$ , more pronounced for smaller particles. Smaller particles affect both $K_L$ and interfacial area, while larger particles only affect $K_L$ .
Beenackers and Van Swaaij (1993)		Review				Initial drop in bubble coalescence with increasing solid loading due to increase in viscosity. Decrease in $K_L a$ dependent on the ratio between solid and fluid densities.
Zheng <i>et al.</i> (1995)	Glass Beads	520-722	1-16.5	2338	Water	Increase in solid loading and size decreased $K_L$ over the entire range.
Gollakota and Guin (1984)	Silica Powder	< 45	0-50 wt%	2650	Water	Dependent on power input, small variation in $a$ for <50wt% loading. $K_L a$ increased drastically for sand addition.
	Silica Sand	350-800	0-60wt%	2650		

Table 2.5: Literature Studies on Non-Biological Solids and their Effect on  $K_L a$ ,  $K_L$  and Interfacial Area

Reference	Solid	Particle Size [ $\mu\text{m}$ ]	Volume Fraction [%]	Solid Density [ $\text{kg}/\text{m}^3$ ]	Liquid	Comments
Alper <i>et al.</i> (1980)	Activated Carbon	< 5	0-16			Fine inert particles have no effect on $K_L$ . Activated carbon increased $K_L$ . No change in $K_L a$ for inert particles up to 16% vol.
	Silica Powder	< 5	0-16		Water	
	Acrylic Beads	15-20	0-16			
Van Weert <i>et al.</i> (1995)	Ground Sand	< 50	0-40	2160	Water	Steady decrease in $K_L$ with increasing solid loading.
	Activated Carbon	11.04	0-2	1640		Retardation of coalescence behavior of bubbles in water by particles in liquid film at gas-liquid interface increases specific $a$ and $K_L$ . Significant increase in $K_L a$ at low solid loadings.
Ozkan <i>et al.</i> (2000)	Diatomaceous Earth	6.84	0-2	2420		
	Calcium Carbonate	3.80	0-2	2750	Water, $n$ -	
	Aluminium Oxide	0.53	0-2	3820	Butanol	
	Barium Sulphate	1.57	0-2	3820		
	Iron(III) Oxide	4.71	0-2	3820		
Oguz <i>et al.</i> (1987)	Sea Sand	< 80	7.5-10	2590		Sea sand has little effect on $K_L a$ , while $\text{TiO}_2$ and $\text{ZnO}$ caused sharp decrease, even at low loadings. For various slurries, $K_L a$ can be approximated using apparent viscosities.
	Diatomaceous Earth	< 50	2.5-10	2070		
	Aluminium Oxide	< 50	5-10	3200		
	Titanium Oxide	< 0.5	2.5-10	4380	Water	
	Iron(II) Oxide	< 0.5	2.5-5	3610		
Albal <i>et al.</i> (1983)	Zinc Oxide	< 1	1-2.5	4720		
	Glass beads	150	0-30	2700		Enhanced surface renewal and mobility increase diffusion and $K_L$ for low solid loading.
Mehta and Sharma (1971)	Oil shale	140	0-30	2270	Water	
	Calcium Carbonate	1	0-15	2710	MEA, DEA,	Fine particles decrease surface mobility and turbulence, drop in $K_L$ . Similar drop in $a$ .
	Sodium Carbonate	1	0-15	2540	DIPA, Water, $\text{Na}_2\text{S}_2\text{O}_2$	
Pal <i>et al.</i> (1982)	Sodium Bicarbonate	1	0-15	2200		
	Activated carbon	4.3, 85	0-0.25wt%		$\text{Na}_2\text{SO}_4$ , Water	Particles < film thickness can substantially increase the absorption.
Derksen <i>et al.</i> (2000)	Silica	13	0-15	2610		Hydrophobic silica has blocking effect. $K_L a$ increase for pyrite.
	Pyrite	14	0-15	5000	Water	

Table 2.6: Literature Studies on Non-Biological Solids and their Effect on  $K_L a$ ,  $K_L$  and Interfacial Area

Reference	Solid	Particle Size [ $\mu\text{m}$ ]	Volume Fraction [%]	Solid Density [ $\text{kg}/\text{m}^3$ ]	Liquid	Comments
Littlejohns and Daugulis (2007)	Nylon 6,6	2590	15	1140		$K_L a$ decrease with solid addition. Nylon shows increase due to low oxygen diffusion coefficient.
	Glass beads	6000	18	940	Water	
	Silicone rubber	2500	14	1150		
	Styrene-Butadiene	3570	7	3180		
Schumpe <i>et al.</i> (1987)	Activated Carbon	5.4	0.5-15	1800		$K_L a$ decrease with solid addition. Nylon shows increase due to low oxygen diffusion coefficient.
	Diatomaceous Earth	6.6	0.2-12	2360	$\text{Na}_2\text{SO}_4$ , Water	
	Aluminium Oxide	8.1	0.3-6.3	3180		
Freitas and Teixeira (2001)	Calcium Alginate	2131,	0-30	1023,	Water	Reduction in $K_L a$ largely due to decrease in $a$ with increasing solids.
		2151		1048		
Kawase and Hashimoto (1996)	Polycarbonate	3000	0-30	1030		$K_L a$ decreases with increasing solid loading. Small increase below 10%, dramatic decreases to 30%.
	Polyvinyl Chloride	2000	0-30	1300	CMC, Water	
Mills and Bar (1987)	Glass beads	44-88	0-40	2460	Water	Dramatic decrease in $K_L a$ caused by drop in $a$ .
Manyuchi (2010)	Deactivated Yeast	3, 14	0-10		$\text{C}_{14-20}$ , Water	Insignificant decrease in $K_L a$ , increase in fluid viscosity and density.
Sada <i>et al.</i> (1986)	Aluminium Oxide	<3	<1.0	3850		Finer particles increased $\epsilon_G$ .
	Calcium Hydroxide	7	<1.0	2240	Water	
	Calcium Carbonate	10	<1.0	Variable		

### 2.4.3.1 Effect of Solid Loading and Particle Size on the Oxygen Transfer Coefficient

Addition of solids to the system causes pronounced and significant changes in the  $K_L$ , and the nature of the impact is highly dependent on the solid size, density and type. Beenackers and Van Swaaij (1993) presented a review in which the effect of inert solids on  $K_L$  was discussed, and propose that  $K_L$  is defined by the diffusivity. Depending on the theory implemented to model mass transfer,  $K_L$  is defined by Equations 2.26 - 2.28. These models clearly illustrate the dependence of  $K_L$  on  $D_{AB}$ . Therefore, moving towards the root cause of the impact of solid particles on  $K_L$  requires examination of the behaviour of  $D_{AB}$ . Alper *et al.* (1980) tout the particle size as playing a major role in defining the impact on diffusion. Smaller solid particles are able to penetrate the stagnant film at the gas-liquid interface and enhancing diffusion when compared with larger particles.

The particle type also plays a major role in  $K_L$  behaviour, especially when considering physically active particles. The previously mentioned 'shuttling' mechanism (Section 2.2.7.1) can be used to enhance diffusion at the gas-liquid interface. However, the experimental evidence is inconclusive. Chisti and Moo-Young (1988) examined the ratio between the  $K_L$  and bubble size in a bubble column and found this to be independent of reactor type, fluid and operating regime, suggesting that  $K_L$  is proportional to the bubble size. However, it was highly dependent on the solid loading. An increase in solid concentration in the system reduced the  $K_L$  for a constant bubble size. This is explained using TFT, with an increase in film thickness caused by a reduction in the turbulence due to increased bulk fluid viscosity as a result of the solid addition. Furthermore, the solids hinder surface renewal at the interface, hampering the diffusion of oxygen from gas to liquid (Chisti and Moo-Young, 1988). A further explanation is due to the lack of diffusion through the solid particles present at the interface, resulting in blocking effect for diffusion (Chisti and Moo-Young, 1988).

Mena *et al.* (2005) found that both the solid loading and particle size have an effect on  $K_L$  in an air-water-calcium alginate beads system. For small particles,  $K_L$  is lowered, and the effect is worsened by higher solid loadings. Larger particles were found to have a damping effect on  $K_L$  while remaining largely independent of solid loading.

Miyachi *et al.* (1981) and Joosten *et al.* (1977) both found that low solid loadings of around 0.1 - 2.5 % resulted in an increase in interfacial turbulence, resulting in a higher  $K_L$ . The heavier particles used in Joosten *et al.* (1977) are thought to promote interfacial turbulence and surface renewal due to the increased inertia. This theory is supported by Miyachi *et al.* (1981). Schumpe *et al.* (1987) also found that the addition of low concentrations of fine, high density solids (diatomaceous earth, aluminium oxide) in a bubble column increased  $K_L$  due to hydrodynamic effects on the liquid film around the bubbles. However, it was also shown that this positive effect is limited to solid concentrations low enough not to have a significant impact on the fluid viscosity. Albal *et al.* (1983) suggest that the solid loading doesn't significantly alter

the viscosity and other system properties for low solid loadings, but rather enhances the surface renewal rate. This increases molecular mobility, the rate of diffusion, and  $K_L$ . Further increases in solid loading increase the viscosity with the associated decrease in  $K_L$ , possibly explaining why  $K_L a$  initially increases and then decreases as solid loadings are further increased (if the effects of the changes in the interfacial area are ignored temporarily).

### 2.4.3.2 Effect of Solid Loading and Particle Size on the Interfacial Area

The total interfacial area in a system is defined by a combination of the mean bubble size and the gas hold up. Solid particles have an impact on both these parameters through their influence on bubble coalescence and break up, as well as fluid viscosity and surface tension.

In their review on mass transfer in slurry reactors, Beenackers and Van Swaaij (1993) state that small particles cover the surface of the bubbles in the reactor, preventing coalescence. As found previously, an decrease in bubble size results in an increase in the interfacial surface area, according to the relationship shown in Equation 2.39. Therefore, an increase in solids loading results in an increased interfacial area. It should be noted that this increase will only happen to a certain extent, thereafter the solids can no longer find a bubble surface to adhere to, and then become obstructions to diffusion and mass transfer through increasing the system's viscosity (Beenackers and Van Swaaij, 1993). Joosten *et al.* (1977) follow a different approach and state that the reduction in  $K_L a$  for all particle sizes is likely caused by the decrease in interfacial area. Additionally, the gas hold-up at high solid loadings decreased due to the formation of larger gas bubbles (caused by the drop in coalescence) and their faster rise time (Joosten *et al.*, 1977).

Sada *et al.* (1986) quote an increase in the  $K_L a$  with a small addition of fine particles, caused by reduced bubble coalescence increasing interfacial area. This however is not always the case. Galindo *et al.* (2000) found that the  $D_{SM}$  of bubbles dropped from 950  $\mu\text{m}$  to 550  $\mu\text{m}$  with an increase in biomass concentration from 0 to 5 g/l with a 10% oil fraction. With a very bimodal bubble size distribution, consisting of a few large bubbles and an abundance of small ones, it is postulated that the effect of solids is not related to any modification of the surface tension. Furthermore, studies using a bulk liquid with polymer-modified viscosity (Nienow, 2004) produce a larger  $D_{SM}$  than what is expected for systems with comparable viscosities and include solids, making it likely that the presence of the solids has an impact on the bubble  $D_{SM}$  through adhesion and the prevention of coalescence and/or physical blocking of the oxygen transfer rather than through increasing the viscosity.

It is clear from the literature on this topic that the impact of solids on both oxygen transfer and gas-liquid interfacial area is not well understood, and can have a variety of effects based on the properties of the system and the density, size and loading of the solid particles.

## 2.5 Dissolved Oxygen Measurement

A number of techniques exist for the measurement of the  $K_La$ , and an appropriate methodology is chosen based on a four factors (Novak, M. & Klekner, 1988), namely: the level of aeration and homogenisation; the bioreactor type and scale; the fermentation medium composition and the possible effects of solid particles and micro-organisms.

The methodologies are summarised in Table 2.7. The chemical and biological methods are based on a reaction in the liquid phase to reduce the dissolved oxygen concentration. The physical methods examine the oxygen concentration in the bulk liquid or fermenter exhaust gas during re-absorption of oxygen into the system following a nitrogen purge. The methods make use of different mathematical models to describe the change in gas-phase oxygen concentrations.

### 2.5.1 Chemical Methods

Chemical methods were the basis for the oldest methods for measuring  $K_La$  in literature, and were once widely accepted. However, the nature of the method means that the physiochemical properties of the bulk fluid are altered when the chemicals are added to the system, impacting especially the bubble coalescence and oxygen solubility. The results of these methods can also overestimate the  $K_La$  because of fast liquid-phase reactions. For these reasons, these methods are not employed in this study.

### 2.5.2 Biological Methods

Typically, biological methods are only employed when organisms are active in the system. The primary method is to calculate the OTR from a mass balance at steady state Wang *et al.* (1979). This involves analysis of the exhaust gas using inline gas analysers

Other biological methods involve correlating the oxygen transfer to the growth rate of a known organism during the exponential phase, amongst other assumptions. However, this is extremely laborious, and the accuracy is questionable. This method was employed by Duetz *et al.* (2000) in their study of *Pseudomonas putida* CA-3.

Biological methods are not discussed further in this study as the system did not include actively respiring cells.

### 2.5.3 Physical Methods

Physical methods make use of a polarographic probe to record the response of the DO concentration to a step change in the oxygen partial pressure in the sparge gas. They form the basis of most investigations into oxygen transfer, because of their applicability to a wide variety of system, ease of implementation and accuracy. Numerous studies have employed physical methods,



Table 2.7: Summary of methodologies for  $K_La$  determination (Moutafchieva *et al.*, 2013)

Measurement Method	$K_La \times 10^2$ [s <sup>-1</sup> ]	Time	Scale	Comments
Chemical	Sulphite Oxidation	Hours	Lab	Labour intensive. Rate of reaction zero order in sulphite. Complex kinetics.
	Absorption of CO <sub>2</sub>	Minutes	Lab	Assumed kinetic constants. Alteration in driving force.
	Dynamic pH Measurement	Half Hour	Any	Assumed kinetic constants. Salt addition has no affect on CO <sub>2</sub> mass transfer.
	Hydrazine Oxidation	Minutes	Pilot	Assume no Hydrazine accumulation, and no chemical enhancement.
	Bio-oxidation of Catechol	Minutes	<100ml	Only applies to small scales, limited by availability of oxidative enzyme.
Physical	Gassing Out	Minutes	>100ml	Solids can be included in system. Probe response critical. Time can become a factor at larger scales.
	Pressure Step	Minutes	>100ml	Inert solids can be employed. Time can become a factor at larger scales.
Biological	Biological Gassing Out	Minutes	Any	Requires high [DO], probe response time critical, hydrodynamic changes will impact metabolic activity. Assume OUR independent of [DO].
	Biological Gassing Out w/ High OUR	Minutes	Any	Assume OUR independent of [DO], probe response time critical.
	Gas Phase Analysis	Hours	>100ml	Well mixed gas and liquid assumptions not always valid on larger scales, also not ideal for small systems because of small gas residence time.

including Gourich *et al.* (2008); Philichi and Stenstrom (2011); Nielsen *et al.* (2003); Clarke and Manyuchi (2012); Correia and Clarke (2009); Clarke *et al.* (2006); Scargiali *et al.* (2010); Ozkan *et al.* (2000); da Silva *et al.* (2006); Neale and Pinches (1994); Rao *et al.* (1967); Soni (2010); Torres-Martínez *et al.* (2009); Moutafchieva *et al.* (2013); Van't Riet (1979); Fugasova *et al.* (2007); Behkish *et al.* (2002); Benedek and Heideger (1970); Mills and Bar (1987). Discussion of physical techniques is more in depth than previous methods because of the accuracy they offer, their ease of implementation and data analysis, and their widespread and accepted usage in oxygen transfer literature.

### 2.5.3.1 Gassing Out Procedure Using a First Order Model

The GOP is also commonly known in literature as the dynamic method, and was developed by Rao *et al.* (1967). The reactor is sparged with pure nitrogen, purging the reactor of oxygen. Once equilibrium is established, the sparge gas is switched back to air, and the DO recovery is measured over time. The DO response is assumed to follow a first order equation (Equation 2.41), the same equation derived in Equation 2.16 representing, where  $C_P$  is the DO concentration as measured by the probe, and  $C_L^*$  is the oxygen solubility, and

$$\frac{dC_P}{dt} = K_{La} \cdot (C_L^* - C_P) \quad (2.41)$$

The first order response assumes that the DO probe has no response lag, meaning that  $C_P = C_L$ , where  $C_L$  is the actual DO concentration in the system. This is linearised and integrated to reach Equation 2.42, where  $C_{L1}$  is the initial DO concentration.

$$\ln \left( \frac{C_L^* - C_L}{C_L^* - C_{L1}} \right) = -K_{La} \cdot t \quad (2.42)$$

Since  $C_{L1}$  is equal to 0, a plot of  $\ln \left( 1 - \frac{C_L}{C_L^*} \right)$  vs.  $t$  will yield a straight line of gradient  $-K_{La}$ . This method is used extensively for  $K_{La}$  measurement, although numerous authors (Hassan and Robinson, 1977; Aiba and Huang, 1969; Linek *et al.*, 1987; Clarke and Correia, 2008) raise issues about the accuracy because of the  $C_P = C_L$  assumption. Clarke and Manyuchi (2012) quantify this inaccuracy in hydrocarbon-aqueous dispersions, demonstrating overestimation of  $K_{La}$  by up to 45% at the highest agitation rate. Due to the lack of a response lag, the faster the rate of change of DO, the less accurate the probe readings will become. This model is used to model the probe response lag when using the second order model, discussed in the subsequent section.

### 2.5.3.2 Gassing Out Procedure Using a Second Order Model

The polarographic probes used to measure DO make use of a membrane-covered solid electrode system (Benedek and Heideger, 1970). The probe measures the DO by measuring the current caused by the reduction reaction at the cathode (see Appendix F for the complete operating principle of the probe). The membrane and electrolyte represent a barrier to DO measurement which cause a lag time ( $\tau_p$ ) in the probe's reading when the system is not at steady state (during the transient phases of the GOP). The inverse of  $\tau_p$ ,  $K_p$ , is defined as the probe constant.

Ruchti *et al.* (1981) state that the lag can be attributed to the time required for the diffusion of oxygen through the outer liquid film, and through the probe's membrane. 5 areas of the probe have been identified as possible causes of instrument lag (Benedek and Heideger, 1970), namely: the bulk liquid phase; the DO probe membrane; the DO probe electrolyte; the DO probe cathode (*Negligible*); and the DO probe anode (*Negligible*).

The probe response to a step change in the DO probe environment from an oxygen purged to an oxygen saturated system is modelled as a first order function (Aiba and Huang, 1969). The first order response is defined according to Equation 2.43 (Fuchs *et al.*, 1971; Van't Riet, 1979).

$$\frac{dC_P}{dt} = K_P \cdot (C_L - C_P) \quad (2.43)$$

Under conditions of the experiment,  $C_L = C_L^* = C_P^*$  (where the probe is transferred to an oxygen saturated system) and with  $\tau_p$  equal to  $\frac{1}{K_p}$ , Equation 2.43 can be rearranged to yield Equation 2.44.

$$\tau_p \cdot \frac{dC_P}{dt} = (C_L^* - C_P) \quad (2.44)$$

Separation of variables in Equation 2.44 yields Equation 2.45, and with integration between  $t$  and  $t_0$  gives Equation 2.46.

$$\frac{dC_P}{C_L^* - C_P} = \frac{dt}{\tau_p} \quad (2.45)$$

$$\ln \frac{C_L^* - C_{PO}}{C_L^* - C_P} = \frac{t - t_0}{\tau_p} \quad (2.46)$$

Since the initial concentration,  $C_{PO}$  at  $t_0$ , is equal to zero, Equation 2.46 is reduced to Equation 2.47 (Fuchs *et al.*, 1971).

$$\ln \frac{C_P^*}{C^* - C_P} = \frac{t - t_0}{\tau_P} \quad (2.47)$$

Rearranging Equation 2.47 yields Equation 2.48. The probe response time is taken when  $t = \tau_P$  (Fuchs *et al.*, 1971), simplifying Equation 2.48 to Equation 2.49.

$$\frac{C_P}{C^*} = 1 - e^{-\frac{t}{\tau_P}} \quad (2.48)$$

$$\frac{C_P}{C^*} = 1 - e^{-\frac{\tau_P}{\tau_P}} = 0.632 \quad (2.49)$$

$\tau_p$  is therefore the time the probe output takes to reach 63.2% of the final saturation value when the probe experiences a step change in the DO concentration, and  $K_P$  is the inverse of this value. To ensure accurate  $K_P$  this should be performed for each reactor configuration, as different conditions have an impact on the probe response time (Clarke and Manyuchi, 2012).

Development of the second order model, which takes into account the response of the DO to a step change while incorporating the influence of the probe response lag, requires simultaneous solution of Equations H.1 and H.2 to yield Equation 2.52. The complete mathematical derivation is provided in Appendix H.

$$\frac{dC_P}{dt} = K_P \cdot (C_L - C_P) \quad (2.50)$$

$$\frac{dC_P}{dt} = K_{La} \cdot (C_L^* - C_L) \quad (2.51)$$

$$\frac{C_P}{C_P^*} = 1 - \frac{1}{(K_P - K_{La})} \left( K_P \cdot e^{-K_{La}t} - K_{La} \cdot e^{-K_P t} \right) \quad (2.52)$$

Due to the accuracy of this methodology (Clarke and Manyuchi, 2012) this is considered a preferred approach.

### 2.5.3.3 Pressure Step Procedure

The pressure step procedure (PSP) was initially described by Linek *et al.* (1987). The PSP involves a step change in the inlet oxygen concentration, effected by changing the inlet pressure by 20%, either positively or negatively. This method accounts for any non-uniformity of the gas concentration (Correia and Clarke, 2009).

Table 2.8: Dissolved Oxygen Probe Response in Literature

Reference	Response Lag Time [s]	$K_La$ Range, [ $s^{-1}$ ]	3 <sup>rd</sup> Phase
Nielsen <i>et al.</i> (2003)	11.2	0-0.0556	Alkane
Godbole <i>et al.</i> (1984)	4.7-14.1	0.01-0.045	Cellulose
Dang <i>et al.</i> (1977)	14.2	0.01-0.04	Cellulose
Gourich <i>et al.</i> (2008)	7	0.01-0.02	Propanol
Ruchti <i>et al.</i> (1981)	10-13	0.021-0.19	Cellulose
Correia and Clarke (2009)	N/A	0.01-0.07	Alkane
Clarke and Manyuchi (2012)	16.9-35.7	0.01-0.04	Alkane

Correia and Clarke (2009) report good accuracy with the PSP in determining  $K_La$  in alkane-aqueous dispersions. However, similar accuracies were achieved with the GOP when the DO probe response lag was incorporated, as demonstrated by Clarke and Manyuchi (2012). Since the GOP is experimentally and analytically simpler to execute than the PSP, the GOP remains the preferred methodology.

## 2.5.4 Effect of System Conditions on the Probe Response Lag

Just as changes in the system parameters can have an effect on the  $K_La$  of the process, changes in these same parameters have an effect on the measurement of the  $K_La$ . As described in the previous section, the probe response lag is a function both of the working mechanics of the probe, and the system in which it is operating. Clarke and Manyuchi (2012) found that while inclusion of  $K_p$  is necessary for accurate determination of  $K_La$ , of equal importance is the accurate quantification of  $K_p$  on a per-system basis. Consequently, the  $K_p$  needs to be determined for every change in agitation the system undergoes. Section 2.5.4.1 aims to understand and clarify these effects, in order to better account for them and improve the end accuracy and precision of the quantification of  $K_La$ .

### 2.5.4.1 Effects of Agitation on Probe Response Lag

Correia and Clarke (2009) undertook a study of the  $K_La$  measurement methodology in an alkane-aqueous system over a range of agitation rates. The study used both the PSP and GOP with 1st (Equation 2.41) and 2nd order (Equation H.23) models, and compared the results. It was found that  $K_La$  found using the  $GOP_1$  became progressively damped with increasing agitation (Correia and Clarke, 2009). At the higher agitation rates, the error in  $K_La$  was significant (greater than 40% for 1200 RPM) which indicates that the probe response lag has major impact on  $K_La$  measurement. The results record  $K_p$  of the same order of magnitude as  $\frac{1}{K_La}$  under these conditions. This is confirmed in literature (Van't Riet, 1979) where it was determined that the probe response lag is only negligible if  $K_p \ll \frac{1}{K_La}$ .

Gourich *et al.* (2008) similarly report that values of  $K_La$  are suppressed when  $K_p$  isn't considered in both pure aqueous systems and systems with 0.05% v/v propanol. Furthermore, the observed variance between  $K_La$  calculated without probe lag and with probe lag is magnified with increasing superficial velocity. Nielsen *et al.* (2003) stated that for system conditions where  $K_La > 0.25$ , the probe response lag, inclusion of  $K_p$  resulted in  $K_La$  values of up to 25% greater than without  $K_p$ .

Dang *et al.* (1977) found that the probe response lag in water decreased for an increase in agitation. It was concluded that the increase in shear forces thinned the liquid film surrounding the probe, reducing the time taken for the probe to respond to a step change in oxygen concentration. The study goes on to suggest that the probe response is influenced by the gas dynamics, which in turn is a function of the gas holdup in the system. An increase in agitation would increase the holdup as bubbles are flung radially before having a chance to rise, and as a result influence the  $K_p$ . Clarke and Manyuchi (2012), who analysed the  $K_p$  in a system containing alkanes with varied agitation from 600 to 1200 RPM, on the contrary showed no discernible influence of agitation on the  $K_p$ .

#### 2.5.4.2 Effects of Alkane Concentration on Probe Response Lag

Dang *et al.* (1977) studied a system containing an aqueous-carboxymethyl cellulose (CMC) dispersion, and found that the probe response lag was a function of the fluid viscosity. More viscous fluids increased gas hold up, and thickened the fluid boundary layers, hampering diffusion. Both these factors serve to indicate that an increase in the alkane concentration would increase the probe response time.

Clarke and Manyuchi (2012) established that  $K_p$  was significantly depressed in a system containing increased percentages of alkane. Furthermore, an increase in the alkane chain length also negatively affected the  $K_p$ . The end result was a large (up to 48%) variation in the  $K_p$  across the range of chain lengths and concentrations. The study attributed the increase in  $\tau_p$  to increases in the fluid viscosity, hampering oxygen diffusion to the probe, which is in agreement with the findings of Dang *et al.* (1977). However, as reported by (Correia and Clarke, 2009), an increase in the fluid viscosity also reduces the  $K_La$ , and as a result the influence of  $K_p$  on the accuracy of  $K_La$  becomes less significant. Therefore, due to the observed variation in  $K_p$  with the fluid viscosity, it is important to establish  $K_p$  for every alkane concentration considered in the experimental phase.

#### 2.5.4.3 Effect of Solids on Probe Response Lag

The effect of solid loading on the probe response lag is not well documented in literature. In their study of the three-phase slurry system, Mills and Bar (1987) found that for a polarographic probe with a teflon membrane, the probe time constant remained largely independent of the

system parameters. Their conclusion was that the resistance of the membrane to oxygen transfer was the dominating effect.

Ruchti *et al.* (1981) found that the probe response time increased with increasing CMC concentration due to increasing fluid viscosity. See Figure 2.19.

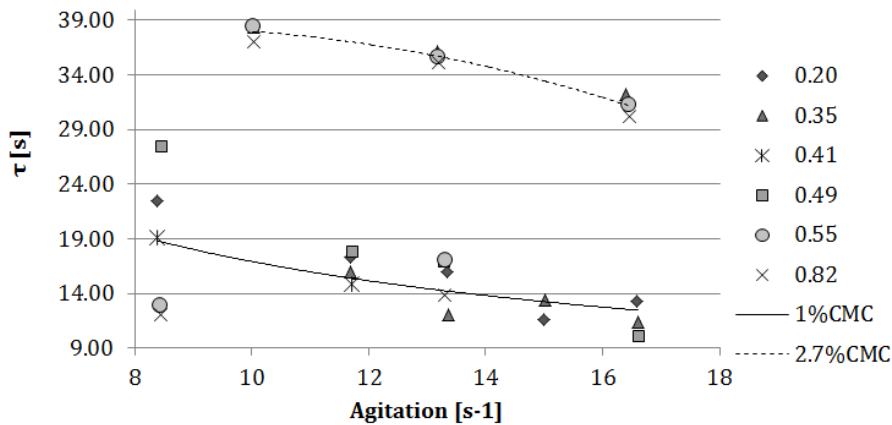


Figure 2.19: Effect of solid concentration on probe response time ( $\tau_p$ ) as a function of agitation (adapted from Ruchti *et al.* (1981))

In a system very similar to this study, Manyuchi (2010) found that both the solid loading and solid size had a negligible effect on  $K_p$ . In a system containing 2.5% (v/v)  $C_{14-20}$ -aqueous dispersion at 1000 RPM, increasing the solid loading from 1 to 10 g/l using  $3\mu\text{m}$  solids changed the  $K_p$  by less than 5%. Similarly, changing the solid size from 3 to  $14\mu\text{m}$  at a concentration of 1 g/l changed the  $K_p$  by 2%.

#### 2.5.4.4 Effect of Membrane Type, Membrane Age and Electrolyte Age on Probe Response Lag

Aiba and Huang (1969) performed a comprehensive study on the oxygen permeability and diffusivity through polymer membranes immersed in liquids, and the effect on the probe response lag. The silicone rubber membranes were found to have by far the highest oxygen diffusivity and permeability of all the membranes tested (almost 10 times that of Teflon). This would result in the smallest probe response time to a step change in system conditions. However, it isn't possible to make use of a silicone membrane as it is not resistant to the hydrocarbon. Therefore, a Teflon membrane needs to be used in a hydrocarbon-based system.

Manyuchi (2010) found that the membrane and electrolyte age also had a significant effect on the probe response in 2.5% (v/v)  $C_{14-20}$ -aqueous dispersions at 1000 RPM. The  $K_p$  was found to decrease from  $0.0559\text{ s}^{-1}$  to  $0.0329\text{ s}^{-1}$  over a period of 5 days (a decrease of over 42%). This decrease wasn't as significant if the electrolyte was replaced, dropping to only  $0.0457\text{ s}^{-1}$  over the same time period.

## 2.6 Measurement of Interfacial Area

The study of the interfacial area in a model hydrocarbon-based system, and its impact on  $K_La$  in response to changing system conditions, is of great importance when optimising the system. By performing a simultaneous evaluation of  $K_La$  and interfacial area behaviour due to changes in bulk fluid composition and turbulence, valuable insight can be gained into establishing oxygen transfer pathways and contribute to a fundamental understanding of mass transfer in multiphase systems.

Variations in interfacial area in a system are brought about by a large number of inter-related factors, thus making it difficult to characterize. The bubble size and therefore the area in an agitated bioprocess is a balance between the dispersive forces of the turbulent flow regime, and the viscous and surface tension forces of the fluid (Calderbank, 1958). As a result, interfacial area is highly dependent on the system parameters, both external (temperature) and internal (agitation, shear forces, fluid properties), and is a function of the bubble break up and coalescence that they impart. Added to this, interfacial area isn't stable, and is continually fluctuating inside the churning reactor. To combat this, the recorded instantaneous interfacial area must be averaged over a series of samples for every system configuration. Based on this, the specific interfacial area can be found. To expand this to yield the total contact area between the gas and liquid phases within the system, the gas hold up within the system must be known. This is also dependent on the system properties, and needs to be measured concurrently with the specific interfacial area.

Initial methodologies to determine interfacial area have had to use either film photography and manual image analysis, capillary tubes, measurement of diffused light, chemical reactions, correlations derived from mathematical models, or any combination of these techniques. The result was very time consuming, and thus hasn't been examined as much as  $K_La$ .

Bossier III *et al.* (1973) used the oxidation of aluminium alkyl to study the interfacial area in a baffled stirred tank reactor. The choice of the reaction system is based a series of requirements (Bossier III *et al.*, 1973): very fast reaction between the gas and liquid phases to maintain a boundary layer reaction; the reaction between the two phases must be represented by a single first or second order rate equation; the reaction taking place should form no gaseous products; and finally the liquid phase component in the reaction should have negligible vapour pressure, confining the reaction to the liquid phase boundary layer.

This reaction technique was also employed by Das *et al.* (1985) using the absorption of  $\text{CO}_2$  in NaOH solution. This method is not appropriate for this study because it is not suitable for a model bioprocess. The addition of the required reactants and their resulting products, along with the reaction conditions, make it impossible apply to a system containing living organisms. However, the trends found by these studies are relevant, and provide insight into the behaviour



of gas-liquid systems.

Another technique employed to measure bubble size is to use bubble sampling. This was used by Barigou and Greaves (1992) in their study of bubble size distributions in gas-liquid contactors. A vacuum was used to pull a continuous stream of gas-liquid dispersion from a point within the reactor. This was fed into a precision capillary tube of known diameter, creating slug flow. Detectors measure the length of the gaseous slugs, and calculate the volume. This was then used to find the diameter of a sphere with the same volume. Bubble sampling technique works well once it has been constructed and calibrated. The system also makes it very easy to sample from multiple points within the reactor. However, implementation of this technique required significant design and fabrication work, with very careful control on the suction so as not to promote bubble breakup in the sampling nozzle.

Slightly newer techniques use intrusive probes, such as the double optical probe technique. This involves the insertion of a fibre optic probe into the dispersion where it can detect infra red light from a source. When the probe tip is in fluid, the light is refracted back into the bulk phase, and when it is in gas (bubble), light is transmitted back along the fibre optic probe to a detector. This is then recorded for analysis. While this method has been shown to be an accurate measure of interfacial area, it requires bespoke equipment.

Investigations into interfacial area have been greatly simplified with the advent of high speed and high resolution digital photography, and more recent studies have all used some form of digital photography to find the interfacial area in multiphase systems. Mena *et al.* (2005) studied a bubble column system containing air, water and calcium alginate beads, and examined the interfacial area under varied conditions using a high speed camera and a diffused backlight. The primary difficulties involved with this method are providing enough light to capture clear images, removing optical distortion, and the accurate analysis of the images. The first difficulty is dealt with using either stroboscopic light sources, or diffused halogen lamps, while the optical distortion is removed using a square perspex jacket filled with liquid (Galindo *et al.*, 2005). The analysis of the images is done largely using computer simulations manipulating the images to enhance the bubbles, and extract their sizes. Galindo *et al.* (2005) made use of a very similar methodology using a stereoscopic microscope connected to a video camera. The advantages of this system include good versatility and a wide range of applications, full digital capturing and analysis (good reliability), good reproducibility, quick turn around times between experimental work and results, minimal intrusion into the flow inside the STR (no probes, sensors etc), can be applied to any size bioreactor and can be used to study flow patterns within the bioreactor. The advantages of this technique make it suitable for examination of interfacial area in model hydrocarbon-based bioprocesses.

## 2.7 Conclusions

Bioprocesses present a clear opportunity for the functionalisation of alkanes to higher value commodities under moderate pressure and temperature conditions. The extent and value of the end products provide significant motivation for the use of alkanes as a feedstock for commercial bioprocessing technologies. However, while the industrial opportunity is there, it must be tempered against the difficulty associated with the use of alkanes and multi-phase systems. The lack of any oxygen source in the hydrocarbon substrate means that meeting the oxygen demand of aerobic organisms under these conditions is a challenge, especially when considering the scale up of any process. This requirement is exacerbated by the observed depression of  $K_La$  when using a hydrocarbons hydrocarbon systems. Failure to acknowledge these issues would easily result in a transport limited operation, ultimately compromising product yield.

Fundamental theories for the mechanisms of oxygen transfer in hydrocarbon-based systems form a basis of the understanding of the behaviour of the system. However, empirically defining the oxygen transfer mechanism or pathways is difficult. This is primarily because it is highly unlikely that a single pathway is at play, with oxygen transfer taking place via a multitude of pathways in parallel, and the relative impact of each pathway differing for each operating regime and experimental condition. Tools such as the spreading coefficient mean that some oxygen transfer pathways become less likely, but ultimately are not able to define the pathway.

In order to study the  $K_La$  behaviour in an environment that is applicable to an operational bioprocess, use of a model bioprocess with all the attributes of the function bioprocess is required. To this end, previous work conducted by Correia *et al.* (2010), Clarke and Correia (2008), Correia and Clarke (2009), on oxygen transfer in hydrocarbon-aqueous systems, and Clarke and Manyuchi (2012) is extended to include an inert solid, deactivated *Saccharomyces cerevisiae*, bringing the experimental system in line with a model hydrocarbon-based bioprocess.

Through use of modern analysis tools, such as the incorporation of dissolved oxygen probe response lag enabling accurate measurement of  $K_La$ , and the ability to quantify interfacial area in operational systems, allow for simultaneous study of both  $K_La$  and interfacial area in the same system. Through individually understanding how changes in the system parameters affect  $K_La$  and interfacial area independently allows for study of the dominant oxygen transfer rate controlling parameter ( $K_L$  or interfacial area) and ultimately contributes to the fundamental understanding of oxygen transfer in these complex systems. These results have application in optimisation of full-scale bioprocesses, as well as in the efficient scale-up of lab-scale systems.

# Chapter 3

## Research Scope and Hypotheses

### 3.1 Research Scope

In hydrocarbon-aqueous dispersions, it has been established that trends exist in  $K_La$  and  $a$  behaviour which are heavily dependent on the system properties. Previous studies have documented this behaviour, and postulated possible driving factors and mechanisms that explain the trends observed. This study builds on this work through the inclusion of a solid phase modelling a bioprocess under controlled conditions.

The variables of the system are split into two categories, the first being the composition of the system (alkane concentration, alkane chain length, solid loading and type) and the impact on the fluid properties. The second category involves the turbulence, which is defined by the variable power input and its hydrodynamic effects. It is highly unlikely that these factors only have an effect on  $K_La$  and  $a$  through an individual contribution, but rather through a complex mechanism of interactions which create composite trends in  $K_La$  and  $a$ .

Based on the motivation provided in the literature review, hypotheses were developed to structure the findings. The hypotheses were divided into two major fields examining the  $K_La$  and interfacial area behaviour, each composing several further research questions aimed at quantifying the impact agitation, alkane concentration and solid loading on a model hydrocarbon-based bioprocess.

### 3.2 Hypotheses

**Hypothesis 1:** It is necessary to account for the probe constant ( $K_P$ ) in the determination of  $K_La$ . Due to the resistance to oxygen transfer across the probe membrane, a system-specific  $K_P$  is needed for the accurate quantification of  $K_La$ .

**Hypothesis 2:**  $K_La$  behaviour in simulated hydrocarbon based-bioprocesses is dependent on

the system turbulence and fluid properties in addition to their interactions. More specifically:

- i An increase in agitation will enhance  $K_La$
- ii An increase in alkane concentration will initially enhance  $K_La$  to increase initially, go through a maximum, followed by depression at higher concentrations
- iii An increase in solid loading will decrease the  $K_La$

Based on extensive studies in literature,  $K_La$  is highly dependent on the level of turbulence within the reactor. Turbulence is controlled by the geometry of the reactor system (which is to be maintained as a constant) and the power input into the system (controlled by varying the rate of agitation). However, the exact mechanism defining the relationship between agitation and  $K_La$  is not known, and this will be investigated in light of the theoretical work described the literature review.

The dependence of  $K_La$  on the liquid composition is likely due the different pathways through which the hydrocarbon affects the oxygen transfer and the negative influence of viscosity. The ultimate behaviour of the oxygen transfer is a balance between the alkane's ability to enhance  $K_La$  at low concentrations and the depression of  $K_La$  at higher concentrations caused by increased viscosity. Consequently,  $K_La$  is expected to go through a maximum with an increase in alkane concentration.

Literature suggests that solid particles will depress the  $K_La$  by increasing the bulk fluid viscosity, and having a physical blocking effect at the gas-liquid interface. Solid particles also increase the viscosity of the bulk fluid within the system which will increase the mean bubble size.

**Hypothesis 3:** The interfacial area behaviour in simulated hydrocarbon-based bioprocesses is dependent on the system turbulence and fluid properties in addition to their interactions. More specifically:

- i An increase in agitation will increase the interfacial area
- ii Increasing the alkane concentration will reduce the interfacial area
- iii An increase in solid loading will decrease the interfacial area

Turbulence has been shown to dramatically decrease the mean bubble size in a reactor. This relates to an increase in the interfacial surface area available for oxygen transfer. Smaller bubbles have a slower rise time resulting in an increased gas hold-up. Examination of these factors will be augmented through examination of the interaction between agitation and the other system properties through measurement of  $K_La$  and interfacial area

at increasing agitation levels.

The increase in viscosity imparted by the presence of alkane in the system decreases the turbulence, meaning an increase in the mean bubble size. A drop in the gas hold up caused by the increased rise time associated with larger bubbles will also contribute to a decrease in the interfacial area. This will be investigated through measurement of  $K_La$  and interfacial area at increasing alkane concentrations.

Finally, adhesion of the solid particles to the bubble's surface will prevent coalescence. Combined, this means a decrease in the total surface area. To demonstrate this, the  $K_La$  and interfacial area will be measured while increasing the yeast loading.

### 3.3 Objectives

The objectives of this study are defined to prove or disprove the hypotheses outlined above.

1. Measurement of the probe response to a step change in DO and subsequent use of a first order model to calculate  $K_p$  for each set of experimental conditions.
2. Measurement of system DO in response to a step change in the oxygen partial pressure of the feed gas.
3. Calculation of  $K_La$  using the system DO in response to a step change in the oxygen partial pressure of the feed gas, the probe constant and a second order model.
4. Measurement of  $K_La$  at a constant solid loading with varied agitation and alkane concentration.
5. Measurement of  $K_La$  at a constant alkane concentration with varied agitation and solid loading.
6. Measurement of  $K_La$  at a constant agitation with varied alkane concentration and solid loading.
7. Measurement of  $D_{SM}$  using photography and image analysis.
8. Calculation of interfacial area using  $D_{SM}$  and gas holdup.
9. Measurement of interfacial area at a constant solid loading with varied agitation and alkane concentration.
10. Measurement of interfacial area at a constant alkane concentration with varied agitation and solid loading.
11. Measurement of interfacial area at a constant agitation with varied alkane concentration and solid loading.

# Chapter 4

## Experimental Materials and Apparatus

### 4.1 Materials

To develop a model aerated hydrocarbon-based bioprocess, four phases need to be supplied: air, water, hydrocarbon and solids, where the hydrocarbon and solids need to be typical of such a process. To this end, a  $n\text{-C}_{14-20}$  straight chain alkane cut (Section 4.1.1) and non-viable yeast solids (Section 4.1.2) were used.

#### 4.1.1 Hydrocarbon

A single  $n\text{-C}_{14-20}$  mixture was used in this study, with samples taken from the same batch to ensure the chain length composition remains constant. The composition and technical data are given in Tables 4.1 and 4.2 respectively.

Table 4.1:  $n\text{-C}_{14-20}$  composition as determined using GC

Alkane	Name	Composition, Weight%
$n\text{-C}_{13}$	$n$ -Tridecane	0.81
$n\text{-C}_{14}$	$n$ -Tetradecane	28.06
$n\text{-C}_{15}$	$n$ -Pentadecane	26.62
$n\text{-C}_{16}$	$n$ -Hexadecane	22.67
$n\text{-C}_{17}$	$n$ -Heptadecane	15.51
$n\text{-C}_{18}$	$n$ -Octadecane	5.37
$n\text{-C}_{19}$	$n$ -Nonadecane	0.82
$n\text{-C}_{20}$	$n$ -Eicosane	0.10
$n\text{-C}_{21}$	$n$ -Heneicosane	0.03
Impurities		6.00

Table 4.2: Physical properties of  $n\text{-C}_{14-20}$  as supplied by Sasol Wax (via Organic Synthesis)

Property	Units	Value
Flash point	°C	110
Initial boiling point	°C	250
Dry point	°C	315
Appearance		Bright & clear
Colour	Saybolt	30
Sulphur	mg/kg	1 max
Aromatics	mass %	0.5 max
Pour point	°C	6
Density at 15 °C	g/cm <sup>3</sup>	0,81
Water solubility	g/l	insoluble
Lower explosion limit:	vol-%	0,6
Upper explosion limit:	vol-%	6,5

### 4.1.2 Non-Viable Yeast Solids

The yeast solids employed in this study were *Saccharomyces cerevisiae* in the form of commercially available dried bakers yeast pellets. These yeast cells were deactivated to prevent cellular respiration, and meaning the oxygen utilization rate (OUR) is zero for the duration of the experiments. The particle size distribution is supplied in Figure 4.1.

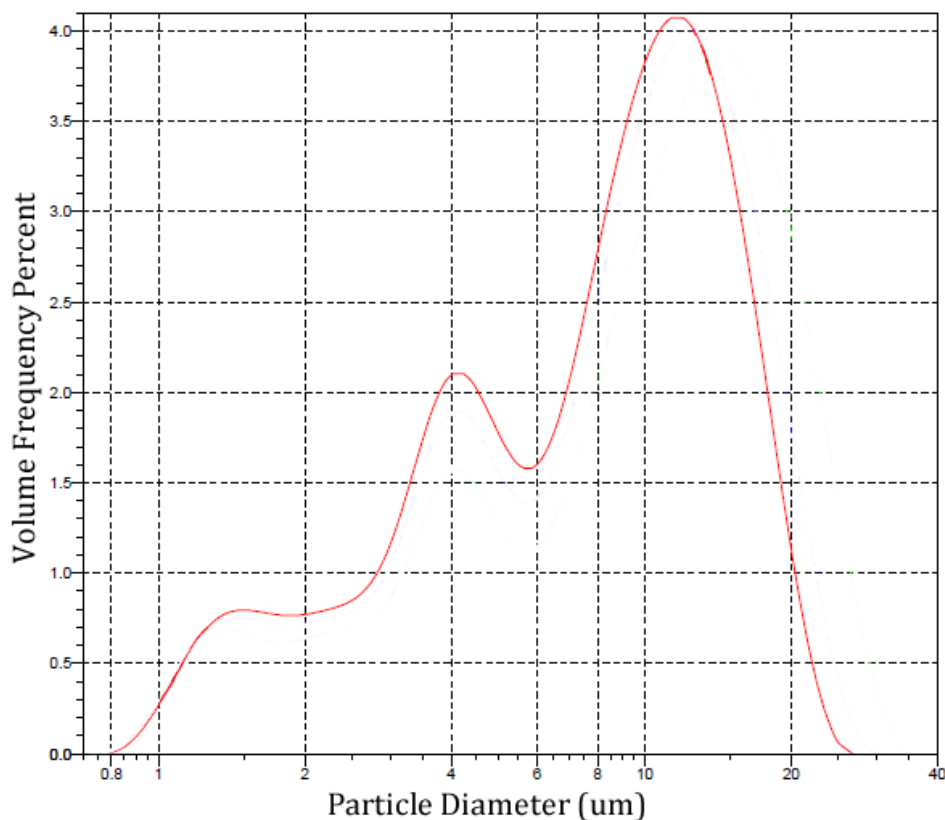


Figure 4.1: None-viable yeast solid size distribution

## 4.2 Apparatus

### 4.2.1 Bioreactor System

All experiments were conducted using a New Brunswick Bio Flow 110 with a total volume of 7.5 litres and a working volume of 5 litres (Figure 4.2). The bioreactor had a domed bottom, with four internal, equally spaced baffles. The geometry was identical to that used by prior studies (Correia *et al.* (2010) and Correia and Clarke (2009)) and is shown in Figure 4.2 with corresponding dimensions in Table 4.3. The probe locations were maintained throughout all the experiments, to ensure internal mixing was as uniform as possible between experiments. The layout is reflected in Figure 4.4

Agitation was achieved using two six bladed Rushton turbines, with a variable speed electric drive. Rushton turbines are radial flow impellers, and consist of 6 evenly spaced, vertical blades, mounted to a horizontal disk. Disk type impellers provide uniform radial flow, with the disk acting as a baffle on the shaft, preventing gas bubbles from rising adjacent to the shaft. When the radial flow was combined with suitable baffles, strong top to bottom mixing currents were generated. Rushton turbines are widely reported to be highly effective in gas-liquid and liquid-liquid dispersions. A dimensioned diagram of the turbine is provided in Figure 4.3.

Table 4.3: Bioreactor Geometry, Adapted from Correia (2007)

Label	Dimension [mm]
$H_t$	220
$D_t$	180
$D_i$	$D_t/3$
$S_i$	100
$H_i$	50



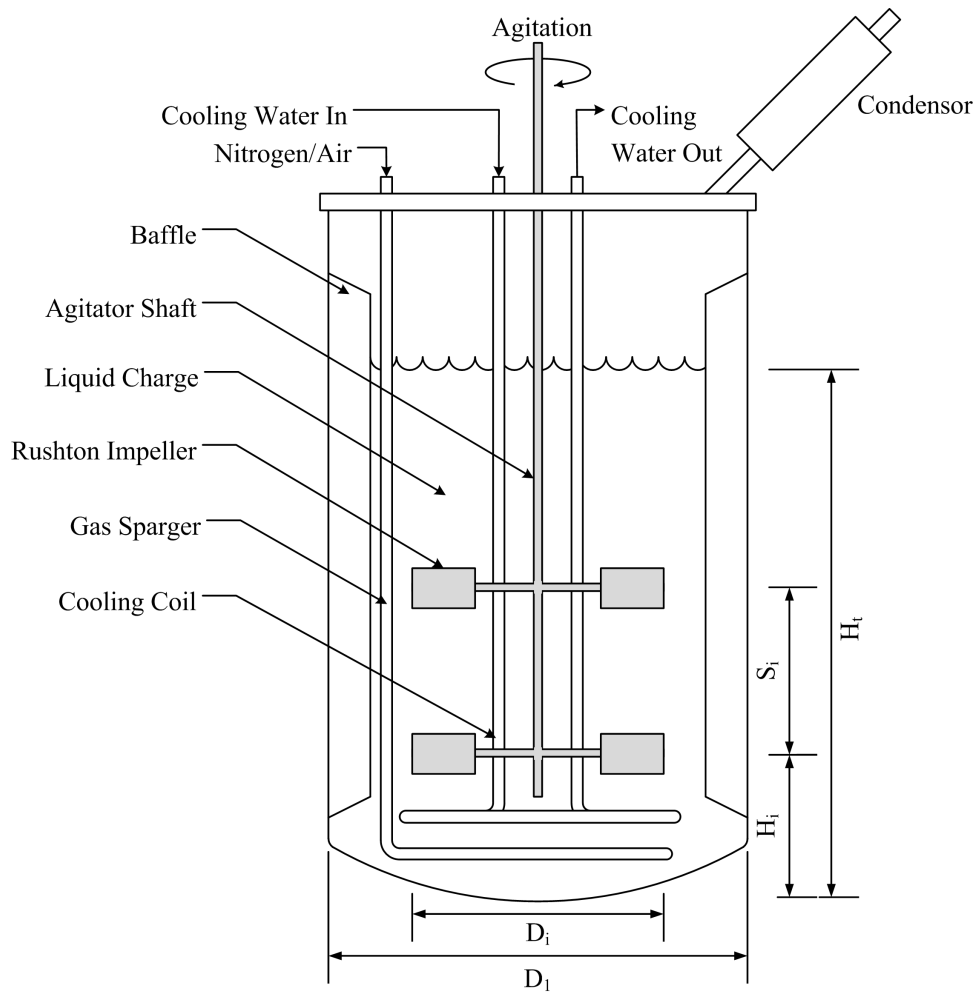


Figure 4.2: Bioreactor used for Experiments, Adapted from Correia (2007)

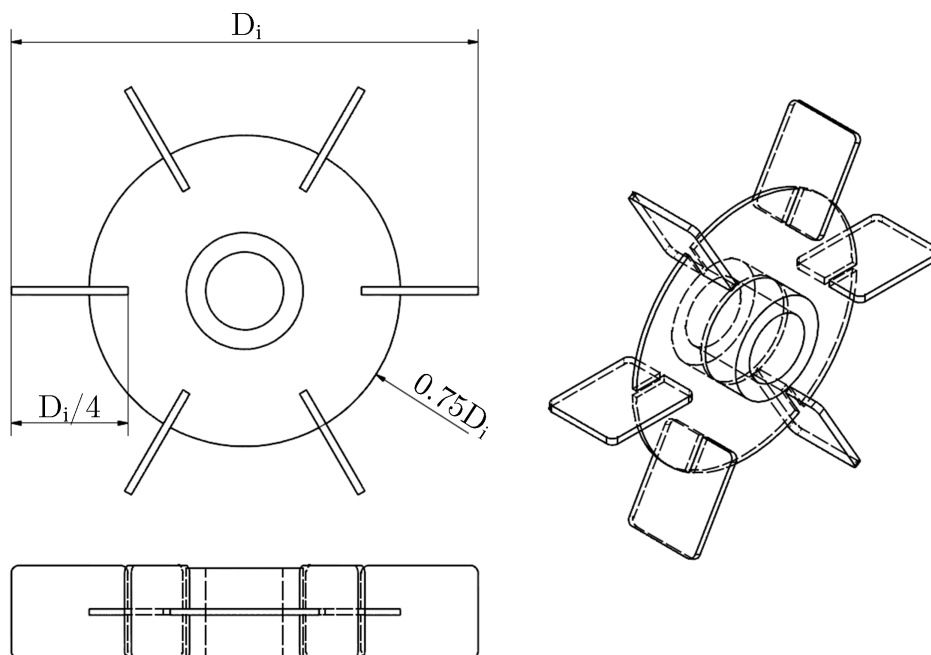


Figure 4.3: Rushton Turbine Geometry

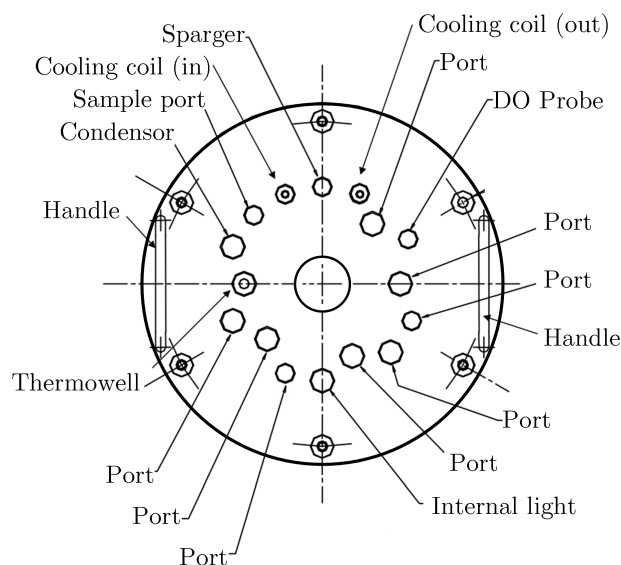


Figure 4.4: Bioreactor Headplate Geometry (Adapted from (Toledo, 2013))

The bioreactor was equipped with a sparger located directly beneath the lower Rushton turbine, and aeration was set to 0.8 vvm (4 litres per minute using the supplied geometry). The exhaust gases were routed through a condenser, designed to condense liquid escaping with the gas, and ensured the mass balance around the bioreactor was maintained. An ice-bath with a second centrifugal pump was used to recirculate chilled salt water through the condenser. This water was maintained at 2°C by periodically replenishing with crushed ice. The nitrogen (Afrox) was > 99.5 % pure. The oxygen was sparged into the system in the form of filtered compressed air.

The bioreactor system had provision for temperature control through the use of an internal cooling coil, combined with an external electric heating jacket. However, the external jacket was replaced by a water jacket to facilitate the photography, as discussed in Section 4.2.2. The temperature probe was placed in a glycerol filled thermowell suspended in the bulk liquid. This probe was used solely to monitor the internal bioreactor temperature and not to implement any form of control.

All experiments were conducted at the same ambient temperature of 22°C ± 0.2°C. The atmospheric pressure was recorded on a daily basis for calibration of the dissolved oxygen probe. Pressure data was obtained from a local weather station located in the vicinity of the laboratory (Meijers).

#### 4.2.2 Temperature Control

Oxygen solubility and diffusion are strongly dependent on the temperature of the bulk liquid phase. For this reason, an accurate temperature control and regulation system was required. However, the conventional heating jacket could not be used because of the requirement of an

external water jacket to eliminate optical distortion (Section 4.2.5). Therefore, to control the temperature in this system, a separate temperature-controlled water bath and centrifugal pump were used to circulate water in the perspex jacket (Figures 4.5 - 4.7). Water was pumped from the bath into the bioreactor jacket via the internal cooling coils (to aid heat transfer), as shown in Figure 4.5. An overflow pipe returned the water back to the temperature-controlled bath. A 5% sodium hypochlorite solution (household bleach) was added to the recirculated water to inhibit any biological growth. The recirculation pump operated continuously for the duration of the experiment, and temperature control was maintained at the setpoint  $\pm 0.2^\circ\text{C}$ .

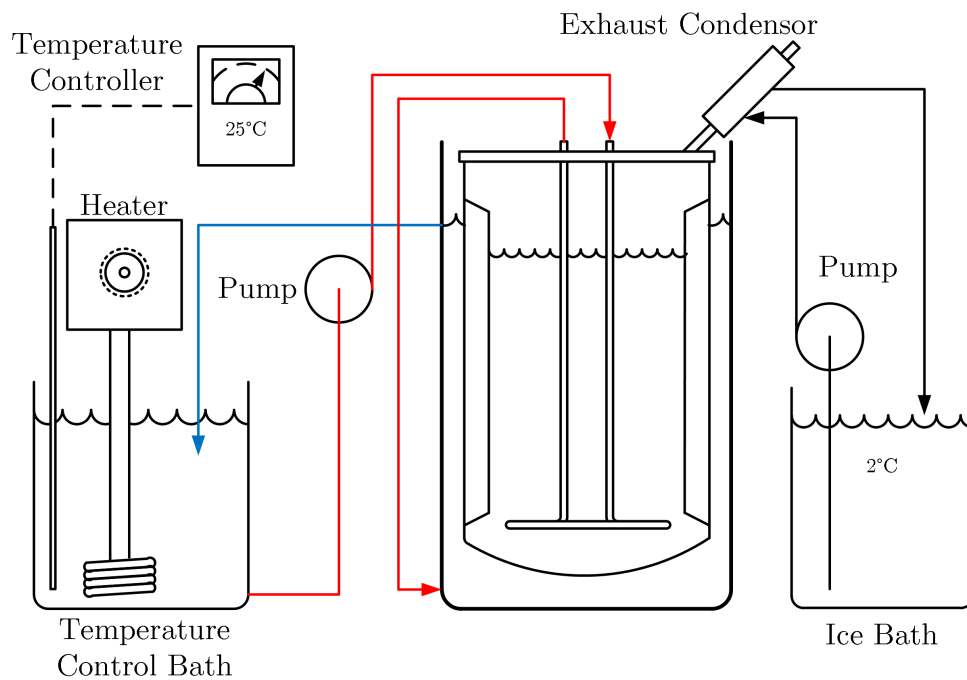


Figure 4.5: Water Recirculation Configuration for Accurate Temperature Control

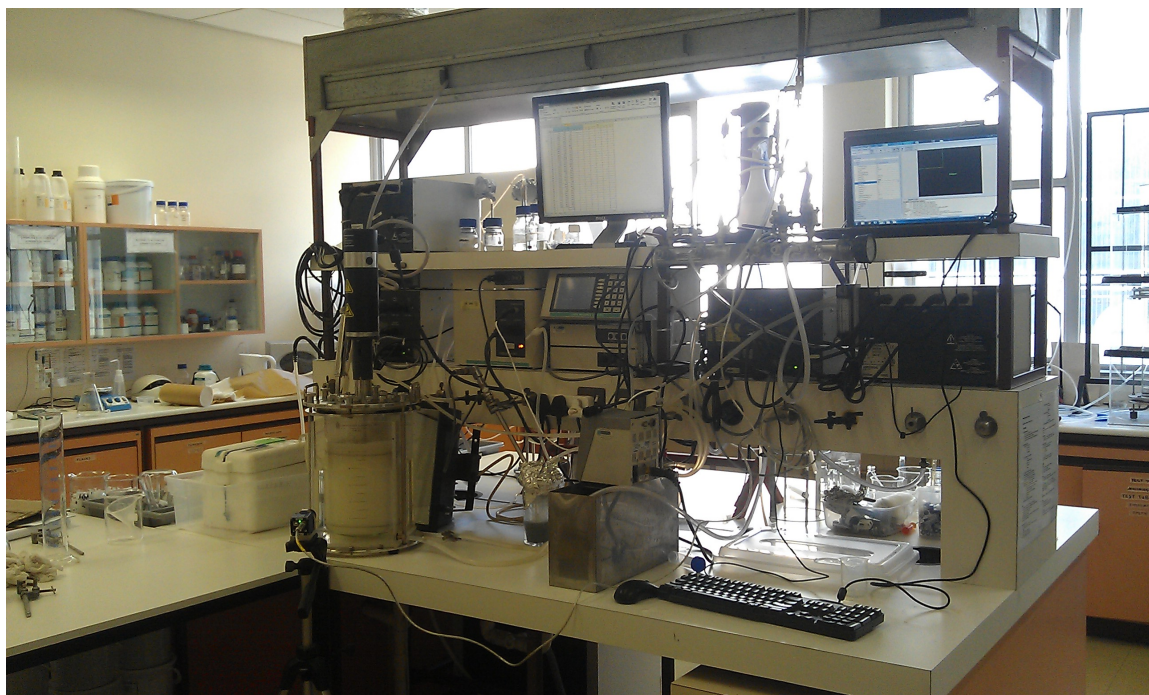


Figure 4.6: Final Experimental Set Up Depicting Camera Location and Water Recirculation



Figure 4.7: Bioreactor and Water Jacket in Operation

### 4.2.3 Dissolved Oxygen Probe

The DO measurement was completed using a polarographic probe, which recorded the real-time dissolved oxygen concentration as a percentage of the saturated oxygen concentration in the liquid. The DO probe employed was a Mettler-Toledo® InPro® 6800 Series polarographic, using 12mm Teflon membranes. The operating principle of the probe is discussed in detail in Appendix F.1, along with the probe diagram (F.2), guidelines for probe polarisation (F.3) and probe specifications (F.4). Teflon membranes were used because they are more resistant to hydrocarbon systems when compared with their silicone counterparts. The increased lag time caused by the use of this membrane type was accounted for in the measured DO. The membrane age was thought to play a role in the probe's performance, and for consistency was maintained by renewal every 2 weeks. Furthermore, the electrolyte was replaced on a daily basis, to purge the probe of silver ions. The membrane and electrolyte replacement procedure, along with the polarisation voltage, are supplied in Appendix F.

All measurements were completed using a Mettler-Toledo® M300 DO transmitter (Figures 4.8a and 4.8b), details of which, along with the calibration procedure and other specifications, are provided in Appendix G.

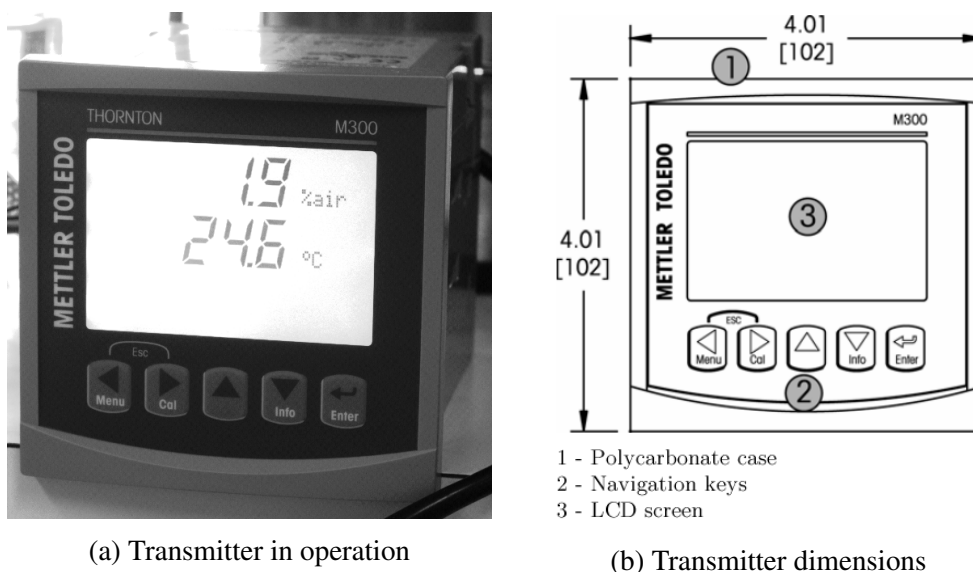


Figure 4.8: Mettler Toledo M300 transmitter used for DO measurement

(Toledo, 2013)

### 4.2.4 Camera and Lighting

One of the outcomes of this study included the development of an easily replicable image acquisition system to provide reliable results. The camera used was a Matrix-Vision mvBlue-FOX 124G, a compact industrial CCD and CMOS camera, which was used in conjunction with

various light sources. The complete specifications of the camera are given in Table E.1, Appendix E.3.

The light solution employed for all experimental runs used a 10 watt fluorescent tube, installed through a bespoke fitting in the bioreactor lid and submerged in a water-tight tube. This equipment was designed and manufactured specifically for the purpose of this study. This is shown in Figure 4.9. Further details of the light fitting are given in Appendix E.1.4, while the lighting development process is described in detail in Appendix E.1.

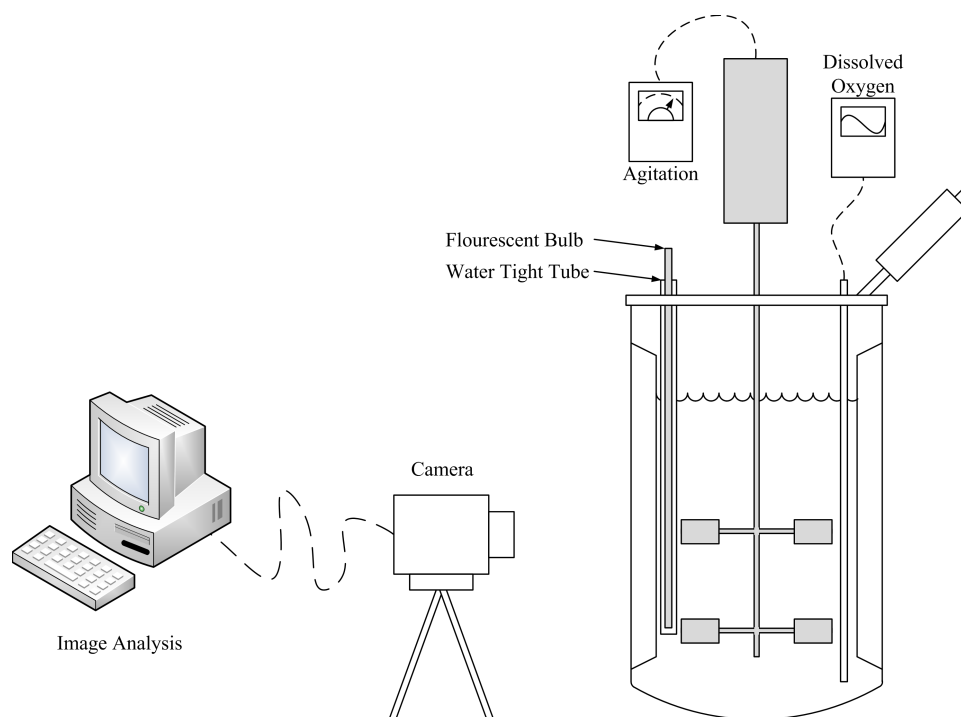


Figure 4.9: Final Set Up for Recording the Interfacial Area (Not to Scale)

The camera set up, location and focal plane was maintained for each of the experiments performed, and the same location in the bioreactor was photographed using the methodology detailed in Appendix E.2. This effectively eliminated the effect of external factors (such as ambient lighting and location dependent bubble size distributions within the bioreactor) on the results. Alignment of the camera was performed using a viewing aperture, a template of which is also supplied in Appendix E.2. The camera was then aligned such that the viewing aperture fully occupied the camera's field of vision. This maintained the location of the camera relative to the bioreactor, and ensured the same region was analysed for each experiment.

#### 4.2.5 Elimination of Optical Distortion

To prevent optical distortion of the bubbles caused by refraction of light as it passed from the light source to the camera lens via the curved glass wall of the bioreactor, the bioreactor was placed in a rectangular perspex box which was then filled with water. This meant that the plane

through which the camera was recording images was parallel to the plane of the camera lens, eliminating any source of distortion. The bioreactor and perspex box are shown in Figures 4.10.

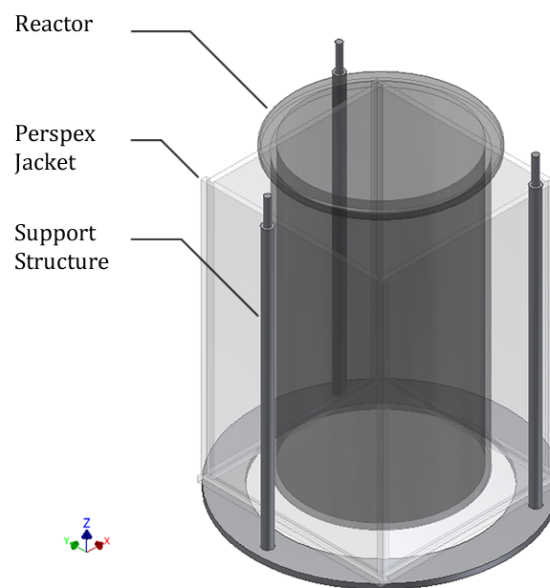


Figure 4.10: Design of the Perspex Box

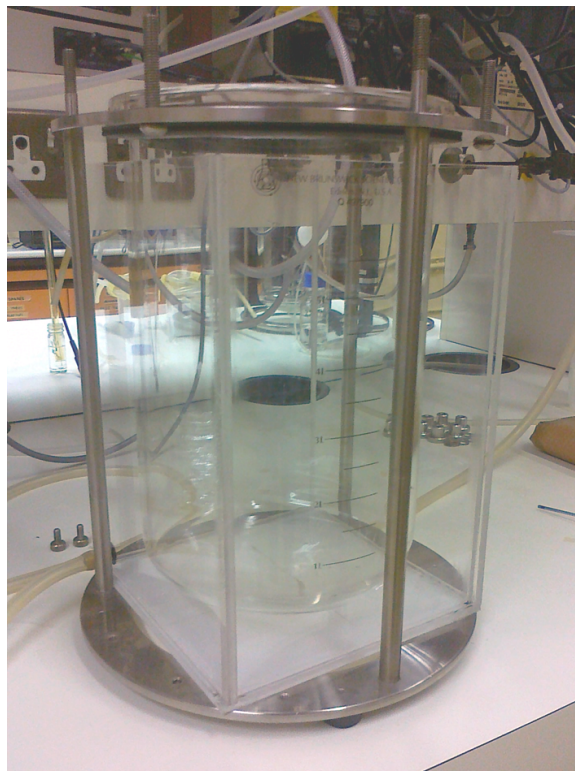


Figure 4.11: Perspex Box Designed to Remove Optical Distortion

### 4.2.6 Microscope Photography

All microscope photography in this study was completed using a Zeiss AxioStar Plus binocular microscope (Figure 4.13), capable of up to 1000 x magnification, equipped with a port to allow for the connection of a camera. The same camera used for high speed photography (myBlue-FOX 124G) was adapted for this application through the use of a 20 mm extension tube, placed in between the camera body and main lens (as shown in Figure 4.13).

The camera aperture was set to the maximum, with the brightness of the images controlled either by dimming the main light source, or adjusting the exposure time. The light of the microscope can then be dimmed until the contrast is correct. The camera was then placed in the camera port of the microscope, and connected to the computer. Focussing was achieved using the observation eyepiece, before switching to the camera port, allowing images to be recorded.

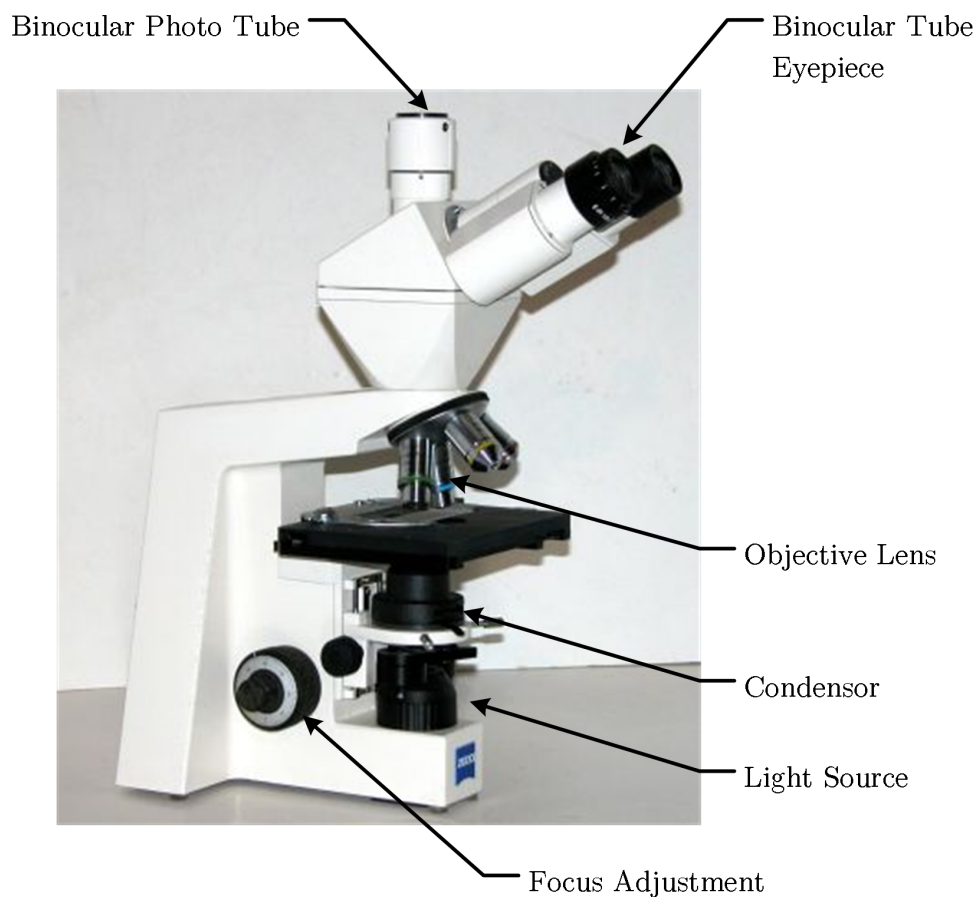


Figure 4.12: Zeiss AxioStar Plus Binocular Microscope



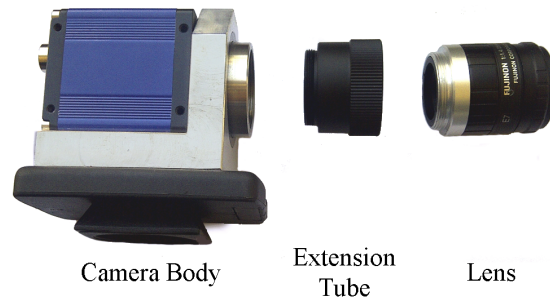


Figure 4.13: Camera Configuration for Microscope Photography

# Chapter 5

## Experimental Methodology

### 5.1 Determination of Overall Volumetric Oxygen Transfer Coefficient

The overall volumetric oxygen transfer coefficient,  $K_La$ , was determined using the GOP and a second order model incorporating probe response lag. It was necessary to determine the probe response lag for each bioreactor charge and configuration, as these parameters had an effect on the lag. The experimental determination and calculation of the response lag and  $K_La$  was detailed in the following Sections 5.1.2 and 5.1.3 respectively.

#### 5.1.1 Probe Maintenance and Transmitter Calibration

The DO membrane and electrolyte required periodic maintenance. This was completed 6 hours before any experiments took place to allow the probe to re-polarise. The membrane was replaced every 2 weeks during the experimentation period, while the electrolyte was replaced every 24 hours, following the daily experiments. It was found that the probe performance and stability decayed rapidly once the membrane was older than 14 days.

To confirm the reproducibility of the probe, the performance was evaluated over 5 runs in pure water at 25°C, 725 RPM. The results are shown in Figure 5.1. The maximum standard deviation is less than 1%, signifying minimal variation between the 5 runs. Following any maintenance performed on the probe and the associated re-polarisation period (Appendix F.3), the transmitter was calibrated using a single point procedure, details of which are provided in the operating manual (Toledo, 2013).

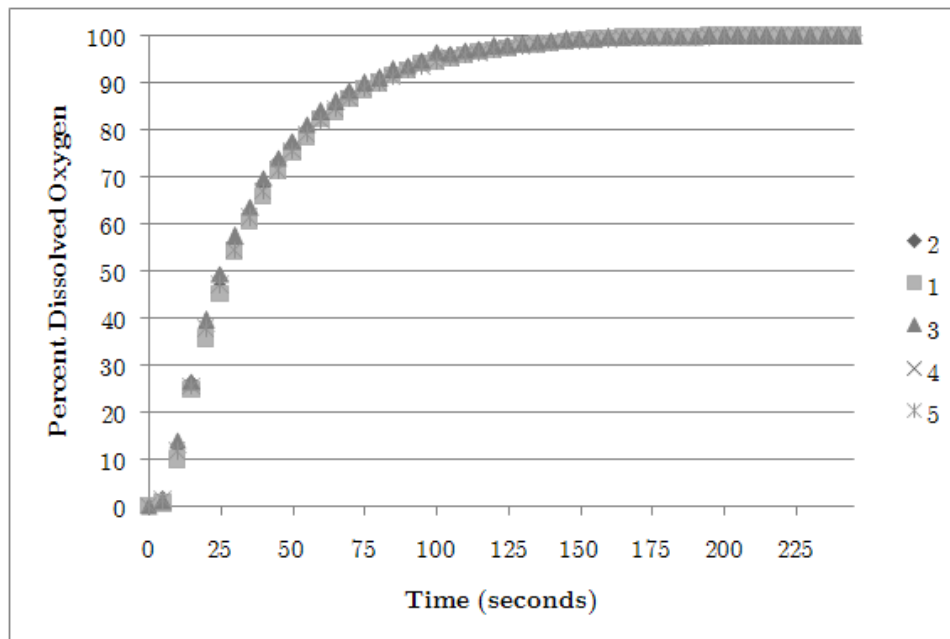


Figure 5.1: DO Probe Reproducibility in Pure Water at 25°C, 725 RPM

### 5.1.2 Determination of the Probe Response Lag

Implicit in the use of the second order model was the requirement to establish the speed of the probe response to a step change in DO concentration, which was modelled according to a first order relationship (derived in detail in Section 2.5.3.1). To ensure accuracy and repeatability, it was necessary to complete this for every experimental configuration as the operating parameters have an effect on the probe response lag.

The bioreactor was sparged with air continuously. Sufficient time (approximately 10 minutes) was allowed for the bioreactor to reach equilibrium at 100% DO concentration. At the same time, a secondary vessel was de-oxygenated using  $N_2$  supplied via a pumice stone sparger (Figure 5.2) as a jacketed nitrogen cell.

The DO probe was placed in the secondary vessel and allowed to equilibriate (until the DO readings were stable at 0%). The secondary vessel was positioned as close to the bioreactor as possible, with a clear path between it and the DO probe port. To measure the response lag, the probe was physically transferred between the secondary vessel and the bioreactor as quickly as possible (approximately 1 second), simultaneously starting the data logger. Measurements were then taken every 5 seconds until the probe indicated 100% DO in the bioreactor. This procedure was completed 5 times for each bioreactor charge, to ensure repeatability.

The response lag was calculated from the time the probe took to reach 63.2% of the final saturation value (derived in Equation 2.49), and  $K_p$  from the inverse of the probe response lag.

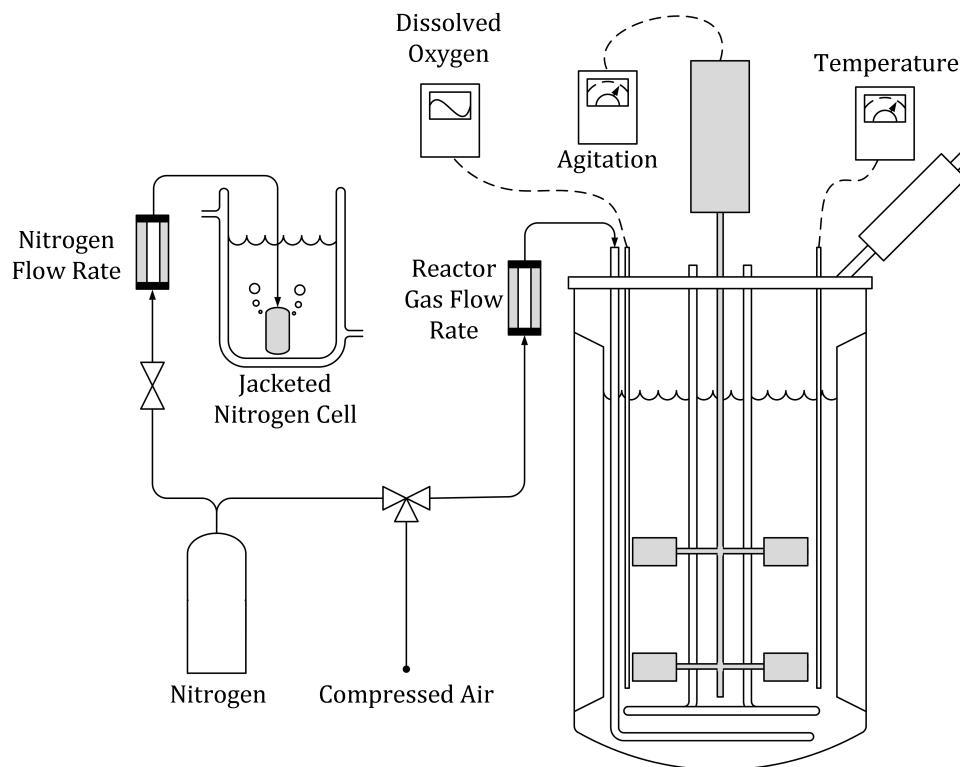


Figure 5.2: Experimental Set Up for Probe Response Lag Determination

### 5.1.3 Determination of Overall Volumetric Oxygen Transfer Coefficient

To determine the  $K_L a$ , the bioreactor was sparged with  $N_2$  and allowed to reach equilibrium at 0% DO concentration. The DO probe was placed in the bioreactor. Using a three-way-valve system and a manifold the sparge gas was switched back to air (Figure 5.3). The DO reading was recorded until steady state was reached at 100% DO concentration. During the step change, the gas flow rate was kept constant (0.8 vvm). The results of a trial experiment of this type are shown in Figure 5.4 for illustration purposes.

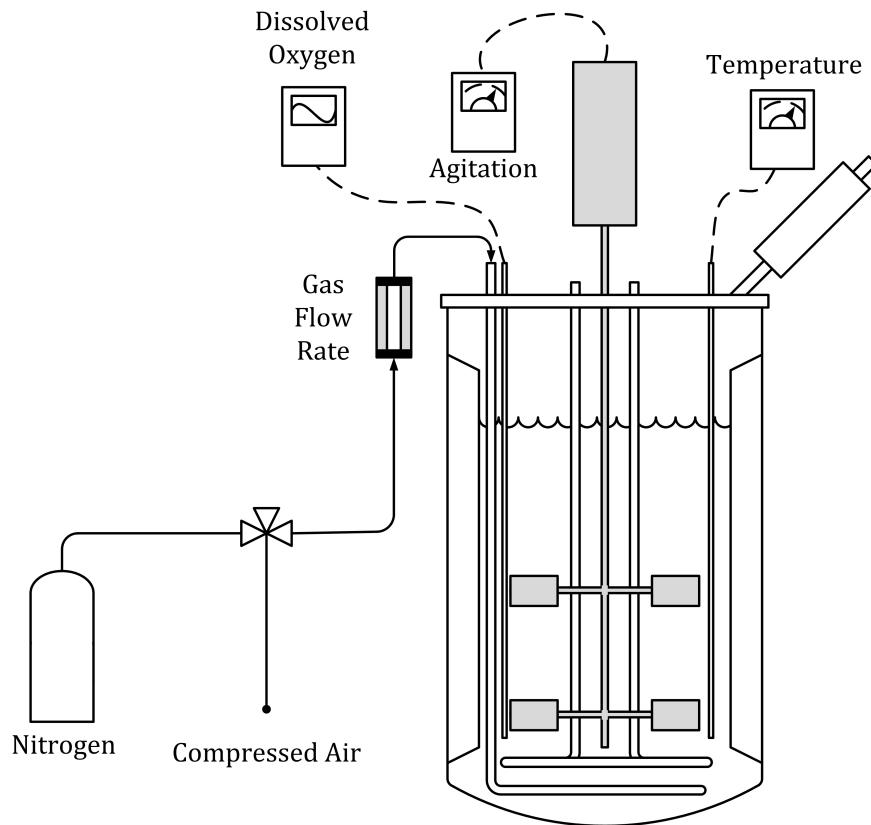


Figure 5.3: Experimental Set Up for GOP

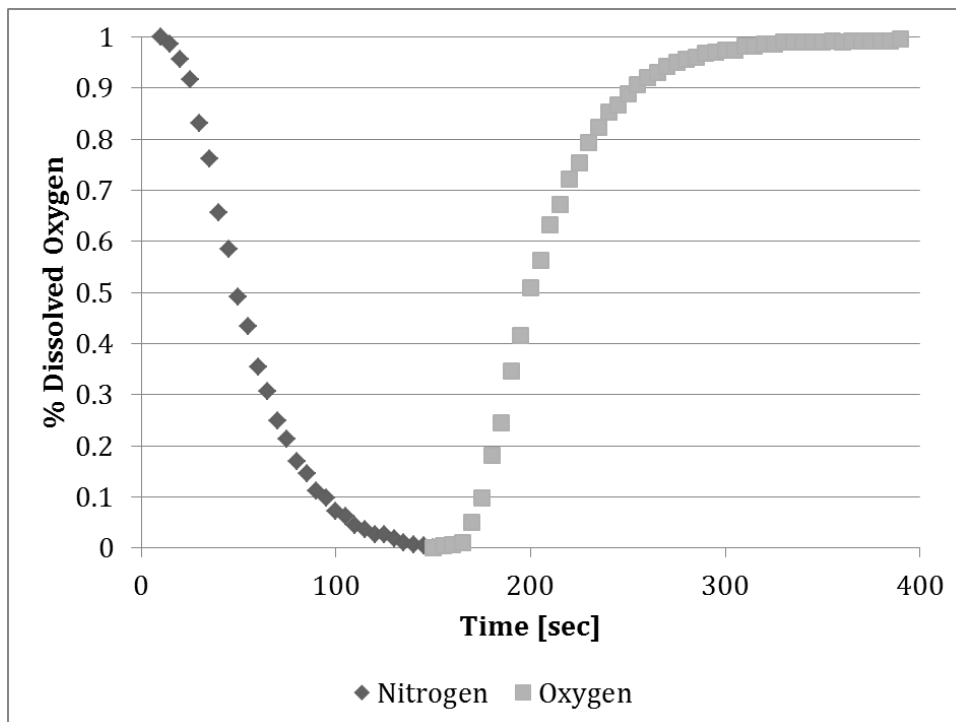


Figure 5.4: Dissolved Oxygen Concentration

Using this data and the calculated value for  $K_P$ , it was then possible to find  $K_{La}$  iteratively by minimizing the sum of the square root of the error between experimental  $C/C^*$  data and those predicted by Equation H.23 using a MATLAB routine, supplied in Appendix B.

### 5.1.4 Data Reproducibility and Benchmarking

In order to establish the reproducibility of the results generated in this study, the  $K_{La}$  values generated were benchmarked against a similar study conducted by Clarke and Manyuchi (2012). The authors presented a reliable method for the accurate quantification of  $K_{La}$  in hydrocarbon-aqueous dispersions containing yeast solids in an STR using the GOP while incorporating the probe response lag. While not all of the experimental parameters were identical to those used in this study, comparison of the nearest values will demonstrate the reproducibility during the determination of  $K_{La}$ . The authors went on to show that this method is comparable to results obtained using the PSP, thus establishing reproducibility across studies and experimental methodologies.

Figure 5.5 shows that an increase in agitation increased  $K_{La}$  regardless of the experimental parameters. Particularly close are the trends for 11.0 and 11.25 % (v/v) and 5.5 g/l yeast solids (square markers). The slightly higher solid loading used in this study (represented by the solid diamond) resulted in the  $K_{La}$  being slightly lower than that found by Clarke and Manyuchi (2012) (open diamonds).

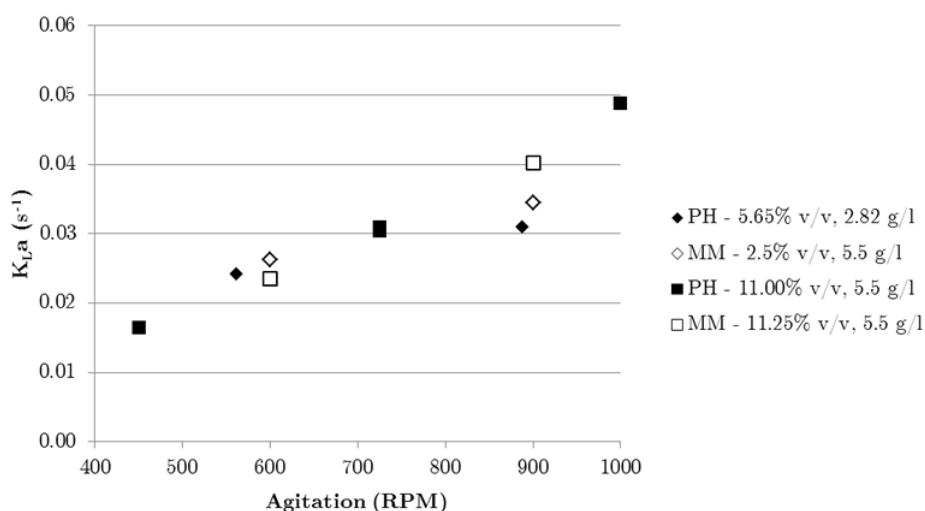


Figure 5.5: Comparison of  $K_{La}$  values obtained in this study (solid markers) with the experimental results of Clarke and Manyuchi (2012) (open markers) with variation in agitation

Figure 5.6 compares the  $K_{La}$  with an increase in alkane concentration. The values found by Clarke and Manyuchi (2012) at 900 RPM and 5.5 g/l (open squares) are slightly lower for both alkane concentrations than those found in this study (888.5 RPM and 2.82 g/l, black square)

because of the higher solid loading. Nonetheless, the values compare favourably. The lower agitation configurations show that Clarke and Manyuchi (2012) (represented by the open diamonds) found an increase in  $K_{La}$  with increasing alkane concentration, while these results are not evident in this study (black diamonds). However, in this study a peak in  $K_{La}$  with increasing alkane concentration was found to exist at 11.5 % (v/v), and there is simply a lack of experimental data points at comparable experimental configurations to represent this fully.

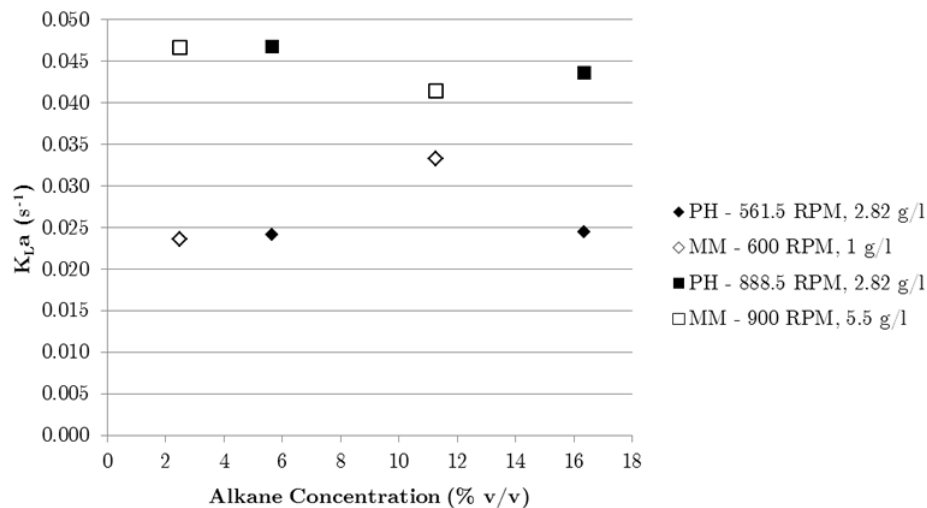


Figure 5.6: Comparison of  $K_{La}$  values obtained in this study (solid markers) with the experimental results of Clarke and Manyuchi (2012) (open markers) with variation in alkane concentration

Finally, Figure 5.6 compares the  $K_{La}$  with an increase yeast loading. Both set of results clearly show a decrease in  $K_{La}$  with an increase in yeast loading of comparable magnitudes.

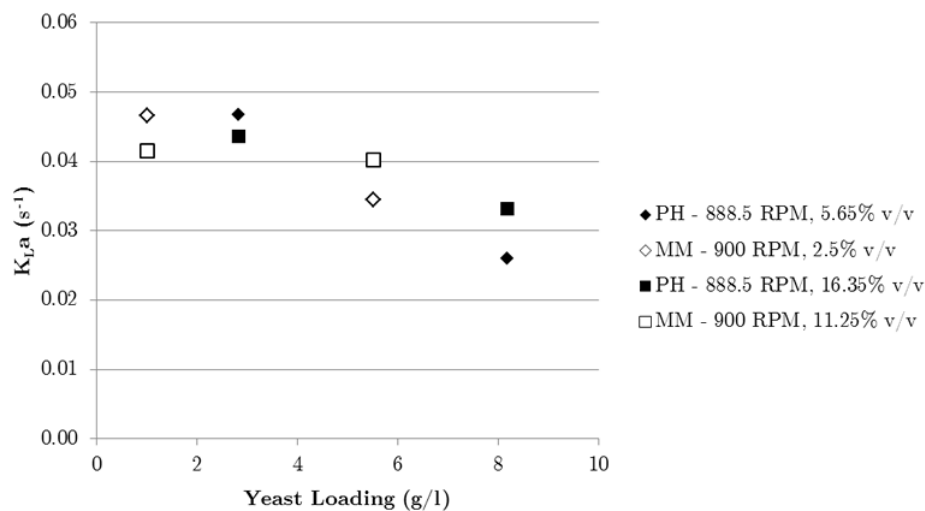


Figure 5.7: Comparison of  $K_{La}$  values obtained in this study (solid markers) with the experimental results of Clarke and Manyuchi (2012) (open markers) with variation in yeast loading

Form these comparisons, it was determined that the results of this study were repeatable and reproducible and constitute an accurate method for the quantification of  $K_La$  in simulated hydrocarbon-based bioprocesses.

## 5.2 Determination of Interfacial Area

### 5.2.1 Calculation of Interfacial Area

During the DO experiments, 12-15 images were captured once the system has reached equilibrium. Of these, the 10 clearest were chosen for image analysis. For statistical repeatability, approximately 600-800 bubbles are required in total (Mena *et al.*, 2005). Each image contained a minimum of 200 bubbles, making the total number of bubbles a minimum of 2000 per experimental configuration, allowing for statistically significant calculation of  $a$ . Each bubble yielded a projected area ( $A_P$ ) from which the Feret diameter ( $D_F$ ) was calculated according to Equation 5.1, where  $D_F$  is the diameter of a circle with an area equal to  $A_P$ .

$$D_F = 2 \cdot \sqrt{\frac{A_P}{\pi}} \quad (5.1)$$

Using  $D_F$ , the Sauter mean diameter,  $D_{SM}$  was calculated. This is defined in Equation 5.2, and simplified to Equation 5.3:

$$D_{SM} = \frac{\int_0^{\infty} x^3 f(x) dx}{\int_0^{\infty} x^2 f(x) dx} \quad (5.2)$$

$$D_{SM} = \frac{\sum_{i=1}^N n_i \cdot D_{F,i}^3}{\sum_{i=1}^N n_i \cdot D_{F,i}^2} \quad (5.3)$$

The gas hold up ( $\varepsilon_G$ ) of the system was the fraction of gas in the liquid at any point. It was assumed to be steady, as the superficial gas velocity was constant.  $\varepsilon_G$  was measured by recording the difference in the liquid volume in the bioreactor when the gas was off, and when the gas is present (on) as illustrated in Figure 5.8 (Schugerl, 1981; Dhanasekaran and Karunanithi, 2012). The difference between the two is the volume occupied by the gas. It is defined in Equation 5.4, and calculated in practice using Equation 5.5. Due to the turbulent conditions inside of the reactor, the fluid surface was unsteady. To perform an accurate measurement, a ruler was attached vertically to the side of the perspex water jacket (smallest distance to the submerged reactor). An additional ruler was held perpendicularly and moved up and down to establish an average height of the turbulent fluid surface. This was repeated 3 times during the experiment to ensure accuracy.



$$\varepsilon_G = \frac{\text{volume gas}}{\text{volume liquid} + \text{volume gas}} \quad (5.4)$$

$$\varepsilon_G = \frac{V - V_C}{V} \quad (5.5)$$

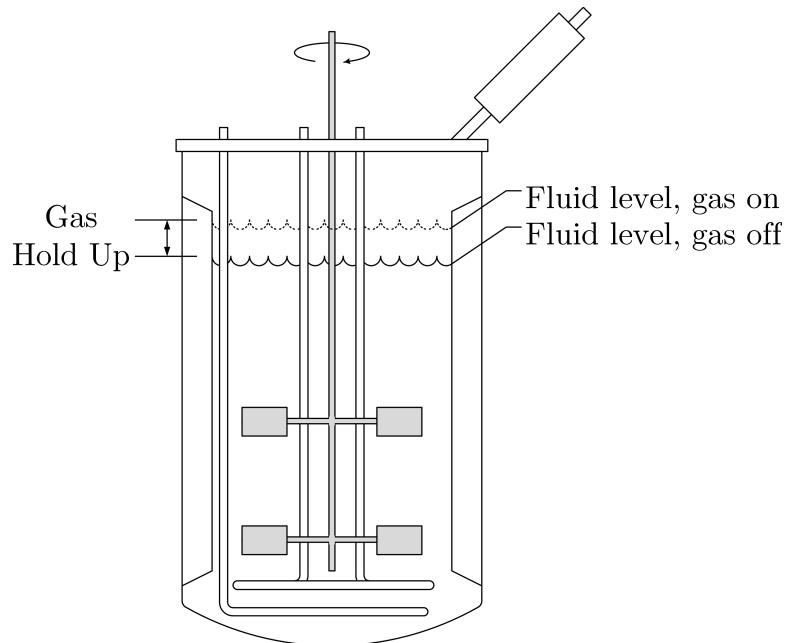


Figure 5.8: Measurement of the Gas Hold Up

Interfacial area was then calculated using  $D_{SM}$  and gas hold-up (Equation 5.8).

$$a = \frac{\text{area gas}}{\text{volume liquid} + \text{volume gas}} \quad (5.6)$$

$$= \frac{3}{r} \times \varepsilon_G \quad (5.7)$$

$$a = 6 \cdot \frac{\varepsilon_G}{D_{32}} \quad (5.8)$$

### 5.2.2 Determination of Bubble Diameter

The images were processed using a MATLAB® routine, the basic structure of which was originally developed by Correia (2007) (Appendix C). This enhances the images, and determines contrast gradients to find the  $D_{SM}$ , and also allows for the calculation of the size distribution of the bubbles, as well as the interfacial area (when combined with the gas holdup).

Before accurate image analysis could take place, the scale of the images needed to be determined. This was done by comparing a real world dimension with the number of pixels it occupies in the photograph. For this study, the size of the field of vision was known because of the template used to align the camera (supplied in Appendix E.2). The known real world dimension from the template was then divided through the corresponding value in pixels to yield the ratio of pixels per millimetre. This is then valid for any object in the field of vision, on the focal plane. This method was employed as it gives an accurate measurement very close to the bubbles, and was highly reproducible and calibration was easy to perform.

In the MATLAB® routine developed by Correia (2007) the execution of the image analysis code proved tedious, and as a result the original code was integrated into an automated data processing structure, capable of iteratively loading and analysing images, and saving the analysis output. This greatly increased the rate at which images could be processed, jumping from one image per routine execution to an average of 10 images. The complete routine code is provided in Appendix C.

The image analysis process used by the programme is outlined below:

1. The images were captured by the MATRIX VISION® software, and saved as .jpg;
2. The MATLAB® code was initialised, and the experiment number was entered. This was for filing purposes, as the images were saved in folders based on the experimental conditions, and the final data was saved in the same folder, with each run being recorded on a sheet in the EXCEL® file;
3. The MATLAB® code was executed, and the appropriate image read in using `imread` (Figure 5.9);

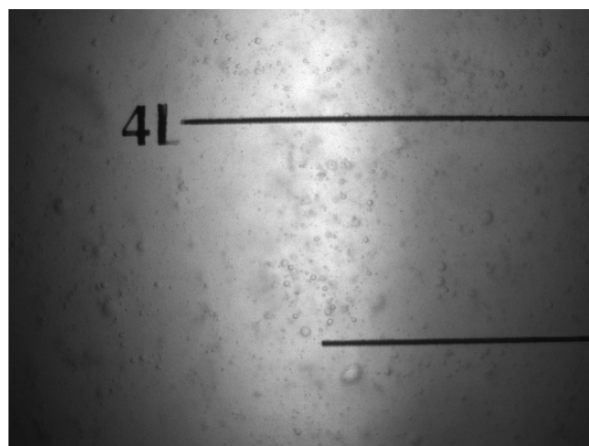


Figure 5.9: The Original Image Before Cropping

4. The image was displayed on screen, allowing the user to select the appropriate region in the image for analysis. The cropping coordinates were saved, allowing the image to be cropped using `imcrop` (Figure 5.10);

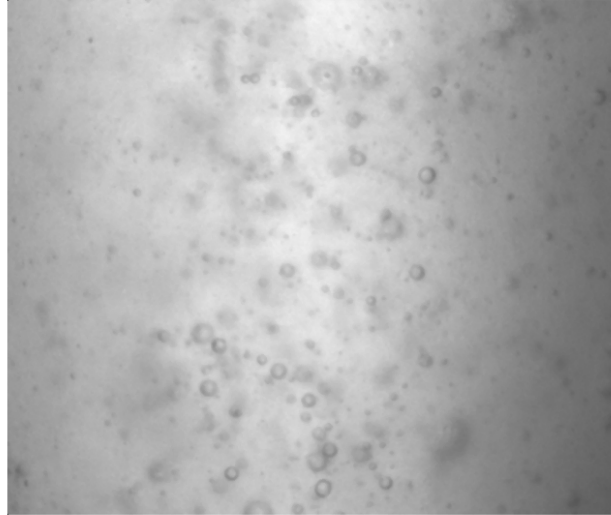


Figure 5.10: Image After Cropping

5. The image was then manipulated to improve the image for further processing. The first step was to apply a median filter (`medfilt2`) to the image. The median filter was far less susceptible to noise than a mean filter, and set each pixel to the median of the surrounding pixels which removed excessive noise in the image;
6. The contrast of the image was then increased using `adapthisteq`, which divided the image into regions, and adjusted the contrast to match that of a predefined histogram (Figure 5.11);

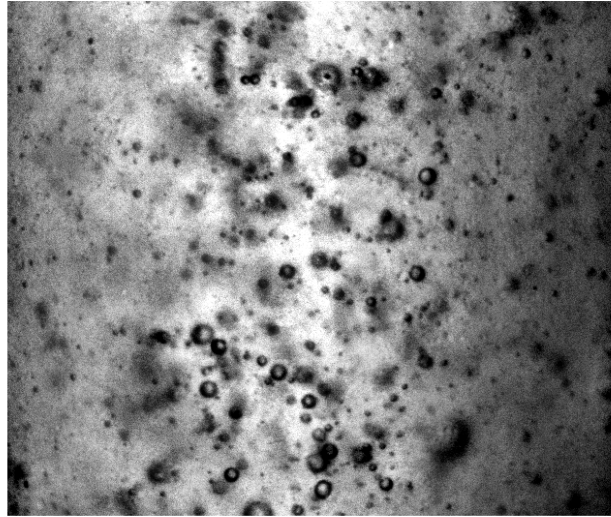


Figure 5.11: Increased Contrast

7. After manipulation, the image was passed to the edge function, which determined regions of a sudden increase in contrast. This was then defined as the bubble boundary (Figure 5.12);

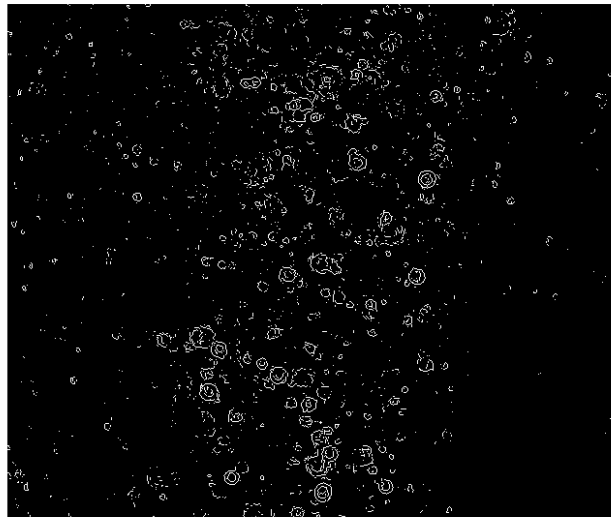


Figure 5.12: Bubble Boundaries

8. Any gaps that were present in the bubble outlines were then joined to the rest of the bubble outline by dilating, using the function `imdilate`. The bubble outlines were then filled using `imfill` (Figure 5.13);

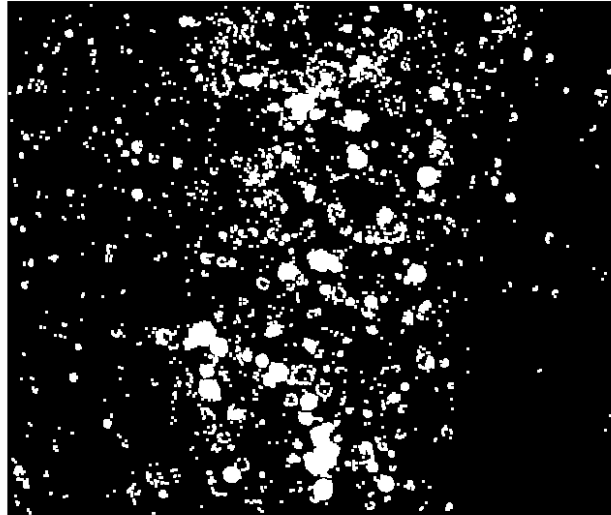


Figure 5.13: Bubbles Dilated and Filled

9. As a final filter, any outlined and filled artefact identified by the programme to be less than 10 pixels across were removed using `bwareaopen` (Figure 5.14);

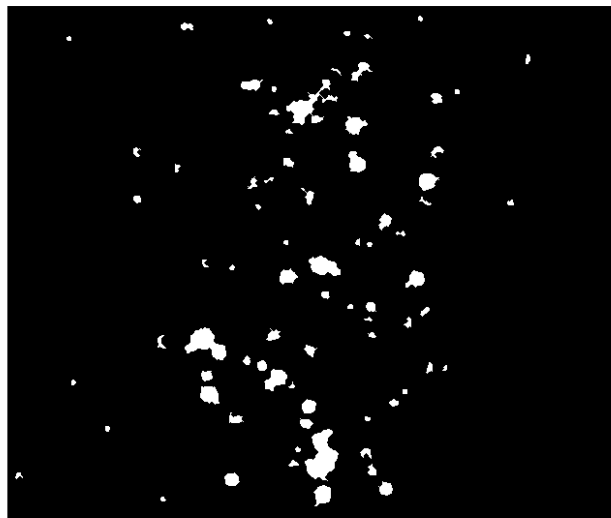


Figure 5.14: Small Objects Removed

10. The bubbles as identified by the programme were then traced on the original image using `beboundaries`, showing the results of the image recognition (Figure 5.15);

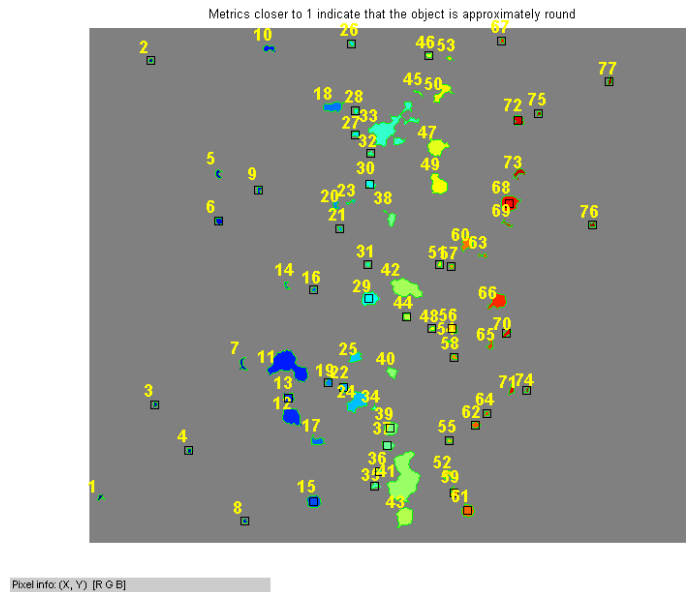


Figure 5.15: Image Recognition Results

11. The bubbles were then scaled using a real world measurement. Function `regionprops` then extracts the required data from the image for each bubble, namely the cross sectional area, major and minor axis length, perimeter, and eccentricity;
12. This information was then written to an EXCEL spreadsheet using `xlswrite`, and the next image loaded to continue analysis.

### 5.3 Yeast Deactivation

Non-viable yeasts were used as solids in the experiment. Two methods to produce non-viable yeasts were trialled, namely deactivation by ethanol and deactivation by thermal shock. The first deactivation methodology trialled was the use of ethanol as an antizymotic agent to deactivate the yeast. However, the effect of the ethanol on the cell membrane was thought to contribute to the increased break-up with consequent reduction in particle size, and the foaming observed during experiments, so this method was abandoned in favour of a thermal shock technique.

Thermal shock was the second method employed to deactivate the yeast. It was chosen because of the maintenance of cell integrity, the ease of implementation on a large scale, and it has no requirement for toxic chemicals. To perform the deactivation, a measured amount of yeast was added to a physiological saline (0.9% sodium chloride) solution in a 50ml Eppendorf centrifuge tube to effect dissolution of the pellets (2.5 g yeast pellets in 40 ml saline). The mixture was then vortexed to ensure a homogeneous suspension. The Eppendorf was then placed in a 75°C water bath for 20 minutes before being transferred to crushed ice to rapidly cool the contents. It was then centrifuged for 5 minutes at 10 000 RPM to form a yeast pellet. The saline was then removed from the Eppendorf using a Pasteur pipette, leaving only the yeast pellet in the

Eppendorf. The saline was then replaced with 40 ml of distilled water. The Eppendorf was vortexed to return the yeast back into suspension, which was then ready for addition to the bioreactor as required.

Samples of yeast suspension were taken before and after deactivation. The purpose of this was two-fold. Firstly, by plating the yeast on potato dextrose agar and incubating for 48 hours at 30°C, growth of the active yeast could be compared with that of the deactivated yeast. Secondly, the samples were analysed under a microscope, to check for signs of disintegration.

As can be seen in Figure 5.16, no growth was detected using the thermal shock technique for the deactivated yeast after 48 hours. These plates were allowed to incubate for a further week, and again no growth was detected. This satisfied the requirement that the yeast be fully deactivated. Figure 5.17 shows the cells at 400 x magnification using a Zeiss AxioStar Plus binocular microscope, and it can be seen that no significant lysis or disintegration took place following a set of experiments in the bioreactor. Consequently, the thermal shock methodology was used to provide non-viable yeasts for the experiments.



Figure 5.16: Yeast Cells Before (Left) and After (Right) Deactivation

## 5.4 Experimental Design

The experiments necessary to gather data were completed using a central composite design (CCD). Fundamentally, this means that a conventional full factorial experiment was augmented by a star design through the addition of central and axial points. These differences, illustrated by a  $2^2$  full factorial and CCD design with  $\alpha = \sqrt[4]{8}$ , are shown in Figure 5.18. The CCD is a highly rotatable design, which means that the variance of any value predicted by the model for the dependent variable is only dependent on the distance of the point from the design's

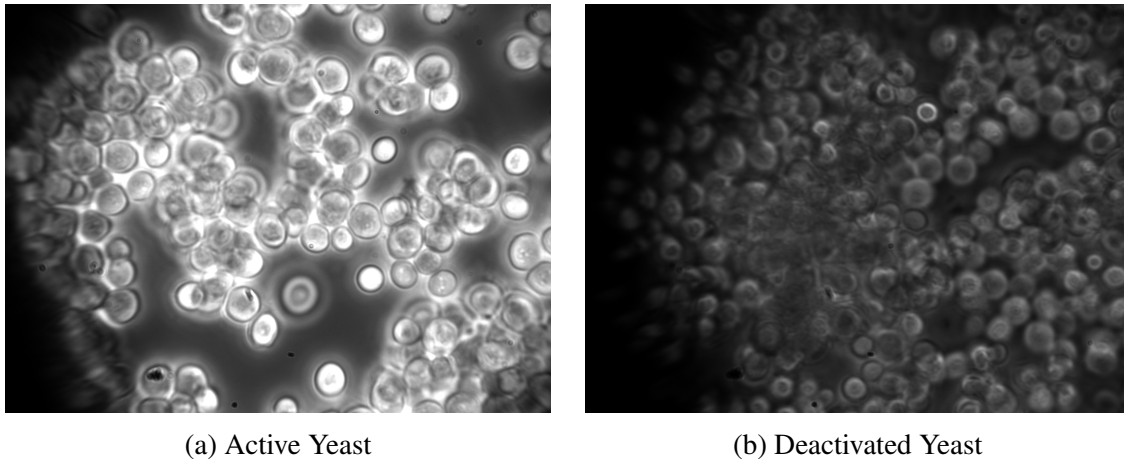


Figure 5.17: Comparison of active and deactivated yeast cells at 400 x magnification

central point, irrespective of the direction. This means that the variance of an estimated point is constant, and equal to all other data points the same distance from the central point. In turn, this assures equal precision of estimations in all directions. The rotatability of the design ( $\alpha$ ) is determined using Equation 5.9.

$$\alpha = \sqrt[4]{2^k} \quad (5.9)$$

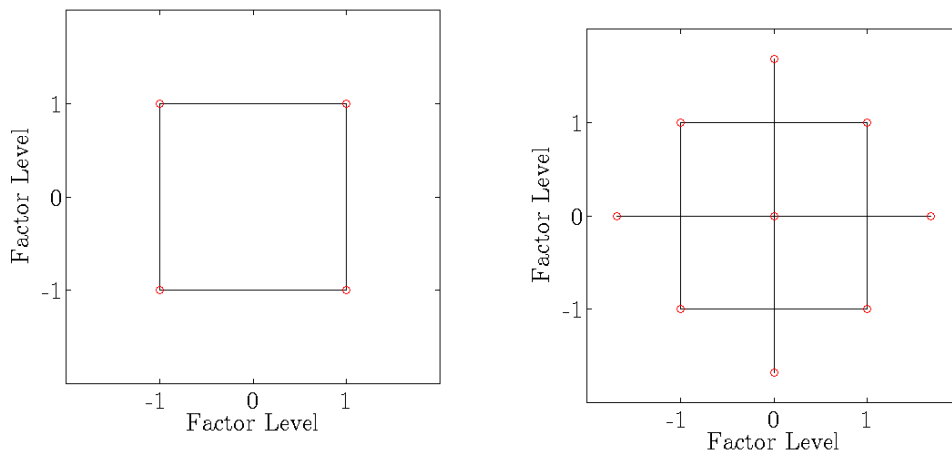
When  $\alpha > 1$ , each factor was assessed at 5 levels ( $-\alpha$ ,  $-1$ ,  $0$ ,  $1$  and  $\alpha$ ). In this case,  $\alpha = 1.68179$ . These values were used to determine factor levels for each independent variable. Empirical data was then used to fit a response surface model, that described the dependent variable as a continuous surface within the experimental boundaries.

The advantages of this method include the ability to extract the maximum amount of data from the minimum number of experiments, reducing the cost and time involved during the experimental phase of this study. It also allowed for the examination of the interaction of the independent variables (agitation, alkane concentration and solid loading) on the dependent variables ( $K_La$ ,  $K_P$  and  $a$ ), as well as their combined effects.

#### 5.4.1 Impact of Agitation, Alkane Concentration and Solid Loading on $K_La$ , $K_P$ and $a$

In this study, the impact of agitation, alkane concentration and solid loading on  $K_La$ ,  $K_P$  and  $a$  were examined. This was completed using a CCD approach with the factor levels are shown in Table 5.1. The design can be seen in Figure 5.19. The factor levels were chosen by considering typical ranges in a hydrocarbon bioprocess, and align with literature values. A sample of the order of experiments is given in Table 5.2.





(a) Two factor, two level ( $2^2$ ) full factorial design

(b) Central Composite Design ( $\alpha = 2^{1/4}$ )

Figure 5.18: Comparison of active and deactivated yeast cells at 400 x magnification

Table 5.1: Factor Levels for Dependent Variables, Experiment Set 1

Variables	Units	ExLow	Low	Mid	High	ExHigh
Factor Level		-1.68	-1.00	0.00	1.00	1.68
Agitation	RPM	450	561.48	725	888.52	1000
Alkane Concentration	(%v/v)	2	5.65	11	16.35	20
Yeast Loading	g/l	1	2.82	5.5	8.18	10

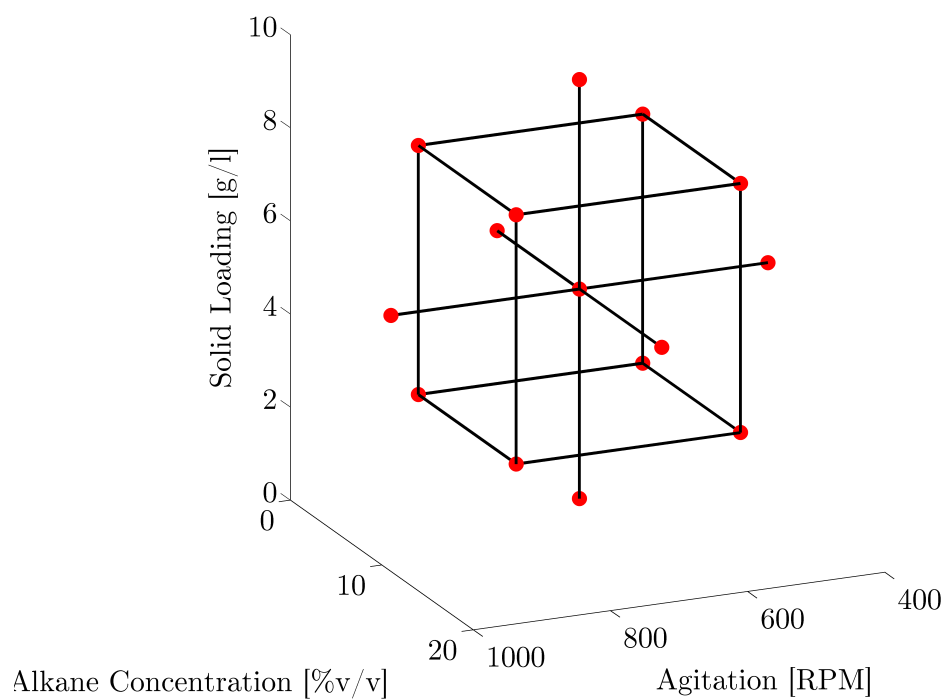


Figure 5.19: CCD Factor Levels, Experiment Set 1

Table 5.2: Running order and factor levels, experiment set 1

Run	Agitation	Alkane Conc.	Solid Loading
1	-1.00	-1.00	-1.00
2	-1.00	-1.00	1.00
3	-1.00	1.00	-1.00
4	-1.00	1.00	1.00
5	1.00	-1.00	-1.00
6	1.00	-1.00	1.00
7	1.00	1.00	-1.00
8	1.00	1.00	1.00
9	-1.68	0.00	0.00
10	1.68	0.00	0.00
11	0.00	-1.68	0.00
12	0.00	1.68	0.00
13	0.00	0.00	-1.68
14	0.00	0.00	1.68
15	0.00	0.00	0.00
16	0.00	0.00	0.00

### 5.4.2 Analysis of Variance

For the CCD experiments, data analysis was completed using ANalysis Of VAriance (ANOVA), fundamentally aimed at testing for significant deviation from a mean value. In this case, significance refers to the probability that an observed value occurred by chance (or experimental inaccuracies) or was driven by a change in experimental conditions. This means that it becomes possible to quantify the extent to which a relationship between dependent and independent variables is true and the strength of the relationship.

A relationship between an dependent and independent variable can be described by both the magnitude and the reliability. Magnitude describes the strength of the relationship between two variables. The larger the magnitude, the stronger the relationship. Reliability provides an indication of how representative a result is within the sample population. In other words, it quantifies the likelihood of a similar relationship occurring if the experiment was repeated with other samples drawn from the same population. This becomes important when extrapolating data beyond what was measured in the sample population, and gives an indication of the trustworthiness of a predicted value.

One method for the quantification of the statistical significance is the p-value, a descriptor of the reliability of an experimental result. High p-values indicate that the predicted relationship between two variables is less trustworthy, and is a representation of the probability of an error in the relationship. A p-value of 0.05 equates to a 5% probability that a relationship is based on non-representative experimental data, and corresponds to a 95% confidence interval. The

ANOVA analyses completed in this study were all based on a 95% confidence interval.

Intrinsic to ANOVA are three assumptions, namely that the dependent variables should be normally distributed, and measured on an interval scale, the use of multiple dependent variables requires that any correlations are homogeneous across the entire design, and finally that residuals for a dependent variable are homogeneous. This is known as homoscedasticity, the residuals associated with any model predictions are equally likely to be either larger or smaller than the actual observation. In addition, the residuals should be independent of the magnitude of the observation and factor levels and of the time at which an observation was taken.

If these assumptions are valid, then ANOVA provides a robust analysis tool, and the results can be used to identify not only the major contributor to an effect on an dependent variable, but also interaction between the effects of the independent variables. The results of each section are discussed with these assumptions in mind, and the validity of each assumption is assessed for each result.

# Chapter 6

## Results and Discussion

The results of the experimental chapter of this study are presented to assess and validate the hypotheses, and offer commentary, explanations and recommendations for future experimental work. The interlinked and codependent nature of the dependent and independent variables make it difficult to assess the impact of a single parameter on  $K_P$ ,  $K_La$  or interfacial area. Consequently, the results and discussions are grouped into sections, each quantifying the impact of two independent variables on a single dependent variable. Combined, these sections form a complete explanation and understanding of trends in oxygen transfer behaviour in a model hydrocarbon-based bioprocess in stirred tank reactors.

### 6.1 Influence of System Parameters on $K_P$

Intrinsic to accurate measurement of DO using a polarographic DO probe is consideration of a response lag. This relates to the time taken for an instantaneous step change in DO concentration to impact on the reading of the probe. The results shown by Correia and Clarke (2009), when benchmarking the second order GOP in comparison with the PSP, indicate that the second order GOP is accurate under the conditions used in this study. It would therefore be prudent not to ignore the probe response lag when calculating  $K_La$ .

As described in Section 2.5.3.2, the lag is equal to the time the probe takes to reach 63.2% of the final saturation value (derived in Equation 2.49), and  $K_P$  is the inverse of the time lag. By way of example, the  $K_P$  determination for the first experimental configuration is shown in Figure 6.1. The good agreement between the DO response ( $C_p/C^*$ ) for the two centre point experimental runs (Figure 6.2) underlines the repeatability of this method.

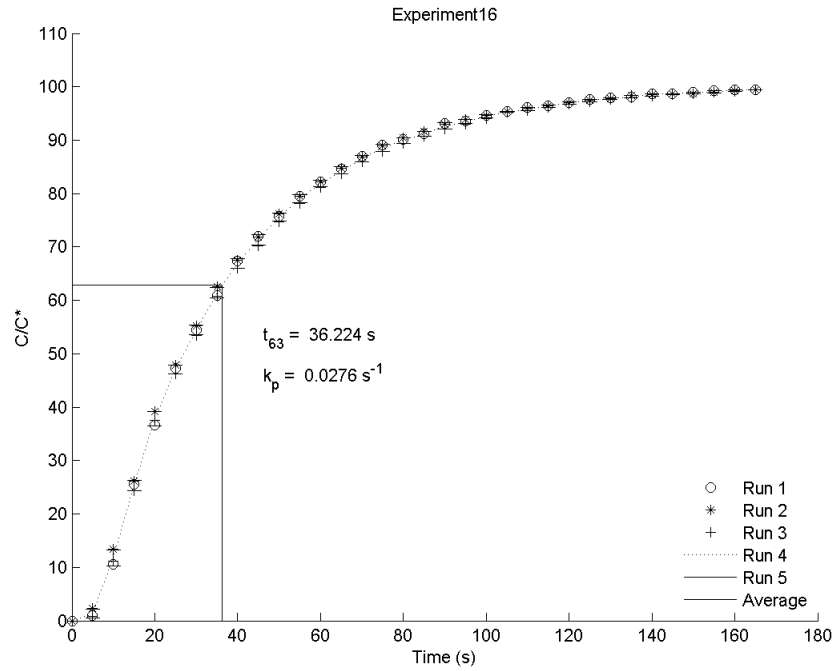


Figure 6.1: Determination of the probe response lag and  $K_p$  for the first centre point experimental configuration (all parameters mid (0) level)

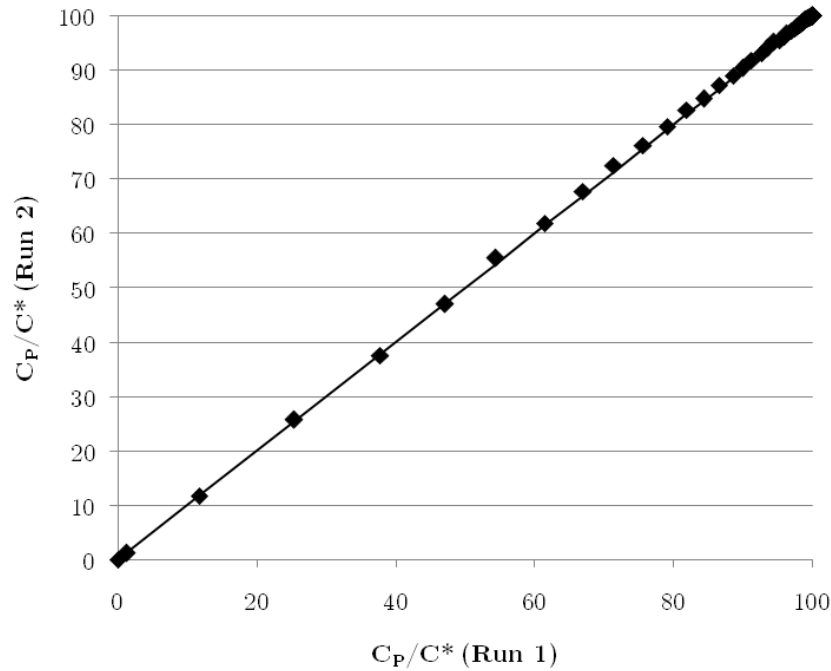


Figure 6.2: Reproducibility of DO response ( $C_p/C^*$ ) for the two centre point runs (all parameters mid (0) level)

To understand the impact of incorporating the probe response lag, both first and second order

models were fitted to the same experimental data set (Figure 6.3). The first order model predicts the response of the DO without incorporating the probe response lag (Equation 2.42), while the second order model incorporates the probe response lag (Equation H.23). It is apparent that under these conditions, the first order model under-predicts the  $K_{La}$ . This conclusion is supported by a comparison of the remainder of the  $K_{La}$  values calculated using the first and second order models (Figure 6.4), which underlines the importance of using a second order probe response mode. The first order model under-predicts the  $K_{La}$  across the board, and the difference between the two models increases with increasing  $K_{La}$  value, with a difference of up to 50% at the highest  $K_{La}$  values. Similar results were reported by Clarke and Manyuchi (2012), who experienced differences of up to 45% depending on the alkane concentration in a system containing 0 to 20%v/v  $n$ -C<sub>14-20</sub> alkane - aqueous dispersions at agitation rates between 600 and 1200 RPM.

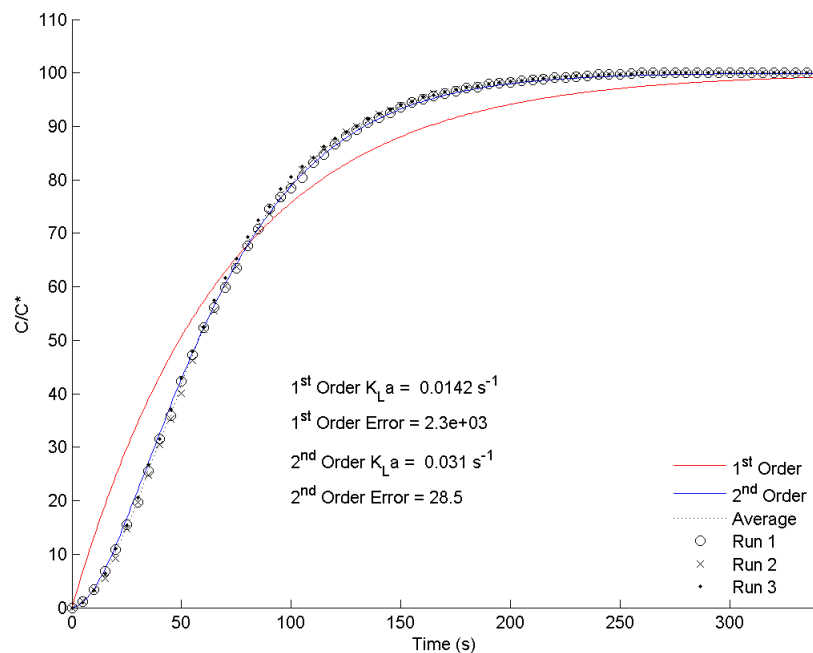


Figure 6.3: Model comparisons for the prediction of DO from the first experimental configuration (agitation = 561 RPM, alkane concentration = 5.35%v/v, yeast loading = 2.82 g/l)

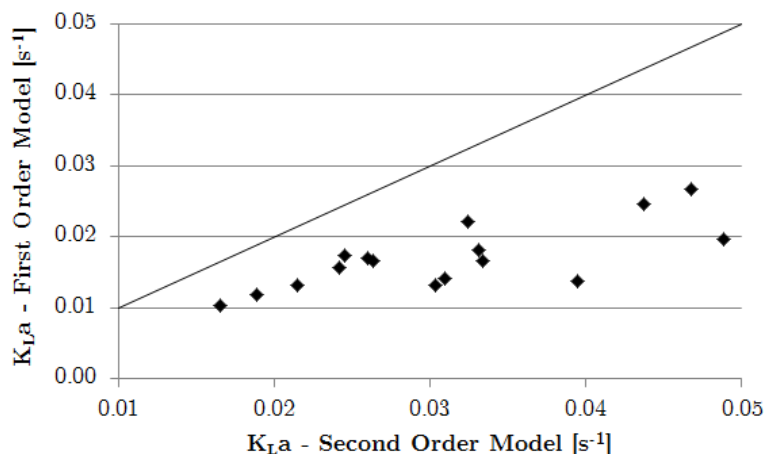


Figure 6.4: Comparison of the  $K_{La}$  results derived using the first ( $K_p$  excluded) and second order ( $K_p$  included) models with 0% to 20% (v/v)  $n\text{-C}_{14-20}$  between 450 and 1000 RPM

Use of the second order probe response model was based on the demonstrated need to include the DO probe dynamics in the determination of  $K_{La}$ , and the DO probe response for each experimental configuration was determined for this purpose. Consequently, it is possible to apply a statistical model to these results, and quantify the effect of system parameter on the probe response lag. This could be employed to predict the magnitude of the probe response lag in a proposed experiment, negating the need to experimentally determine the DO probe response lag for additional experimental configurations.

Using a linear model with two-way interaction and a 95% confidence interval, the relative effects of the parameters on  $K_p$  are shown in Figure 6.5. As indicated by a p-test value of 0.034, the yeast loading was the most statistically significant parameter, with a negative effect on  $K_p$ , followed by the alkane concentration. The mean square residual on this model was 0.201355, as shown in the ANalysis Of VAriance (ANOVA), Table 6.1.

Table 6.1: ANOVA for  $K_p$  using a linear model with two way interaction

	Sum of Squares	Mean Square	F-test	p-test
(1) Agitation	0.003	0.003	0.017	0.899
(2) Alkane Concentration	0.143	0.143	0.710	0.421
(3) Yeast Loading	1.245	1.245	6.181	-0.034
(1) by (2)	0.011	0.011	0.057	0.817
(1) by (3)	0.062	0.062	0.309	0.592
(3) by (2)	0.000	0.000	0.000	0.998
Error	1.812	0.201		
Total SS	3.277			

A normal plot of the residuals displays a straight line relationship, is given in Figure D.2 in

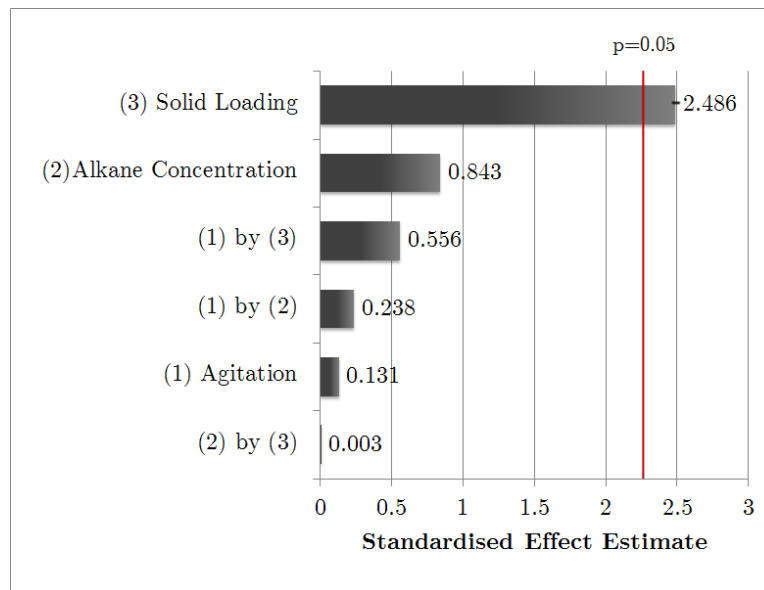


Figure 6.5: Pareto chart for the effect of independent variables and interaction on  $K_P$  within a 95% confidence interval

Appendix D, indicative of a normal distribution of residuals. This means that deviations in the model are equally likely to be positive or negative, meaning the inaccuracies associated with the model will not skew any conclusions.

Since this model was verified by the experimental  $K_P$  data, it can be used to predict the impact of the system parameters on the probe response lag, a conclusion supported by the agreement between the observed (experimental) values and the values predicted by the model (Figure D.1). The x- and y- axes represent the associated factor level for each parameter (Table 5.1), while the z-axis represents the ratio of the system  $K_P$  to that of pure water ( $K_P^*$ ). Since  $K_P$  is inversely proportional to  $\tau_P$ , any values above the the transparent surface in the following plots indicate a shorter response time and consequently a faster probe response than in water. A value of  $K_P/K_P^*$  equal to one would indicate that the  $K_P$  in the system is identical to that in pure water.

Figure 6.6 shows the effect of agitation and alkane concentration on  $K_P/K_P^*$  for a constant yeast loading relative to a pure water system. Overall, the maximum value for  $K_P/K_P^*$  was 2.37, with alkane concentration at 11% v/v and 1000 RPM and a yeast loading of 5.5 g/l. This corresponds to a value of 0.0661 for  $K_P$  and a  $\tau_P$  of 15.1 seconds. This result is comparable to the findings of Manyuchi (2010), who determined the maximum value for  $K_P$  as  $0.0434 \text{ s}^{-1}$  with 2.5% v/v  $C_{14-20}$  alkane-aqueous dispersion at 1200 RPM, corresponding to a  $\tau_P$  of 14.7 seconds. Clearly evident at low alkane concentrations is the increase in  $K_P$  with an increase in agitation. It follows that an increase in the turbulence within the system aids mixing, increases the rate of diffusion, and thins the stagnant boundary layer at the probe interface. These factors combined mean a high turnover of oxygen saturated liquid in the vicinity of the probe.



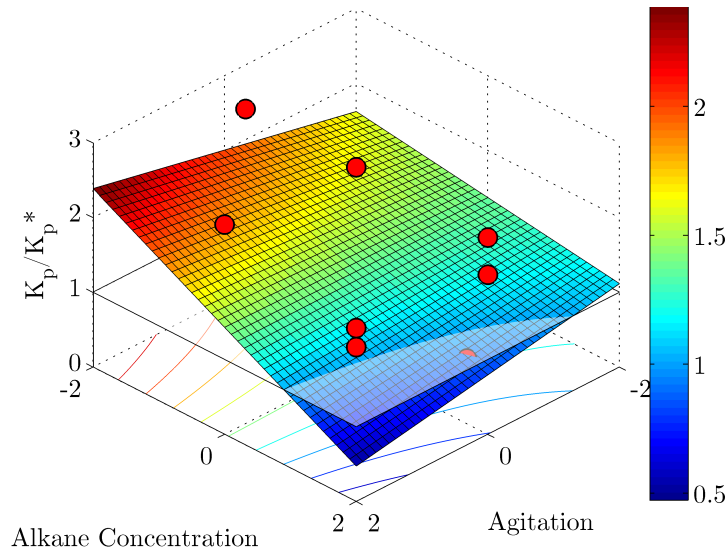


Figure 6.6: The effect of agitation and alkane concentration on  $K_p$  at constant mid (0) yeast loading

However, as the alkane concentration was increased, the  $K_p$  was depressed, eventually dipping below that of pure water, an effect which was magnified at high agitation levels. The likely cause for this is the increase in fluid viscosity with increase alkane concentration. An increase in the viscosity will damp the fluid turbulence, hamper mixing, and slow the rate of diffusion of oxygen to the probe membrane, as found by Queimada *et al.* (2003). The lowest  $K_p$  recorded in this study was  $0.024 \text{ s}^{-1}$ , for a system with extra high yeasts loading with mid agitation and mid alkane concentration. This corresponds to a  $\tau_p$  of 41.6 seconds, over 2.8 times longer than the fastest probe response. This underlines the importance of including the  $K_p$  in the calculation of  $K_L a$  using the GOP, especially in a system with increased viscosity.

Figure 6.7 shows the combined impact of agitation and yeast loading on the  $K_p$  with the alkane concentration at the mid factor level. At low yeast loading, an increase in agitation resulted in an increase in the  $K_p$  ratio, a trend which was reversed at higher solid loadings. An increase in yeast loading resulted in an increase in  $K_p$  ratio for all agitations.

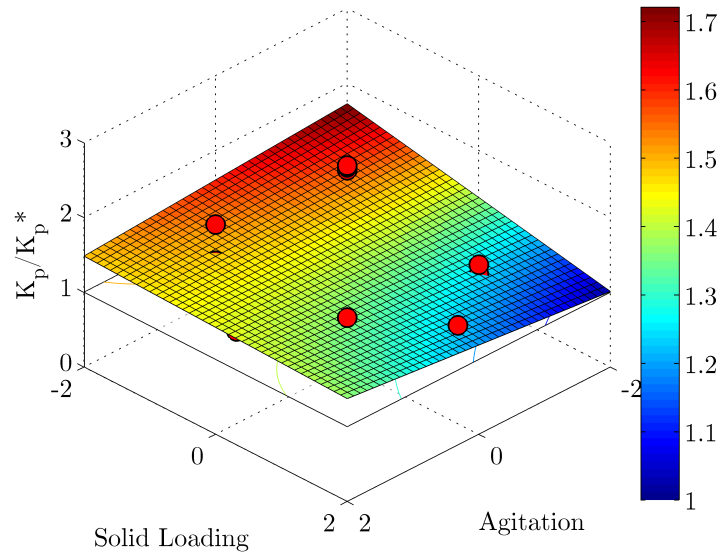


Figure 6.7: The effect of agitation and yeast loading on  $K_p$  at medium alkane concentration

The most significant enhancement in  $K_p$  was experienced at low agitations and low yeast loadings. This result indicates that the low yeast loading and mid alkane concentration are able to reduce the probe response lag if they do not cause a significant increase in viscosity. This is also indicative of the lesser role agitation has to play in the probe response lag, when compared with the other two parameters.

Figure 6.8 shows the relationship between alkane concentration and yeast loading at medium agitation. Here the most significant result is depression of the  $K_p$  ratio at high yeast loading and high alkane concentrations, most likely a consequence of increased viscosity. Combined at high factor levels, these parameters depress the  $K_p$  well below what is experienced in a pure water system, with the capacity to increase  $\tau_p$  to over 45 seconds. On the other hand, lower factor levels of each are able to decrease  $\tau_p$  to 2.4 times that in a pure water system. The reduced bubble coalescence may be the driving force behind this enhancement.

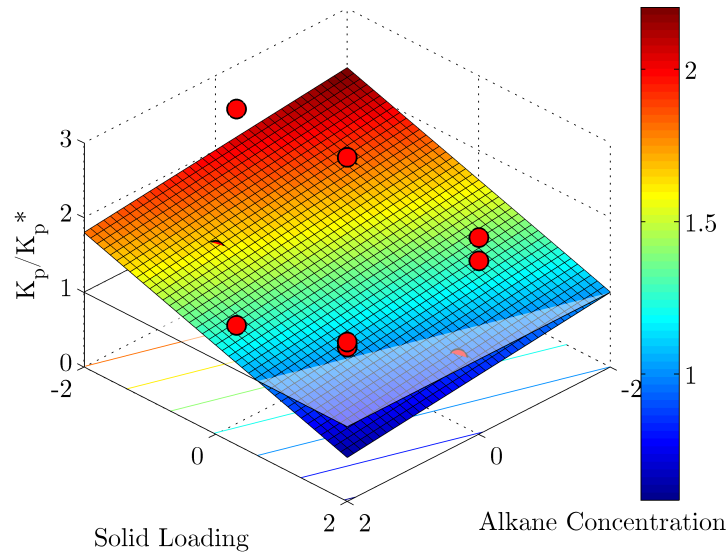


Figure 6.8: The effect of alkane concentration and yeast loading on  $K_p$  at constant mid (0) agitation

## 6.2 Influence of System Parameters on the $K_{La}$

Once the probe response lag for a system configuration is known, it is possible to employ the second order model to determine  $K_{La}$ . Furthermore, it is also possible to examine the effects of varied process parameters on  $K_{La}$ , the significance of each effect and the magnitude of the interaction between the system parameters. With  $K_{La}$  being a lumped parameter, it is not always immediately evident which parameter is dominant in defining the  $K_{La}$  behaviour, but using a statistical approach it becomes possible to quantify the individual effects, as well as any combination of the parameters. For this reason, a quadratic model with two way interaction was fitted to the experimental data. To illustrate the magnitude of the individual system parameters on  $K_{La}$ , a Pareto chart of the effects is given in Figure 6.9 with a 95% confidence interval. The ANOVA summary is provided in Table 6.2.

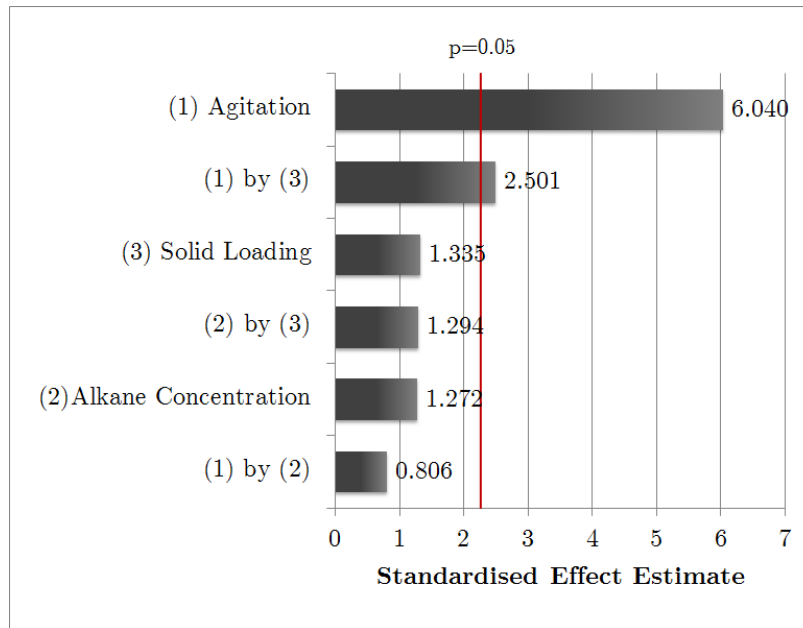


Figure 6.9: Pareto chart for the effect of independent variables and interaction on  $K_{La}$  within a 95% confidence interval

Table 6.2: ANOVA for  $K_{La}$  using a quadratic model with two way interaction

	Sum of Squares	Mean Square	F-test	p-test
(1) Agitation	0.8114	0.8114	36.482	0.0001
(2) Alkane Concentration	0.0360	0.0360	1.6187	0.2351
(3) yeast Loading	0.0396	0.0396	1.7814	0.2147
(1) by (2)	0.0144	0.0144	0.6494	0.4410
(1) by (3)	0.1391	0.1391	6.2539	0.033818
(3) by (2)	0.0372	0.0372	1.674	0.2279
Error	0.2001	0.0222		
Total SS	1.278			

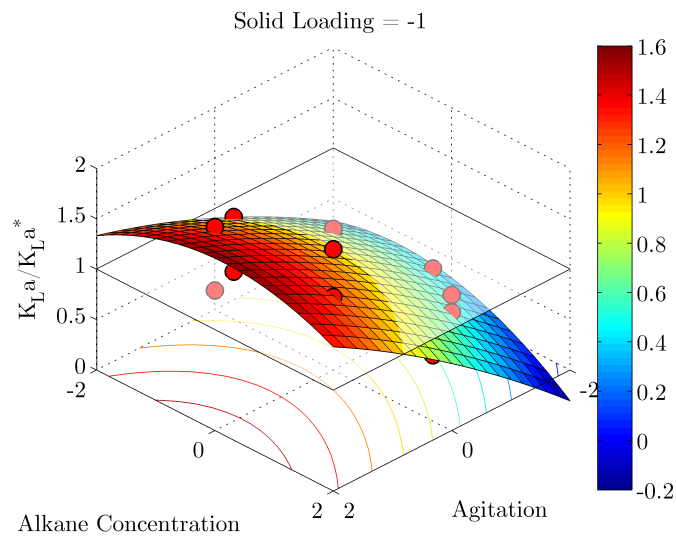
Using the quadratic model with 2 way interaction resulted in the agitation and the interaction between agitation and yeast loading being the most statistically significant variables. Both display contributions exceeding the 95% confidence interval. There is good agreement between the observed (experimental) values and the values predicted by the model (Figure D.3, Appendix D). An  $R^2$  value of 0.943 also indicates a good fit of the model to the experimental data. A straight line relationship in the normal plot of residuals (Figure D.4) indicates a normal distribution of the residual, confirming the robustness of the ANOVA analysis for this model. This model can therefore be used to describe the trends in the experimental data for  $K_{La}$ . As with the  $K_P$ , all the results shown here are in terms of the enhancement ratio,  $K_{La}/K_{La}^*$ , and describes the  $K_{La}$  relative to a baseline of pure water at medium agitation.

### 6.2.1 The Influence of Agitation Rate and Alkane Concentration on $K_La$ at Constant Yeast Loading

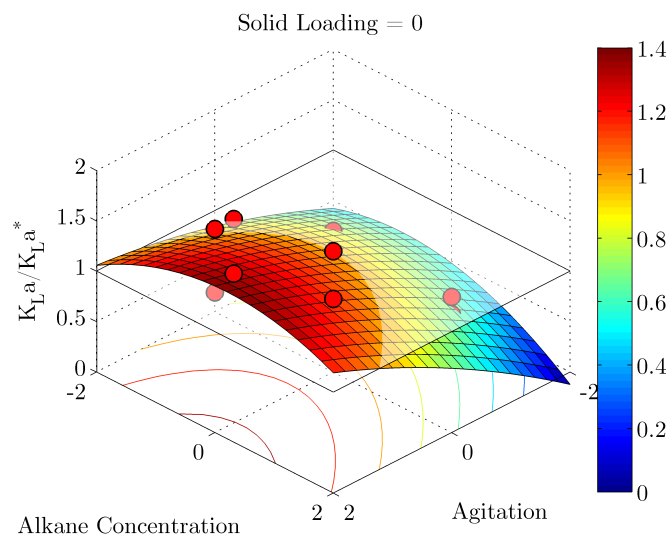
The impact of agitation and alkane concentration on  $K_La$  was analysed at three discrete constant yeast loadings. Figure 6.10b shows the relationship between alkane concentration and agitation at the yeast loading midpoint, with results for the low and high yeast loading factor levels in Figures 6.10a and 6.10c. As revealed by the statistical model, agitation is the most significant independent variable, and has the largest effect on the  $K_La$  enhancement ratio. An increase in the agitation increased the  $K_La$  across all factor levels. The  $K_La$  increased from  $0.017\text{ s}^{-1}$  at 450 RPM to  $0.049\text{ s}^{-1}$  at 1000 RPM with medium (11%v/v) alkane concentrations, with the latter resulting in a peak  $K_La$  enhancement ratio of 1.45.

Higher agitation intensifies the turbulent regime in the bulk liquid, which increases the rate of diffusion in the bulk liquid. This trend is in agreement with the findings in the review by Clarke and Correia (2008), who state that agitation has a positive effect on both the  $K_L$  and interfacial area. Clarke *et al.* (2006) found that  $K_La$  increased with agitation up until 1000 RPM, valid for  $C_{12-13}$  concentrations varied between 10 and 20% v/v in an alkane-aqueous dispersion not containing solids. Manyuchi (2010) found that  $K_La$  increased from  $0.025\text{ s}^{-1}$  to  $0.050\text{ s}^{-1}$  in a system with 2.5 % v/v  $C_{14-20}$  and 1 g/l inert yeast when the agitation was increased from 600 to 1200 RPM. Similarly, Ozbek and Gayik (2001) found that  $K_La$  increased from 0.0085 to  $0.0101\text{ s}^{-1}$  when agitation was increased from 100 to 500 RPM in a 1 litre bioreactor with Scotch-Brite® biomass support particles and distilled water. Cascaval *et al.* (2006) found an increase in  $K_La$  with an intensification in mixing in suspensions of *Saccharomyces cerevisiae* in *n*-dodecane and water systems. This is driven by a decrease in cell-bubble adhesion (reducing any physical blocking effect on oxygen transfer) and increasing the interfacial area (through a reduction in  $D_{SM}$ ).

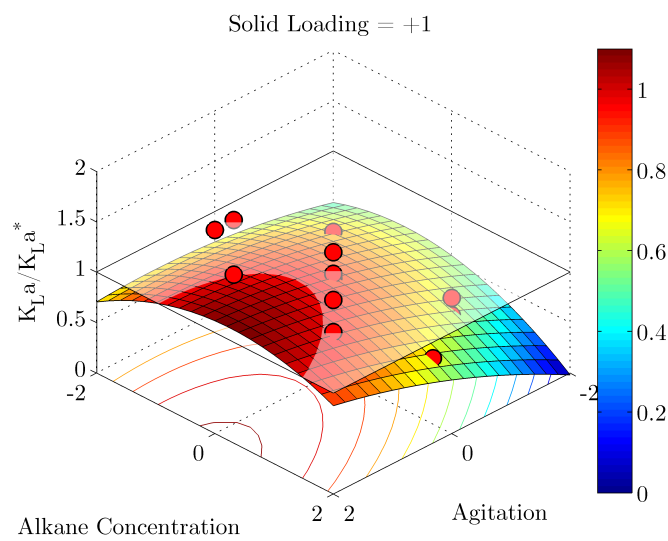
On the contrary, Galaction *et al.* (2004a) and Galaction *et al.* (2004b) observed a decrease in  $K_La$  with an increase in the specific power input into non-respiring biomass suspensions of *Propionibacterium shermanii*, *Saccharomyces cerevisiae* or *Penicillium chrysogenum*. The authors postulated that a decrease in  $D_{SM}$  promoted the adhesion of cells onto the bubble surface thus increasing the physical blocking effect. In support of this theory, the same studies found an increase in  $K_La$  when examining a suspension of *P. chrysogenum* pellets which promote interfacial turbulence and consequently enhance oxygen transfer. The increase in agitation increased both the interfacial turbulence and decreases  $D_{SM}$ . For this reason, Galaction *et al.* (2004a) concludes that it is possible to achieve the peak oxygen transfer rate at low power consumption for biomass suspensions. This finding highlights the interrelated nature of the process parameters used, the specific behaviour of the solids in the suspension and their interaction with the other phases in the bioreactor.



(a) Constant low (-1) yeast loading



(b) Constant mid (0) yeast loading



(c) Constant high (+1) yeast loading

Figure 6.10:  $K_{L,a}$  enhancement factor with changes in agitation rate and alkane concentration at constant yeast loadings

An increase in the alkane concentration initially resulted in an increase in the  $K_{La}$ , but beyond the midpoint (11%v/v), any additional alkane resulted in a decrease in  $K_{La}$ . This trend was observed for all agitation rates and yeast loadings (Figure 6.10). This relationship is explored in detail in Section 6.3.1 in conjunction with the analysis of the interfacial area results.

## 6.2.2 Influence of Yeast Loading on $K_{La}$

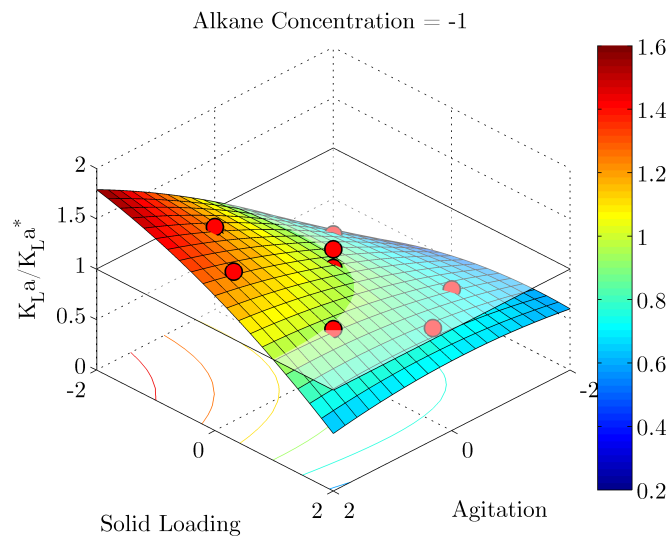
### 6.2.2.1 The Influence of Yeast Loading on $K_{La}$ at Varying Agitation Rates

While the previous section examined the impact of agitation and alkane concentration in a system containing yeast, the yeast loading was maintained at constant discrete factor levels. To better elucidate the impact of on oxygen transfer, yeast loadings were also varied while keeping firstly the alkane concentration constant, and secondly, under constant agitation conditions.

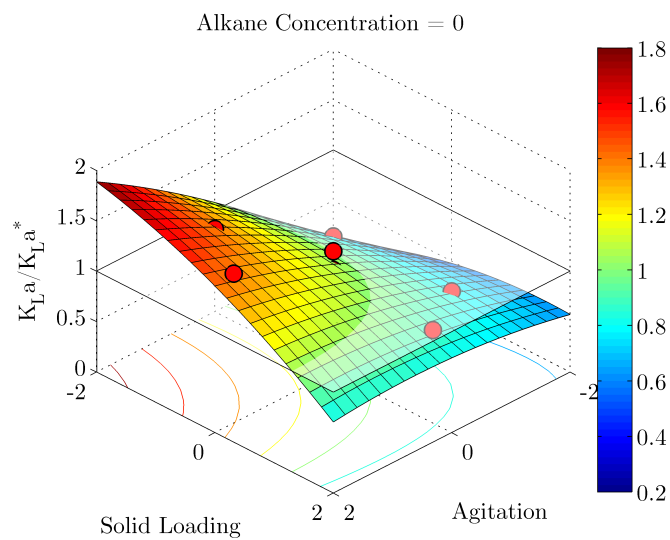
The impact of yeast loading on  $K_{La}$  was investigated in conjunction with the impact of agitation, while maintaining a constant alkane concentration. An increase in the yeast loading at high agitation levels resulted in a decrease in the  $K_{La}$  enhancement ratio (Figures 6.11a - 6.11c). This trend is reversed at low agitation levels, where an increase in the yeast loading increase the enhancement ratio, albeit only by a small amount. An increase in agitation increases the enhancement ratio for all bar the very highest yeast loadings.

At high agitation levels, the decrease in  $K_{La}$  through the addition of yeast (Figure 6.11b) is driven by the increase in  $D_{SM}$ , caused by an increase in the apparent fluid viscosity. Cascaval *et al.* (2006) examined  $K_{La}$  in *Propionibacterium shermanii* broths in an STR, and found that  $K_{La}$  was depressed at high yeast loadings, irrespective of power input into the system. The study reported a 4-5 fold reduction in  $K_{La}$  when the biomass concentration was increased from 30.5 to 120.5 g/l. These results were repeated using *Saccharomyces cerevisiae* in the same study. This study found that an increase in fluid viscosity was found to underpin the depression of  $K_{La}$ .

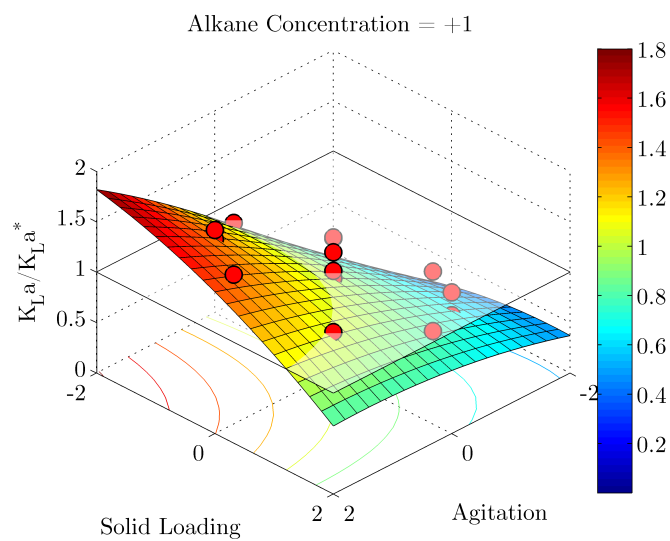
Similar results were also reported by Galaction *et al.* (2004a), using *Propionibacterium shermanii*, *Saccharomyces cerevisiae* and *Penicillium chrysogenum* free mycelia. The most significant depression was observed in the latter, with  $K_{La}$  was reduced 3.7 fold for a solid content of between 4 and 36.5 g/l. In all three cases, the trend was continuously downwards, with no enhancement in  $K_{La}$  observed. Again, these results were reportedly driven by the increase of apparent viscosity of the bulk fluid, due to increased biomass concentrations. This conclusion is supported by Albal *et al.* (1983), who postulated that observed decreases in  $K_{La}$  for systems with more than 5 vol% yeast (glass beads and oil shale particles in water) was driven by an increase in viscosity and a concomitant reduction in surface renewal.



(a) Constant low (-1) alkane concentration



(b) Constant mid (0) alkane concentration



(c) Constant high (+1) alkane concentration

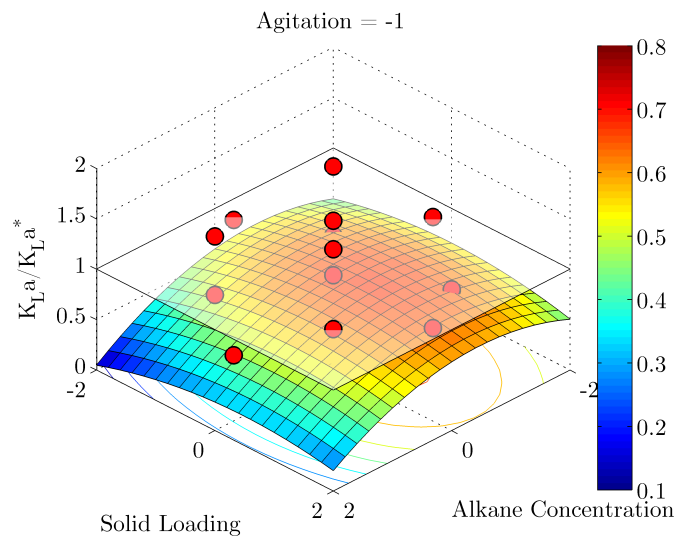
Figure 6.11:  $K_{La}$  enhancement factor with changes in agitation rate and yeast loading at constant alkane concentrations



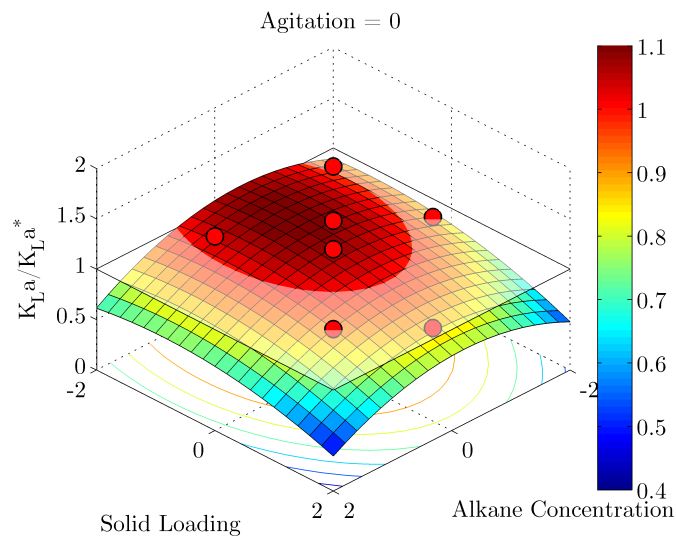
At lower levels of agitation, the increase in  $K_La$  with an increase in yeast loading (Figure 6.11b) was caused by yeast particles being trapped by the stagnant fluid film at the gas liquid interface, preventing bubble coalescence. Less turbulent conditions are causing an increase in thickness of the stagnant boundary layer at the bubble surface, resulting in the boundary layer being thicker than the diameter of the yeast particles. yeast particles adhere to the bubble surface, and rather prevent bubble coalescence, increasing  $D_{SM}$  (Figure 6.21) and reducing the available interfacial area. This theory is documented by both Joosten *et al.* (1977), Albal *et al.* (1983) and Miyachi *et al.* (1981).

### 6.2.2.2 The Influence of Yeast Loading on $K_La$ at Varying Alkane Concentrations

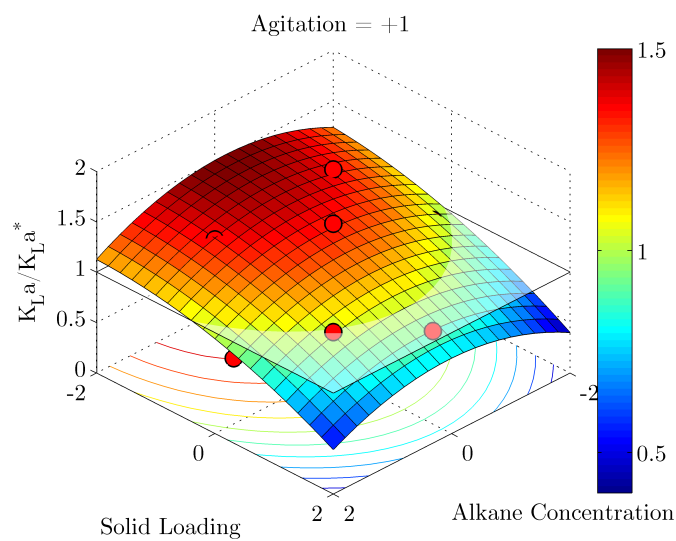
The final set of results analysed changes in  $K_La$  stemming from changes in the alkane concentration and the yeast loading, at constant agitation levels. (Figures 6.10a - 6.10c). An increase in the yeast loading depressed the  $K_La$  enhancement factor at all alkane concentrations when examined at a constant midpoint agitation rate (Figure 6.12b). As observed in Section 6.2.1, an increase in the alkane concentration initially results in an increase in  $K_La$ . Further alkane addition then begins to depress  $K_La$ , resulting in a distinct peak. This is true for all yeast loadings. The maximum  $K_La$  increase was observed at the alkane concentration midpoint, with the a maximum  $K_La$  enhancement factor ( $>1$ ) occurring at the maximum agitation rate (1000 RPM), mirroring the trend observed under conditions of varying alkane concentrations at discrete constant yeast loadings (Figure 6.10b). At lower (450 RPM) constant agitation rate, however, the alkane concentration at which the peak  $K_La$  was observed shifted to a lower value (Figure 6.12a), and conversely higher constant agitation rates (1000 RPM) increased the magnitude of the  $K_La$  peak (Figure 6.12c).



(a) Constant low (-1) agitation rate



(b) Constant mid (0) agitation rate



(c) Constant high (+1) agitation rate

Figure 6.12:  $K_{L,a}$  enhancement factor with changes in alkane concentration and yeast loading at constant agitation rates

### 6.3 Influence of System Parameters on Interfacial Area

The lumped nature of the  $K_{La}$  means that changes in process parameters have an effect on either  $K_{La}$ , interfacial area, or both concurrently. To establish which of these factors underpins the behaviour of  $K_{La}$  in a model hydrocarbon-based bioprocess, the interfacial area was analysed independently under the same experimental conditions as those used for evaluating the effects on  $K_{La}$ . A central composite design was employed using factor levels as described in Table 5.1 and illustrated in Figure 5.19, with the interfacial area being the dependent variable. The interfacial area is defined in Equation 5.8, and is calculated using the gas hold-up and the Sauter mean bubble diameter ( $D_{SM}$ ). The experimental methodology and procedure is given in detail in Section 5.2.

As with the  $K_{La}$  quantification, the central composite design allows for examination of the individual and combined effect of each independent variable, using a quadratic model to fit the data. A Pareto chart of effects is shown in Figure 6.13, while an ANOVA chart is given in Table 6.3. The most significant independent variable was again the agitation, with a positive relationship between agitation and interfacial area. While not statistically significant (falling outside the 95% confidence interval) the yeast loading also had a positive effect (1.53) as did the alkane concentration (0.77).

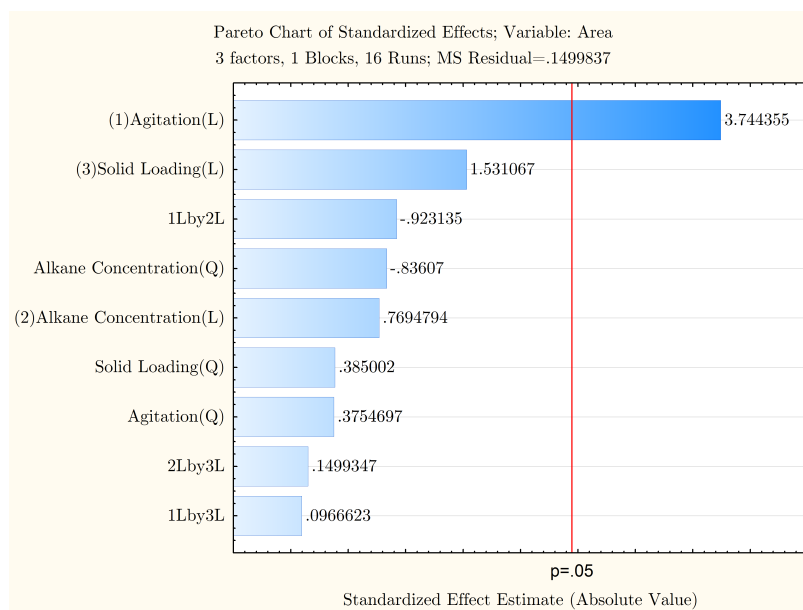


Figure 6.13: Pareto chart for the effect of independent variables and interaction on interfacial area within a 95% confidence interval

Table 6.3: ANOVA for interfacial area using a quadratic model with two way interaction

Factor	SS	df	MS	F	p
(1) Agitation (L)	31.1155	1	0.00000	4.699760	0.073275
Agitation (Q)	0.8823	1	0.88232	0.133268	0.727590
(2) Alkane Concentration (L)	12.0243	1	12.02430	1.816178	0.226426
Alkane Concentration (Q)	9.4151	1	9.41511	1.422080	0.278079
(3) yeast Loading (L)	0.0131	1	0.01314	0.001985	0.965907
yeast Loading (Q)	0.4337	1	0.43369	0.065506	0.806545
1L by 2L	0.5744	1	0.57435	0.086751	0.778273
1L by 3L	2.7950	1	2.79502	0.422166	0.539921
2L by 3L	1.4811	1	1.48105	0.223702	0.652949
Error	39.7240	6	6.62066		
Total SS	101.8333	15			

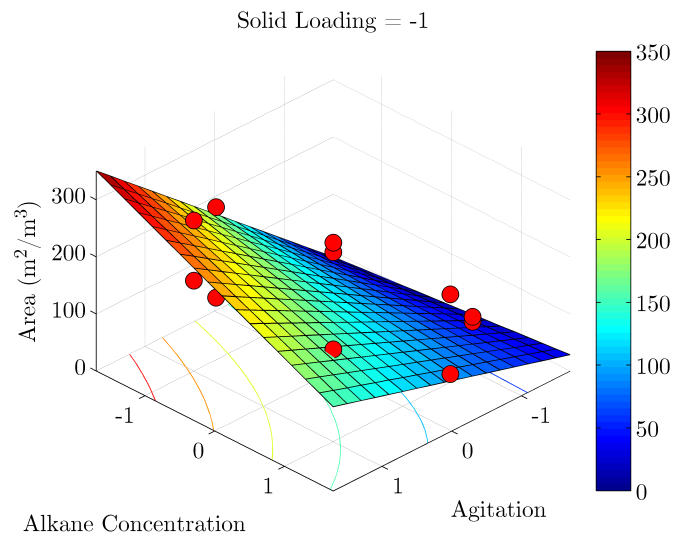
### 6.3.1 Influence of Agitation Rate and Alkane Concentration on Interfacial Area at Constant Yeast Loading

Across all alkane concentration factor levels, an increase in the agitation resulted in an increase in the interfacial area (Figure 6.14). At the mid point in the alkane concentration, the interfacial area increased from 30.7 to 232.5  $\text{m}^2/\text{m}^3$ . The increase in interfacial area is most significant at low alkane concentrations and yeast loadings, where an increase from 158.4 to over 263.8  $\text{m}^2/\text{m}^3$  was observed driven by increasing agitation rates. Higher alkane concentrations damped the magnitude of the agitation driven increase in interfacial area.

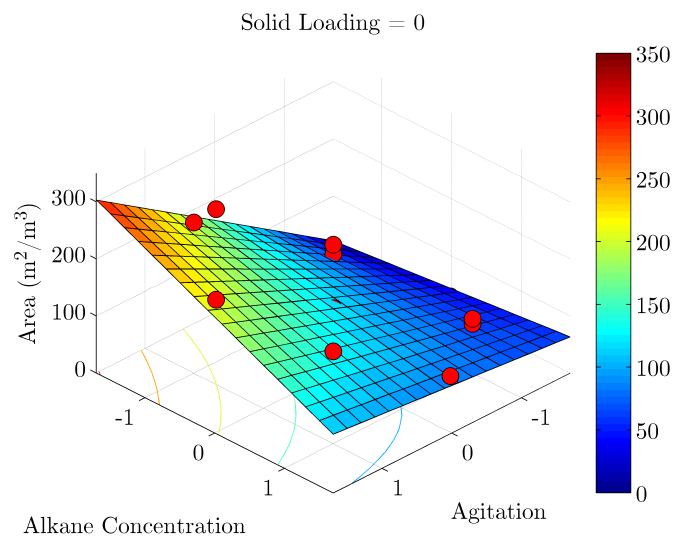
An increase in the turbulence had four primary methods for increasing the interfacial area in the agitated system. Firstly, increased turbulence will decrease the  $D_{SM}$ . Secondly, it will decrease the time for bubble formation and growth at the sparger resulting in smaller bubbles. The third reason for an increase in interfacial area with increased agitation is an increase in gas hold-up by entraining more bubbles in the bulk liquid phase. Finally, the smaller bubble diameter caused by increased agitation slows the rise time of the bubbles while concomitantly increasing the gas hold-up.

The main reason for the observed increase in interfacial area is the decrease in the  $D_{SM}$  with an increase in agitation (Figure 6.15) with little impact on gas hold-up (Figure 6.16) (additional results for  $D_{SM}$  and hold up at the high and low yeast loading configurations are supplied in Figure A.1b through Figure A.2a in Appendix A). The effect of an increase in agitation was enhanced at low alkane concentrations, largely because the higher alkane concentration increases the viscosity, damping the turbulence in the bioreactor.

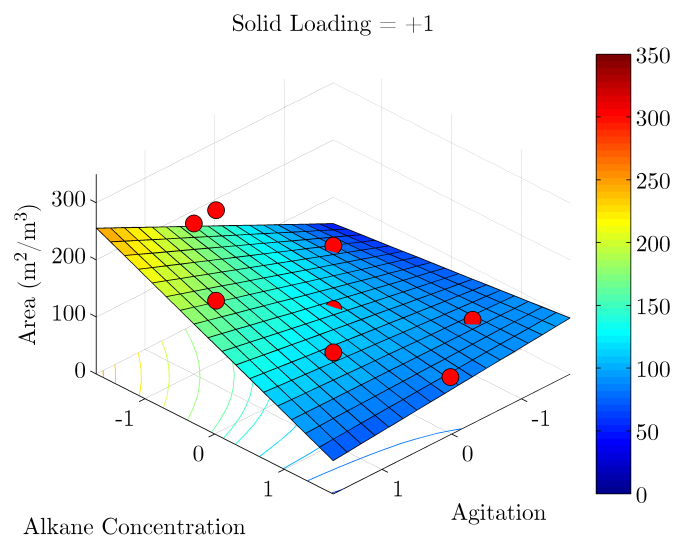
The  $D_{SM}$  is a measure of impact of a change in parameters on bubble size. It is a measure of the mean of the bubble size distribution. Therefore, to fully understand the impact of agitation on bubble size, the bubble size distribution needs to be analysed. There was a shift towards



(a) Constant low (-1) yeast loading



(b) Constant mid (0) yeast loading



(c) Constant high (+1) yeast loading

Figure 6.14: Interfacial area with changes in agitation rate and alkane concentration at constant yeast loadings

a higher percentage of smaller bubbles from the very lowest agitation (Figure 6.17a) to the highest agitation (Figure 6.17b) accompanied by a narrowing of the distribution with both the alkane concentration and yeast loading at their respective mid-points, increasing the uniformity of the distribution and approaching a normal distribution. The small number of larger bubbles for lower levels of agitation (evident in Figure 6.17a) had a significant impact on both the  $D_{SM}$  and interfacial area, resulting in an increase of the former, and a decrease of the latter.

The results in Figures 6.10b and 6.14b show a clear correlation between  $K_La$  and interfacial area, and it can be concluded that the increase in  $K_La$  with an increase in agitation is primarily caused by a decrease in  $D_{SM}$  (Figure 6.15).

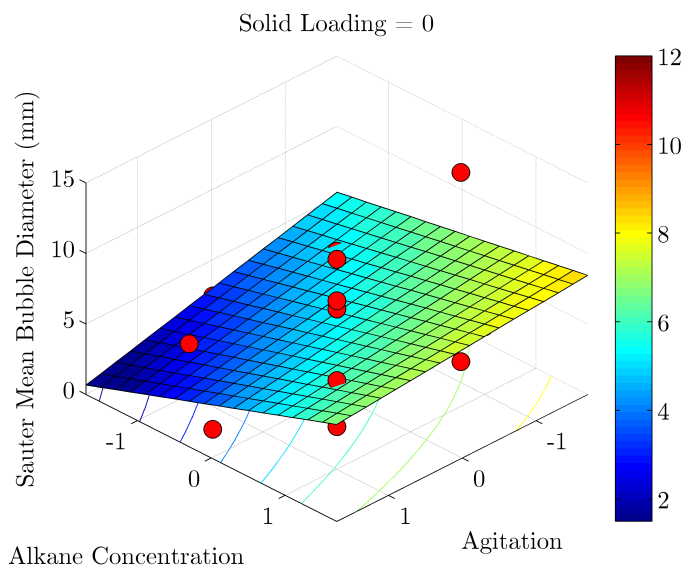


Figure 6.15:  $D_{SM}$  with changes in agitation rate and alkane concentration at constant (midpoint) yeast loading

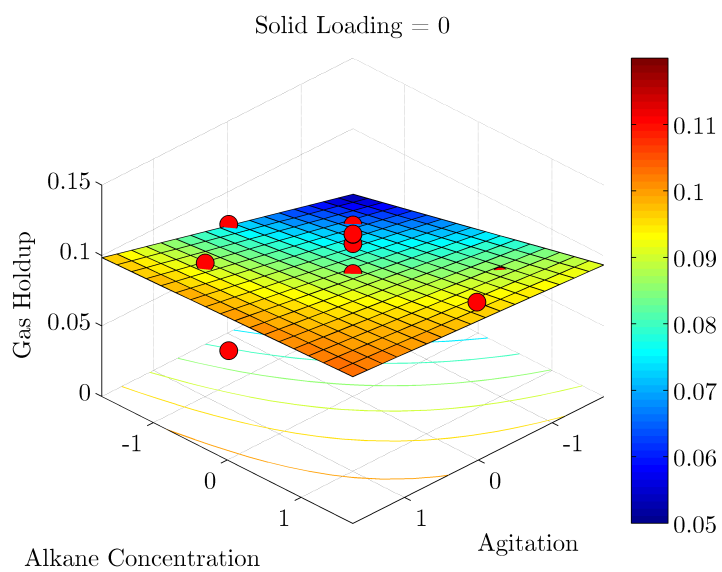
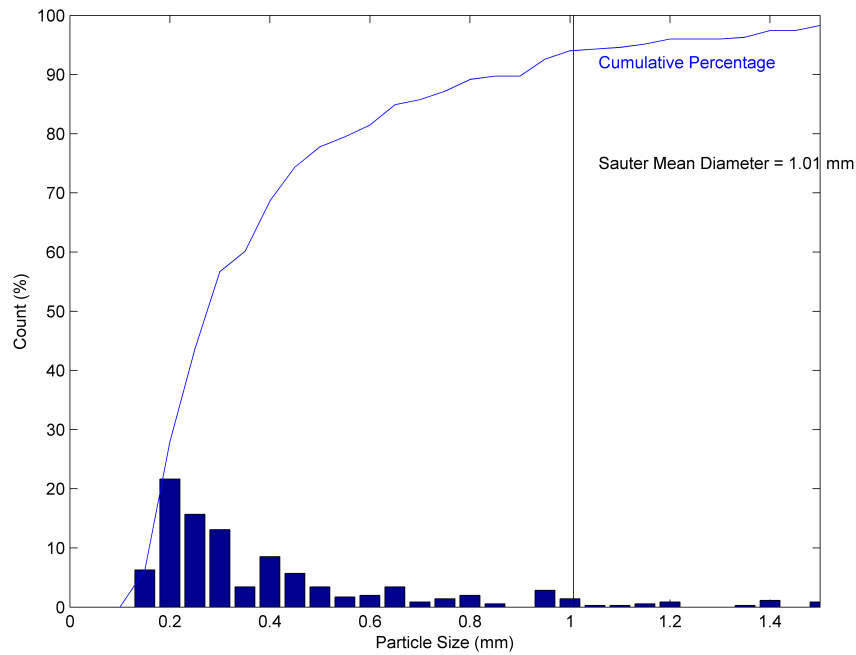
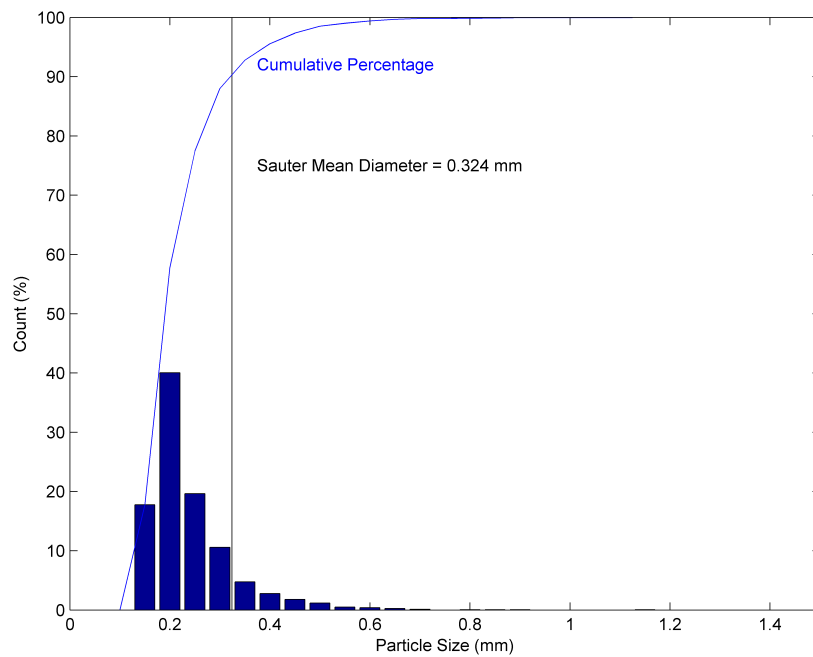


Figure 6.16: Gas hold up with changes in agitation rate and alkane concentration at constant (midpoint) yeast loading



(a) Very low agitation (450RPM) at constant midpoint alkane concentration



(b) Very high agitation (1000RPM) at constant midpoint alkane concentration

Figure 6.17: Bubble size distribution and  $D_{SM}$  for varied alkane concentration at constant midpoint agitation

In addition to the positive effect of agitation on interfacial area, the effect of alkane was also



reported (Figure 6.14). An increase in alkane concentration at high agitations resulted in a decrease in interfacial area, coinciding with an increase in  $D_{SM}$  underpinned by an increase in the bulk fluid viscosity. An increase in alkane concentration at low agitations has negligible impact on either area or  $D_{SM}$ . The gas hold up was not observed to change significantly with variation in either agitation or alkane concentration (Figure 6.16), with a slight decrease occurring with an increase in agitation at low alkane concentrations. The observed decrease in the interfacial area with increasing alkane concentration, driven by the increase in fluid viscosity imparted by the alkane, is not replicated in  $K_L a$  (Figure 6.10b), where an initial increase in alkane concentration enhances the  $K_L a$  up to the alkane concentration midpoint. Beyond this, a further alkane addition begins to depress the  $K_L a$ . Since this peak is not evident in the interfacial area, the  $D_{SM}$ , or the gas hold up, it is likely that this is a result of a change in  $K_L$ . This can be observed in the peak in  $K_L$  with increasing alkane concentration in Figure 6.18. It is clear that low alkane concentrations have a significant positive impact on  $K_L$ . This may be due the beading behaviour of the alkane at the gas-liquid interface, with alkane droplets acting as rigid spheres and enhancing interfacial turbulence. This concept is supported fundamentally by the SRT, which suggests increasing the rate of fluid element replacement at the gas-liquid interface would increase  $K_L$ . However, the alkane concentration increase has two primary effects. Firstly, the fluid viscosity is increased, meaning turbulence in the bulk fluid becomes damped, which in itself hinders mass transfer. Secondly, the higher viscosity also results in a thicker stagnant layer at the gas-liquid interface, acting as a barrier to mass transfer. Combining both these factors, as well as the overall decrease in interfacial area, means that  $K_L$ , and concomitantly  $K_L a$ , is depressed.

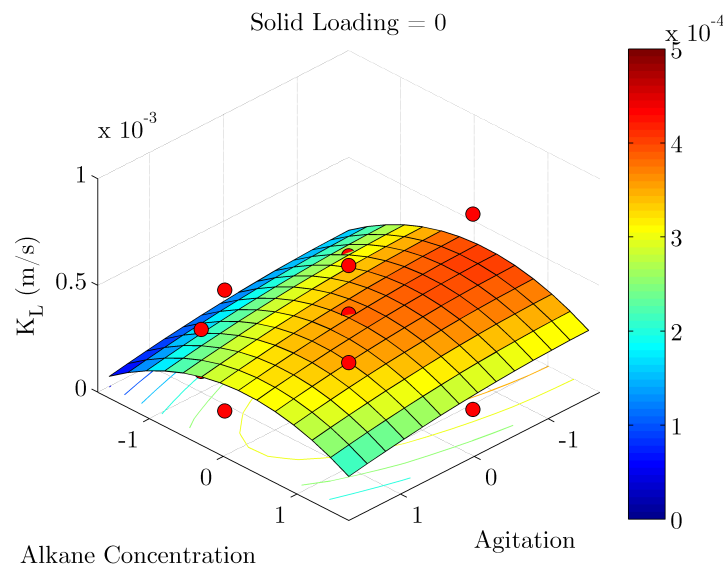
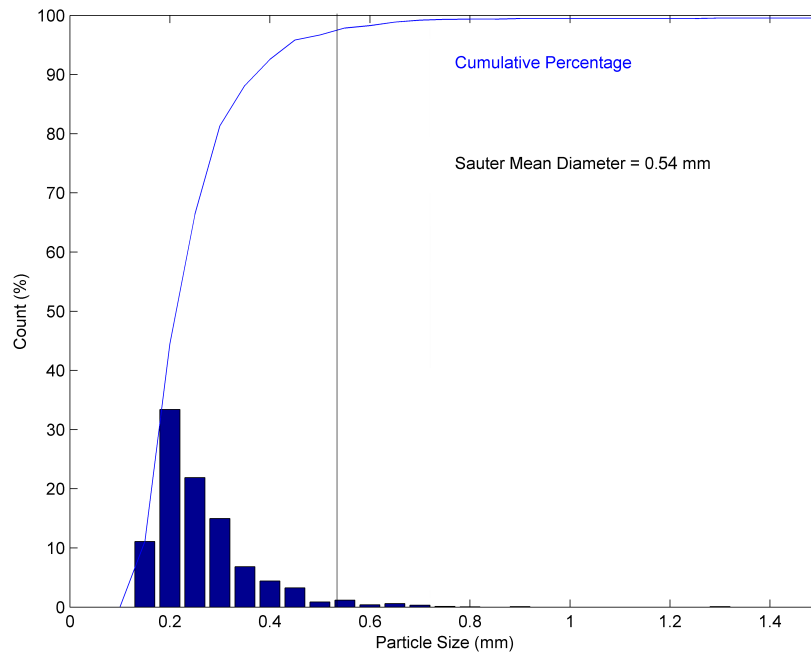


Figure 6.18:  $K_L$  with changes in agitation rate and alkane concentration at constant (midpoint) yeast loading

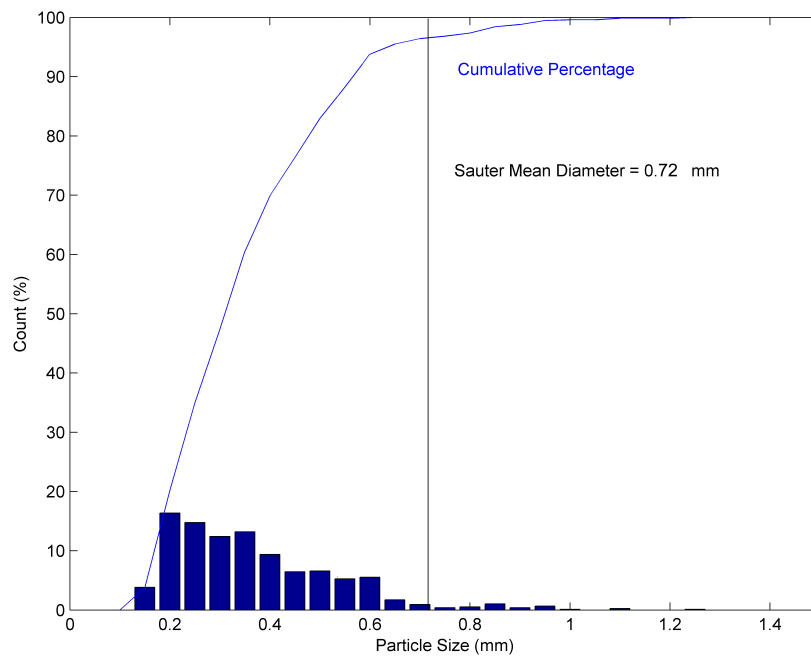
Furthermore, the increased viscosity damps the fluid turbulence, decreasing the energy of the

eddy currents within the bioreactor which reduces bubble breakage. This results in both a larger  $D_{SM}$  (Figure 6.15) and a skewing of the bubble size distribution towards larger diameters. This shift is evident in the bubble size distributions (Figure 6.19), with a broadening of the distribution with increasing alkane concentration. Other studies (Merten *et al.*, 2002; Behkish *et al.*, 2002; Arjunwadkar *et al.*, 1998) have reported a similar widened bubble size distribution with increasing viscosity. However, these authors also noted a decrease in gas hold-up with increasing viscosity with an increase in the number of larger bubbles due to the increased viscosity. Additionally, the smaller bubbles experienced increased entrainment in the bulk fluid contributing to the increased hold-up. No increase in hold-up was evident in this study (Figure 6.16). This is primarily due to the faster rise time (and lower residence time) of the larger gas bubbles compared with smaller gas bubbles. Galindo *et al.* (2000) observed larger (2 - 3 mm) bubbles rising quickly through the reactor, combined with a broadening of the bubble size distribution. This decreased residence time means that

Similar results were reported by Clarke *et al.* (2006), where a peak in  $K_La$  was demonstrated to exist for an  $n\text{-C}_{12-13}$  system between 600 and 1200 RPM. At 1200 RPM, the  $K_La$  was shown to increase from  $0.045\text{ s}^{-1}$  to  $0.05\text{ s}^{-1}$  at 5% v/v alkane. Again, the magnitude of enhancement was increased at elevated levels of agitation. Maximum enhancement was observed between 5 and 10 % v/v for all agitation levels above 800 RPM. Correia *et al.* (2010) also demonstrated Type 1 behaviour using  $n\text{-C}_{10-13}$ . They observed that  $K_La$  was enhanced as alkane concentration was increased from 2.5% to 5% at 800-1200 RPM, where after it declined as alkane concentration was increased from 5% to 20%. This is classified as Type 1 behaviour by Clarke and Correia (2008). This conclusion is supported by the findings of Rols *et al.* (1990) and der Meer and Beenackers (1992), who also observed the  $K_La$  to initially increase, reach a peak, followed by a depression upon hydrocarbon addition.



(a) Very low alkane concentration (2% v/v) at constant midpoint agitation



(b) Very high alkane concentration (20% v/v) at constant midpoint agitation

Figure 6.19: Bubble size distribution and  $D_{SM}$  for varied alkane concentration at constant mid-point agitation

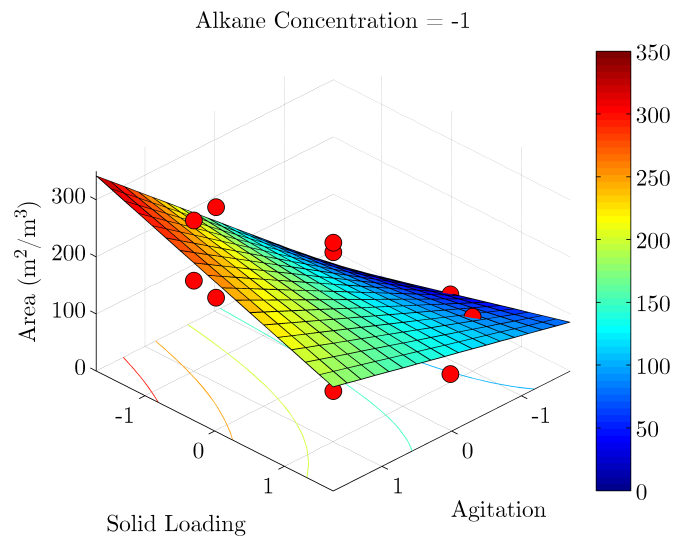
## 6.3.2 The Influence of Yeast Loading on Interfacial Area

### 6.3.2.1 The Influence of Yeast Loading on Interfacial Area at Varying Agitation Rates

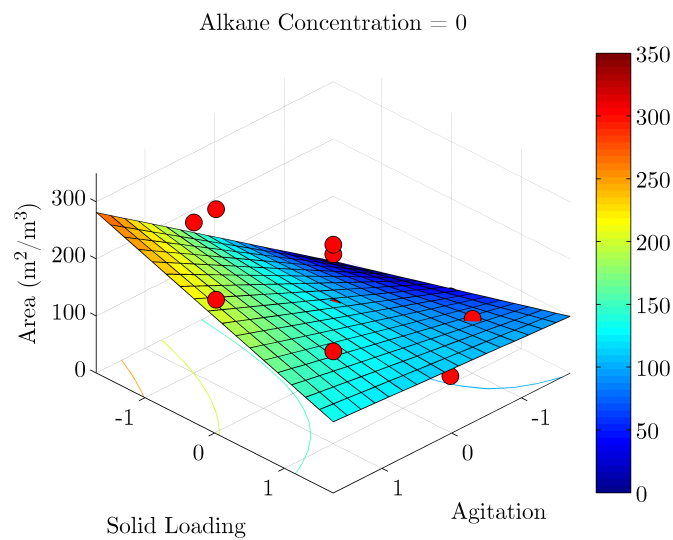
An increase in the yeast loading from 1 to 10 g/l resulted in a decrease in the interfacial area, dropping from over  $260 \text{ m}^2/\text{m}^3$  to less than  $160 \text{ m}^2/\text{m}^3$  under high agitation conditions (Figures 6.20a - 6.20c). This behaviour is however reversed for low agitation levels, where a similar increase in yeast loading increased the interfacial area. An increase in agitation had the most significant effect at low yeast loadings, where an increase from 450 RPM to 1000 RPM increase the area from less than to 85 to over  $260 \text{ m}^2/\text{m}^3$ . However, under conditions of high yeast loading (10 g/l) the agitation had a much less significant effect.

Comparison of Figures 6.20b and 6.21 indicate that the parameter likely underpinning the interfacial area trends is the  $D_{SM}$ . An increase in the agitation at low yeast loadings results in a decrease in the  $D_{SM}$ , while at high solid loadings the impact of the agitation increase is reduced. At high agitations, an increase in the yeast loading resulted in an increase in  $D_{SM}$ , while the opposite is true at low agitations.

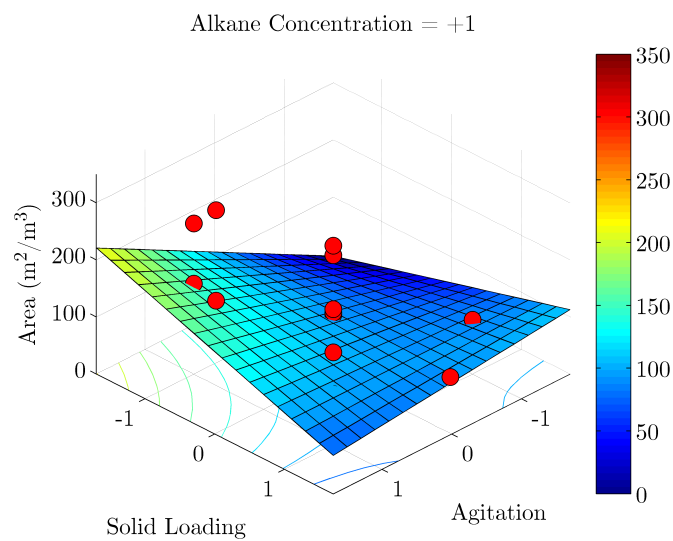
The hold up is not affected significantly by agitation of yeast loading (Figure 6.22), with the most distinct trend a result an increase in hold up driven by an increase in agitation at high yeast loadings. Results for other alkane concentration factor levels are provided in Figures A.3b and A.4a in Appendix A, Section A.2.



(a) Constant low (-1) alkane concentration



(b) Constant mid (0) alkane concentration



(c) Constant high (+1) alkane concentration

Figure 6.20: Interfacial area with changes in agitation rate and yeast loading at constant alkane concentrations

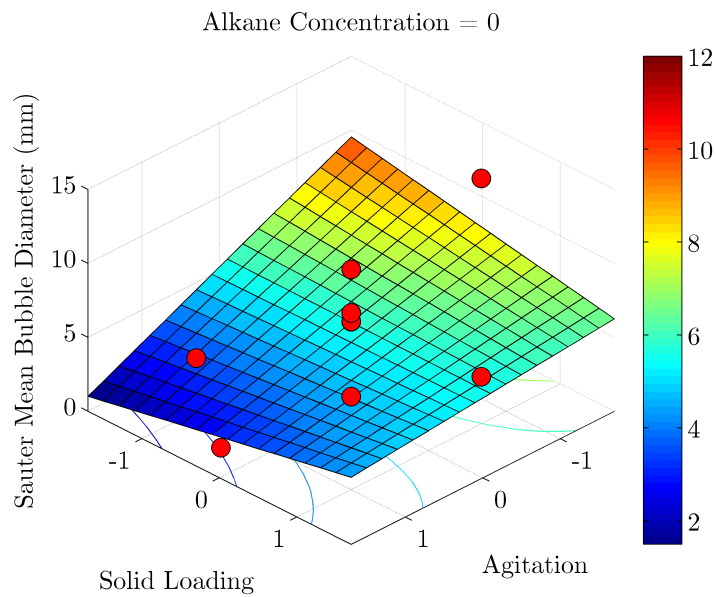


Figure 6.21:  $D_{SM}$  with changes in agitation rate and yeast loading at constant midpoint (0) alkane concentration

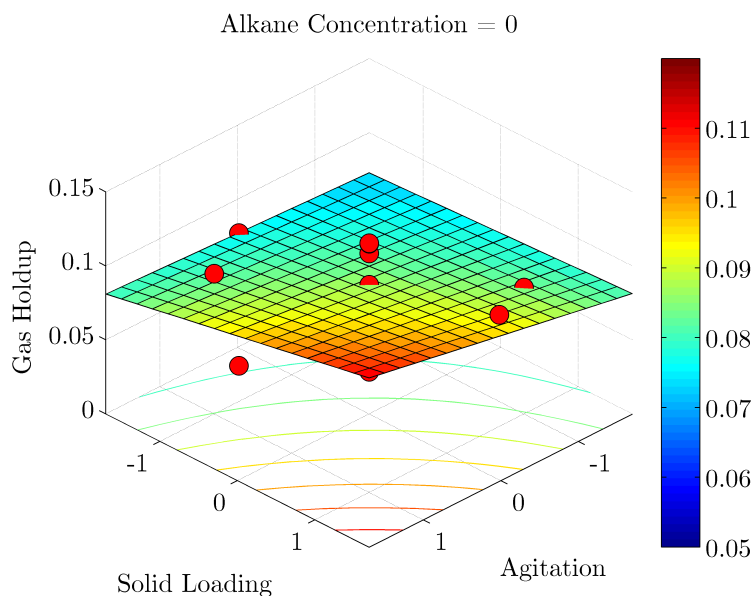


Figure 6.22: Gas hold up with changes in agitation rate and yeast loading at constant midpoint (0) alkane concentration

The behaviour of the interfacial area closely follows that of the  $K_La$  (Figures 6.11b and 6.20b), clearly suggesting that interfacial area plays a defining  $K_La$ . When combined with the  $D_{SM}$  trends (Figure 6.21) it becomes clear that the bubble diameter is the dominant factor in controlling  $K_La$  under these conditions. This is supported by the minimal changes in  $K_L$  evident in Figure 6.23.

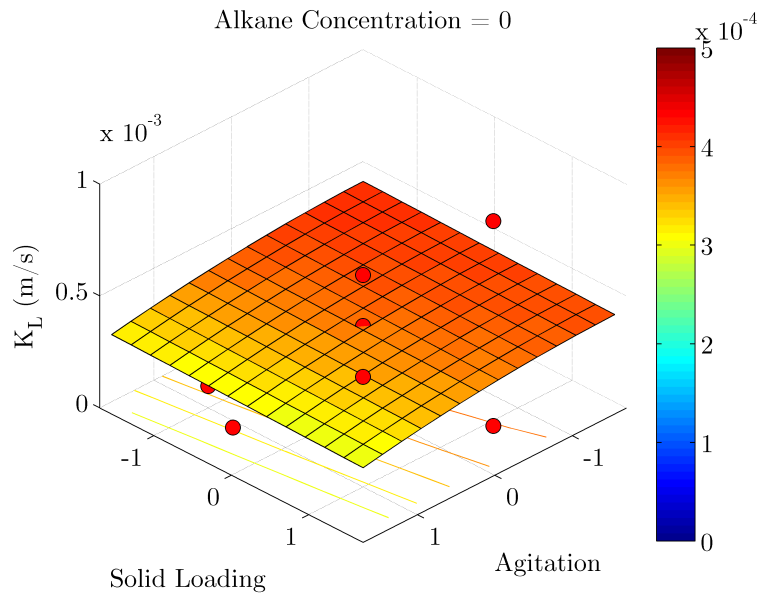


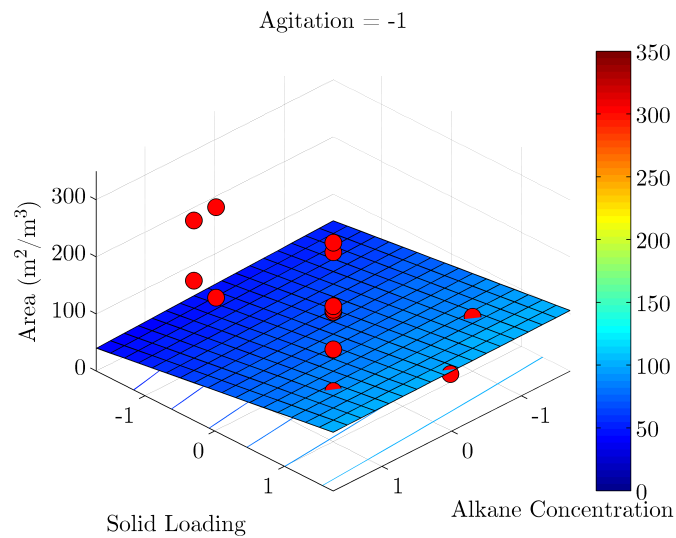
Figure 6.23:  $K_L$  with changes in agitation rate and yeast loading at constant midpoint (0) alkane concentration

### 6.3.2.2 The Influence of Yeast Loading on Interfacial Area at Varying Alkane Concentrations

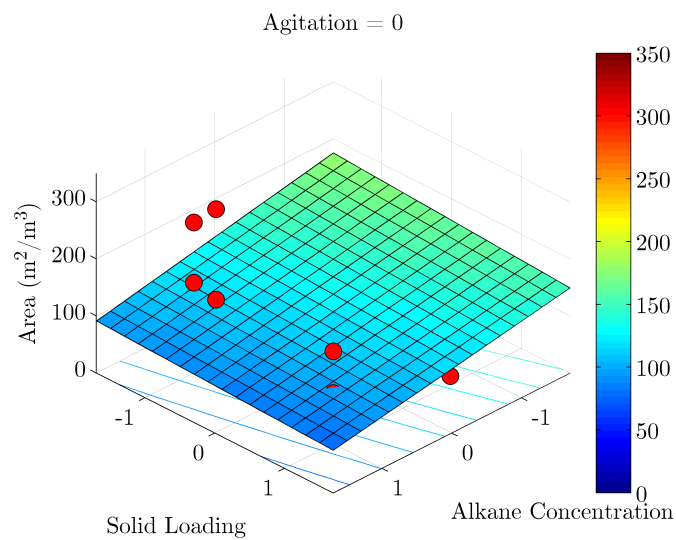
The peak evident in  $K_L a$  was not fully replicated in the interfacial area under analogous conditions where the absence of a peak  $K_L a$  with alkane addition was notable (Figure 6.24b). Results for other agitation factor levels are provided in Figures 6.24a and 6.24c. At low constant agitation (Figure 6.24a), an increase in the yeast loading resulted in an increase in interfacial area for all alkane concentrations. However, at higher constant agitation levels (Figures 6.24b and 6.24c), the yeast loading has a negative influence on interfacial area, particularly at lower alkane concentrations.

At low constant agitation (Figure 6.24a), alkane concentration was not observed to have a significant impact on interfacial area, irrespective of the yeast loading. However, at increased levels of agitation (Figures 6.24b and 6.24c), increasing the alkane concentration has a negative influence on interfacial area for all yeast loadings.

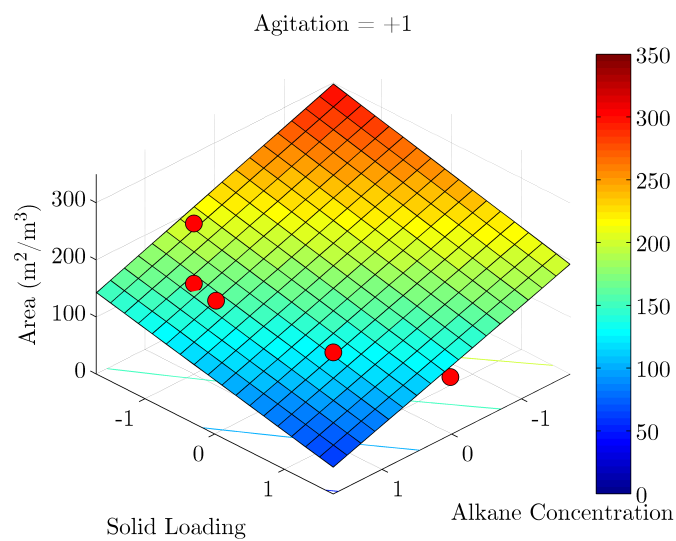
The decrease in interfacial area with an increase in alkane concentration (Figure 6.24b) is driven by the increase in  $D_{SM}$  (Figure 6.25), with very little change in gas hold up (Figure 6.26) under analogous conditions. Results for other agitation factor levels are provided in Figures A.5a and A.6b in Appendix A, Section A.3.



(a) Constant low (-1) agitation rate



(b) Constant mid (0) agitation rate



(c) Constant high (+1) agitation rate

Figure 6.24: Interfacial area with changes in alkane concentration and yeast loading at constant agitation rates



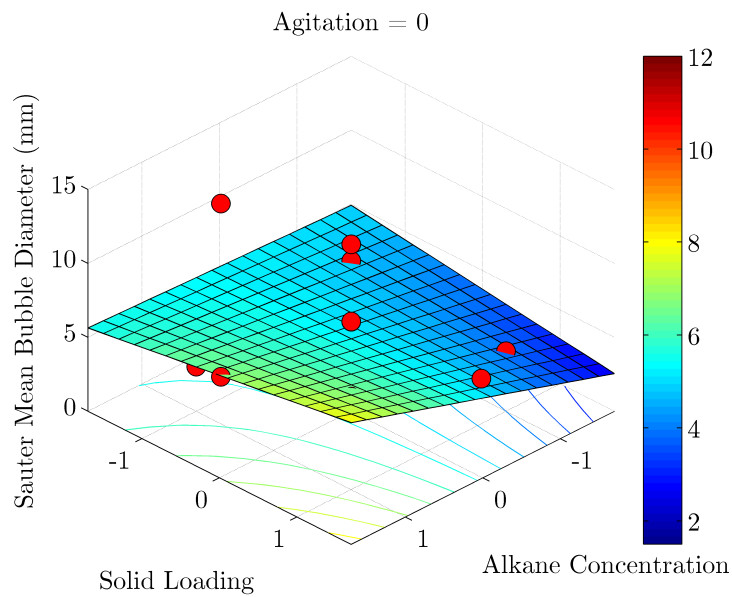


Figure 6.25:  $D_{SM}$  with changes in alkane concentration and yeast loading at constant midpoint (0) agitation rate

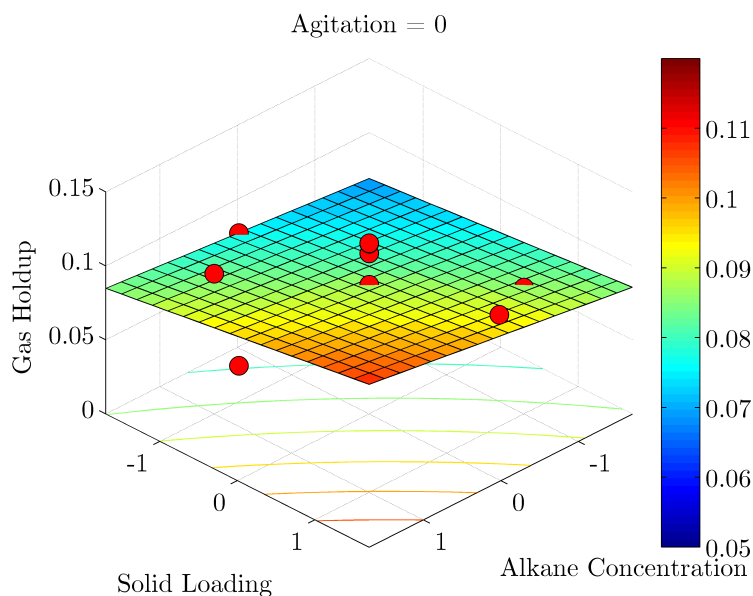


Figure 6.26: Gas hold up with changes in alkane concentration and yeast loading at constant midpoint (0) agitation rate

The maximum interfacial area occurs under conditions of high yeast loading and low alkane concentration, irrespective of the agitation. It is likely that the adhesion of the yeast particles to the gas-liquid interface is preventing coalescence, resulting in the lower  $D_{SM}$  observed in this region. However, this effect is over ridden through increases in the alkane concentration which increases the fluid viscosity, resulting in increased coalescence, damped turbulence and longer

bubble formation time at the gas sparger. Gas hold up again does not play a defining roll, with minimal change observed with changes in alkane concentration and yeast loading. The decrease in interfacial area with an increase in alkane concentration is analogous to that observed in Figure 6.14b, and is attributed to an increase in  $D_{SM}$  driven by the increased viscosity. From these results, it therefore follows that the changes in interfacial area are underpinned by the variation in  $D_{SM}$ .

Given that the peak  $K_L a$  is observed at the lowest yeast loading and the midpoint alkane concentration (Figure 6.24b), a trend which is not replicated in the interfacial area, it follows that this is the region where  $K_L$  becomes a defining factor of in the oxygen transfer. Figure 6.27 supports this, and shows a peak in  $K_L$  with an increase in alkane concentration. The beading nature of the alkane (spreading coefficient  $< 0$ ) means that the gas-liquid interface is populated with alkane droplets. The droplets have momentum as they come into contact with the gas bubble, and the contact between the two gives rise to interfacial turbulence, which is known to enhance  $K_L$  (Clarke *et al.*, 2006).

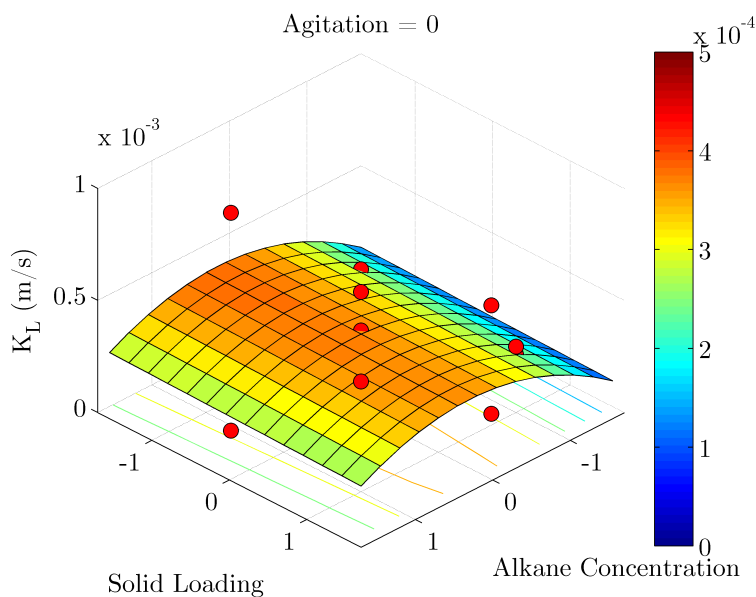


Figure 6.27:  $K_L$  with changes in alkane concentration and yeast loading at constant midpoint (0) agitation rate

Further alkane addition beyond this results in a decline in both  $K_L$  and  $K_L a$  caused by the dominant role the fluid viscosity plays in this region. As previously discussed, viscosity has a negative impact on the rate of diffusion. This is also combined with the steady decrease in interfacial area caused by the addition of alkane. This supports the theory that the effect of viscosity becomes dominant at higher alkane concentrations.

Regardless of the impact of the alkane concentration, any increase in the yeast loading results

directly in a drop in the  $K_La$  (Figure 6.12b). This trend is also not evident when comparing these results with the interfacial area (Figure 6.24b), suggesting that two factors are at play: firstly, yeast are depressing  $K_La$  by negatively acting on  $K_L$ , and secondly, while there may be an overall increase in the interfacial area, the adhesion of yeast particles to the gas-liquid interface means that not all of it is available for mass transfer caused by the yeast particles have a physical blocking effect (Chisti and Moo-Young, 1988). Both of these factors are difficult to provide empirical evidence for, as both concepts exist only as theoretical entities. These findings confirm the hypothesised negative influence of yeast particles on  $K_La$ .

# Chapter 7

## Conclusion

$K_La$  behaviour is well documented in aqueous systems, and recent research has been directed towards  $K_La$  behaviour in hydrocarbon-aqueous systems. Building on a knowledge base of  $K_La$  behaviour in aerated hydrocarbon-aqueous dispersion, this study set out to provide a new understanding of oxygen transfer in hydrocarbon-based systems containing solids, a system which more closely models and aerated hydrocarbon bioprocess. Particular attention was paid to aligning the operational parameters (agitation, alkane concentration and yeast loading) with a typical operational bioprocess. To this end, the solids used throughout were non-viable yeast solids with particle size and density typical of micro-organisms used in bioprocesses. The effects of the operating parameters on  $K_La$  and interfacial area behaviour were established and explained in terms of the hydrodynamic and physiochemical properties imparted by the system conditions. Independent quantification of  $K_L$  and interfacial area allowed for examination of the relative influence of  $K_L$  and interfacial area on  $K_La$  for each set of operating parameters. This represents a step forward in defining oxygen transfer behaviour in hydrocarbon-based bioprocesses, with application in the efficient and economical operation of bioprocesses on an industrial scale.

Underpinning the results of this study was the successful incorporation of the DO probe response, and implementation of a second order probe response model, making the results comparable to those obtained using the PSP. The photography and image recognition system allowed for recording of the interfacial area, and along with the physical solution implemented to eliminate optical distortion and the bespoke reactor internal lighting system, was found to offer repeatable results across multiple runs. In addition, the potential value modern high speed image analysis brings to the field has been demonstrated. As a tool, it was shown to be effective at quantifying interfacial area, establishing an ideal platform for future research into the interfacial area behaviour.

The results presented how variation of the operating parameters impacted firstly on  $K_La$ , and

secondly how interfacial area and  $K_L$  impacted independently on  $K_La$ . As predicted by hypothesis 2, part 1, increased agitation was found to enhance  $K_La$  for all alkane concentrations, underpinned by a combined increase in both the  $K_L$  and interfacial area. The increased area was a direct result of a decrease in  $D_{SM}$  due to promotion of bubble break-up with the intensified turbulence. An enhancement of  $K_L$  resulted from an increased rate of diffusion under the same conditions.

An increase in the alkane concentration resulted in a peak in  $K_La$  at the midpoint alkane concentration with a concomitant steady decrease in interfacial area, with both findings proving hypotheses 1 and 2, parts 2 respectively. The decline in interfacial area was due to increased viscosity driving increased coalescence (and a resultantly larger  $D_{SM}$ ). The differing trends in interfacial area and  $K_La$  suggest that low alkane concentrations positively influence  $K_L$ . It is proposed that the alkane droplets enhanced interfacial turbulence through droplets colliding with the bubble surface, reducing the transfer resistance. This effect was minimised at higher concentrations, where the negative influence of viscosity on resistance becomes dominant and reverses the positive trend in  $K_L$  and consequently, in  $K_La$ .

The effect of yeast solids on  $K_La$  and interfacial area was found to be dependent on the agitation rate. At low agitation rates, any increase in yeast loading resulted in an improved  $K_La$ . The opposite was true at high agitation rates where increased loadings caused  $K_La$  to decline, partially proving hypothesis 2, part 3. Interfacial area was shown to follow analogous trends, indicative of its dominant role in defining  $K_La$  under these conditions, again partially proving hypothesis 3, part 3. Increased yeast loading sharply decreased interfacial area at the high agitation rate. The decrease in interfacial area with increasing yeast loading was damped with decreasing agitation until, at the lowest agitation, increased yeast loading was observed to slightly increase interfacial area. A decrease in area was a likely result of corresponding increases in coalescence and  $D_{SM}$  with a rise in viscosity. However, yeast particles adhering to the bubble surface can also prevent coalescence, with a consequent decrease in  $D_{SM}$  and increase in area. The latter mechanism is postulated to become increasingly significant as agitation is lowered since at the lower agitation, the thicker boundary layer around the bubble surface is likely better able to enable bubble adherence. These similar trends in area and  $K_La$  suggest that the  $K_La$  behaviour is driven by changes in area under these conditions.

Increased yeast loading was also observed to depress the  $K_La$  for all alkane concentrations and medium and high agitation levels. Concomitantly, under the same conditions increased yeast loading caused a decrease in interfacial area for all alkane concentrations. These results were reversed under low agitation conditions, where an increase in yeast loading increased the interfacial area for all alkane concentrations, and a peak in  $K_La$  at the midpoint yeast loading. The decreased area at medium and high agitation is caused by the increased viscosity, promoting coalescence and increasing  $D_{SM}$  caused by the yeast particles. The positive influence of yeast

particles on interfacial area at the low agitation level could potentially be caused by entrapment of the solid particles in the liquid-side stagnant fluid film at the gas-liquid interface preventing coalescence, and decreasing  $D_{SM}$ . Increased levels of agitation thin the fluid film, meaning the solid particles enter the bulk fluid dispersion, and increase the fluid viscosity. The agreement between the trends in  $K_La$  and area with increasing solids for all agitation levels suggests that interfacial area underpins  $K_La$  behaviour in this regime.

Concurrent analysis of the  $K_La$  and interfacial area results have allowed for determination of the dominant factor responsible for defining  $K_La$  in hydrocarbon-based bioprocesses. It has been shown that agitation and yeast loading impact on  $K_La$  through changes in interfacial area, while the alkane concentration provides an optimum  $K_La$  by simultaneously positively influencing  $K_L$  and depressing interfacial area. In addition, while agitation defines the direction of the contribution yeast loading has on  $K_La$  and interfacial area, the trends in  $K_La$  and interfacial area remain congruent, indicative of the defining role yeast loading has on interfacial area for all levels of agitation.

This knowledge contributes to a fundamental understanding of the factors that impact on  $K_La$ , both quantitatively and qualitatively, in a model hydrocarbon-based bioprocess. The shifting dominance between  $K_L$  and interfacial area under different operating conditions underlines the complex nature of these systems. This has far-reaching application in the scale-up and operation of industrial processes, and provides the necessary knowledge to ensure these systems are kinetically, rather than transport, limited.

# Chapter 8

## Recommendations

### 8.1 Contributions Resulting from this Project

The findings of this project have presented unique insight into the fundamental behaviour of oxygen transfer in hydrocarbon-based bioprocesses in an STR through quantification of both  $K_La$  and interfacial area. A major contribution of this study was the extension of current knowledge of  $K_La$  behaviour in alkane-aqueous dispersions (Correia *et al.*, 2010) to  $K_La$  behaviour in a model hydrocarbon-based bioprocess comprising alkane-aqueous dispersions with suspended yeast solids. While the impact of solids on oxygen transfer has been documented in literature (Joosten *et al.*, 1977; Alper *et al.*, 1980; Ozkan *et al.*, 2000; Derksen *et al.*, 2000; Oguz *et al.*, 1987; Littlejohns and Daugulis, 2007; Schumpe and Deckwer, 1987; Sada *et al.*, 1986), these were not a type or concentration representative of a hydrocarbon bioprocess. Consequently, the findings offer a novel viewpoint on oxygen transfer in a hydrocarbon-based bioprocess and define the dominant factors that underpin  $K_La$  behaviour in these systems under a range of agitation rates, alkane concentrations and yeast loadings. This new knowledge represents a significant step forward in understanding oxygen transfer in hydrocarbon-based bioprocesses and makes a valuable contribution towards optimisation and scale-up of commercial bioprocesses. These results are currently being compiled into a manuscript intended for journal submission.

A further contribution of this study was the critical analysis of the existing literature on the  $K_La$  and the parameters which define its behaviour in hydrocarbon-based bioprocesses. A review is currently being compiled which is primarily aimed at deriving new knowledge via comparison, classification and analysis of the existing understanding of oxygen transfer in these systems.

### 8.2 Proposal for PhD

The focus of the extension of this research is two fold. Firstly, it will present a direct comparison of oxygen transfer and interfacial area in STR and bubble columns in model hydrocarbon-based

systems. This will serve as an extension of the work completed in an STR, with special focus being applied to operating the bioreactors under comparable conditions.

The second focus point will be on improvement of the interfacial area analysis system, which will be addressed in three ways: analysis of the response of the system to light sources outside of the visible range, improvement of the current imaging hardware (camera, lenses and wavelength-specific filters) and refinement of the image analysis computational methodology.

The results of this work will have application in the design of all hydrocarbon-based bioprocesses irrespective of the specific hydrocarbon substrate, as well as scale up from lab to industrial scale, ensuring that the bioprocesses not become oxygen limited.

### 8.2.1 Objectives of the PhD Study

Specific objectives of the extension of this study include:

- Investigation into  $K_{La}$  and interfacial area in bubble columns for comparison with STRs under parallel operating conditions. Bubble columns are documented to offer several advantages over STRs, such as high heat and mass transfer rates due to efficient contact between the phases, and a very small physical footprint (Akita and Yoshida, 1974; Quicker *et al.*, 1984; Vandu *et al.*, 2004; Behkish *et al.*, 2002; Kantarci *et al.*, 2005; Bouaifi *et al.*, 2001). These factors are combined with low initial, operating and maintenance costs due to the complete lack of moving parts, make bubble columns ideal for industrial implementation. It is therefore recommended that the current STR results are benchmarked against what is achievable in a bubble column.
- Quantification of power input into the system (rather than agitation rate) to describe bulk fluid turbulence. Power input and agitation need not be directly correlated depending on the efficiency of the agitators (Ascanio *et al.*, 2004). This will make the experimental configurations more comparable system with different dimensions, as well as different reactor types (such as bubble columns).
- Inclusion of the impact of alkane concentration and yeast loading on viscosity, surface tension, density and diffusivity of the bulk fluid. This would allow for analysis of  $K_{La}$  and area as a function of the relative influence the physiochemical properties of the fluid.
- Improvement of image clarity in opaque multiphase systems through selection of a light source with an optimised wavelength, combined with tuned filters on the camera. This will reduce anomalies generated by ambient light, and aid reproducibility across multiple experimental runs.
- Investigation into macro photography to examine the interactions between yeast particles and alkane droplets at the bubble surface. A number of findings in this study were



explained by the behaviour of the yeast particles and alkane droplets at the bubble surface, and while beading behaviour was observed, macro images would provide additional justification of the  $K_La$  and area behaviour.

- Initiation of the use of computational fluid dynamics (CFD) for benchmarking empirical results. Development of a robust CFD simulation tool for both STR and bubble column based bioprocesses has potential for method validation (comparison with what is achieved empirically) and scale up simulations (valuable for industrial applications). Development of accurate computational models would stimulate investigation into oxygen transfer correlations.
- Increasing the resolution of the experimental design to more accurately understand the impact of process parameters. This is especially applicable to alkane concentration (below 10%) and yeast loading (below 5 g/l).
- Investigation into  $K_La$  and interfacial area in model bioprocesses using yeast solids with a variable size distribution, while retaining the remainder of their physical properties. This would allow for examination of particle-bubble adhesion and the role of particle size and interaction with the stagnant fluid layer at the gas-liquid interface.

## 8.2.2 Additional Contributions

It is envisaged that the proposed work will advance understanding of oxygen transfer in both STRs and bubble columns. The use of both reactor types will allow for characterisation of the oxygen transfer regimes and the factors that underpin  $K_La$  under a variety of operating conditions. Factors that will be investigated in terms of their contribution toward underpinning the  $K_La$  behaviour include the interfacial area, bubble diameter and size distribution, and the physiochemical properties of the bulk liquid. Furthermore, the focus placed on the refinement of the image analysis and interfacial area quantification will result in the will irrefutably define the dependence of  $K_La$  on both  $K_L$  and interfacial area.

In addition to the paper detailing the results of this study, two further publications are envisaged. The first is a review paper based on the literature presented in this work. The current available literature is presented and analysed in light of the methodologies used to determine  $K_La$ , the systems in which  $K_La$  is studied and the potential pathways available for oxygen transfer in those systems. The second paper augments the rigorous analysis of oxygen transfer in simulated hydrocarbon-based bioprocesses in STRs through inclusion of bubble columns operate under comparable condition. This will inform on the optimal conditions for operation of both reactor type, as well as provide further insight into to driving forces behind the oxygen transfer in these systems.

### 8.3 Proposed Timeline

The timeline for the proposed extension is supplied in Table 8.1.

Table 8.1: Proposed timeline for completion of PhD

Year	Months	Actions
2015	January - September	Literature study on oxygen transfer in STR and bubble column bioreactors, completion of review paper
	January - March	Literature study on high speed photography and image analysis
	February - March	Design of high speed photography system and image analysis software
	March	Testing and characterisation of image analysis system
	April	Design of high speed photography system and image analysis software
	April - May	Benchmark factor levels completed in MEng study in bubble column (measurement of $K_La$ and interfacial area) according to experimental design
	June - October	Additional new experiments in both the STR and bubble column according to experimental design
	September - February	Data extraction and analysis
2016	January - June	Compilation of results, completion of project documentation and thesis, write up, completion of results paper for publication

# References

- Aiba, S. and Huang, S. (1969 July). Oxygen permeability and diffusivity in polymer membranes immersed in liquids. *Chemical Engineering Science*, vol. 24, no. 7, pp. 1149–1159.
- Akita, K. and Yoshida, F. (1974). Bubble size, interfacial area, and liquid-phase mass transfer coefficient in bubble columns. *Industrial & Engineering Chemistry Process Design and Development*, vol. 13, no. 1, pp. 84–91.
- Albal, R., Schumpe, A., Shah, Y. and Carr, N. (1983). Mass Transfer in Multiphase Agitated Contactors. *The Chemical Engineering Journal*, vol. 27, pp. 61–80.
- Alper, E., Wichtendahl, B. and Deckwer, W.D. (1980). Gas absorption mechanism in catalytic slurry reactors. *Chemical Engineering Science*, vol. 35, no. 1-2, pp. 217–222.
- Alves, S.S., Maia, C. and Vasconcelos, J. (2004 July). Gas-liquid mass transfer coefficient in stirred tanks interpreted through bubble contamination kinetics. *Chemical Engineering and Processing*, vol. 43, no. 7, pp. 823–830.
- Amaral, P., Freire, M., Rocha-Leão, M., Marrucho, I., Coutinho, J. and Coelho, M. (2008). Optimization of oxygen mass transfer in a multiphase bioreactor with perfluorodecalin as a second liquid phase. *Biotechnology and bioengineering*, vol. 99, no. 3, pp. 588–598.
- Arjunwadkar, S.J., Sarvanan, K., Kulkarni, P.R. and Pandit, A.B. (1998 October). Gas-liquid mass transfer in dual impeller bioreactor. *Biochemical Engineering Journal*, vol. 1, pp. 99–106.
- Ascanio, G., Castro, B. and Galindo, E. (2004). Measurement of power consumption in stirred vessels - a review. *Chemical Engineering Research and . . .*, vol. 82, no. September, pp. 1282–1290.
- Bailey, M., Gomez, C. and Finch, J. (2005 October). Development and application of an image analysis method for wide bubble size distributions. *Minerals Engineering*, vol. 18, no. 12, pp. 1214–1221.
- Barigou, M. and Greaves, M. (1992). Bubble-size distributions in a mechanically agitated gas-liquid contactor. *Chemical engineering science*, vol. 47, no. 8, pp. 2009–2025.
- Barigou, M. and Greaves, M. (1996). Gas holdup and interfacial area distributions in a mechanically agitated gas-liquid contactor. *Chemical engineering research & design*, vol. 74, no. 3, pp. 397–405.

- Beenackers, A. and Van Swaaij, W.P.M. (1993). Mass transfer in gas-liquid slurry reactors. *Chemical engineering science*, vol. 48, no. 18, pp. 3109–3139.
- Behkish, A., Men, Z., Inga, J.R. and Morsi, B.I. (2002 August). Mass transfer characteristics in a large-scale slurry bubble column reactor with organic liquid mixtures. *Chemical Engineering Science*, vol. 57, no. 16, pp. 3307–3324.
- Benedek, A. and Heideger, W. (1970). Polarographic oxygen analyzer response: The effect of instrument lag in the non-steady state reaeration test. *Water Research*, vol. 4, no. 9, pp. 627–640.
- Bi, Y., Hill, G.A. and Sumner, R.J. (2001). Enhancement of the Overall Volumetric Oxygen Transfer Coefficient in a Stirred Tank Bioreactor Using Ethanol. *The Canadian Journal of Chemical Engineering*, vol. 79, no. June, pp. 463–467.
- Blanc, C. and Batiste, M. (1970). Solubility coefficient of oxygen in paraffins. *Bulletin du Centre de Recherches de Pau*, vol. 4, no. 1, pp. 235–241.
- Bonn, D., Eggers, J., Indekeu, J., Meunier, J. and Rolley, E. (2009 May). Wetting and spreading. *Reviews of Modern Physics*, vol. 81, no. 2, pp. 739–805.
- Bossier III, J., Farritor, R., Hughmark, G. and Kao, J. (1973). Gas-liquid interfacial area determination for a turbine agitated reactor. *AIChE Journal*, vol. 19, no. 5, pp. 1065–1067.
- Bouaifi, M., Hebrard, G., Bastoul, D. and Roustan, M. (2001). A comparative study of gas hold-up, bubble size, interfacial area and mass transfer coefficients in stirred gas-liquid reactors and bubble columns. *Chemical Engineering and Processing*, vol. 40, pp. 97–111.
- Boulton, C.A. and Ratledge, C. (1984). The physiology of hydrocarbon-utilizing organisms. *Topics in Enzyme and Fermentation Biotechnology*, vol. 19, pp. 11–77.
- Calderbank, P. (1958). Physical rate processes in industrial fermentation Part I: The interfacial area in gas-liquid contacting with mechanical agitation. *Chemical Engineering Research and Design*, vol. 36, no. a, pp. 443–463.
- Calderbank, P. and Moo-Young, M. (1961). The continuous phase heat and mass-transfer properties of dispersions. *Chemical Engineering Science*.
- Cascaval, D., a. I. Galaction, Folescu, E., Turnea, M. and Galaction, A.-I. (2006 August). Comparative study on the effects of n-dodecane addition on oxygen transfer in stirred bioreactors for simulated, bacterial and yeasts broths. *Biochemical Engineering Journal*, vol. 31, no. 1, pp. 56–66.
- Chisti, M. and Moo-Young, M. (1988). Hydrodynamics and oxygen transfer in pneumatic bioreactor devices. *Biotechnology and bioengineering*, vol. 31, pp. 487–494.
- Clarke, K. and Manyuchi, M. (2012). Methodology for advanced measurement accuracy of the overall volumetric oxygen transfer coefficient with application to hydrocarbon-aqueous dispersions [IN PRESS]. *Journal of Chemical Technology & Biotechnology*.

- Clarke, K.G. and Correia, L.D.C. (2008 May). Oxygen transfer in hydrocarbon-aqueous dispersions and its applicability to alkane bioprocesses: A review. *Biochemical Engineering Journal*, vol. 39, no. 3, pp. 405–429.
- Clarke, K.G., Williams, P., Smit, M. and Harrison, S. (2006 March). Enhancement and repression of the volumetric oxygen transfer coefficient through hydrocarbon addition and its influence on oxygen transfer rate in stirred tank bioreactors. *Biochemical Engineering Journal*, vol. 28, no. 3, pp. 237–242.
- Correia, L. and Clarke, K. (2009 December). Measurement of the overall volumetric oxygen transfer coefficient in alkane-aqueous dispersions. *Journal of Chemical Technology & Biotechnology*, vol. 84, no. 12, pp. 1793–1797.
- Correia, L.D.C. (2007). *Oxygen transfer in hydrocarbon-aqueous dispersions and its applicability to alkane-based bioprocesses*. Ph.D. thesis, University of Stellenbosch.
- Correia, L.D.C., Aldrich, C. and Clarke, K.G. (2010). Interfacial gas - liquid transfer area in alkane - aqueous dispersions and its impact on the overall volumetric oxygen transfer coefficient. *Biochemical Engineering Journal*, vol. 49, no. 1, pp. 133–137.
- Cussler, E. (2000). Forced Convection. In: *Diffusion: Mass Transfer in Fluid Systems*, 2nd edn, pp. 334–340. Cambridge University Press, Cambridge.
- da Silva, T., Calado, V., Silva, N., Mendes, R., Alves, S., Vaconcelos, J. and Reis, A. (2006). Effects of hydrocarbon additions on gas-liquid mass transfer coefficients in biphasic bioreactors. *Biotechnology and Bioengineering*, vol. 11, pp. 245–250.
- Danckwerts, P. (1951). Significance of liquid-film coefficients in gas absorption. *Industrial & Engineering Chemistry*, vol. 43, no. 6, pp. 1460–1467.
- Dang, N.D.P., Karrer, D.A. and Dunn, I.J. (1977). Oxygen transfer coefficients by dynamic model moment analysis. *Biotechnology and Bioengineering*, vol. 19, no. 6, pp. 853–865.
- Darlington, W.A. (1964). Aerobic hydrocarbon fermentation-a practical evaluation. *Biotechnology and Bioengineering*, vol. 6, no. 2, pp. 241–242.
- Das, T., Bandopadhyay, A., Parthasarathy, R. and Kumar, R. (1985 January). Gas-liquid interfacial area in stirred vessels: The effect of an immiscible liquid phase. *Chemical engineering*, vol. 40, no. 2, pp. 209–214.
- der Meer, A.V. and Beenackers, A. (1992). Gas/liquid mass transfer in a four-phase stirred fermentor: effects of organic phase hold-up and surfactant concentration. *Chemical engineering ...*, vol. 47, no. 9.
- Derksen, J.J., Buist, K., Van Weerv, G. and Reuters, M.A. (2000). Oxygen transfer in agitated silica and pyrite slurries. *Minerals engineering*, vol. 13, no. 1, pp. 25–36.
- Dhanasekaran, S. and Karunanithi, T. (2012 February). Improved gas holdup in novel bubble column.

- The Canadian Journal of Chemical Engineering*, vol. 90, no. 1, pp. 126–136. ISSN 00084034.  
Available at: <http://doi.wiley.com/10.1002/cjce.20509>
- Doran, P. (1995). *Bioprocess engineering principles*. Elsevier Ltd. ISBN 978-0-12-220855-3.
- Duetz, W.a., Rüedi, L., Hermann, R., O'Connor, K., Büchs, J. and Witholt, B. (2000 June). Methods for intense aeration, growth, storage, and replication of bacterial strains in microtiter plates. *Applied and environmental microbiology*, vol. 66, no. 6, pp. 2641–6.
- Dumont, E., Andrès, Y. and Le Cloirec, P. (2006 June). Effect of organic solvents on oxygen mass transfer in multiphase systems: Application to bioreactors in environmental protection. *Biochemical Engineering Journal*, vol. 30, no. 3, pp. 245–252.
- Dumont, E. and Delmas, H. (2003 June). Mass transfer enhancement of gas absorption in oil-in-water systems: a review. *Chemical engineering and processing*, vol. 42, no. 6, pp. 419–438.
- Einsele, A., Fiechter, A. and Knöpfel, H. (1972 January). Respiratory activity of *Candida tropicalis* during growth on hexadecane and on glucose. *Archiv für Mikrobiologie*, vol. 82, pp. 247–253.
- Freitas, C. and Teixeira, J.a. (2001 September). Oxygen mass transfer in a high solids loading three-phase internal-loop airlift reactor. *Chemical Engineering Journal*, vol. 84, no. 1, pp. 57–61.
- Froessling, N. (1938). Über die verdunstung fallender tropfen. *Gerlands Beiträge zur Geophysik*, vol. 52, pp. 170–215.
- Fuchs, R., Ryu, D.D.Y. and Humphrey, A.E. (1971). Effect of surface aeration on scale-up procedures for fermentation processes. *Industrial & Engineering Chemistry Process Design and Development*, vol. 10, no. 2, pp. 190–196.
- Fujasova, M., Linek, V. and Moucha, T. (2007 March). Mass transfer correlations for multiple-impeller gas-liquid contactors. Analysis of the effect of axial dispersion in gas and liquid phases on local  $k_L a$  values measured by the dynamic pressure method in individual stages of the vessel. *Chemical Engineering Science*, vol. 62, no. 6, pp. 1650–1669.
- Fukui, S. and Tanaka, A. (1980). *Production of useful compounds from alkane media in Japan*.
- Galaction, a., Cascaval, D., Oniscu, C. and Turnea, M. (2004 August). Prediction of oxygen mass transfer coefficients in stirred bioreactors for bacteria, yeasts and fungus broths. *Biochemical Engineering Journal*, vol. 20, no. 1, pp. 85–94.
- Galaction, A.-I., Cascaval, D., Oniscu, C. and Turnea, M. (2004 July). Enhancement of oxygen mass transfer in stirred bioreactors using oxygen-vectors. 1. Simulated fermentation broths. *Bioprocess and biosystems engineering*, vol. 26, no. 4, pp. 231–238.
- Galindo, E., Larralde-Corona, C.P., Brito, T., Córdova-Aguilar, M.S., Taboada, B., Vega-Alvarado, L. and Corkidi, G. (2005 March). Development of advanced image analysis techniques for the in situ

- characterization of multiphase dispersions occurring in bioreactors. *Journal of biotechnology*, vol. 116, no. 3, pp. 261–70.
- Galindo, E., Pacek, A.W. and Nienow, A.W. (2000 July). Study of drop and bubble sizes in a simulated mycelial fermentation broth of up to four phases. *Biotechnology and bioengineering*, vol. 69, no. 2, pp. 213–21.
- Garcia-Ochoa, F. and Gomez, E. (2005 December). Prediction of gas-liquid mass transfer coefficient in sparged stirred tank bioreactors. *Biotechnology and bioengineering*, vol. 92, no. 6, pp. 761–72.
- Garcia-Ochoa, F. and Gomez, E. (2009). Bioreactor scale-up and oxygen transfer rate in microbial processes: an overview. *Biotechnology advances*, vol. 27, no. 2, pp. 153–76.
- Godbole, S., Schumpe, A. and Shah, Y. (1990). The effect of solid wettability on gas-liquid mass transfer in a slurry bubble column. *Chemical engineering science*, vol. 45, no. 12, pp. 3593–3595.
- Godbole, S.P., Schumpe, A., Shah, Y.T. and Carr, N.L. (1984). Hydrodynamics and mass transfer in non-Newtonian solutions in a bubble column. *AIChE Journal*, vol. 30, no. 2, pp. 213–220.
- Gogate, P., Beenackers, A. and Pandit, A. (2000 October). Multiple-impeller systems with a special emphasis on bioreactors: a critical review. *Biochemical engineering journal*, vol. 6, no. 2, pp. 109–144.
- Gollakota, S.V. and Guin, J.A. (1984). Comparative study of gas-liquid mass transfer coefficients in stirred autoclaves, tubing bomb microreactors, and bubble columns. *Industrial & Engineering Chemistry Process Design and Development*, vol. 23, no. 1, pp. 52–59.
- Golubev, I.F. and Petrov, V.A. (1959). Viscosity of gases and gaseous mixtures. *Fizmatgiz, Moscow*, vol. 8.
- Gourich, B., Vial, C., El Azher, N., Belhaj Soulami, M. and Ziyad, M. (2008 April). Influence of hydrodynamics and probe response on oxygen mass transfer measurements in a high aspect ratio bubble column reactor: Effect of the coalescence behaviour of the liquid phase. *Biochemical Engineering Journal*, vol. 39, no. 1, pp. 1–14.
- Hassan, I.T.M. and Robinson, C.W. (1977). Oxygen transfer in mechanically agitated aqueous systems containing dispersed hydrocarbon. *Biotechnology and Bioengineering*, vol. 19, no. 5, pp. 661–682.
- Hesse, P. and Battino, R. (1996). Solubility of Gases in Liquids. 20. Solubility of He, Ne, Ar, Kr, N<sub>2</sub>, O<sub>2</sub>, CH<sub>4</sub>, CF<sub>4</sub>, and SF<sub>6</sub> in n-Alkanes nC<sub>1</sub>H<sub>2</sub>1+ 2 (61 16) at 298.15 K. *Journal of Chemical & ...*, vol. 2, pp. 195–201.
- Higbie, R. (1935). The rate of absorption of a pure gas into still liquid during short periods of exposure. *AIChE*, vol. 31, no. 2, p. 365.
- Hines, A. and Maddox, R. (1985). *Mass Transfer Fundamentals and Applications*. Prentice-Hall. ISBN 0-13-559609-2.

- Ho, C.S., Ju, L.-K. and Baddour, R.F. (1990). Enhancing penicillin fermentations by increased oxygen solubility through the addition of n-hexadecane. *Biotechnology and Bioengineering*, vol. 36, no. 11, pp. 1110–1118.
- Holstvoogd, R.D., van Swaaij, W.P.M. and van Dierendonck, L.L. (1988). The absorption of gases in aqueous activated carbon slurries enhanced by adsorbing or catalytic particles. *Chemical Engineering Science*, vol. 43, no. 8, pp. 2181–2187.
- Humphrey, A. (1967). A critical review of hydrocarbon fermentations and their industrial utilization. *Biotechnology and Bioengineering*, vol. 9, pp. 3–24.
- Jia, S., Li, P., Park, Y.S. and Okabe, M. (1996 January). Enhanced oxygen transfer in tower bioreactor on addition of liquid hydrocarbons. *Journal of fermentation and bioengineering*, vol. 82, no. 2, pp. 191–193.
- Joosten, G.E.H., Schilder, J.G.M. and Janssen, J.J. (1977). The influence of suspended solid material on the gas liquid mass transfer in stirred gas liquid contactors. *Chemical Engineering Science*, vol. 32, pp. 563–566.
- Ju, L. and Ho, C. (1989 November). Oxygen diffusion coefficient and solubility in n-hexadecane. *Biotechnology and bioengineering*, vol. 34, no. 9, pp. 1221–4.
- Kantarci, N., Borak, F. and Ulgen, K.O. (2005 June). Bubble column reactors. *Process Biochemistry*, vol. 40, no. 7, pp. 2263–2283.
- Kawase, Y. and Hashimoto, N. (1996). Gas hold-up and oxygen Transfer in Three-Phase External-Loop Airlift Bioreactors: Non-Newtonian Fermentation Broths. *Journal of Chemical Technology & Biotechnology*, pp. 325–334.
- Kluytmans, J., van Wachem, B., Kuster, B. and Schouten, J. (2003 October). Mass transfer in sparged and stirred reactors: influence of carbon particles and electrolyte. *Chemical Engineering Science*, vol. 58, no. 20, pp. 4719–4728.
- Koide, K., Hayashi, T. and Sumino, K. (1976). Mass transfer from single bubbles in aqueous solutions of surfactants. *Chemical Engineering*, vol. 31, pp. 963–967.
- Kundu, A., Dumont, E., Duquenne, A.-M. and Delmas, H. (2003). Mass Transfer Characteristics in Gas-Liquid-Liquid System. *The Canadian Journal . . .*, vol. 81, no. August, pp. 640–646.
- Lewis, W. and Whitman, W. (1924). Principles of Gas Absorption. *Industrial & Engineering Chemistry*, vol. 16, no. 12, p. 1215–1220.
- Lide, D.R. (2004). *CRC Handbook of Chemistry and Physics 2004-2005: A Ready-Reference Book of Chemical and Physical Data*. CRC press.
- Linek, V., Vacek, V. and Benes, P. (1987). A critical review and experimental verification of the correct use of the dynamic method for the determination of oxygen transfer in aerated agitated vessels to



- water, electrolyte solutions and viscous liquids. *The Chemical Engineering Journal*, vol. 34, no. 1, pp. 11–34.
- Littlejohns, J.V. and Daugulis, A.J. (2007 May). Oxygen transfer in a gas-liquid system containing solids of varying oxygen affinity. *Chemical Engineering Journal*, vol. 129, no. 1-3, pp. 67–74.
- Liu, H.-S., Chiung, W.-C. and Wang, Y.-C. (1994). Effect of lard oil, olive oil and castor oil on oxygen transfer in an agitated fermentor. *Biotechnology Techniques*, vol. 8, no. 1, pp. 17–20.
- Maia, C., Fonseca, M., Vasconcelos, J., Alves, S. and Mora, A. (1999). Effect of antifoam addition on gas-liquid mass transfer in stirred fermenters. *Bioprocess Engineering*, vol. 20, pp. 165–172.
- Makranczy, J., Megyery-Balog, K., Ruzs, L. and Patyi, L. (1976). Solubility of gases in normal-alkanes. *Hung. J. Ind. Chem*, vol. 4, no. 2, pp. 269–280.
- Manyuchi, M.M. (2010). *Measurement and behavior of the overall volumetric oxygen transfer coefficient in aerated agitated alkane based multiphase systems*. Ph.D. thesis, University of Stellenbosch.
- McMillan, J. and Wang, D. (1987). Enhanced Oxygen Transfer Using Oil-in-Water Dispersions. *Annals of the New York Academy of Sciences*, vol. 506, no. 1, pp. 569–582.
- Mehta, V. and Sharma, M. (1971). Mass transfer in mechanically agitated gas-liquid contactors. *Chemical Engineering Science*, vol. 26, no. 3, pp. 461–479.
- Meijers, J. (). University of Stellenbosch weather.  
Available at: [weather.sun.ac.za](http://weather.sun.ac.za)
- Mena, P., Pons, M., Teixeira, J. and Rocha, F. (2005 September). Using image analysis in the study of multiphase gas absorption. *Chemical Engineering Science*, vol. 60, no. 18, pp. 5144–5150.
- Merten, C., Eigenberger, G. and Sch, R. (2002). Bubble size distributions in a bubble column reactor under industrial conditions. *Experimental and Thermal Fluid Science*, vol. 26, pp. 595–604.
- Mills, D. and Bar, R. (1987). Effect of solids on oxygen transfer in agitated three-phase systems. *AIChE journal*, vol. 33, no. 9, pp. 1542–1549.
- Miyachi, M., Iguchi, A. and Uchida, S. (1981). Effect of solid particles in liquid phase on liquid side mass transfer coefficient. *The Canadian Journal of Chemical Engineering*, vol. 59, no. 5, pp. 640–641.
- Montes, F., Galan, M. and Cerro, R. (1999 July). Mass transfer from oscillating bubbles in bioreactors. *Chemical Engineering Science*, vol. 54, no. 15-16, pp. 3127–3136.
- Moo-Young, M. (1975). Microbial reactor design for synthetic protein production. *The Canadian Journal of Chemical Engineering*, vol. 53, no. 1, pp. 113–118.
- Moo-Young, M., Shimizu, T. and Whitworth, D.A. (1971). Hydrocarbon fermentations using *Candida lipolytica*. I: Basic growth parameters for batch and continuous culture conditions. *Biotechnology and ...*, vol. 13, no. 6, pp. 741–760.

- Moutafchieva, D., Popova, D. and Tchaoushev, S. (2013). Experimental Determination of the Volumetric Mass Transfer Coefficient. *Journal of Chemical Technology and Metallurgy*, vol. 48, no. 4, pp. 351–356.
- Neale, J.W. and Pinches, A. (1994). Determination of gas-liquid mass-transfer and solids-suspension parameters in mechanically-agitated three-phase slurry reactors. *Minerals Engineering*, vol. 7, no. 2-3, pp. 389–403.
- Nernst, W. (1904). Theory of reaction velocity in heterogenous systems. *Zeit. physikal. Chem*, vol. 47, pp. 52–55.
- Ngo, T.H. and Schumpe, A. (2012). Oxygen Absorption into Stirred Emulsions of n-Alkanes. *International Journal of Chemical Engineering*, vol. 2012, no. Table 1.
- Nielsen, D.R., Daugulis, A.J. and McLellan, P.J. (2003 September). A novel method of simulating oxygen mass transfer in two-phase partitioning bioreactors. *Biotechnology and bioengineering*, vol. 83, no. 6, pp. 735–742.
- Nielsen, D.R., Daugulis, A.J. and McLellan, P.J. (2005). A Restructured Framework for Modeling Oxygen Transfer in Two-Phase Partitioning Bioreactors. *Biotechnology and bioengineering*, vol. 91, no. 6, p. 2005.
- Nienow, A. (2004 May). Break-up, coalescence and catastrophic phase inversion in turbulent contactors. *Advances in colloid and interface science*, vol. 108-109, pp. 95–103.
- Nocentini, M., Fajner, D., Pasquali, G. and Magelli, F. (1993 January). Gas-liquid mass transfer and holdup in vessels stirred with multiple Rushton turbines: water and water-glycerol solutions. *Industrial & Engineering Chemistry Research*, vol. 32, no. 1, pp. 19–26.
- Novak, M. & Klekner, V. (1988). Comparison of various methods of KLa estimation in cultures of filamentous microorganisms. *Biotechnology Techniques*, vol. 2, pp. 243–248.
- O' Connor, C.T.O., Randall, E.W. and Goodall, C.M. (1990). Measurement of the Effects of Physical and Chemical Variables on Bubble Size. *International Journal of Mineral Processing*, vol. 28, pp. 139–149.
- Oguz, H., Brehm, A. and Deckwer, W. (1987). Gas-liquid mass transfer in sparged agitated slurries. *Chemical engineering science*, vol. 42, no. 7, pp. 1815–1822.
- Ozbek, B. and Gayik, S. (2001 March). The studies on the oxygen mass transfer coefficient in a bioreactor. *Process Biochemistry*, vol. 36, no. 8-9, pp. 729–741.
- Ozkan, O., Calimli, A., Berber, R. and Oguz, H. (2000). Effect of inert solid particles at low concentrations on gas-liquid mass transfer in mechanically agitated reactors. *Chemical engineering science*, vol. 55, no. 14, pp. 2737–2740.

- Ozturk, S.S. and Schumpe, A. (1987). The influence of suspended solids on oxygen transfer to organic liquids in a bubble column. *Chemical engineering science*, vol. 42, pp. 1781–1785.
- Pal, S., Sharma, M. and Juvekar, V. (1982). Fast reactions in slurry reactors: catalyst particle size smaller than film thickness: oxidation of aqueous sodium sulphide with activated carbon particles as catalyst at elevated temperatures. *Chemical engineering science*, vol. 37, no. 2, pp. 327–336.
- Perlmutter, D. (1961). Surface-renewal models in mass transfer. *Chemical Engineering Science*, vol. 16, pp. 287–296.
- Philichi, T.L. and Stenstrom, M.K. (2011). Effects of dissolved oxygen lag on oxygen transfer estimation probe parameter. *Water Environment Federation*, vol. 61, no. 1, pp. 83–86.
- Pinho, H.J.O. and Alves, S.a.S. (2010 August). Effect of Spreading Coefficient on Gas-Liquid Mass Transfer in Gas-Liquid-Liquid Dispersions in a Stirred Tank. *Chemical Engineering Communications*, vol. 197, no. 12, pp. 1515–1526.
- Queimada, A.J., Marrucho, I.M., Stenby, E.H. and Coutinho, J.A.P. (2003 August). Generalized Relation Between Surface Tension and Viscosity : a Study. *Building*, vol. 222-223, pp. 1–13.
- Quicker, G., Schumpe, A. and Deckwer, W. (1984). Gas-liquid interfacial areas in a bubble column with suspended solids. *Chemical Engineering Science*, vol. 39, no. 1, pp. 183–185.
- Rao, G., Bandyopadhyay, B. and Humphrey, A.E. (1967 December). Dynamic measurement of the volumetric oxygen transfer coefficient in fermentation systems. *Biotechnology and*, vol. 104, no. 5, pp. 841–853.
- Rhodes, M. (2008). *Introduction to Particle Technology*. 2nd edn. John Wiley and Sons.
- Riege, P., Blasig, R., Miiller, H.-G., Heidenreich, G. and Bauch, J. (1989). Influence of oxygen and substrate supply on the metabolism of *Candida maltosa* during cultivation on n-alkanes. *Applied Microbiology and Biotechnology*, vol. 32, pp. 101–107.
- Rols, J., Condoret, J. and Fonade, C. (1990). Mechanism of enhanced oxygen transfer in fermentation using emulsified oxygen vectors. *Biotechnology and Bioengineering*, vol. 35, pp. 427–435.
- Rols, J.L. and Goma, G. (1989 January). Enhancement of oxygen transfer rates in fermentation using oxygen-vectors. *Biotechnology advances*, vol. 7, no. 1, pp. 1–14.
- Ruchti, G., Dunn, I.J. and Bourne, J.R. (1981). Comparison of dynamic oxygen electrode methods for the measurement of KLa. *Biotechnology and Bioengineering*, vol. 23, no. 2, pp. 277–290.
- Ruthiya, K., van der Schaaf, J., Kuster, B. and Schouten, J. (2003 December). Mechanisms of physical and reaction enhancement of mass transfer in a gas inducing stirred slurry reactor. *Chemical Engineering Journal*, vol. 96, no. 1-3, pp. 55–69.
- Sada, E., Kumazawa, H. and Lee, C. (1986). Influences of Suspended Fine Particles on Gas Holup and

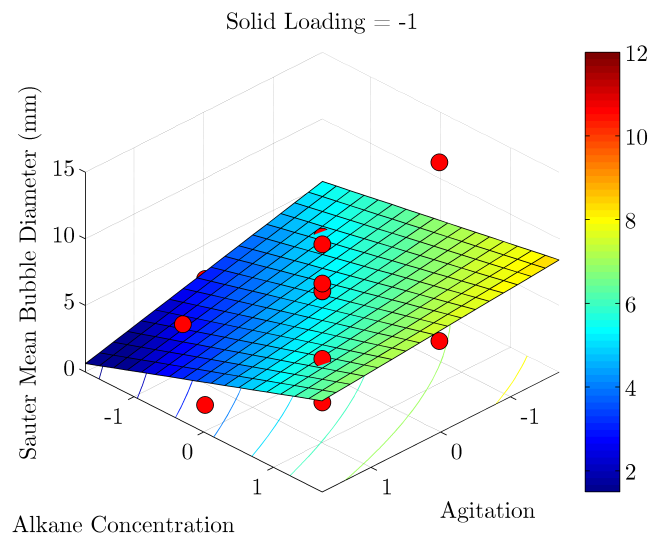
- Mass Transfer Characteristics in a Slurry Bubble Column. *American Institute of Chemical Engineers Journal*, vol. 32, no. 5, pp. 853–856.
- Sasol (2011). Gas To Liquid.
- Scargiali, F., Busciglio, A., Grisafi, F. and Brucato, A. (2010 April). Simplified dynamic pressure method for k<sub>L</sub>a measurement in aerated bioreactors. *Biochemical Engineering Journal*, vol. 49, no. 2, pp. 165–172.
- Schmid, A., Sonnleitner, B. and Witholt, B. (1998). Solvent-cell transfer rates in two-liquid phase, *Pseudomonas oleovorans* cultures. *October*, vol. 60, no. 1, pp. 10–23.
- Schugerl, K. (1981). Oxygen transfer into highly viscous media. In: *Reactors and Reactions*, vol. 19 of *Advances in Biochemical Engineering/Biotechnology*, pp. 71–174. Springer Berlin / Heidelberg. ISBN 978-3-540-10464-3.
- Schumpe, A. and Deckwer, W. (1987). Bioprocess Engineering Viscous media in tower bioreactors : Hydrodynamic characteristics and mass transfer properties. *Bioprocess Engineering*, vol. 2, pp. 79–94.
- Schumpe, A., Saxena, A. and Fang, L. (1987). Gas/liquid mass transfer in a slurry bubble column. *Chemical engineering science*, vol. 42, no. 7, pp. 1787–1796.
- Seader, J. and Henley, E. (2006). *Separation process principles*. 2nd edn. John Wiley and Sons, Hoboken.
- Shennan, J. and Levi, J.J. (1974). The growth of yeasts on hydrocarbons. *Progress in Industrial Microbiology*, vol. 13, pp. 1–57.
- Shuler, M. and Kargi, F. (2009). *Bioprocess Engineering: Basic Concepts*. 2nd edn. Prentice Hall. ISBN 0-13-081908-5.
- Smit, G., Straver, M.H., Lugtenberg, B.J. and Kijne, J.W. (1992 November). Flocculence of *Saccharomyces cerevisiae* cells is induced by nutrient limitation, with cell surface hydrophobicity as a major determinant. *Applied and environmental microbiology*, vol. 58, no. 11, pp. 3709–14.
- Soni, M. (2010). *The effect of solid micro particles on mass transfer in agitated dispersions*. Ph.D. thesis, University of KwaZulu-Natal.
- Tadmor, R. (2004 August). Line energy and the relation between advancing, receding, and young contact angles. *Langmuir : the ACS journal of surfaces and colloids*, vol. 20, no. 18, pp. 7659–64.
- The World Bank (2009). World Bank, GGFR Partners Unlock Value of Wasted Gas.
- Toledo, M. (2013). Operation Manual Transmitter pH M300. pp. 1–76.
- Torres-Martínez, D., Melgarejo-Torres, R., Gutiérrez-Rojas, M., Aguilera-Vázquez, L., Micheletti, M., Lye, G.J. and Huerta-Ochoa, S. (2009 August). Hydrodynamic and oxygen mass transfer studies in a

- three-phase (air-water-ionic liquid) stirred tank bioreactor. *Biochemical Engineering Journal*, vol. 45, no. 3, pp. 209–217.
- van der Zon, M., Hamersma, P., Poels, E. and Bliëk, A. (1999 January). Gas-solid adhesion and solid-solid agglomeration of carbon supported catalysts in three phase slurry reactors. *Catalysis Today*, vol. 48, no. 1-4, pp. 131–138.
- Van Weert, G., Van Der Werff, D. and Derksen, J. (1995). Transfer of O<sub>2</sub> from air to mineral slurries in a rushton turbine agitated tank. *Minerals engineering*, vol. 8, no. 10, pp. 1109–1124.
- Vandu, C., Koop, K. and Krishna, R. (2004 November). Volumetric mass transfer coefficient in a slurry bubble column operating in the heterogeneous flow regime. *Chemical Engineering Science*, vol. 59, no. 22-23, pp. 5417–5423.
- Van't Riet, K. (1979 July). Review of Measuring Methods and Results in Nonviscous Gas-Liquid Mass Transfer in Stirred Vessels. *Industrial & Engineering Chemistry Process Design and Development*, vol. 18, no. 3, pp. 357–364.
- Versteeg, G., Blauwhoff, P. and van Swaaij, W. (1987). The effect of diffusivity on gas-liquid mass transfer in stirred vessels. Experiments at atmospheric and elevated pressures. *Chemical Engineering Science*, vol. 42, no. 5, pp. 1103–1119.
- Vinke, H., Bierman, G., Hamersma, P. and Fortuin, J. (1991). Adhesion of small catalyst particles to gas bubbles: determination of small effective solid-liquid-gas contact angles. *Chemical engineering . . .*, vol. 46, no. 10, pp. 2497–2506.
- Vinke, H., Hamersma, P. and Fortuin, J. (1993). Enhancement of the gas-absorption rate in agitated slurry reactors by gas-adsorbing particles adhering to gas bubbles. *Chemical engineering science*, vol. 48, no. 12, pp. 2197–2210.
- Viswanath, D.S. and Natavajan, G. (1989). Data book on the viscosity of liquids.
- Walker, G.M. (1998). *Yeast: Physiology and Biotechnology*. John Wiley and Sons.
- Wang, D., Cooney, C. and Demain, A. (1979). *Fermentation and enzyme technology*, vol. 107. John Wiley & Sons New York.
- Weiss, R. (1970). The solubility of nitrogen, oxygen and argon in water and seawater. *Deep Sea Research and Oceanographic Abstracts*, vol. 17, no. January, pp. 721–735.
- Wentzel, A., Ellingsen, T.E., Kotlar, H.-K., Zotchev, S.B. and Throne-Holst, M. (2007 October). Bacterial metabolism of long-chain n-alkanes. *Applied microbiology and biotechnology*, vol. 76, no. 6, pp. 1209–21.
- Yagi, H. and Yoshida, F. (1974). Oxygen absorption in fermenters: Effects of surfactants, antifoaming agents, and sterilized cells. *Journal of Fermentation Technology*, vol. 52, no. 12, pp. 905–916.

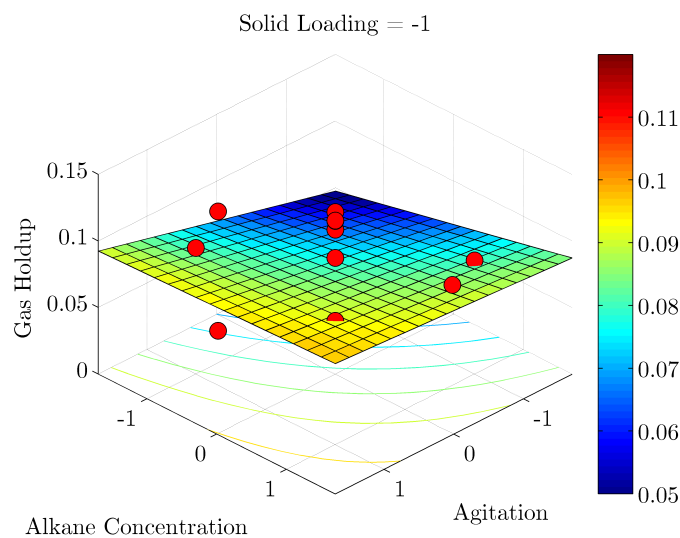
- Yoshida, F., Yamane, T. and Miyamoto, Y. (1970 October). Oxygen Absorption into Oil-in-Water Emulsions. A Study on Hydrocarbon Fermentors. *Industrial & Engineering Chemistry Process Design and Development*, vol. 9, no. 4, pp. 570–577.
- Yoshida, T., Yokoyama, K., Chen, K., Sunouchi, T. and Taguchi, H. (1977). Oxygen Transfer in Hydrocarbon Fermentation by *Candida rugosa*. *Journal of Fermentation Technology*, vol. 55, no. 1, pp. 76–83.
- Young, T. (1805). An essay on the cohesion of fluids. *Philosophical Transactions of the Royal Society of ...*, vol. 95, no. 1805, pp. 65–87.
- Zahradnik, J., Drapal, L., Kastanek, F., Zahradnik, J., Drápal, L., Kastánek, F. and Reznickova, J. (1992). Hydrodynamic and mass transfer characteristics of sectionalized aerated slurry reactors. *Chemical engineering and processing*, vol. 31, no. 4, pp. 263–272.
- Zhang, G.D., Cai, W.F., Xu, C.J. and Zhou, M. (2006 January). A general enhancement factor model of the physical absorption of gases in multiphase systems. *Chemical Engineering Science*, vol. 61, no. 2, pp. 558–568.
- Zheng, C., Chen, Z., Feng, Y. and Hofmann, H. (1995 May). Mass transfer in different flow regimes of three-phase fluidized beds. *Chemical Engineering Science*, vol. 50, no. 10, pp. 1571–1578.

# Appendix A. Influence of System Parameters on $D_{SM}$ and Gas Hold-Up: Additional Data

## A.1 Influence of Agitation and Alkane Concentration

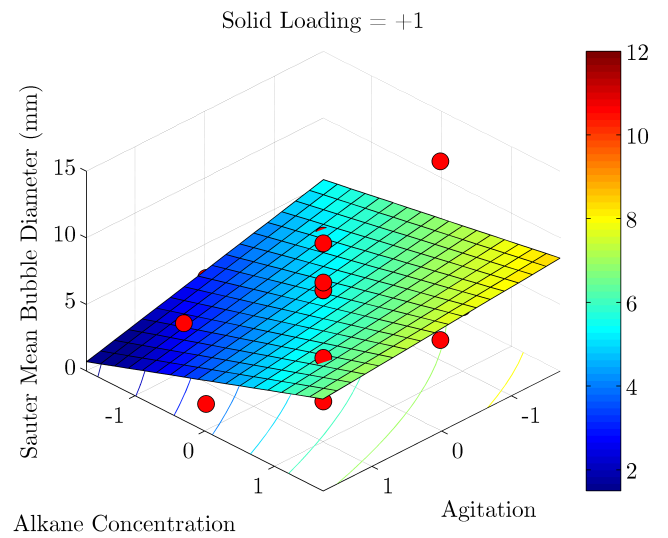


(a)

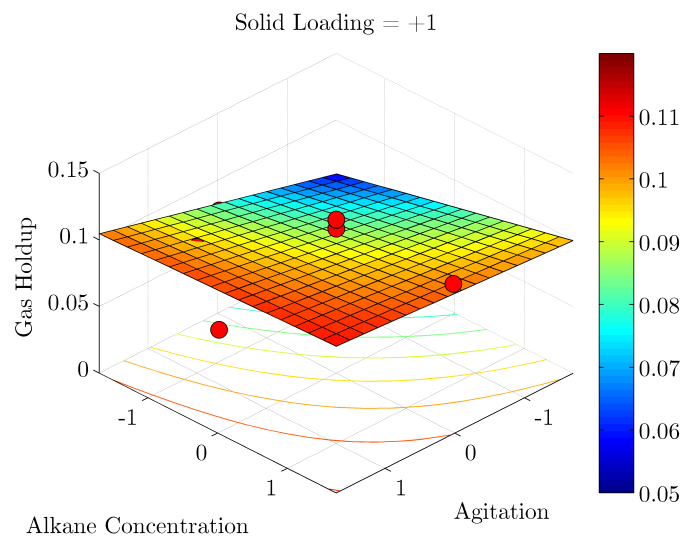


(b)

Figure A.1:  $D_{SM}$  (a) and gas hold-up (b) with changes in agitation rate and alkane concentration at constant low (-1) yeast loading



(a)



(b)

Figure A.2:  $D_{SM}$  (a) and gas hold-up (b) with changes in agitation rate and alkane concentration at constant high (+1) yeast loading



## A.2 Influence of Agitation and Yeast Loading

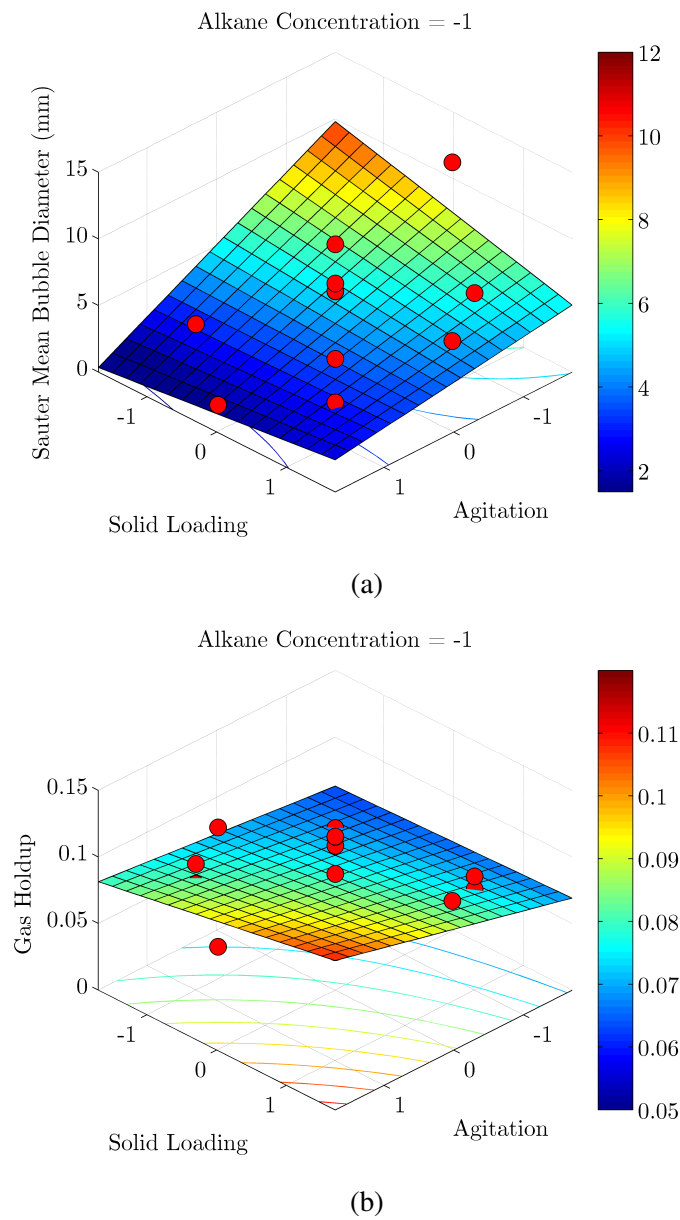
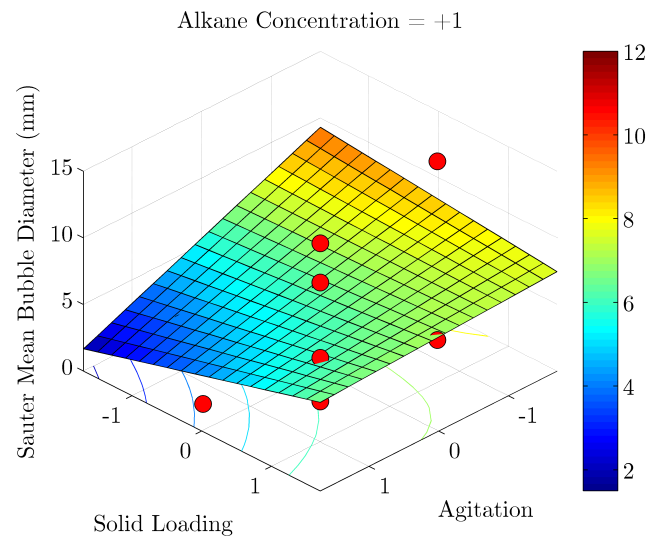
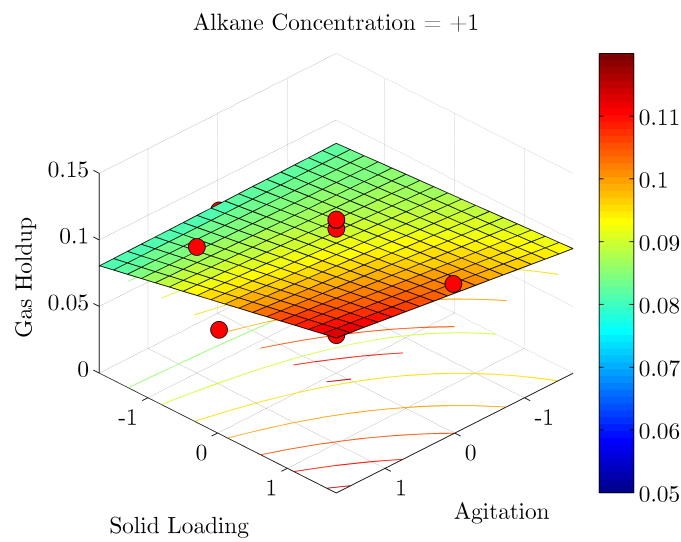


Figure A.3:  $D_{SM}$  (a) and gas hold-up (b) with changes in agitation rate and yeast loading at constant low (-1) alkane concentration



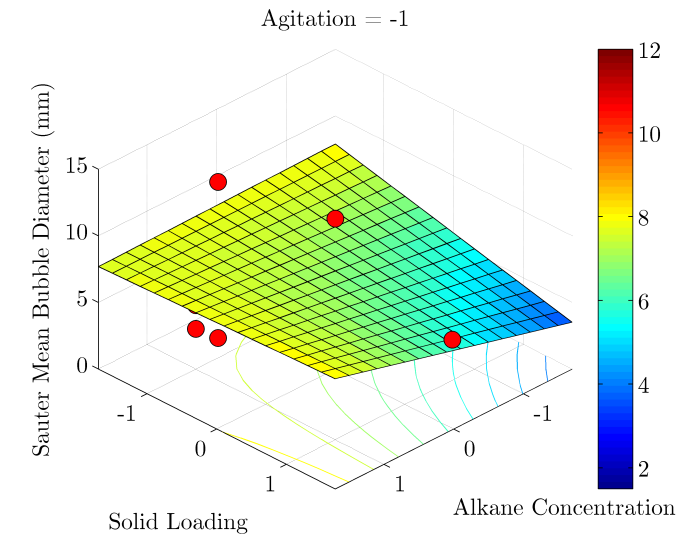
(a)



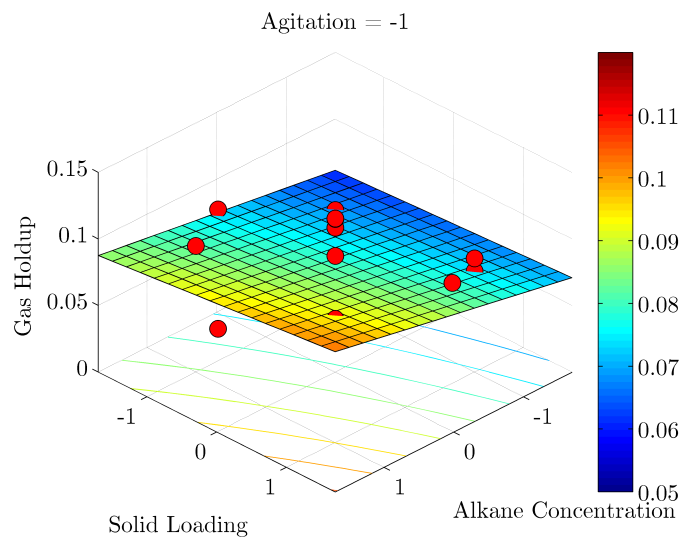
(b)

Figure A.4:  $D_{SM}$  (a) and gas hold-up (b) with changes in agitation rate and yeast loading at constant high (+1) alkane concentration

### A.3 Influence of Alkane Concentration and Yeast Loading

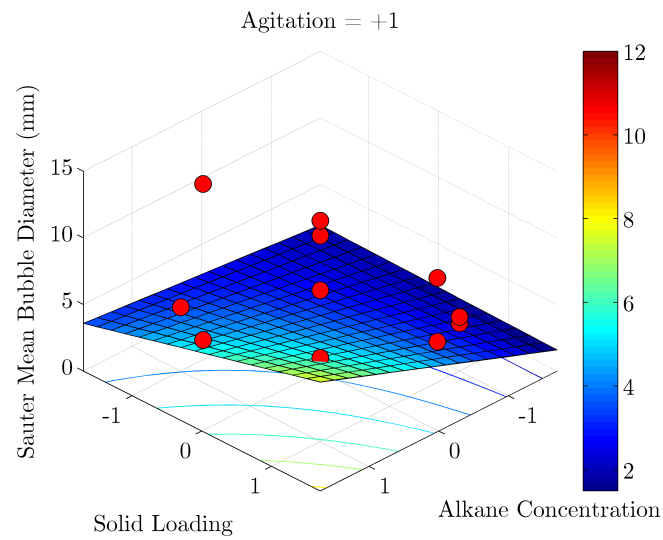


(a)

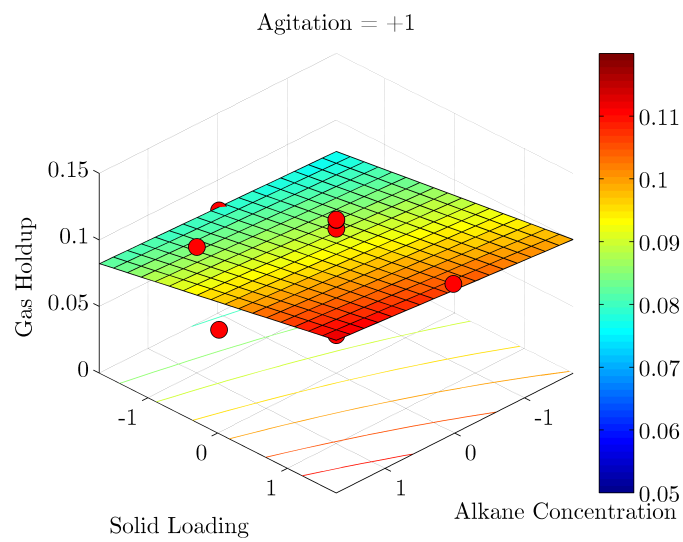


(b)

Figure A.5:  $D_{SM}$  (a) and gas hold-up (b) with changes in alkane concentration and yeast loading at constant low (-1) agitation rate



(a)



(b)

Figure A.6:  $D_{SM}$  (a) and gas hold-up (b) with changes in agitation rate and yeast loading at constant high (+1) agitation rate

## Appendix B. Overall Volumetric Oxygen Transfer Coefficient Determination Code

The following code was used to determine  $K_La$  via the second order model and GOP.  $K_p$  was found as the inverse of the time taken for the probe response to reach 63% of the final value (derived in Section 2.5.3.2) and substituted into the second order model (Equation H.23). The model was solved to yield  $K_La$  by minimising the sum of the least squared error between the model and the experimental data. The routine was executed in MATLAB, while the output data was stored in Excel spreadsheets.

```
%Reads from Excel Spreadsheet defined in directory
```

```
clc;
```

```
read_new = 1; %must be 1 or 0, specifies whether new data is read from spreadsheet
```

```
%exp_ind = [6 7 8 9 10 11 12 13 15 16 17 18 19 20 21];
```

```
exp_ind = [2]; %experimental index - refers to Excel sheet
```

```
for i = 1:length(exp_ind)
```

```
    if read_new == 1
```

```
        clearvars -except i exp_ind;
```

```
        filename_results = 'carbon_experiments.xlsx'
```

```
        read_new = 1; %must be 1 or 0, specifies whether new data is read from spreadsheet
```

```
        experiment = exp_ind(i); %spreadsheet tab on which the results are stored
```

```
        save_graphs = 1; %must be 1 or 0, specifies whether final graphs are saved to file (.png)
```

```
        time = xlsread(filename_results,experiment, 'B4:B72');
```

```
        data = xlsread(filename_results,experiment, 'C4:E37');
```

```
        kla_raw_data = xlsread(filename_results,experiment, 'I4:K72');
```

```
    end
```

```
    if read_new == 0
```

## APPENDIX B. OVERALL VOLUMETRIC OXYGEN TRANSFER COEFFICIENT DETERMINATION CODE152

```
clearvars -except time data kla_raw_data;
end

tic;
[rows cols] = size(kla_raw_data);
zero_count(1:cols) = 0;

for k = 1:cols
    for j = 1:rows
        if kla_raw_data(j,k) == 0
            zero_count(k) = zero_count(k) + 1;
        end
    end
end

for o = 1:cols
    for p = 2:rows
        if p + zero_count(o) <= rows
            kla_raw_data(p,o) = kla_raw_data(p+zero_count(o),o);
        end
    end
end

end_test = 0;
row_test = 1;
row_final = 1;

for l = 1:cols
    while end_test == 0 && row_test <= rows
        if kla_raw_data(row_test,l) == 100
            end_test = 1;
            row_final = row_test;
        elseif kla_raw_data(row_test,l) ~= 100
            row_test = row_test+1;
        end
    end
end

for m = 1:cols
```

## APPENDIX B. OVERALL VOLUMETRIC OXYGEN TRANSFER COEFFICIENT DETERMINATION CODE 153

```
    for n = row_final:rows
        kla_raw_data(n,m) = 100;
    end
end
disp('Raw data manipulation complete');
toc;

tic;

[status,sheets] = xlsfinfo(filename_results); %get the Excel sheet names for
use as labels

time_kp = time(1:length(data)); %define the time vector for Kp analysis
kp = kp_det(time_kp, data, experiment, save_graphs, sheets); %send time,
kp data, experiment number, save graph indicator and sheet names to
subroutine, returns KP vector

kp_mean = mean(kp);

save kpData kp_mean; %saving the kp for calling in the second order function
routine

disp('KP data saved');

[x y] = size(kla_raw_data);

for i = 1:x
    kla_data(i) = mean(kla_raw_data(i,:));
end

kla_data = kla_data';

%the initial value for kla for 1st order model
initialCoeffs1 = [0.1];

%generates new 1st order kla by minimising the error between the 1st
order model and average data value at discrete time intervals
%error is the sum of the error squared
[newCoeffs1,error1] = lsqcurvefit(@first_order_function, initialCoeffs1,
```

## APPENDIX B. OVERALL VOLUMETRIC OXYGEN TRANSFER COEFFICIENT DETERMINATION CODE 154

```
time, kla_data);

%the initial value for kla for 2nd order model
initialCoeffs2 = [0.1];

%generates new 2nd order kla by minimising the error between the 2nd order model
%and average data value at discrete time intervals
%error is the sum of the error squared
[newCoeffs2,error2] = lsqcurvefit(@second_order_function, initialCoeffs2, time,
kla_data);

toc;

timeNew = (0:1:time(length(time)));
y1 = first_order_function(newCoeffs1,timeNew);
y2 = second_order_function(newCoeffs2,timeNew);

dirname = 'C:\Documents and Settings\phollis\My Documents\Masters\Experiments';
kp_filename = strcat(sheets(experiment),'.png');
kla_filename = strcat(sheets(experiment),'.png');
file1 = fullfile(dirname,'KP 3',kp_filename{1});
file2 = fullfile(dirname,'KLa 3',kla_filename{1});

figure;
hold on;
plot(timeNew, y1, 'r', ...
timeNew, y2, 'b', ...
time, kla_data, ':k');

plot(time, kla_raw_data(:,1), 'ok',...
time, kla_raw_data(:,2), 'xk',...
time, kla_raw_data(:,3), '.k');

legend('1st Order', '2nd Order', 'Average', 'Run 1', 'Run 2', 'Run 3',
'Run 4', 'Run 5', 'location', 'southeast');
legend('boxoff');
text(100,41,['1st Order KLa = ',num2str(newCoeffs1(1),3),' s-1']);
text(100,35,['1st Order Error = ',num2str(error1,3)]);
text(100,27,['2nd Order KLa = ',num2str(newCoeffs2(1),3),' s-1']);
```



## APPENDIX B. OVERALL VOLUMETRIC OXYGEN TRANSFER COEFFICIENT DETERMINATION CODE 155

```
text(100,21,['2^n^d Order Error = ',num2str(error2,3)]);
text(100,14,['k_p = ',num2str(kp_mean/1.8,3),' s^-^1']);
axis([0 time(length(time)) 0 110]);
xlabel('Time (s)');
ylabel('C/C*');
title(sheets(experiment));
hold off;

if save_graphs == 1
    saveas(gcf,file2,'png');
end

close(gcf);

final_results = [kp_mean, newCoeffs1(1), newCoeffs2(1)];

filename = 'final_results_3.xlsx'; %filename for writing results to file

A = {'Kp', 'KLa_1', 'Error 1', 'KLa_2', 'Error 2'};
B = {kp_mean, newCoeffs1(1), error1, newCoeffs2(1), error2};
sheet = 1; %sheet within spreadsheet for data

xlRange = 'C2';
xlswrite(filename,A,sheet,xlRange); %write headings

xlRange = strcat('B', num2str(experiment + 1));
xlswrite(filename,sheets(experiment),sheet,xlRange); %write experiment name

xlRange = strcat('C', num2str(experiment + 1));
xlswrite(filename,B,sheet,xlRange); %write experiment name

end
```

## Appendix C. Image Recognition Code

The following code was used to perform the image recognition necessary for this study. It was originally written by Correia (2007), but was adapted for the purposes of this study. Changes to the code included automation of the image input process, making it possible to enqueue a series of images for analysis which greatly increased the rate at which images could be analysed. The code was also modified to output and store the bubble size distribution as a histogram for each image in addition to calculation of all the bubble metrics. It is executed in MATLAB while all data is output in Excel spreadsheets.

```
clear; clc;

%%%IMAGE INPUT
%*****
%% Step 1: Read image
%*****
fol_num_input = input('Number of folder containing images to be analysed: ');
num_im_input_max = input('Number of images to be analysed: ');

for num_im_input = 1:num_im_input_max

    dirname = 'C:\Users\phollis\Documents\Masters\Pictures\Experimental Runs';
    fol_num = sprintf('Run %d', fol_num_input);
    img_num = sprintf('%d.jpg', num_im_input);
    I = imread(fullfile(dirname, fol_num, img_num));

    img_num_xl = sprintf('Results Experiment %d.xls', fol_num_input);
    xl_filename = fullfile(dirname, fol_num, img_num_xl);
    %filename for results to be written to

    sheet = img_num;
    %sheet in the excel file results will be written to

    % Read in the |test.jpg| image, which is a test image.
    %Supports jpeg, tiff and bitmap

    figure(1); imshow(I), title('Original image');
```

```

write_data = 1;
%if write_data = 1, results will be written to spreadsheet after analysis.

%*****
%% Step 2: Manual Cropping
%*****
% IMCROP crops an image to a specified rectangle

%imgCrop = imcrop(I(:,:,1));
imgCrop = I;
%figure(2), imshow(imgCrop);

%%% IMAGE PREPROCESSING
%*****
%% Step 3: Enhance Image
%*****
% To enhance the image for preprocessing, several options are
% available:

%% Filter Image
% The FSPECIAL function produces several kinds of predefined
%filters, in the form of correlation kernels.
H = fspecial('unsharp', 0.5);

%This may be applied directly to the image data using IMFILTER.
sharpened = imfilter(imgCrop,H);
%figure(3), imshow(sharpened);

% Median filtering produces each output pixel as an average of
% the pixel values in the neighborhood of the correpsnding input
% pixel as determined by the median of the neighborhood pixels.

Medfilter = medfilt2(imgCrop);
%figure(4), imshow(Medfilter);

%% Enhance Contrast
% The intensity contrast in the image is maximized by using the

```

```
% ADAPTHISTEQ function, which performs contrast-limited adaptive
% histogram equalization. Rescale the image intensity using
% IMADJUST so that it fills the data type's entire dynamic range.
```

```
claheI = adapthisteq(imgCrop, 'NumTiles', [10 10]);
claheI = imadjust(claheI);
%figure(5), imshow(claheI);
```

```
%%IMAGE ANALYSIS
```

```
%*****
```

```
%% Step 4: Detect bubbles using |edge| function
```

```
%*****
```

```
% Another word for object detection is segmentation. The object
% to be segmented differs greatly in contrast from the background
% image. Changes in contrast can be detected by operators that
% calculate the gradient of an image. One way to calculate the
% gradient of an image is the Sobel operator. To create the
% binary gradient mask, we use the 'edge' function.
```

```
[BWs, thresh] = edge(imgCrop, 'sobel');          %sobel, canny
%figure(6), imshow(BWs)
```

```
%*****
```

```
%% Step 5: Dilate the image
```

```
%*****
```

```
%% Linear structuring element
```

```
% The binary gradient mask shows lines of high contrast in the
% image. These lines do not quite delineate the outline of the
% object of interest. Compared to the original image, you can see
% gaps in the lines surrounding the object in the gradient mask.
% These linear gaps will disappear if the image is dilated using
% linear structuring elements, which we can create with the
% 'strel' function.
```

```
se90 = strel('line', 2, 90);
se0 = strel('line', 2, 0);
```

```
%% Dilation
```

```

% The binary gradient mask is dilated using the vertical
% structuring element followed by the horizontal structuring
% element. The 'imdilate' function dilates the image.

BWsdil = imdilate(BWs, [se90 se0]);
%figure(7), imshow(BWsdil)

%*****
%% Step 6: Fill interior gaps
%*****
% The dilated gradient mask shows the outline of bubbles, but
% there are still holes in the interior of some bubbles. To fill
% these holes we use the imfill function.

BWdfill = imfill(BWsdil, 'holes');
%figure(8), imshow(BWdfill);

%*****
%% Step 7: Remove connected objects on border
%*****
% The bubbles of interest has been successfully segmented, but it
% is not the only object that has been found. Any objects that
% are connected to the border of the image can be removed using
% the imclearborder function. The connectivity in the
% imclearborder function was set to 4 to remove diagonal
% connections.

BWnobord = imclearborder(BWdfill, 4);
%figure(9), imshow(BWnobord)

%*****
%% Step 8: Erode the object
%*****
% Finally, in order to make the segmented object look natural, we
% smoothen the object by eroding the image twice with a diamond
% structuring element. We create the diamond structuring element
% using the |strel| function.

seD = strel('disk',1);

```

```

BWfinal = imerode(BWnobord, seD);
BWfinal = imerode(BWfinal, seD);
%figure(10), imshow(BWfinal),

%*****
%% Step 9: Remove the noise
%*****
% Using morphology functions, remove pixels which do not belong
% to the objects of interest. Remove all object containing fewer
% than 30 pixels

bw = bwareaopen(BWfinal,20);
%figure(11), imshow(bw)

%%DATA EXTRACTION
%*****
%% Step 10: Display bubble outlines
%*****
% An alternate method for displaying the segmented object would
% be to place an outline around the segmented cell. The outline
% is created by the 'bwperim' function.

BWoutline = bwperim(BWfinal);
Segout = I;
Segout(BWoutline) = 255;
%figure(12), imshow(Segout)

%*****
%% Step 11: Find the boundaries
%*****
% Concentrate only on the exterior boundaries. Option 'noholes'
% will accelerate the processing by preventing 'bwboundaries'
% from searching for inner contours.

[B,L,N] = bwboundaries(bw,'noholes');

% Display the label matrix and draw each boundary

```

```

%figure(13), imshow(label2rgb(L, @jet, [.5 .5 .5]))
imshowinfo
hold on
for k = 1:length(B)
    boundary = B{k};
    plot(boundary(:,2), boundary(:,1), 'g', 'LineWidth', 1)
end

%*****
%% Step 12: Scaling
%*****
%Scaling data is obtained using the ruler method

%   prompt={'Enter the scale in mm',...
%           'Enter the scale in pixels:'};
%   def={'1', '1'};
%   dlgTitle='Scaling: user input required';
%   lineNo=1;
%   answer=inputdlg(prompt,dlgTitle,lineNo,def);
%   Scaledata = str2num(char(answer{:}));
Scaledata(1) = 4;
Scaledata(2) = 108;
scale=Scaledata(1)/Scaledata(2);

%*****
%% Step 13: Extract Data
%*****
% Estimate each object's area and perimeter. Use these results to
% form a simple metric indicating the roundness of an object:
% metric = 4*pi*area/perimeter^2.
% This metric is equal to one only for a circle and it is less
% than one for any other shape. The discrimination process can be
% controlled by setting an appropriate threshold. In this example
% use a threshold of 0.76.

% Use 'regionprops' to obtain estimates of the area for all of
% the objects. Notice that the label matrix returned by
% 'bwboundaries' can

```

```
% be reused by 'regionprops'.

stats = regionprops(L, 'Area', 'Centroid', 'Majoraxislength', 'Minoraxislength',
threshold = 0.76;

% loop over the boundaries
for k = 1:length(B)

    Number(k) = k;

    % Obtain (X,Y) boundary coordinates corresponding to label 'k'
    boundary = B{k};

    % Obtain the area calculation corresponding to label 'k'
    area = stats(k).Area;
    perimeter = stats(k).Perimeter;

    % Compute the sphericity metric
    metric = 4*pi*area/perimeter^2;

    % display the results
    metric_string = sprintf('%d',k);

    % mark objects above the threshold with a black circle
    if metric > threshold
        centroid = stats(k).Centroid;
        plot(centroid(1),centroid(2),'sk');
    end

    text(boundary(1,2)-10,boundary(1,1)-13,metric_string,'Color','y',...
        'FontSize',14,'FontWeight','bold');

    Shape(k) = metric;

%Scaling of parameters
areascale(k) =area.*scale^2;
perimeterscale(k) = perimeter.*scale;
majoraxisscale(k) = (stats(k).MajorAxisLength)*scale;
minoraxisscale(k) = (stats(k).MinorAxisLength)*scale;
```



```
    equivdiameterscale(k) = (stats(k).EquivDiameter)*scale;

end

title(['Metrics closer to 1 indicate that ',...
      'the object is approximately round']);

%*****
%% Step 14: Write data to excel spreadsheet
%*****
if write_data == 1

    xlswrite(xl_filename, {'Number' 'Shape' 'Area' 'Equiv. Diameter' 'Perimeter'
                          'Major Axis' 'Minor Axis' 'Eccentricity'}, sheet , 'H')

    xlswrite(xl_filename, [Number]', sheet , 'A3')
    xlswrite(xl_filename, [Shape]', sheet, 'B3')
    xlswrite(xl_filename, [areascale]', sheet, 'C3');
    xlswrite(xl_filename, [equivdiameterscale]', sheet, 'D3')
    xlswrite(xl_filename, [perimeterscale]', sheet, 'E3')
    xlswrite(xl_filename, [majoraxiscale]', sheet, 'H3')
    xlswrite(xl_filename, [minoraxiscale]', sheet, 'I3')
    xlswrite(xl_filename, [stats.Eccentricity]', sheet, 'J3')
end
end
```

## Appendix D. Statistical Model Validation

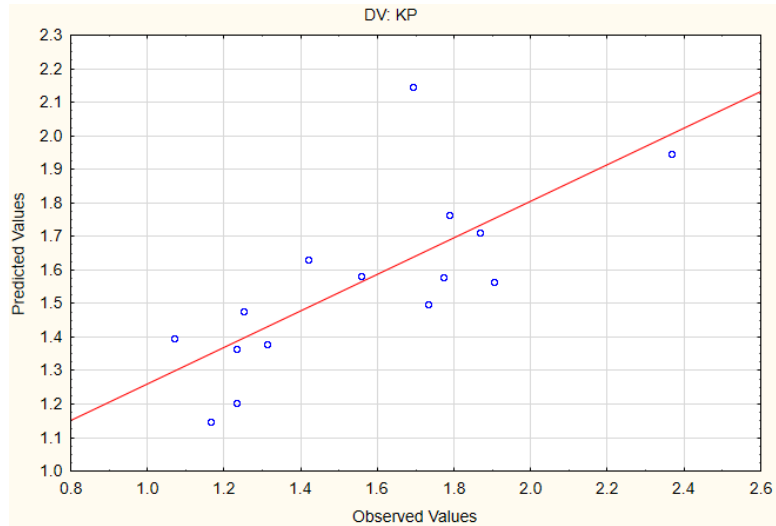


Figure D.1: Observed vs. predicted values for  $K_P$

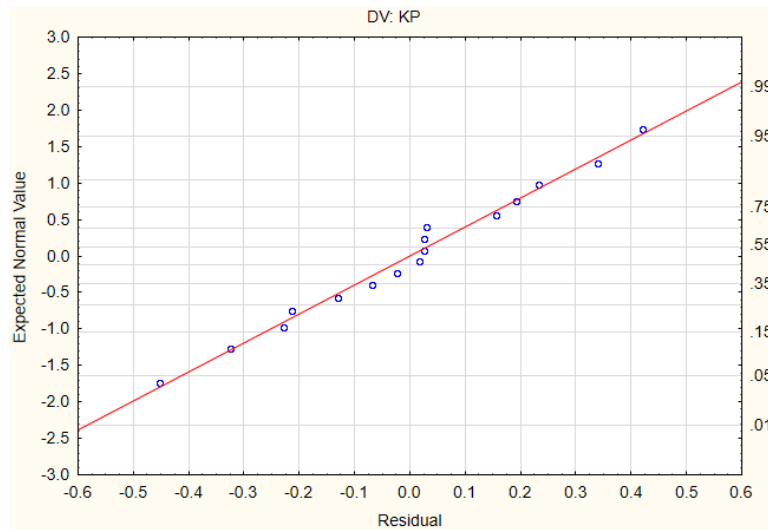


Figure D.2: Normal probability plot for  $K_P$

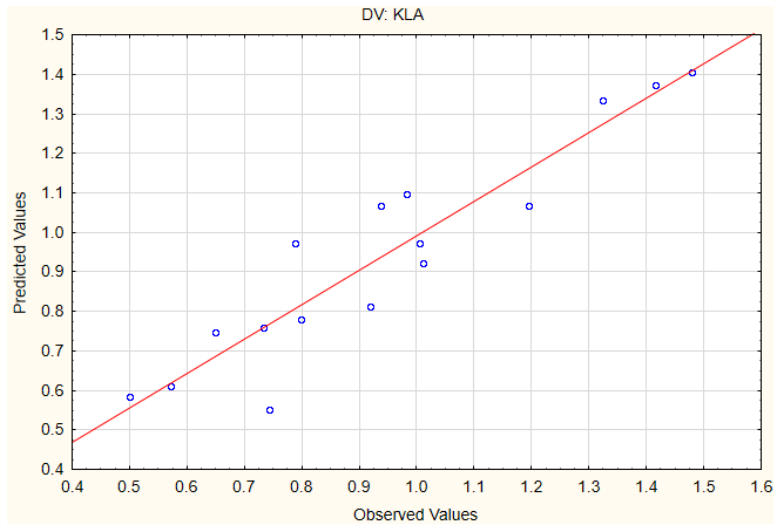


Figure D.3: Observed vs. predicted values for  $K_{La}$

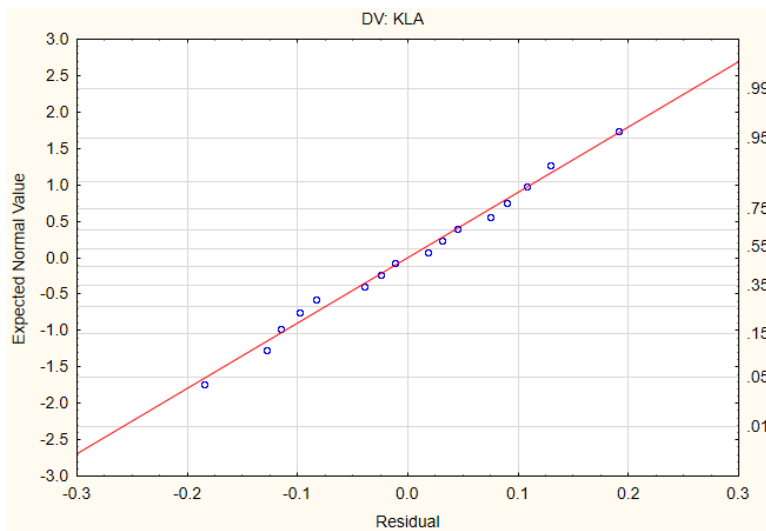


Figure D.4: Normal probability plot for  $K_{La}$

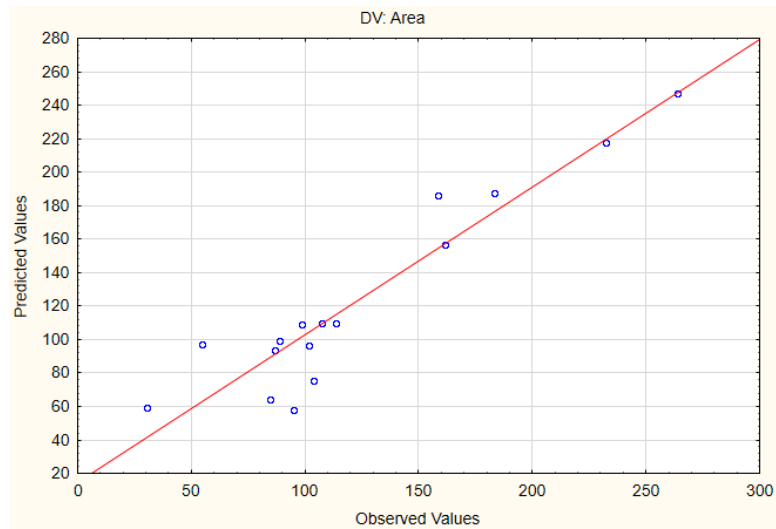


Figure D.5: Observed vs. predicted values for interfacial area

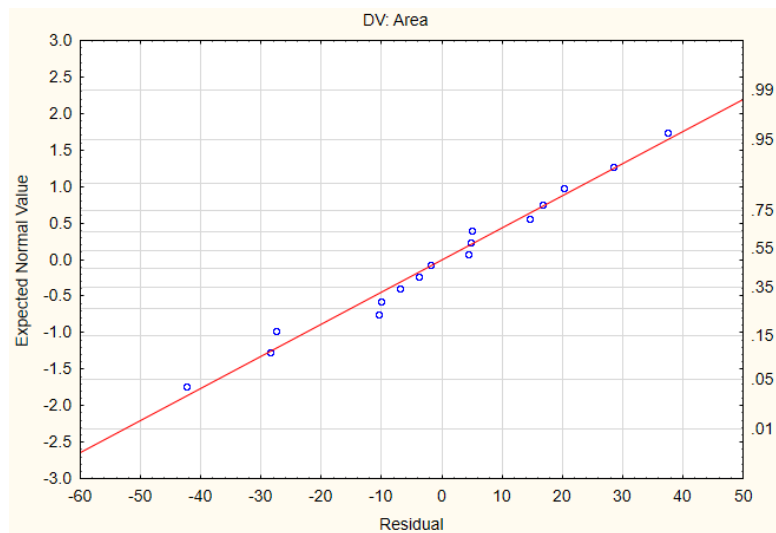


Figure D.6: Normal probability plot for interfacial area

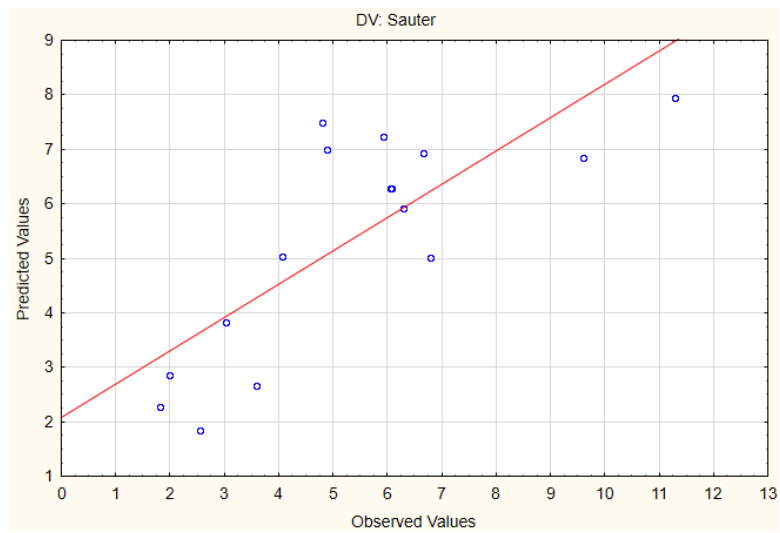


Figure D.7: Observed vs. predicted values for  $D_{SM}$

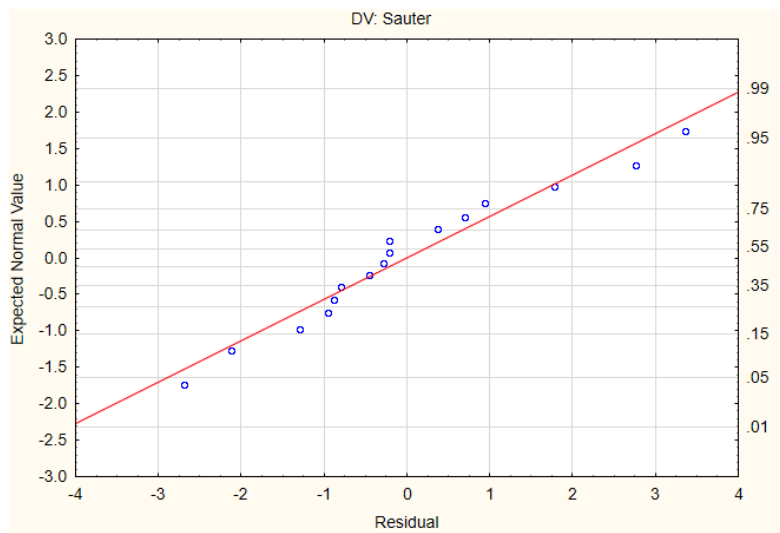


Figure D.8: Normal probability plot for  $D_{SM}$

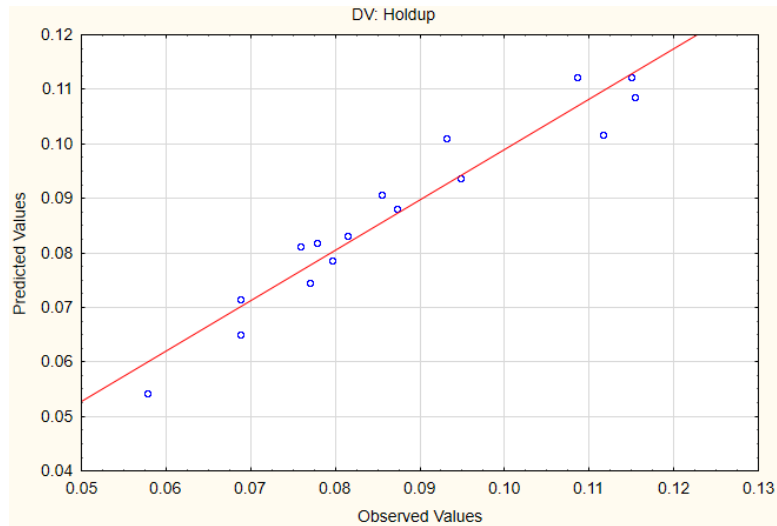


Figure D.9: Observed vs. predicted values for gas hold-up

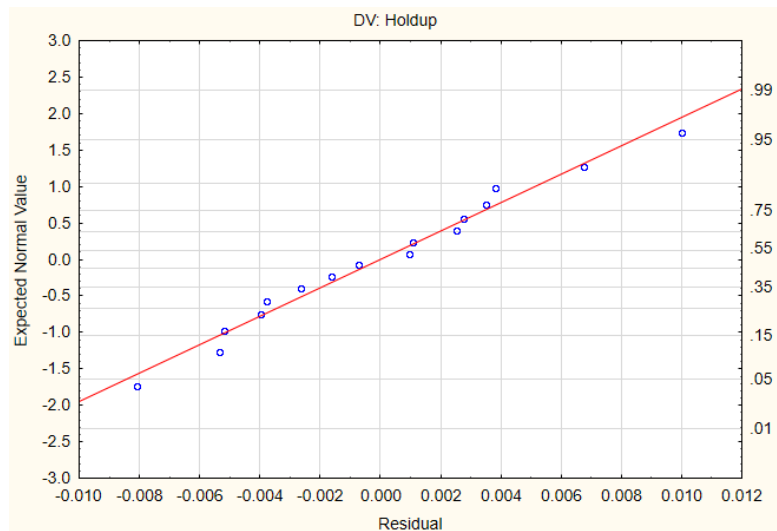


Figure D.10: Normal probability plot for gas hold-up

## Appendix E. Image Acquisition Methodology

### E.1 Development of Lighting Solution

During the process of developing an accurate system for characterising  $D_{SM}$ , a number of different lighting configurations were trialled. Details of each of configuration are supplied, along with findings regarding their effectiveness and ease of use. The internal fluorescent lighting solution (Section E.1.4) was chosen as the lighting solution, and all experiments were performed using this configuration.

#### E.1.1 Backlit Halogen Lighting

The first configuration made use of a 1500 watt halogen tube light placed behind the bioreactor (Figures E.1 and E.2). The light was placed behind the bioreactor, and provided backlit illumination through the liquid contents.

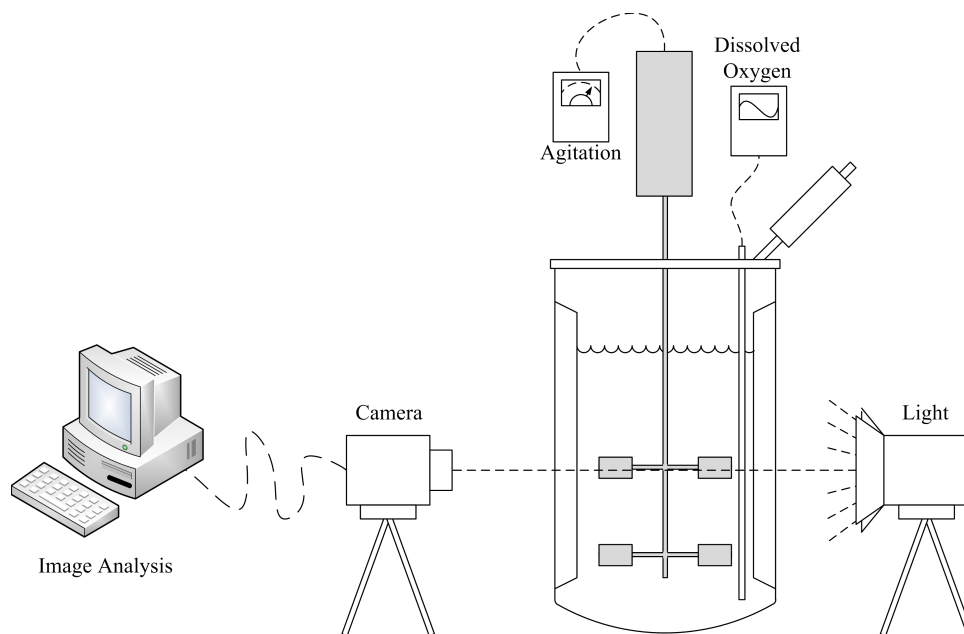


Figure E.1: Initial Lighting Configuration for Recording the Interfacial Area (Not to Scale)



Figure E.2: Initial Lighting Configuration for Recording the Interfacial Area

This was rejected as not enough light was passing through the bioreactor to obtain clear images. In addition, the 1500 watt halogen light emitted a significant amount of heat causing fluctuations in the bioreactor temperature if it remained on for too long.

### **E.1.2 External Light Emitting Diode Lighting**

To reduce the heat being emitted by the halogen light, it was swapped for a series of LED lights (Figure E.3) placed externally above the bioreactor (Figure E.4).





Figure E.3: 12 Volt LED Strip Light

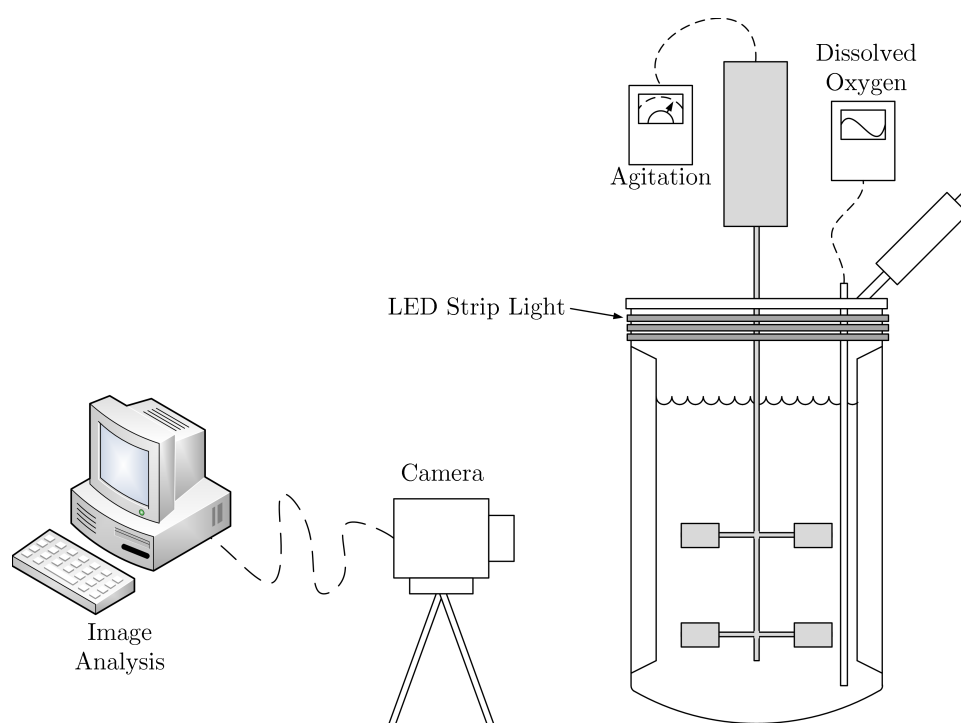


Figure E.4: Second Set Up for Recording the Interfacial Area (Not to Scale)

This system was rejected because it failed to provide enough light inside the bioreactor. As a consequence, images were either very dark (if the camera used a short exposure) or blurry (if a longer exposure time was used).

### E.1.3 Internal Light Emitting Diode Lighting

To increase the amount of light, the LED strip was placed inside a water-tight tube, and submerged inside the bioreactor in the bulk fluid (Figure E.5). This meant enough light was available for obtaining clear images. However, the LED strip was effectively a series of point light sources which caused bright spots in the images. This in turn meant that bubbles were not detected evenly across the focal plane which was undesirable for reliable image processing. A diffuser was also tested, but this failed to provide an even light distribution. For this reason, this configuration was rejected.

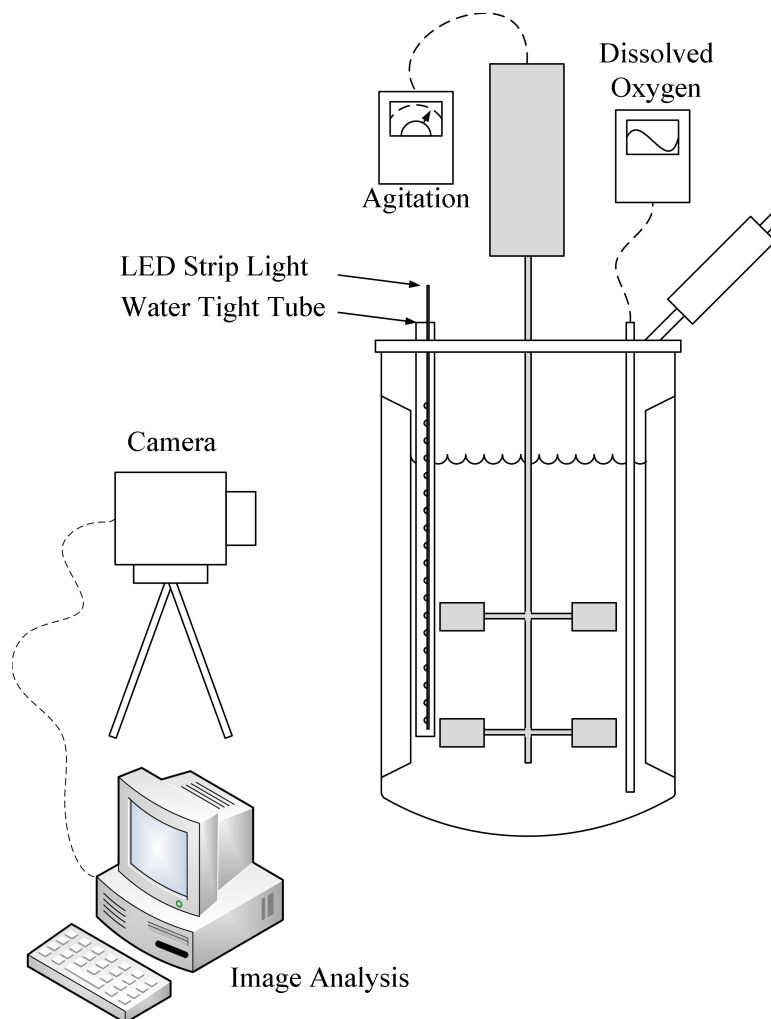
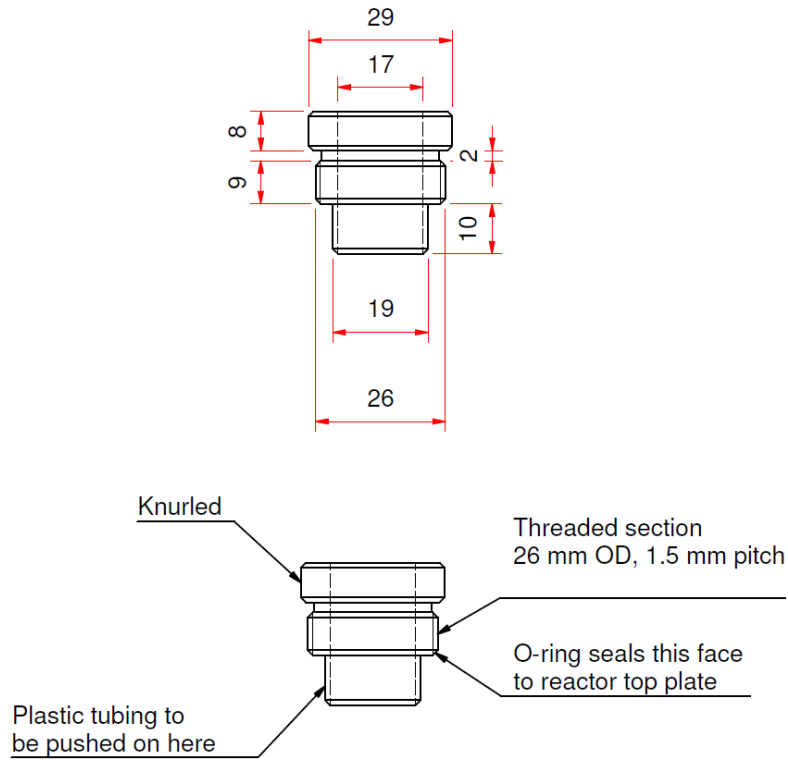


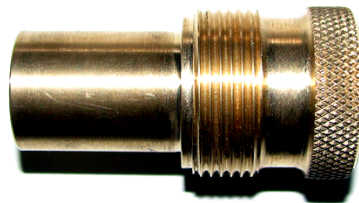
Figure E.5: Third Set Up for Recording the Interfacial Area (Not to Scale)

### E.1.4 Internal Fluorescent Lighting

To provide an evenly dispersed light source, a fluorescent tube was placed inside a watertight tube and mounted to the bioreactor lid using a machined fitting (Figure E.6). It was inserted



(a) Drawing



(b) Picture

Figure E.6: Design and Manufacture of Bioreactor Light Fitting

through the 28mm port ('1' in Figure E.7). The waterproof housing extended down into the bulk liquid (Figure E.8).

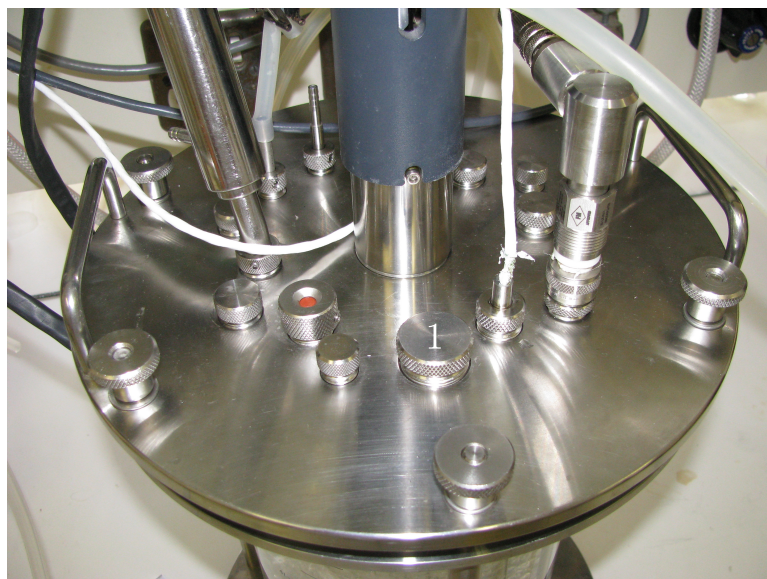


Figure E.7: Location of 28mm Port Used for Installing Fluorescent Light (Indicated by 1)

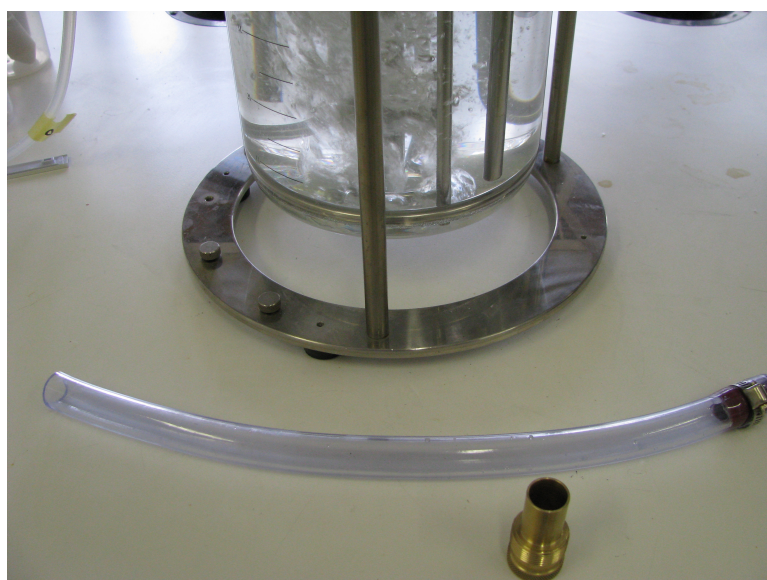


Figure E.8: Prototype Waterproof Housing for Fluorescent Light

The fluorescent tube and water-tight housing remained in the bioreactor for the duration of an experimental run and only illuminated when photography was taking place. Minimal heat build up was observed while the light was on with the tube becoming slightly warmer than ambient. During changes to the bioreactor and contents, the fluorescent tube was removed.

This solution gave optimal and repeatable images when combined with the methodology explained in Section 5.2.2 and was used for all experimental runs.

## E.2 Development of Photography Methodology

In order to achieve clear, undistorted images, the camera settings were optimised for the shortest possible shutter speed using the internal fluorescent tube (Section E.1.4). This meant using the largest possible aperture to increase the amount of light available to the CCD sensor in the camera. Combined with the use of a large aperture is the associated decrease in depth of field (DOF) (Figure E.9). DOF refers to the distance between the closest and furthest objects in an image that appear in focus. The advantage of using a large aperture was a very shallow DOF, and therefore only bubbles in the correct focal range were photographed. Bubbles along the wall (too shallow) and bubbles deeper in the bioreactor were ignored by the image analysis routines because they were out of focus and consequently their outlines were too blurry to be detected. This improved both image clarity (less bubble overlap) and the computational time needed for image analysis as no time was spent analysing out of focus bubbles.

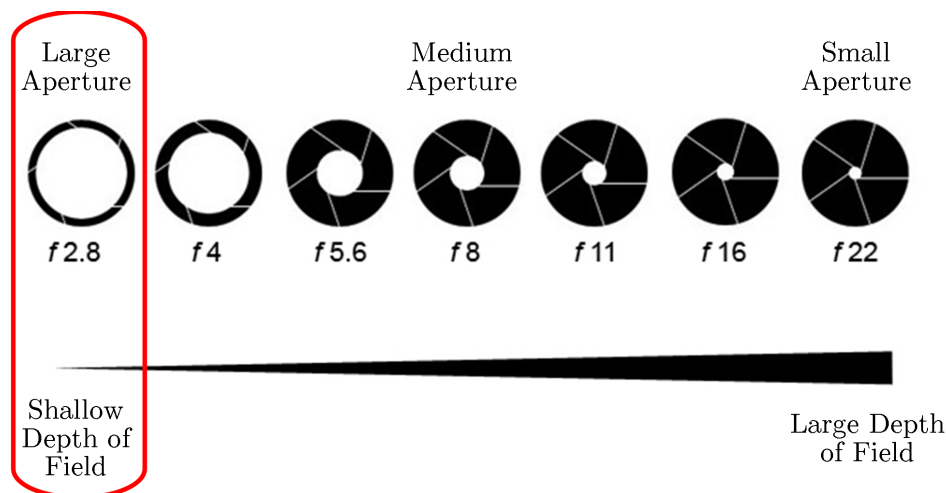


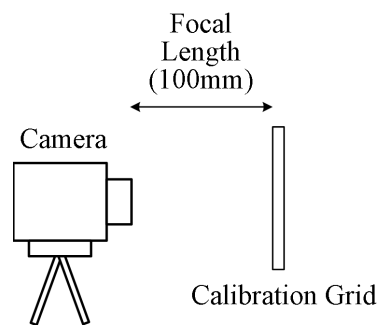
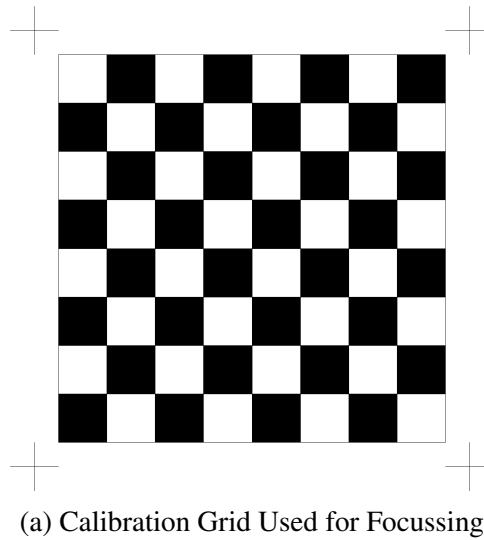
Figure E.9: Relationship Between Depth of Field and Aperture with Desired Aperture Circled

The shallow depth of field had another consequence, namely the requirement for a very accurate focus. If the focus was not accurately set and maintained for the duration of the experiments, some variation could be introduced at the expense of image clarity and repeatability. Focussing the camera on the moving bubbles proved difficult so a stationary focus grid was used (Figure E.10a). To focus the camera, the focus grid was mounted 100mm from the objective lens of the camera, and the focus adjusted. Once a clear focus had been achieved, the camera was transferred to a position 75mm in front of the bioreactor. Consequently, the focal point was 25mm inside of the walls of the bioreactor. Bubbles passing through the field of view 25mm inside of the bioreactor were therefore clearly in focus (Figure E.10b).

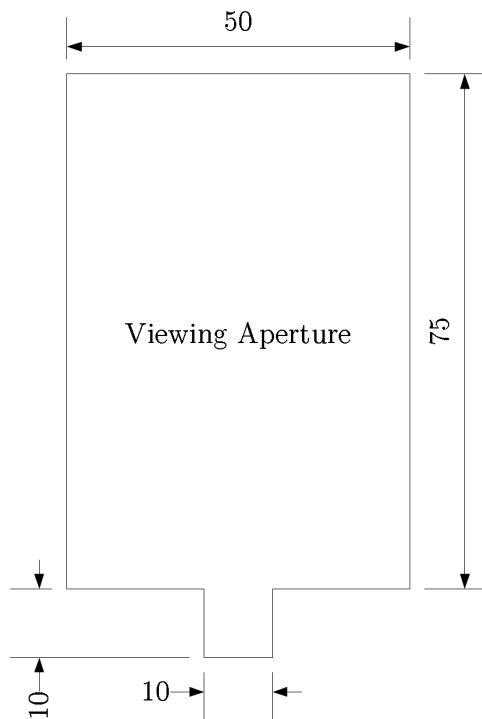
Once the focus had been set, it was necessary to record an object with known dimensions to scale the images. This allowed for accurate scaling of the images to give the actual bubble

diameters. Calibration was done using the camera focus grid (Figure E.10a). The grid was printed such that one square represents 10 x 10mm (and the entire grid 80 x 80mm). An image of the grid was recorded with the camera 100mm from the grid, and the corresponding distance was measured on the computer in pixels. Dividing the number of pixels along the length of one square by the real world dimension (10mm) gave the ratio in terms of pixels per millimetre. This factor was then used to scale all the images. Calibration was completed in both the x and y directions to ensure there was no distortion caused by the camera lens. Focusing and calibration was completed at the start of each experiment to ensure consistency.

The final variable was to ensure correct placement of the camera in relation to the bioreactor. The same portion of bioreactor was photographed for all experiments. To ensure the correct placement, a template was made for the front surface of the bioreactor (Figure E.10c). This was printed, and the interior cut out, ensuring the dimensions were correct. The template was then placed on the front surface of the bioreactor once the camera had been focussed, and all images were recorded through this aperture. As a back-up for calculating the pixel/mm ratio, a 10mm slot was cut in the bottom of the aperture, and this could also be used to scale the bubbles. This was not as accurate as the calibration using the focus grid because of differences in the distance from the camera's objective lens. Scaling of images was always performed using the focus grid.



(b) Camera Configuration During Focussing



(c) Viewing Aperture Used for High Speed Photography

Figure E.10: Focus Grid, Camera Configuration and Field of View Aperture for Photography

### E.3 Camera Specifications

Table E.1: mvBlueFox 124G Compact Industrial CCD and CMOS Camera Specifications

USB interface (up to 480 Mbit/s with USB 2.0)	
All versions are USB 1.1 compatible	
8 Megapixels memory	Hardware LUT 10 bits lossless image transfer and bus bandwidth via USB bulk transfer method
Connectors:	
- USB type B	USB
- Binder 4-pin with lock	USB
- D-Sub 9-pin male	digital I/O
Digital I/O opto-isolated:	
- 2 inputs (trigger)	logic / PLC level
- 2 outputs (strobe)	30 V / 100 mA
Features:	<p>C-mount. CS-mount or optional S-mount          CCD sensor with full frame shutter          CMOS sensor with rolling shutter          Back-focus-adjustment          automatic gain control (AGC)          Automatic exposure control (AEC)          All parameters adjustable via bus interface          ADC resolution: up to 12 bits (transfer 10/8 bits)          Horizontal and vertical mirroring          Expose and image transfer possible at the same time          Hardware Real-Time Controller (HRTC) for time critical I/O and acquisition control by defining a sequence of operating steps          Bus powered &lt; 2.5W</p>
Permissible ambient temperature:	
- operation: - storage:	0 to 45 °C / 30 to 80 %RH -20 to 60 °C / 20 to 90 %RH
Weight without lens:	approx. 120g
Size without lens (w x h x l):	38.8 x 38.8 x 35 mm
Protection class:	IP40
Conformity:	Immunity: EN 61000-6-2:2005;
Emission: EN 61000-6-3:2007, FCC class B; RoHs; CE	

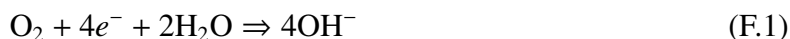


## Appendix F. Dissolved Oxygen Probe

A Mettler Toledo InPro 6800 polarographic DO probe was used for all experiments. The operating principle (F.1), an exploded view diagram (F.2), the method of polarisation (F.3) and detailed specifications (F.4) are provided.

### F.1 Operating Principle

The operating principle of an amperometric polarographic DO probe was based on a Clark probe, which measured the reduction of oxygen on the surface of a catalytic platinum surface based on reactions at the cathode (Equation F.1) and anode (Equation F.2).



The electrodes were separated from the sample medium by an oxygen-permeable Teflon membrane. The transmitter supplied a constant polarization voltage to the cathode, which was needed to reduce oxygen. The reduction took place at the cathode, where oxygen molecules that have permeated the membrane were reduced. Oxidation took place at the anode and oxidized the anode metal was released in the form of silver ions into the electrolyte. The electrolyte closed the electric circuit between anode and cathode. The current produced by Equations F.1 and F.2 was measured by the transmitter and was proportional to the partial pressure of oxygen ( $p_{\text{O}_2}$ ) in the sample medium, which was recorded by the transmitter. An additional electrode was used as a reference to stabilise the anode (Toledo, 2013).

## F.2 Dissolved Oxygen Probe Diagram

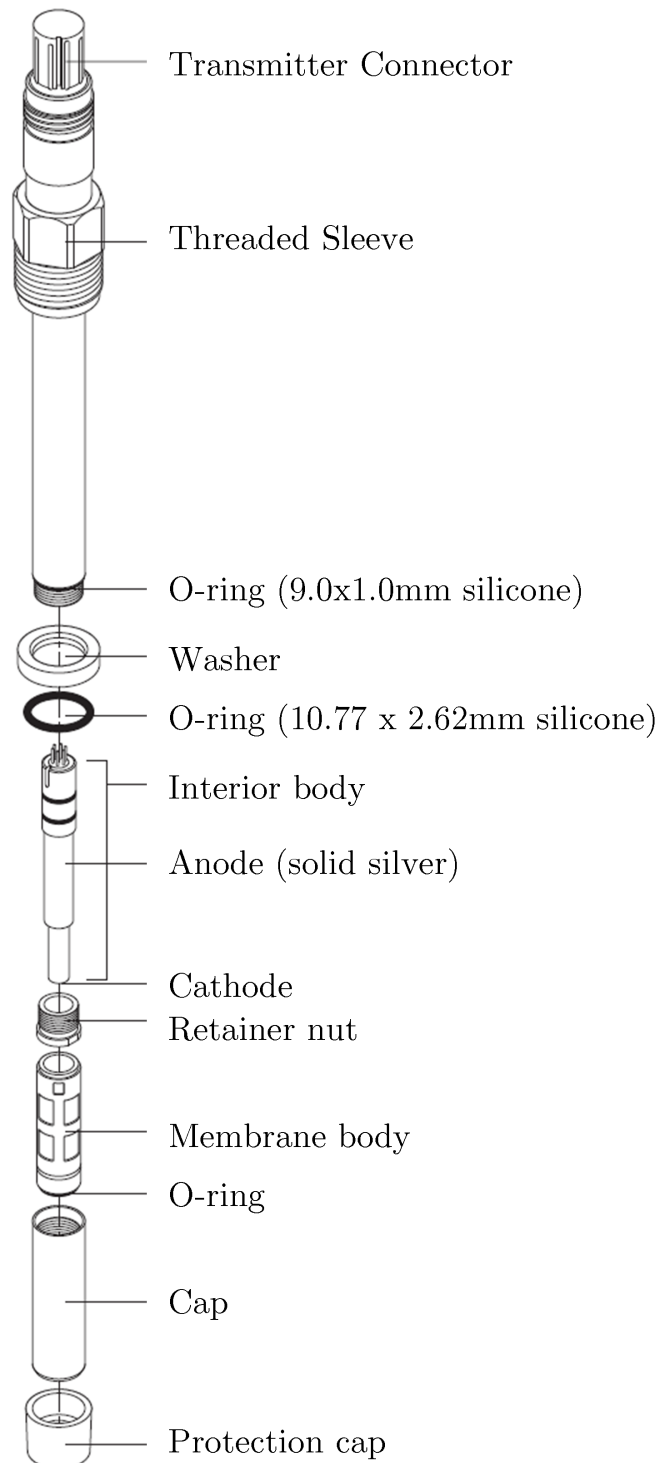


Figure F.1: 12mm Mettler Toledo® Inpro® 6800 Dissolved Oxygen Probe Exploded View (Toledo, 2013)

### F.3 Polarising the Dissolved Oxygen Probe

Following connection of the DO to the transmitter for the first time, or following an extended period for which the probe had been disconnected from the transmitter, it was necessary to re-polarise the electrolyte. Polarisation was performed by connecting the DO probe to the transmitter while the probe was immersed in tap water for at least 6 hours. The recommended polarisation voltage for general purpose applications was -675mV. Should the probe be disconnected for a short period of time (>30 minutes), Table F.1 provides the length of time required to re-polarise the probe. Depolarization refers to the time for which no polarization voltage was supplied to the probe. This was the case when the electrolyte was changed, the membrane was changed, the cable was disconnected or no transmitter was connected to the probe. Polarization time was the time for which a polarisation voltage was supplied to the sensor.

Table F.1: Depolarisation and Repolarisation Time

Depolarization time <sup>1</sup> ( $t_{\text{depol}}$ ) [min.]	Minimum required polarization time <sup>2</sup> [min.]
$t_{\text{depol}} > 30$	360
$30 > t_{\text{depol}} > 15$	$6 \times t_{\text{depol}}$
$15 > t_{\text{depol}} > 5$	$4 \times t_{\text{depol}}$
$t_{\text{depol}} < 5$	$5 \times t_{\text{depol}}$

## F.4 Dissolved Oxygen Probe Specifications

Table F.2: 12mm Mettler Toledo® Inpro® 6800 Dissolved Oxygen Probe Specifications, Adapted from (Toledo, 2013)

<b>Measurement principle</b>	Amperometric, Polarographic
<b>Working conditions</b>	
Pressure resistance measurement	0.2 - 6 bar absolute
Mechanical pressure resistance	max. 12 bar absolute
Measuring temperature range	0-80 °C
Temperature range	-5-140 °C (sterilizable, autoclavable)
<b>Construction</b>	
Temperature compensation	Automatic with built-in RTD
Cable connection	VarioPin (IP68) straight or angled, K8S straight (digital ISM sensors)
O-ring material	Silicone FDA and
USP	VI approved
Membrane material	PTFE/Silicone/PTFE (reinforced with steel mesh)
Wetted metal parts	Stainless steel, Special material on request
Quick disconnect interior body	Standard
Cathode	Pt
Anode	Ag
Guard ring	No
<b>Dimensions</b>	
Sensor diameter	12 or 25 mm
Immersion length for 12mm sensor	70, 120, 220, 320, 420 mm
Immersion length for 25mm sensor	80,160, 260, 360 mm
<b>Performance</b>	
Detection limit	6 ppb
Accuracy	±1 % + 6 ppb of reading in liquids
Response time at 25°C	(air/N <sub>2</sub> ) 98 % of final value <90 s
Sensor signal in ambient air (25 °C)	50-110 nA
Residual signal in oxygen-free medium	<0.1% of the signal in ambient air
Maximum flow error	0.05
<b>Certification</b>	
EHEDG, 3A	Yes
3.1 B (EN 10204.3/1.B)	Yes
ATEX certificate	Yes
FM Approval	Yes
FDA/USP VI	Yes
Quality control	Yes

## Appendix G. Dissolved Oxygen Transmitter Calibration

The transmitter used for all measurements was a Mettler Toledo M300 single channel 1/4 DIN DO meter. A single-point sensor calibration was used to calibrate the transmitter. Calibration was completed every 24 hours, following repolarisation of the electrolyte. An air calibration was used which required the barometric pressure and relative humidity. These values were obtained from the weather station at the University of Stellenbosch Engineering Faculty (<http://weather.sun.ac.za/>) on a daily basis. The calibration procedure in the Operating Instructions (Toledo, 2013) was followed.

### G.1 Dissolved Oxygen Transmitter Specifications

Table G.1: Dissolved Oxygen Transmitter M300 Specifications, Adapted from (Toledo, 2013)

M300 DO Transmitter	
Measuring current range	0 to 900 nA
Concentration range	0.00 to 50.00 ppm (mg/l)
Temperature input	NTC 22 k $\Omega$
Temperature measuring range	-10 to 80 °C
Sensor maximum distance Analogue:	20 m
DO resolution	Auto / 0.001 / 0.01 / 0.1 / 1 (can be selected)
DO accuracy	$\pm 0.5\%$ of full scale reading
Temperature resolution	Auto / 0.001 / 0.01 / 0.1 / 1 °C
Temperature accuracy	$\pm 0.25$ °C
Polarization voltage	-675 mV (for analogue sensors)
Dimensions (housing - H x W x D)	96 x 96 x 140 mm
Front bezel - (H x W)	102 x 102 mm
Max. depth	125 mm (excludes plug-in connectors)
Weight	0.6 kg
Material	ABS/polycarbonate
Ingress rating	IP 65 (front)/IP 20 (housing)

## Appendix H. Derivation of the Second Order Probe Response Model

Calculation of  $K_L a$  was based on the response DO concentration to a step change in sparge gas (Equation H.1). The first order response assumes the DO probe has no response lag, meaning that  $C_L = C_P$  (Equation H.2).

$$\frac{dC_P}{dt} = K_L a (C_L^* - C_L) \quad (\text{H.1})$$

$$\frac{dC_P}{dt} = K_L a (C_L^* - C_P) \quad (\text{H.2})$$

The response lag of the DO probe can be modelled according to the first order relationship described (Equation H.3) (Aiba and Huang, 1969).

$$\frac{dC_P}{dt} = K_P (C_L - C_P) \quad (\text{H.3})$$

Incorporation of Equation H.3 into Equation H.2 yields the second order model. To do so, dimensionless quantities, as defined in Equations H.4 and H.5, can then be introduced (Fuchs *et al.*, 1971).

$$Y_P = \frac{C_P^* - C_P}{C_P^* - C_{P0}} \quad (\text{H.4})$$

$$Y_L = \frac{C_L^* - C_L}{C_L^* - C_{L0}} \quad (\text{H.5})$$

Substituting Equations H.4 and H.5 into Equations H.2 and H.3 respectively:

$$\frac{dY_L}{dt} = -K_L a \cdot Y_L \quad (\text{H.6})$$

$$\frac{dY_P}{dt} = K_P (Y_L - Y_P) \quad (\text{H.7})$$

Separating the variables in Equations H.6 and H.7 to prepare for integration:

$$\frac{dY_L}{Y_L} = -K_L a \cdot dt \quad (\text{H.8})$$

$$\frac{dY_P}{dt} = K_P \cdot Y_L - K_P \cdot Y_P \quad (\text{H.9})$$

Integrating Equation H.8 yields Equation H.10, where  $I$  is the integration constant.

$$\begin{aligned} \ln(Y_L) &= I \cdot -K_L a \cdot t \\ Y_L &= I \cdot e^{-K_L a t} \end{aligned} \quad (\text{H.10})$$

Equation H.10 can then be substituted back into Equation H.9 to yield Equation H.11.

$$\frac{dY_P}{dt} = K_P \cdot I \cdot e^{-K_L a t} - K_P \cdot Y_P \quad (\text{H.11})$$

Equation H.11 can then be solved using non-homogeneous differential equations and the separation of variables as shown in Equations H.12 through H.23 (Manyuchi, 2010).

$$\frac{dY_P}{Y_P} = K_P \cdot dt \quad (\text{H.12})$$

Integration of Equation H.12 yields Equation H.13, where  $J$  is an integration constant.

$$\begin{aligned} \ln\left(\frac{Y_P}{Y_{P0}}\right) &= J \cdot K_P \cdot t \\ Y_P &= J \cdot e^{-K_P t} \end{aligned} \quad (\text{H.13})$$

Equation H.13 is the function form, and can be represented in the associated complimentary form (Equation H.14):

$$Y_C = A' e^{-B' t} \quad (\text{H.14})$$

It therefore follows that the complimentary form of Equation H.11 is Equation H.15

$$dY_C + K_P \cdot Y_C = K_P \cdot A' e^{-B' t} - A' B' e^{-B' t} \quad (\text{H.15})$$

However, the following is known:

$$dY_C + K_P Y_C = K_P \cdot I e^{-K_L a t} \quad (\text{H.16})$$

Therefore, Equations H.15 and H.16 can be equated and simplified to yield H.17

$$(K_P \cdot A' - A' B') = K_P \cdot I \quad (\text{H.17})$$

Since  $B' = K_L a$ , Equation H.17 can be rearranged to give H.18.

$$A' = \frac{K_P I}{K_P - K_L a} \quad (\text{H.18})$$

Setting  $Y'$  as the complimentary form of Equation H.11 and including the probe response lag, Equation H.19 is obtained.

$$Y' = Y_C + Y_P \quad (\text{H.19})$$

Substituting Equations H.13 and H.15 into Equation H.19 yields Equation H.20.

$$Y' = J \cdot e^{-K_P t} + A' e^{-B' t} \quad (\text{H.20})$$

Incorporating Equation H.18 into Equation H.20 yields Equation H.21.

$$\begin{aligned} Y' (K_P - K_L a) &= (K_P - K_L a) \cdot J \cdot e^{-K_P t} + K_P \cdot I \cdot e^{-K_L a t} \\ Y' &= \frac{1}{(K_P - K_L a)} \left( J (K_P - K_L a) \cdot e^{-K_P t} + K_P \cdot I \cdot e^{-K_L a t} \right) \end{aligned} \quad (\text{H.21})$$

Substituting  $J = \frac{-K_L a}{(K_P - K_L a)}$  into Equation H.21 yields Equation H.22, and setting  $I = 1$

$$Y' = \frac{1}{(K_P - K_L a)} \left( -K_L a \cdot e^{-K_P t} + K_P \cdot e^{-K_L a t} \right) \quad (\text{H.22})$$

Since  $Y'$  is defined as the DO with and incorporated probe response lag, it holds that  $Y' = \frac{C_P^* - C_P}{C_P^* - C_{P0}}$ . Substituting this into Equation H.22, and setting the initial concentration,  $C_{P0}$ , to zero, the second order model incorporating a probe response lag is given in Equation H.23.



$$\frac{C_P}{C_P^*} = 1 - \frac{1}{(K_P - K_L a)} (K_P \cdot e^{-K_L a t} - K_L a \cdot e^{-K_P t}) \quad (\text{H.23})$$